Experimental and Gyrokinetic Studies of Impurity Transport in the Core of Alcator C-Mod Plasmas

by

Nathaniel Thomas Howard

B.S. Physics (2005)
University of Illinois at Urbana-Champaign

Submitted to the Department of Nuclear Science and Engineering
in partial fulfillment of the requirements for the degree of

Doctor of Philosophy

at the

MASSACHUSETTS INSTITUTE OF TECHNOLOGY

June 2012

Author .....
Department of Nuclear Science and Engineering
May 2, 2012

Certified by .....
Martin Greenwald
Associate Director of the Plasma Science and Fusion Center
Thesis Supervisor

Certified by .....
Dennis Whyte
Professor, Department of Nuclear Science and Engineering
Thesis Reader

Accepted by .....
Mujid S. Kazimi
TEPCO Professor of Nuclear Science and Engineering
Chair, Department Committee on Graduate Students

Experimental and Gyrokinetic Studies of Impurity Transport in the Core of Alcator C-Mod Plasmas

by

Nathaniel Thomas Howard

Abstract

Using a unique set of diagnostics and modeling tools, a comprehensive study of impurity transport was performed on Alcator C-Mod L-mode discharges. A new, multi-pulse laser blow-off system was designed and constructed to introduce trace amounts of non-recycling, non-intrinsic, impurities in the plasma edge. This system was coupled with an x-ray crystal spectrometer, a single chord x-ray/ultraviolet spectrometer, and measurement of the laser blow-off neutral source at the plasma edge to provide full, time-evolving, radial profiles of a single impurity charge state. An iterative χ^2 minimization scheme was created to infer the experimental impurity transport coefficients and their uncertainty by minimizing the difference in the measured and STRAHL simulated emission. These measurements and data analysis methodology allowed for determination of impurity transport coefficient profiles with realistic errors from $0.0 \leq r/a \leq 0.6$. The gyrokinetic code, GYRO, was use to analyze the same discharges. Motivated by linear stability analysis and a rigorous assessment of simulation sensitivities, nonlinear gyrokinetic simulations were performed such that small modifications of the Ion Temperature Gradient (ITG) drive term, a/L_{T_i} were made to match the simulated ion heat flux, Q_i, to the experimental value. These simulations demonstrated simultaneous, quantitative agreement with experiment across the simulation domain in the ion heat and impurity particle transport channels, and indicated the possibility of missing electron dynamics from the nonlinear gyrokinetic simulation. A study of I_p scaling used four discharges, constituting a scan of I_p from 0.6 to 1.2 MA. These discharges displayed a clear reduction of the experimental impurity diffusion and inward convection, allowing for qualitative and quantitative comparison of experimental with gyrokinetic simulation. Linear stability analysis and high fidelity, global ($0.29 \leq r/a \leq 0.62$), nonlinear GYRO simulation of ion scale turbulence ($k_\theta \rho_s \leq 1.15$) were performed on these discharges with the result that nonlinear gyrokinetic simulation was generally able to reproduce both quantitative values and trends for the measured decrease in impurity diffusion and inward convection observed experimentally. Initial analysis of three discharges operated at various levels of ICRH input power displayed a reduction of the experimental impurity diffusion coefficient with input power. An in-depth linear stability analysis suggests a transition of the turbulence character (ITG to TEM) with input power which may explain changes in the measured diffusion.

Thesis Supervisor: Martin Greenwald
Title: Associate Director of the Plasma Science and Fusion Center

Thesis Reader: Dennis Whyte
Title: Professor, Department of Nuclear Science and Engineering

Acknowledgments

During my six and a half years as a graduate student I interacted with a number of people who directly and indirectly contributed to the thesis work presented here. I want to take just a moment to acknowledge these people.

I would first like to thank my advisor Dr. Martin Greenwald. His door was always open and he provided me with unwavering encouragement and guidance through the rough spots and the good times during my thesis work. I am continually amazed by his physical intuition and his ability to see the best path forward (even when it is far from obvious to me). I want to thank him for always setting me on the right course. I feel extremely fortunate and I am extremely grateful that I had the opportunity to learn from him and to work with him. He has been a truly excellent mentor.

I would also like to specifically thank Professor Anne White, and doctors David Mikkelsen, and Darin Ernst for providing me with constructive feedback and guidance, taking time from their schedules to help me, always having an open ear, and for sharing their knowledge of plasma turbulence with me. I hope I can continue to work with all of them in the future and continue to learn from them as well. It is also important that I recognize the contributions of Mark Iverson and Ed Fitzgerald to this work. They both spent hours working with me on the laser blow-off system and without them its construction would have never been possible. I would like to specifically thank Dan Casey, Arturo Dominguez, and Istvan Cziegler for their friendship over the years. They were the best officemates/classmates that I could have asked for and it is without a doubt that their friendship made the years go by faster and made graduate school much more enjoyable. I hope we continue to be friends in the years to come.

I want to thank all of the scientists, engineers, technicians, and other graduate students on Alcator C-Mod. Most of them, in one way or another, contributed to the completion of this thesis work. I would like to thank John Rice, Yuri Podpaly, Amanda Hubbard, and Yunxing Ma for providing me with much of the data used throughout this thesis. A special thanks is in order to Matt Reinke for providing

the ion temperature, toroidal rotation, and calcium brightness data from HiReX Sr which is central to much of this work. Additionally, the vacuum shop technicians, Tom Toland and Ronnie Rosati, deserve recognition for their help and installation of the laser blow-off system on C-Mod.

Finally, I want to thank my Mom, Maggie Howard, my Dad, Tom Howard, my sister, Caitlin Kirby, and my girlfriend, Daniela Marcus. I know that you are all my biggest fans and have been there for me though everything. No matter what was happening, there was always one constant: I always knew that you were a phone call away, I always knew you would have an open ear, and always knew that you were rooting for me. Whether things were good and bad, you were there for me. Daniela, I know the waiting has been tough, but you stood by me and supported me through the last three and a half years and I hope you will continue to do so for years to come. Thank you for always being there. I love all of you.

Contents

List of Figures

List of Tables

Chapter 1

Introduction

1.1 Nuclear Fusion

Even before the first test of the hydrogen bomb in 1952, there were discussions on harnessing controlled nuclear fusion as an energy source. In turn, these spawned national and international programs to master the underlying science and technology. Unlike nuclear fission which harnesses the energy released from the splitting of massive atoms, nuclear fusion seeks to harness the energy released by fusing the nuclei of light atoms. Fusion's promise of highly energetic reactions without the long-lived radioisotopes and waste products which plague nuclear fission, motivates its study as an alternative energy source. However, creating controlled fusion reactions with sufficient frequency to represent a viable energy source is far from a simple task. Currently the most promising approach for harnessing fusion for steady state reactor operation is the confinement of high temperature plasma using magnetic fields. The magnitude of the fusion cross sections at relatively low temperatures ($\sim 10-100$ keV) make three particular fusion reactions of particular interest for energy production. These are:

$$D + D \rightarrow T(1.01MeV) + H(3.03MeV) \tag{1.1}$$

$$D + D \rightarrow He^3(0.82MeV) + n(2.45MeV) \tag{1.2}$$

$$D + T \rightarrow He^4(3.5MeV) + n(14.1MeV) \tag{1.3}$$

In each of these reactions the fusion "fuel" is in the form of the hydrogen isotopes deuterium and tritium. The relative abundance of deuterium in water makes D+D reactions desirable. However, the temperature dependence of the D+T fusion cross section makes it energetically a much more favorable reaction. As a result, the first fusion reactors will most likely be based on this reaction.

We will refer to a "pure" fusion plasma as one which consists only of fuel ions. In the case of a deuterium/tritium plasma, these isotopes constitute what we will call the "main" ions and have some significant probability of undergoing a fusion reaction in reactor relevant conditions (volume averaged temperature $\sim$ 15 keV). In contrast, any ion or neutral species present in the plasma which is not a main ion is referred to as an impurity species. Unlike the main ion species, the probability that these species undergo any type of fusion process is either effectively zero or energetically impossible in experimentally attainable conditions. Therefore, these ions do not contribute to energy production.

1.2 Nuclear Fusion in Tokamaks

Currently, the most successful means of creating magnetically confined controlled fusion reactions is provided by the tokamak. The word *tokamak* is a Russian acronym which means toriodal chamber-magnetic. As the name implies, this is a device characterized by a toroidal vacuum vessel with large external magnetic field coils. The basic geometry and fields of a tokamak are summarized in Figure 1-1. The combined result of the externally applied and self generated magnetic fields is a helical field structure, similar to the windings on a barber pole. This field configuration confines the high temperature plasmas necessary for the generation of controlled nuclear fusion.

The conditions necessary for obtaining fusion ignition, where the total heating power produced by fusion alpha (He++ ion) particles equals the loss rate from the plasma, are well defined for a 50:50 deuterium and tritium plasma. The necessary criteria for this condition were first established by in 1957 by Lawson [5]. To under-

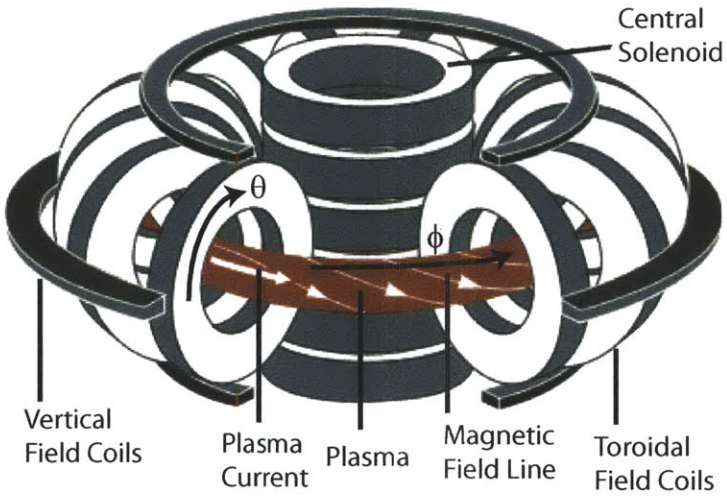

Figure 1-1: The basic layout of a tokamak. Figure taken from [1]

stand this criteria, we must first define the energy confinement time (in sec) for a fusion plasma as:

$$\tau_E = \frac{W}{P_{loss}} \tag{1.4}$$

Where W is the plasma stored energy and P_{loss} (in Watts) is the power loss from the system. We can easily write the plasma energy density as $W/V = 3nkT$, with T in eV, n in m^{-3}, and $k = 1.6 \times 10^{-19}$ J/eV. The fusion power density is a function of both the plasma density and temperature. When the self heating fusion power density due to alpha particles equals or exceeds the power loss per unit volume, the following criterion is established as the ignition condition:

$$n_i \tau_E \geq \frac{12}{E_\alpha} \left(\frac{T}{< \sigma v >} \right) \tag{1.5}$$

Here $< \sigma v >$ is the D-T fusion rate coefficient (in m^3/s) and E_α is the kinetic energy of the fusion alpha particle ($\sim$ 3.5 MeV). We see that the product of the ion density and energy confinement time must exceed a temperature dependent threshold value for the energy losses to be matched by the fusion alpha power. For the D-T reaction, the minimum of the function, $\frac{T}{<\sigma v>}$ occurs at a plasma temperature around 25 keV with the requirement that $n_i \tau_E \sim 1.5 \times 10^{20}$ m^{-3}·s.

In order to achieve long energy confinement times and ultimately ignition conditions, cross field transport in fusion plasmas must be understood. Cross field transport is the loss of energy, particles, and momentum across magnetic field lines. In the plasma core, transport is thought to result from one of two sources: 1) the collisions of particles in a toroidal geometry and 2) plasma turbulence driven unstable by free energy in the plasma's density and temperature gradients. These processes will be described in more detail in Chapter 2 and the remainder of this thesis will attempt to understand the physical mechanisms which dominate the loss of energy and impurities from the plasma core.

To date, no tokamak has achieved the conditions necessary for ignition. However, it is believed that ITER, a reactor-scale tokamak currently under construction in Cadarache, France will take a large step towards achieving such conditions. Upon its construction, ITER will be the world's largest tokamak and will attempt to demonstrate the creation of burning plasma conditions for the first time (i.e. when the plasma is dominantly self heated by alphas, even though it is not yet ignited). Much of the current fusion research worldwide is in support of this device which is scheduled to come online in 2018.

1.3 The Alcator C-Mod Tokamak

A number of smaller scale tokamaks are currently in operation worldwide. All work described in this thesis was performed on the Alcator C-Mod tokamak located at the MIT Plasma Science and Fusion Center. An engineering drawing of the tokamak and support structure is shown in Figure 1-2. This tokamak's approach to the creation of controlled thermonuclear fusion uses a compact, high magnetic field, device to reach the high densities and temperatures needed for reactor relevant conditions. Currently, Alcator C-Mod has the highest attainable magnetic field of any tokamak in the world, reaching values of up to 8.1 Tesla. However, the machine is typically operated at the slightly lower magnetic field of 5.4 Tesla, nominally the operating point of the next generation fusion devices such as ITER. The high field and compact

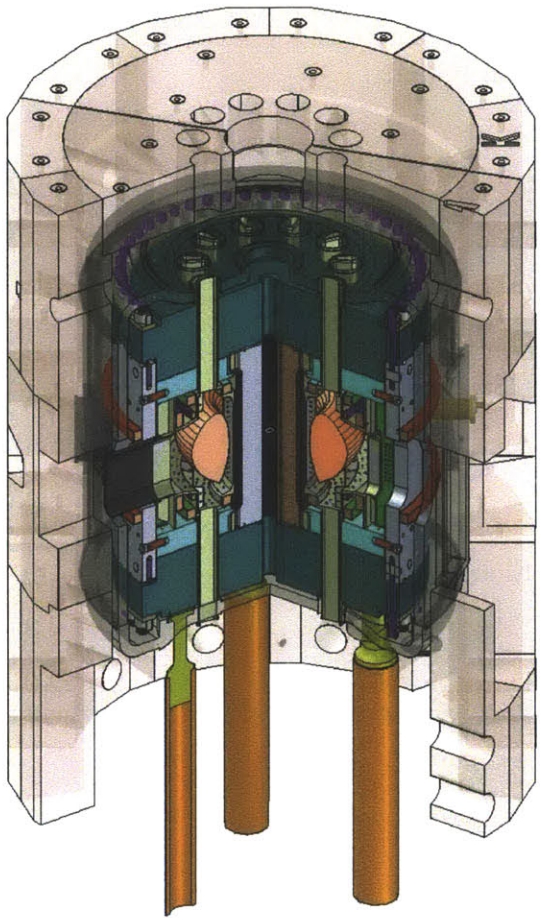

Figure 1-2: Pictured is a computer generated model of the Alcator C-Mod Tokamak

size of C-Mod allows for operation at higher densities than in most other tokamaks. Central densities $> 3 \times 10^{20} m^{-3}$ are readily attained. Electron temperatures of several keV are routinely achieved in the plasma core through both ohmic and radiofrequency heating Ion Cyclotron Resonance Heating (ICRH) and Lower Hybrid (LH)). The high densities and temperatures at which the machine is operated allowed it to achieve the highest plasma pressure, in a magnetic confinement system, recorded to date. The main machine parameters are summarized in the chart below:

Alcator C-Mod Operational Parameters		
Operational Period	-	1992-present
Major Radius	m	0.68
Minor Radius	m	0.22
Toriodal Field	T	2 - 8.1
Plasma Current	MA	0.3 - 1.5
Line Averaged Density	10^{20} m^{-3}	0.2 - 5.0
Central Electron Temperature	keV	9.0
Ion Cyclotron Heating	MW	Up to 5.5
Lower Hybrid Heating	MW	Up to $\sim$ 1.0
Plasma Elongation	-	1.0 - 1.8
Plasma Triangularity	-	0.3 - 0.9
Plasma Duration	s	2.0

The extensive diagnostic suite operational on Alcator C-Mod makes it ideal for the impurity transport studies described here. Recent diagnostic upgrades [6, 7] have improved the accuracy of both electron and ion temperature profile measurements. These upgrades are essential for high quality modeling of transport processes in the plasma core ($r/a \leq 0.6$) and were utilized in the both the experimental and simulation work presented in this thesis. C-Mod also features a wide range of spectroscopic diagnostics which allow for temporally and spatially resolved profiles of intrinsic and non-intrinsic impurity species in the core of the device. The multi-pulse laser blow-off system and impurity source measurement, developed as part of this thesis work, complement existing spectroscopic diagnostics to provide a well characterized source of non-intrinsic, non-recycling impurities at the plasma edge. This allows for some of the most detailed impurity transport studies to date. A complete description of the diagnostics used in this work is presented in Chapter 3.

1.4 Motivation for the Study of Impurities in Tokamaks

1.4.1 Impurity Sources in a Tokamak

Impurities are a natural part of tokamak operation and are introduced into the plasma through a variety of means. Most commonly, impurities enter the plasma due to the interaction of high temperature plasma with material surfaces such as the inner wall, RF antennae, and the divertor. The boundary plasma of fusion devices has sufficiently high temperatures ($\sim$ 10 - 100 eV) to cause sputtering and removal of material atoms from surfaces. The power density in this region is also sufficient to cause thermal removal of materials through melting and evaporation. Plasma surface interactions are an active area of research which studies the response of materials to harsh plasma environments and tries to minimize impurity sources. Molecules of oxygen and nitrogen may also be introduced through insufficient vacuum conditions prior to plasma operation. However, advances in vacuum technology and good vacuum practices have minimized this source in modern tokamaks. In the unique conditions provided by a burning plasma, an additional source of impurities is present in the plasma core. Charged fusion products of the D+T fusion reaction, namely alpha particles, are confined by the magnetic field and remain in the plasma core following a fusion event; this alpha "ash" is required since fusion alphas provide the source of plasma self-heating. Like impurities from materials surfaces and air, these particles are unable to undergo fusion reactions and therefore considered impurities in the fusion plasma.

1.4.2 The Effect of Impurities on Ignition

Equation 1.5, the Lawson criterion for a D-T tokamak plasma, can be used to illustrate the effect of impurities on the realization of fusion energy. Minimum levels of the key plasma parameters, density, temperature, and energy confinement time are needed to satisfy this criterion and to achieve the conditions necessary for fusion energy. The

presence of impurities directly affects our ability to achieve these parameters, making their study an essential area of research in fusion plasma physics. The following sections will address these parameters individually and how the presence of impurities effects them.

1.4.3 Plasma Density, n_i

The effect of impurities on the main ion density is perhaps the most straightforward motivation for the study of impurities in tokamak plasmas. Accumulation of impurities in the plasma core can lead to fuel dilution and decreased fusion power density. For a pure plasma, consisting only of deuterium and tritium fuel, each nucleus has only one proton and the electron and main ion densities can be simply written as:

$$n_e = n_i = n_D + n_T \tag{1.6}$$

Here the quantities n_D and n_T represent the deuterium and tritium densities respectively and n_i represents the total main ion density. In practice, fusion plasmas are not pure. Since global quasineutrality of the plasma must be maintained ($\sum_a n_a e_a = 0$) the addition of an impurity species whose charge is greater than +1 can greatly reduce the main ion density, n_i, at fixed electron density. For a plasma with both main ions and an impurity species of arbitrary Z, we have:

$$n_i = n_e - Z n_z \tag{1.7}$$

It is easily seen that for $Z \gg 1$ small impurity densities can displace a large number of main ions, thus reducing the population of particles able to undergo fusion reactions. Modern tokamaks can contain impurities species present can ranging from He (Z=2) to W (Z=74) making concerns of high-Z fuel dilution of particular relevance.

The deleterious effect of impurities on the main ion density propagates to the overall fusion power density. Consider the fusion power density for a pure 50:50

deuterium and tritium plasma. We can write this expression as:

$$P_f = \frac{n_i^2}{4} < \sigma_f v > kE_\alpha \tag{1.8}$$

Where P_f is the total fusion power density, $< \sigma_f v >$ is the fusion rate coefficient, and E_α is the energy of the fusion alpha particles. If we consider plasmas with an impurity species of arbitrary charge Z, the expression for the fusion power density then becomes:

$$P_f = \frac{n_i^2}{4} < \sigma_f v > kE_\alpha = \frac{n_e^2}{4}(1 - \frac{Zn_z}{n_e})^2 < \sigma_f v > kE_\alpha \tag{1.9}$$

This illustrates the effect of impurity ions on a reactor's fusion power density, namely the quadratic dilution factor caused by the inclusion of impurities in the plasma core. Dilution effects associated with the core accumulation of impurities decrease the number of fuel ions available to undergo fusion reactions which can significantly limit the viability of fusion reactors. However, impurity contamination in a fusion reactor is both unavoidable and, as it turns out, necessary. Many of the reaction products of the fusion reactions can act as diluting species. The fusion reaction between deuterium and tritium (Equation 1.1) creates not only a free neutron which is promptly lost from the tokamak, but also a fusion alpha particle, He^4. In a reactor, this fusion product is the main source of heat and must transfer its energy to the bulk plasma. However, this fusion "ash" is unable to undergo fusion in reactor relevant conditions and is effectively an impurity within the fusion plasma. The buildup of fusion alpha particles can dilute the main ion species and decrease the fusion power density. For this reason, understanding the physical mechanisms which enhance the outward flux of impurities is of great interest in fusion plasma physics.

1.4.4 The Energy Confinement Time, τ_e

Impurities play a critical role in the energy balance of the reactor. The presence of impurities results in radiative loss of energy, degradation of the plasma's energy

confinement time, and consequently a drop in the overall plasma temperature. These losses take the form of bremsstrahlung (free-free transitions) and radiation resulting from free-bound atomic processes such as line radiation, ionization, and recombination. Under normal operating conditions, radiative contributions from the last of these mechanisms is usually small. In contrast, for significant impurity densities, the total power radiated through bremsstrahlung can reach non-negligible fractions of the total input power. The mean free path for bremsstrahlung reabsorption by the plasma is typically much greater than the typical device size, implying that emitted radiation is lost completely from the plasma. To better understand the radiation effects of impurity accumulation, let us first define the effective plasma charge, Z_{eff} as:

$$\mathrm{Z_{eff}} = \frac{\sum_j Z_j^2 n_j}{\sum_j Z_j n_j} = \frac{\sum_j Z_j^2 n_j}{n_e} \tag{1.10}$$

For a pure D+T plasma the effective charge is necessarily equal to 1. The total Bremsstrahlung power density is derived through the analysis of Coulomb scattering and arises as a result of electron acceleration during collision events. The expression for the total Bremsstrahlung radiated power is given by [8, 2, 9]:

$$P_b = 5.35 \times 10^3 Z_{\text{eff}} n_{20}^2 T_{keV}^{0.5} \text{ W/m}^3 \tag{1.11}$$

The power radiated via Bremsstrahlung is proportional to plasma effective plasma charge, $\mathrm{Z_{eff}}$, which scales as the square of the impurity charge.

Due to the their desirable characteristics in power handling, refractory metal, high-Z plasma facing components have been proposed for use in future fusion devices such as ITER [10]. Yet the presence of high-Z impurity densities can result in fuel dilution and in significant radiative power loss. Even at fusion temperatures, higher Z atoms are not fully stripped of their electrons and can radiate power copiously through free-bound processes. The plasma's impurity content, especially of high-Z materials, must therefore be kept to a minimum in order to obtain the criterion for a burning plasma. Figure 1-3. illustrates the effect of impurity content on reactor power balance [2]. In this figure, f is equal to the ratio of impurity density to main

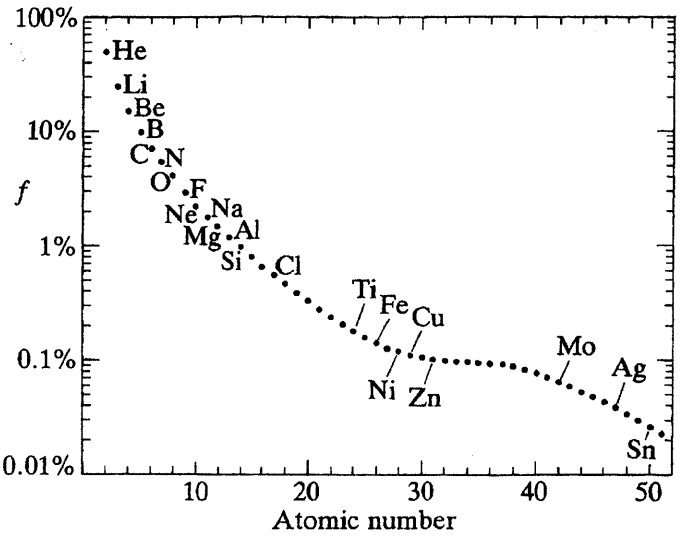

Figure 1-3: The impurity fraction required to radiate away 50% of the total alpha power at 10 keV for a wide range of impurity Z is plotted. Figure taken from [2]

ion density, n_z/n_i. At an assumed temperature of 10 keV, Figure 1-3 demonstrates the impurity fraction, f, required to radiate away 50% of the total power generated by alpha particles in a typical D+T reaction when contributions of Bremsstrahlung and other atomic processes are considered. This plot illustrates the important role impurity accumulation, especially of high-Z elements, can play on the reactor power balance and motivates the study of impurity transport as a means of understanding and reducing the plasma's impurity content. Take molybdenum for example. A plasma containing a molybdenum density of only $.001n_e$ can radiate away 50% of the alpha power at 10 keV. This implies that if all other quantities remained fixed, a doubling of the energy confinement time is required meet the ignition condition. The need for a factor of two increase in τ_E is further complicated by the fact that energy and impurity confinement are often observed to increase together. These consequences make understanding impurity transport crucial for next step fusion devices.

1.4.5 The Study of Impurity Transport

The preceding sections explained how core impurity accumulation can adversely affect a reactor's performance through degradation of the fusion power density and its energy confinement time. Since it is generally desirable to reduce or control impurity content in the plasma, it is clear that understanding the physical mechanisms which contain and expel impurities is of great importance to the field of fusion plasma physics. The movement of impurities both along and across the confining magnetic field, defines the field of impurity transport. With a better understanding of the physical processes dictating impurity transport and the effect of engineering parameters on these process, plasmas can be optimized to reduce core impurity content through cross field transport processes. The work presented here focuses on understanding the physics of impurity transport through accurate experimental measurement and cutting edge computer simulations.

1.5 The Question of this Thesis

Discussion in the previous sections motivates the study of impurity transport in fusion plasmas. A physical understanding of impurity transport may be obtained through experimental study of impurity transport in existing tokamak plasmas. However, it is not enough to simply observe existing experiments. The high cost of new machine construction motivates the need for first principles (*i.e.* from the Maxwell/Boltzmann equations) predictive models for energy, particle, and impurity transport which allow for *a priori* determination of plasma performance and can guide engineering decisions for next generation fusion reactors.

Measured transport levels have been shown to exceed the predictions of neoclassical theory in almost all tokamak operational scenarios [11]. In the core of tokamak plasmas this higher level of observed "anomalous" transport, is generally attributed to the presence of drift wave type plasma turbulence [12]. The gyrokinetic model, implemented by a number of modern turbulence codes, is thought to contain sufficient physics to accurately simulate drift wave turbulence in the confinement zone of toka-

mak plasmas and is the leading candidate for a predictive transport model. Yet before such a model can be applied in a predictive capacity, it must be validated against experiments. This requires rigorous comparison with observations of all transport channels; at all levels of the primacy hierarchy (*i.e.* fluctuations, fluxes, and profiles) [13, 14].

Previous gyrokinetic impurity transport work has aimed predominantly at analyzing experimentally observed transport coefficients qualitatively using quasilinear models of impurity transport [15, 16]. The research presented here advances the field of impurity transport by comparing cutting-edge turbulence models to experimental measurement. The first comparisons of nonlinear gyrokinetic simulation with experimental impurity transport ever performed are described here. The question asked in this thesis work is: **Can we develop new diagnostic techniques and utilize the existing, unique set of diagnostics on the Alcator C-Mod tokamak to make more accurate measurement of experimental impurity transport? If so, can the gyrokinetic model of plasma turbulence help interpret experiment and both qualitatively and quantitatively reproduce the measured impurity transport levels?** The remaining chapters of this thesis attempt to provide answers to these questions.

1.6 Organization of this Thesis

The remainder of the thesis is organized as follows:

- **Chapter 1** - This chapter introduced the topic of nuclear fusion and the fundamental processes at the heart of future fusion devices. The leading magnetic confinement concept, the tokamak was described, including a description of the Alcator C-Mod tokamak located at MIT's Plasma Science and Fusion Center. A brief description of the impurities effects in tokmakas was provided to motivate the study of impurity transport and to introduce the topic of this thesis.

- **Chapter 2** - This chapter provides an overview of existing work in the field

of impurity transport performed both on the Alcator C-Mod tokamak as well as on devices worldwide. The theory of classical particle transport and an overview of the neoclassical theory of impurity transport is presented in this section. Finally, brief descriptions of the drift wave turbulence believed to be responsible for the observed levels of heat and particle transport are presented.

- **Chapter 3** - This chapter overviews all of the experimental tools that are used for studying core impurity transport on the Alcator C-Mod tokamak. The focus of this chapter is the multi-pulse laser blow-off system. This system was designed and constructed as part of this thesis work and enabled the impurity transport studies presented here. Descriptions of the experimental methods and spectroscopic and profile diagnostics used in this work are covered here in detail.

- **Chapter 4** - This chapter covers the modeling tools used to analyze impurity transport experiments. The new synthetic diagnostic developed around the impurity transport code STRAHL and the methodology employed for determining the experimental impurity transport is presented. A brief introduction to the power balance code TRANSP and its use in preparation of gyrokinetic code inputs is explained. Finally, an overview of the gyrokinetic model and its implementation in the GYRO code can be found in this chapter.

- **Chapter 5** - This chapter covers the first quantitative comparison of experimental and gyrokinetic simulated impurity transport. The analysis of a single L-mode, experimental discharge is described in detail. Experimental levels of impurity transport are compared with the simulated levels of impurity transport predicted by the GYRO code. An extensive analysis into the experimental uncertainties and their propagation to the simulated impurity transport output from the GYRO code is presented in order to make a thorough quantitative comparison between theory and experiment.

- **Chapter 6** - This chapter uses both experimental techniques and gyrokinetic simulation to understand the changes in impurity transport seen at different

values of plasma current, I_p, a parameter which strongly affects energy confinement. A series of dedicated plasma discharges are analyzed using experimental techniques and linear and global nonlinear gyrokinetic simulation. Both quantitative and qualitative comparisons of the experiments are made with nonlinear gyrokinetics to asses the ability of the code to reproduce the experimental trends found with changes in engineering parameters.

- **Chapter 7** - This chapter provides the initial results of analysis performed on experiments investigating the dependence of impurity transport on input power, a parameter which along with plasma current is known to affect energy confinement. Analysis of three discharges was performed using linear gyrokinetics and the STRAHL code. Due to incomplete data sets, this analysis was not extended to nonlinear gyrokinetic simulation. However, the results are suggestive of interesting changes in the underlying turbulence physics.

- **Chapter 8** - This chapter provides a summary of the content presented in this thesis and the conclusions drawn on impurity transport physics. A discussion of future work and new directions for impurity transport studies on Alcator C-Mod are also provided.

Chapter 2

Impurity Transport in Tokamaks

This chapter contains a basic description of the transport processes in magnetically confined plasmas. We will begin by examining classical collisional transport processes and eventually present the results of neoclassical transport theory. A brief introduction to the turbulent modes thought to dominate the observed transport levels will be presented with some approximations. Finally, a brief introduction to the gyrokinetic model and existing results in experimental impurity transport will be presented. This chapter serves as an introduction into the transport processes which will be referenced throughout the remainder of this thesis.

2.1 Classical Collisional Transport

A full treatment of classical transport is outside the scope of this thesis. However, the basic concepts are introduced. The reader is referred to the of many texts for the full treatment, [17, 18]. The description presented here will follow Helander and Sigmar [17]. To begin the discussion of classical transport processes, first consider a cylindrical plasma consisting of 2 species, electrons and ions. By poloidal symmetry all derivatives in the θ direction vanish. The magnetic field is in the z direction, $\vec{B} = B\hat{z}$, and background profiles are assumed to be functions of the radial coordinate only.

For a species, a, the equation of motion can be written in the following form:

$$m_a n_a \frac{d\vec{v_a}}{dt} = e_a n_a (\vec{E} + \vec{v_a} \times \vec{B}) - \nabla p_a - \nabla \cdot \vec{\pi}_a + \vec{R}_{ab} \tag{2.1}$$

Here the quantity $\vec{v}_a$ is the fluid velocity for the species, $d/dt \equiv (\partial/\partial t + \vec{v}_a \cdot \nabla)$ is the convective derivative, and π is the stress tensor. The last term of this equation, $\vec{R}_{ab}$, is the friction force term between species a and species b. Defining two directions to be $\parallel$ and $\perp$ to the magnetic field, we can take the cross product of the momentum equation with $\vec{B}$ to obtain the $\perp$ velocity. The expression for the $\perp$ velocity can now be written as:

$$\vec{v}_\perp = \frac{\vec{E} \times \vec{B}}{B^2} + \frac{\vec{b} \times (\nabla p_a + \nabla \cdot \vec{\pi_a} - \vec{R}_{ab} + m_a n_a \frac{d\vec{v_a}}{dt})}{m_a n_a \Omega_a} \tag{2.2}$$

Where the cyclotron frequency for species a is given by $\Omega_a = e_a B/m_a$. Under the approximation of negligible viscosity and slow time variation, the third and fifth terms in the $\perp$ velocity are eliminated. With the assumption of only radially dependent profiles of potential and pressure and symmetry in the θ direction, two of the remaining terms lead to only flow in the θ direction, namely the $\vec{E} \times \vec{B}$ and diamagnetic terms respectively given by:

$$\vec{v}_{\theta,a} = \frac{\vec{E} \times \vec{B}}{B^2} + \frac{\nabla p_a}{m_a n_a \Omega_a} \tag{2.3}$$

However, since motion in the θ direction does not lead to loss from the cylindrical system, we are interested in the radial component of the velocity. The only term which generates radial velocity is the θ component of the friction. Since the magnetic field is primarily in the direction of the axis of symmetry, this velocity can be approximated as:

$$v_r \simeq \frac{R_{ab,\theta}}{m_a n_a \Omega_a} \tag{2.4}$$

Conservation of momentum during elastic Coulomb collisions naturally enforces that the radial particle current density vanishes and as a result, the radial particle trans-

port is inherently ambipolar, $\sum_a e_a \Gamma_{r,a} = 0$. We can see that friction in the θ direction leads to radial velocity and therefore radial particle flux. The form of the θ component of the friction is:

$$R_{ab,\theta} = -\frac{m_a n_a}{\tau_{ab}}(\vec{v}_a - \vec{v}_b)_\theta \tag{2.5}$$

Where τ_{ab} is the momentum exchange collision time between arbitrary species a and b and the thermal force [19] has been neglected. Therefore the velocity in Equation 2.3. contributes directly to the friction in the θ direction. The total flux in the radial direction for species a is therefore of the form:

$$\Gamma_a = n_a v_r = \frac{R_{ab,\theta}}{m_a \Omega_a} \tag{2.6}$$

Since we are considering a pure plasma, let us now identify species a as electrons and b as ions. A more complete derivation by Braginskii [19] reveals the existence of another friction term due to the presence of the electron temperature gradient. The derivation of this term is beyond the scope of this thesis but the reader is referred to both [17] and [19] for a more complete treatment. Here, we simply quote the additional electron-ion friction in the θ direction:

$$R_{ei,\theta} = \frac{3 n_e \frac{\partial T_e}{\partial r}}{2 \Omega_e \tau_{ei}} \tag{2.7}$$

Inserting results from Equations 2.3, 2.5, and 2.7 into Equation 2.6 and performing a number of rearrangements yields the radial particle flux for a two species plasma (electrons and ions).

$$\Gamma_e = \Gamma_i = -n_e \frac{T_e}{m_e \Omega_e^2 \tau_{ei}} \left(\frac{\frac{\partial p_e}{\partial r} + \frac{\partial p_i}{\partial r}}{p_e} - \frac{3}{2} \frac{\frac{\partial T_e}{\partial r}}{T_e} \right) \tag{2.8}$$

Note that for typical tokamak profiles, the pressure and temperature gradients are negative. This implies that the pressure gradient terms tend to lead to outward particle flux while the temperature gradient term results in an inward flux which

reduces the overall loss of particles.

2.1.1 Functional Forms of the Particle Flux

At this point, since we are considering a simple 2 component plasma, a few simplifying assumptions will be made to elucidate key features of particle transport which will be referenced throughout this thesis work. If we were to assume that particle transport was a purely diffusive process, i.e. governed by Fick's Law, then we would expect to be able to cast the particle flux into a form such that:

$$\Gamma = -D\frac{\partial n}{\partial r} \tag{2.9}$$

In this case D, represents the diffusion coefficient, namely the proportionality factor between the flux and gradient. However, it is clear from looking at Equation 5-15. that this is not an appropriate (or at least complete) form. Even in this simple classical picture, there exist terms proportional to the density but not proportional to the density gradient in the flux expression. The simplest form that satisfies the particle continuity equation but allows for non-diffusive processes is the following:

$$\Gamma = -D\frac{\partial n}{\partial r} + Vn \tag{2.10}$$

This form for the particle flux allows for the existence of non-diffusive processes, namely convective flows. All terms which are not proportional to $\frac{\partial n}{\partial r}$ are therefore grouped in the convective velocity for the species. Here inward flow of particles corresponds to negative values of the convective velocity where outward flows are denoted by positive values of convection. This form has been applied in tokamak experiments worldwide and the existence of non-diffusive particle flux terms has been verified experimentally [20]. If we assume in Equation 5-15 that both species have identical temperatures and densities (enforced by quasineutrality), we can easily cast

the equation into this form:

$$\Gamma = -\frac{2T}{m_e \Omega_e^2 \tau_{ei}} \frac{\partial n}{\partial r} + \frac{\frac{\partial T}{\partial r}}{2 m_e \Omega_e^2 \tau_{ei}} n \tag{2.11}$$

Here the diffusion coefficient and convective velocity are given by:

$$D_{CL} = \frac{2T}{m_e \Omega_e^2 \tau_{ei}} \tag{2.12}$$

$$V_{CL} = \frac{\frac{\partial T}{\partial r}}{2 m_e \Omega_e^2 \tau_{ei}} \tag{2.13}$$

Similar arguments, though with more involved math will apply to the existence of diffusive and convective components to neoclassical and turbulent transport.

2.1.2 3 Component Plasma Transport

We now consider the situation of a 3 component plasma consisting of electrons, ions, and impurities. In this situation there exists not only friction between electron and ions, but also friction between ions and impurities. Often, in tokamak plasmas the frictional coupling between ions and impurities dominates that between ions and electrons. We will examine, under rough approximation, the conditions for which this statement is valid. The contribution to the total ion friction from impurities versus electrons can be compared in the following manner:

$$\frac{\vec{R}_{ie}}{\vec{R}_{iZ}} \sim \frac{n_e}{n_Z Z^2} \sqrt{\frac{m_e}{m_i}} \frac{(\vec{v}_i - \vec{v}_e)_\theta}{(\vec{v}_i - \vec{v}_z)_\theta} \tag{2.14}$$

Where we note that the $1/Z^2$ dependence of this expression is the result of the non-linear Z dependence of the Coulomb cross section. If we assume similar temperature gradients between the species and flat density profiles, we can see the relevant theta component of the velocity for species can be obtained from the diamagnetic component of Equation 2.3 (since the E $\times$ B terms cancel). Under these assumptions:

$$\vec{v}_{i,\theta} \sim Z \vec{v}_{z,\theta} \sim \frac{\frac{\partial T_i}{\partial r}}{eB} \tag{2.15}$$

If we now compare the magnitude of the velocity difference between ions and electrons versus that between ions and impurities, assuming an impurity with Z significantly larger than 1, we obtain (under these rough approximations):

$$\frac{(\vec{v}_i - \vec{v}_e)_\theta}{(\vec{v}_i - \vec{v}_I)_\theta} \sim \frac{2\vec{v}_{i,\theta}}{\vec{v}_{i,\theta}} \sim 2 \tag{2.16}$$

This result allows us to simplify Equation 2.14 to:

$$\frac{\vec{R}_{ie}}{\vec{R}_{iZ}} \sim \frac{2n_e}{n_Z Z^2}\sqrt{\frac{m_e}{m_i}} \tag{2.17}$$

Now, if we impose the constraint that the ion frictional coupling to impurities is 5 times greater than that for electrons we see that this is only satisfied if:

$$\frac{n_z}{n_e} > \frac{1}{6Z^2} \tag{2.18}$$

It is straightforward to see if this constraint is satisfied in typical C-Mod conditions. Consider first the most common impurity in Alcator C-Mod, boron, which occurs typical at approximately 1% of the electron density and has Z=5. The condition set in Equation 2.18 suggest that a fraction of greater than 0.66% is needed for ion-impurity friction to dominate. Performing the same test for calcium (average Z of 18) and molybdenum (average Z of 30) we arrive at fractions of 5.1×10^{-4} for calcium and 1.8×10^{-4} for molybdenum. These values can be compared with estimated fractions of 1.0×10^{-3} for calcium laser blow-off injections and intrinsic levels of molybdenum at about 1.0×10^{-4}. These results would suggest that the criterion for dominant ion-impurity friction is marginal or slightly satisfied for impurities typically considered in Alcator C-Mod.

Analogous to the electrons, there exists a contribution to the total impurity-ion friction resulting from the temperature gradient. This term can be obtained through straightforward substitution of ion terms for the electron terms found in Equation 2.7. Following the same procedure outlined in the previous section, we arrive at an

approximate expression for the total radial ion flux for a 3 component plasma:

$$\Gamma_i = -n_i \frac{T_i}{m_i \Omega_i^2 \tau_{iZ}} \left(\frac{\frac{\partial p_i}{\partial r}}{p_i} - \frac{T_z}{Z T_i} \frac{\frac{\partial p_Z}{\partial r}}{p_Z} - \frac{3}{2} \frac{\frac{\partial T_i}{\partial r}}{T_i} \right) \tag{2.19}$$

Now we can estimate the relative radial flux of electrons versus ions.

$$\frac{\Gamma_e}{\Gamma_i} \sim \frac{m_i \Omega_i^2 \nu_{ei}}{m_e \Omega_e^2 \nu_{iZ}} \sim \sqrt{\frac{m_e}{m_i}} \frac{n_e}{n_z Z^2} \tag{2.20}$$

So we determine that the ion flux is generally quite large compared with the electron flux. Under this assumption, we can calculate the impurity flux directly from the ambipolarity condition:

$$e\Gamma_i + Ze\Gamma_z - e\Gamma_e = 0 \tag{2.21}$$

this implies:

$$\Gamma_z = -\frac{1}{Z}\Gamma_i + \Gamma_e \simeq -\frac{1}{Z}\Gamma_i \tag{2.22}$$

This result demonstrates that the direction of the impurity flux is opposite that of the ions, implying that for outward flux of the main ion species that impurity accumulation will result. However, depending on the relative contributions of the terms in Equation 2.19 the main ion flux may be directed either inwards or outwards. For typical tokamak plasma profiles the first term would generally result in outward flux, the second term would be small, and the third term would generate an inward flux.

2.2 Neoclassical Transport Theory

When the classical theory of collisional transport is extended to include the effects of toroidal geometry, the resulting transport is referred to as neoclassical. As discussed in Chapter 1, the total field of the tokamak is made up of a toroidal and poloidal magnetic field which result in a helical magnetic field geometry. It is important to remember that in standard tokamaks, the toroidal field strength is much greater ($> \times 10$) than the poloidal field strength and that the field is $\propto 1/R$, where R is the

tokamak major radius. In this situation, the magnetic field strength at the inner wall of the tokamak cross section exceeds the field at the outer wall. This geometric effect creates a magnetic well for particles as they move along the field lines which wind helically due to the combined toroidal and poloidal fields. Conservation of the first adiabatic invariant, μ, and conservation of the particle's total energy causes some particles to be mirrored as they move into regions of smaller R and leads to the existence of two classes of particles, trapped and passing particles. Passing particles have a sufficient ratio of parallel to perpendicular velocity to make a full poloidal transit around the tokamak without mirroring. In contrast, magnetically trapped particles are incapable of making a full poloidal transit. These particle have insufficient parallel velocity relative to their perpendicular velocity and are therefore reflected at the bounce point in their poloidal transit. Due to their drifts in toroidal geometry (∇B and curvature), trapped and passing particle have orbits which make excursions off of magnetic field surfaces by roughly an order of magnitude greater than their gyroradius, increasing their radial step size and thus increasing the magnitude of collisional transport. Once again, the reader is referred to the references, [21, 17] for a more complete description of neoclassical transport processes.

In neoclassical theory, the orbital dynamics are also affected by the collisionality of the plasma. The collisionality is a measure of the relative frequency of momentum-altering Coulomb collisions compared to the transit frequency or for trapped particles, the bounce frequency. The transit frequency, defined as $\omega_t = v_{th}/qR$, is the frequency at which a particle makes a complete poloidal transit. Large values of collisionality indicate that the particle's mean free path is much shorter than the distance traversed around a flux surface in a single poloidal orbit. The charge and mass dependencies of the collision frequencies lead to the conclusion that, for non-trace fractions, high Z impurities are typically more collisional than bulk electrons and ions. The neoclassical regimes are defined by values of collisionality. They are called the Pfirsch-Schluter, and the banana-plateau regimes. For the case of:

$$\frac{\nu}{v_{th}/qR} \gg 1 \tag{2.23}$$

Where ν is the momentum-exchange collision frequency; a large number of collisions occur for a particle during a single poloidal transit and the plasma is said to be in the Pfirsch-Schluter regime. Particles in the banana-plateau regime are those in the opposite limit, i.e. at low collisionality, namely:

$$\frac{\nu}{v_{th}/qR} \ll 1 \tag{2.24}$$

In the limit of large aspect ratio ($\epsilon = r/R \ll 1$) the banana-plateau is further divided into the banana and plateau regimes. The plateau regime implies:

$$\epsilon^{3/2} \ll \frac{\nu}{v_{th}/qR} \ll 1 \tag{2.25}$$

and in the banana regime we have:

$$\frac{\nu}{v_{th}/qR} \ll \epsilon^{3/2} \tag{2.26}$$

The plateau regime is characterized by passing particles which are generally able to complete their particle orbits but the collision frequency is high enough such that most banana trapped particles are detrapped by particle collisions before completing a complete trapped orbit. In contrast, particles existing in the banana regimes are essentially collisionless and both passing and trapped particles are able to complete their orbits without undergoing significant collisions.

Derivation of the radial impurity fluxes in each regime is out of the scope of this thesis but the reader is referred to the review paper by Hirshman and Sigmar for the most comprehensive treatment of neoclassical impurity transport [22]. In this section, we quote results from Fussman [23] which are obtained from Hirshman's review.
Since the derived impurity fluxes vary depending on the collisionality regime of interest, it is first useful to understand the collisionality regime for heavy impurities under typical fusion conditions. We quote a form for the transit frequency normalized to the collision frequency for two species, a and b, at equal temperatures. This quantity

is given by [23]:

$$\frac{\nu}{v_{th}/qR} = 4.88 \times 10^{-24} \epsilon^{-3/2} \ln\Lambda \frac{RqZ_a^2}{T^2} \sum_b \sqrt{\frac{m_b}{m_a + m_b}} Z_b^2 n_b \tag{2.27}$$

with R in meters, n_b in m^{-3}, and T in keV. Plugging in typical numbers for Alcator C-Mod at mid radius: $\ln\Lambda = 15$, $R = 0.68$, $q = 1.0$, $T = 3.0$keV, $n_D = 1.0 \times 10^{20}$, and considering collisions between an impurity of mass and charge of $A = 40$, and $Z = 20$ (medium Z, like calcium) and deuterium ($A = 2, Z = 1$), we obtain a value of ~ 0.85. Given that this value is of order one, the exactly collisionality regime is somewhat ill-defined. Therefore, we will examine the forms of the impurity flux in both the Pfirsh-Schluter and the Banana-Plateau regimes.

Recall that for $\frac{\nu}{v_{th}/qR} \gg 1$ the impurities are considered to be in the Pfirsch-Schluter regime. These particles can be described by the expression [23]:

$$\Gamma_z = -D_{PS} \nabla n_z + D_{PS} Z [\frac{\frac{\partial n_D}{\partial r}}{n_D} - \frac{1}{2}(1 - Z)\frac{\frac{\partial T}{\partial r}}{T}] n_z \tag{2.28}$$

where the Pfirsch-Schluter diffusion coefficient, D, is defined to be:

$$D_{PS} = (2q^2 + 1)\frac{4}{3(4\pi\epsilon_0)^2}\sqrt{\frac{2\pi m_D m_z}{T(m_D + m_z)}}\frac{\ln\Lambda}{B^2} Z e^2 n_D \tag{2.29}$$

If we now consider the same two interacting species (calcium and deuterium) but instead in the banana-plateau regime we obtain (from Hirshman [22] and Fussman [23]) impurity fluxes of the form:

$$\Gamma_Z^{BP} = -D_Z^{BP}\frac{\partial n_z}{\partial r} + D_Z^{BP} Z \left[\frac{\frac{\partial n_D}{\partial r}}{n_D} + \frac{3(Z-1)}{2Z}\frac{\frac{\partial T}{\partial r}}{T}\right] n_z \tag{2.30}$$

where the impurity diffusion coefficient is of the form:

$$D_Z^{BP} = 4.04 q \frac{\sqrt{A_Z}}{RZ^2}\frac{T^{1.5}}{B_T^2} \mathrm{m}^2/\mathrm{s} \tag{2.31}$$

Where T is in keV, B_T is in Tesla, R is in meters, and A_z is the relative atomic mass. Using the numbers representative of a medium Z, core impurity (see above), we would predict a diffusion coefficient of order $D_Z^{BP} \sim 0.01$ m^2/s. We can make a rough estimate the implications of such a diffusion coefficient on the global impurity confinement time. If we assume $\tau_{imp} \sim a^2/D_{imp} = 0.21^2/.01$, where a is the plasma minor radius, we obtain an impurity confinement time of order 4 seconds for Alcator C-Mod. Typical measured impurity confinement times are found to be approximately 20-25 ms. This simple estimate suggests that neoclassical predictions cannot explain experimentally observed levels of impurity transport.

2.3 Drift Waves and Anomalous Transport in the Tokamak Core

Despite the well developed theory for the classical and neoclassical transport of particles and energy, it is usually found that measured transport levels exceed these predictions by up to a factor of 100. It is generally believed that the observed "anomalous" transport levels are the result of low-frequency (relative to the cyclotron frequency) plasma turbulence. This turbulence arises from the nonlinear interaction of drift waves in the plasma which are driven unstable by the free energy in the background plasma profiles. In this section, we will look at some of the candidate modes which, when unstable, are believed to create the observed turbulence and transport in the tokamak core. These instabilities are identified as the **I**on **T**emperature **G**radient driven mode (ITG), the **T**rapped **E**lectron **M**ode (TEM), and the **E**lectron **T**emperature **G**radient driven mode (ETG). Here we present the linear growth rates for some of these modes and identify their characteristics which will be referenced throughout this thesis work.

2.3.1 A Simple Picture of Drift Wave Instabilities and Particle Transport

Before look at the linear growth rates for the instabilities thought to dominate transport in the plasma core, we will review a simplified picture of drift-wave instabilities, following along with the derivation from [24].

First, assume a simplified slab geometry for the plasma (see Figure 2-1) and that

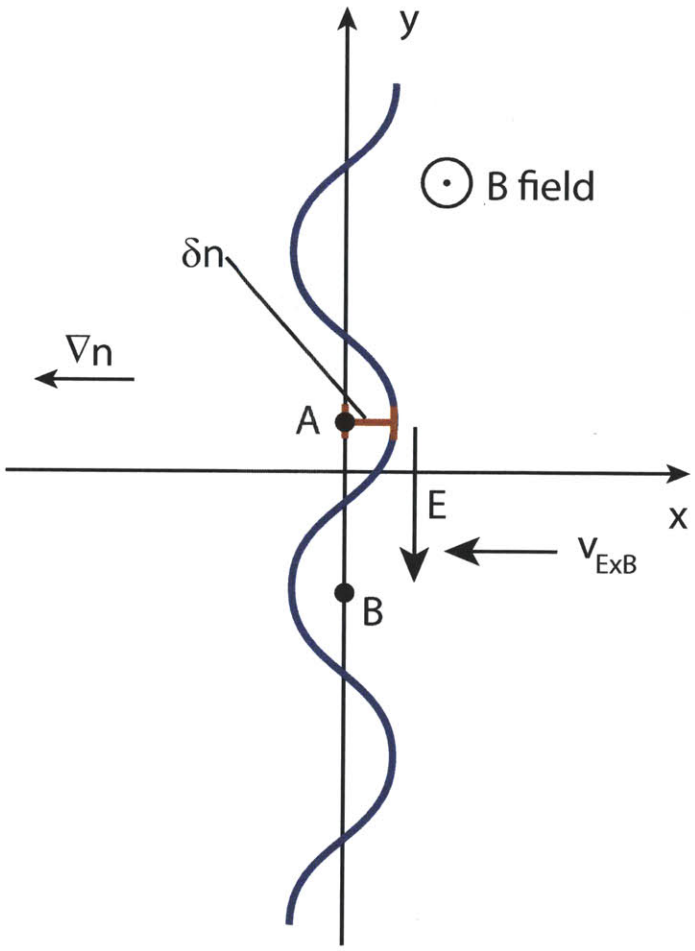

Figure 2-1: A cartoon showing a simple explanation of a plasma drift wave.

there exists a density gradient in the -x direction and a magnetic field coming out of the page. Assume that we have an initial density perturbation varying sinusoidally in the y direction such that the density is larger at point A than it is at point B

(see Figure 2-1). In the presence of a density gradient, and assuming a constant temperature, we have a diamagnetic drift velocity (also in the y direction) given by:

$$v_{*,e} = \frac{-T_e \frac{\partial n}{\partial x}}{neB} \tag{2.32}$$

If the value of $k_\parallel$ for this wave is sufficiently large, the electrons will respond to this variation in density quickly and the Boltzmann relation is valid. This is given by:

$$\frac{\delta n_e}{n} = \frac{e\delta\phi}{T_e} \tag{2.33}$$

This implies that there is a potential perturbation which is in phase with the density perturbation. Since regions of higher δn correspond with regions of higher $\delta\phi$ in this case, an electric field will be generated which creates $E \times B$ drifts as shown in Figure 2-1. This will result in a wave which propagates in the positive y direction with the diamagnetic drift velocity, and a dispersion relation given by:

$$\frac{\omega}{k_y} = v_{*,e} \tag{2.34}$$

As long as the Boltzmann relation holds and the electrons can move along the magnetic field lines to cancel out the electric fields, the drift wave will be stable and purely oscillatory. However, if some dissipation is introduced into the system, and the mobility of the particles is limited, a phase difference will be introduced between the density and the potential. This results in a modified version of the Boltzmann relationship, namely:

$$\frac{\delta n_e}{n} = \frac{e\phi}{T_e}(1 - i\delta) \tag{2.35}$$

where δ represents the phase shift. This phase shift modifies the dispersion relation for this wave to:

$$\omega \simeq k_y v_{*,e}(1 + i\delta) \tag{2.36}$$

Since the time variation of the wave is proportional to $e^{-i\omega t}$, it is readily seen that the imaginary part of ω represents the growth rate for this instability.

The particle flux resulting from this wave in the x direction is given by the time average of the density perturbation, δn, times the $E \times B$ velocity due to the fluctuating potential, $\delta\phi$. If δn and $\delta\phi$ are in phase (the $E \times B$ drift velocity is 90 degrees out of phase), the time averaged radial particle transport is zero due to this wave. However, if dissipation is introduced into the system and there is a delay between the density and potential fluctuations (i.e. the wave is unstable), radial (outward, positive x) particle flux will be produced. It is the physics described in this simple picture that motivates the study of drift wave turbulence in fusion plasmas.

2.3.2 An Introduction to Ion Temperature Gradient and Trapped Electron Modes

Here, as well as in the simulation work presented in later chapters, we assume that the low values of normalized plasma pressure β ($\ll 1$) present in typical C-Mod plasmas justify the assumption of an electrostatic limit, where magnetic field fluctuations are ignored. Here we define β to be:

$$\beta = \frac{n_e T_e + n_i T_i}{B^2/2\mu_0} \tag{2.37}$$

In this low beta limit, all modes are assumed to be electrostatic with a perturbed electric field given by $\delta\vec{E} = -\nabla\delta\phi$. For simplification, we will also assume a geometry where x is the radial coordinate, y is the poloidal direction, and $\|$ is parallel to the static magnetic field. Under these assumptions, we will assume that the perturbed electrostatic potential can be written in the form:

$$\delta\phi = \delta\phi(x) e^{(-i\omega t + ik_y y + ik_\| z)} \tag{2.38}$$

Before we discuss the linear growth rates for Ion Temperature Gradient (ITG) and Trapped Electron Modes (TEM), we need to define a number of quantities. These are:

$L_n = n/\mid \nabla n \mid$, $L_T = T/\mid \nabla T \mid$, $\eta = L_n/L_T$, $g = v_{th}^2/R$, $\omega_d = k_y g/\Omega_c$, $b_i = k_y^2 \rho_i^2/2$, $D_b = cT/ZeB$, $\omega_* = k_y D_b/L_n$, $\epsilon_n = L_n/R_0$, $\tau = T_e/T_i$.

2.3.3 The Ion Temperature Gradient (ITG) mode

The ion temperature gradient mode is generally thought to be the primary contributor to the high levels of anomalous transport which are observed in the tokamak core in most operating regimes. As such, it has been the subject of large amounts of both theoretical and experimental work [25, 26, 27]. In present day experiments, it is commonly found that the L-mode plasma discharges are linearly unstable to ITG type turbulence in the confinement zone and that nonlinear simulations indicate that these modes can account for a vast majority of the observed experimental heat flux.

We begin the discussion on modes driven by the ion temperature gradient with the simplest mode of this type, the slab ITG or η_i mode. This mode results from the interaction of ion acoustic waves with the radial ion pressure gradient. In a slab geometry and in the limit of $\eta_i \gg 1$ we can obtain the linear growth rate for this mode given by:

$$\gamma_{s,ITG} \sim (k_\parallel^2 c_s^2 \eta_i \omega_{*,i})^{1/3} \tag{2.39}$$

The explicit dependence of this mode's linear growth rate on the value of η_i is where it derives it name. However, it is important to note that in the limit of a flat density profile, this mode is characterized by a critical value of the electron temperature gradient and hence it is identified as an ITG mode [28]. A more comprehensive derivation of this mode and its properties can be found in Horton *et. al* [29].

Additional ion temperature gradient driven modes have been derived in toroidal geometry. We consider now the toroidal ITG mode with a growth rate of:

$$\gamma_{ITG} \sim (k_y \rho_i)\sqrt{\frac{\eta_i g_i}{L_n}} \tag{2.40}$$

or inserting $\eta_i = L_{T_i}/L_n$ we can determine that the linear growth rate is simply:

$$\gamma_{ITG} \sim (k_y \rho_i)\sqrt{\frac{g_i}{L_{T_i}}} \tag{2.41}$$

The key features of the ITG mode are displayed by this simplified linear growth rate. Unlike the slab version of the ITG, this mode is driven unstable by the curvature effects included in the effective curvature term, g_i. This mode derives its name from the inverse dependence on the ion temperature gradient scale length, L_{T_i}. For a full derivation of this ITG mode and its generation of heat and particle transport, the reader is referred to [30] and [28].

2.3.4 Trapped Electron Modes (TEM)

Trapped Electron Modes (TEM) actually consist of a whole class of instabilities with slightly different driving mechanisms. Two such trapped electron instabilities will be discussed here.

Here we will investigate approximate linear growth rate expressions for two distinct modes, the dissipative and the collisionless trapped electron modes. Some of the original work on dissipative trapped particle instabilities was performed by Kadomtsev and Pogutse [31] and the reader is referred to this work for a complete derivation of the linear growth rate presented here. The dissipative trapped electron mode's growth rate can be written as:

$$\gamma_{D,TEM} \sim \frac{\epsilon^{3/2}\omega_{*e}^2}{\nu_{ei}}(\frac{3}{2}\eta_e) \tag{2.42}$$

Here we wish to identify the key driving mechanisms for this mode. Since the fraction of trapped particles in a tokamak system is $\propto \sqrt{\epsilon}$, it is clear that the $\epsilon^{1.5}$ dependence of the linear growth rate demonstrates some dependence on the trapped particle fraction. However, the primary drive term for this instability can be identified as the ratio of the electron gradient scale lengths, a/L_{T_e} and a/L_{n_e} which enter in the η_e term. Note that an additional dependence on density gradient scale length is present

implicity in the ω_{*e}^2 factor. Collisions enter the growth rate through the ν_{ei} term and provide a stabilizing effect (decrease the growth rate). These drive and stabilization mechanisms will be studied in detail through numerical simulation presented later in this work.

Finally, we investigate the linear growth rate of the collisionless trapped electron mode. The full derivation of the quoted linear growth rate can be found in [32] but it should be noted that the form derived in this paper and quoted here is very crude, and should be view only as an rough scaling of the growth rate. Here we quote this linear growth rate simply to identify key dependencies of this trapped electron mode.

$$\gamma_{C,TEM} \approx \omega_{*e}(2\pi\epsilon)^{.5}\eta_e(\frac{R}{L_n})^{1.5}(\frac{R}{L_n} - \frac{3}{2})e^{-R/L_n} \tag{2.43}$$

The growth rate for the collisionless trapped electron mode demonstrates some key features of trapped electron mode instabilities. The leading factor of $(2\epsilon)^{.5}$ once again demonstrates the dependence of this mode on the trapped particle fraction but perhaps more importantly the explicit dependence on the normalized density gradient scale length R/L_n should be noted. This dependence on the density gradient scale length is complicated and can have a stabilizing or destabilizing effect depending on its value.

Above we presented the linear growth rates for two types of trapped electron modes. It was found that the driving terms for these instabilities included, ν_{ei}, a/L_{T_e}, and a/L_n. The purpose of this section was to illustrate these key dependencies as it will be demonstrated in later chapters that these driving terms play an important role in the stability of experimental plasma conditions and the observed levels of anomalous heat and particle transport.

2.3.5 The Electron Temperature Gradient (ETG) mode

The electron temperature gradient (ETG) is the analog of the ITG mode with the roles of electrons and ions simply interchanged. A rigorous derivation of ETG modes can be found here [33]. Here we present a very brief version to illustrate the key

features of this mode. We can obtain an approximate expression for the ETG linear growth rate:

$$\gamma_{ETG} \sim (k_y \rho_e)\sqrt{\eta_e \frac{g_e}{L_n}}. \tag{2.44}$$

or inserting $\eta_e = L_{T_e}/L_n$ we can write:

$$\gamma_{ETG} \sim (k_y \rho_e)\sqrt{\frac{g_e}{L_{T_e}}}. \tag{2.45}$$

This expression elucidates the key aspects of the the electron temperature gradient mode. First, like the ITG mode, the ETG linear growth rate has a dependence on the magnetic curvature of the system. However, the main driving term for this mode results from the inverse dependence on L_{T_e}. Hence, this mode is known as the electron temperature gradient mode.

It is important to contrast the linear growth rates of the ITG and ETG modes at this point. For the ITG growth rate we found a dependence of $\gamma \propto k_y \rho_i$ which is similar to the dependence of ETG, namely $\gamma \propto k_y \rho_e$ but differs by the square root of the ion to electron mass ratio ($\sqrt{m_i/m_e} \sim 60.6$). However, quasilinear theory of turbulent transport suggests that the particle and thermal diffusivity should scale as $D, \chi \sim \gamma/k_y^2$. It is therefore estimated that, for the same value of k_y, the ETG turbulence results in approximately 60 times lower values of both particle and thermal transport. This simplistic estimate of the transport level would indicate that high-k ETG turbulence plays only a small role in explaining the overall levels of observed anomalous transport in tokamak systems. However, nonlinear effects of these modes may result in non-negligible levels of transport. The role of ETGs is still an area of active research but there is evidence that electron-scale turbulence can play an important role in determining transport levels in the plasma core [34].

2.3.6 The Gyrokinetic Model

The simple derivation of the linear growth rates presented in the previous sections provides useful insight into the physical mechanisms which drive ITG, TEM, and

ETG instabilities in the plasma core. However, the linear picture is insufficient for predicting measured transport levels after the linear growth phase. In this section, we briefly overview the origin of the gyrokinetic equation and the validity of its application in tokamak plasmas.

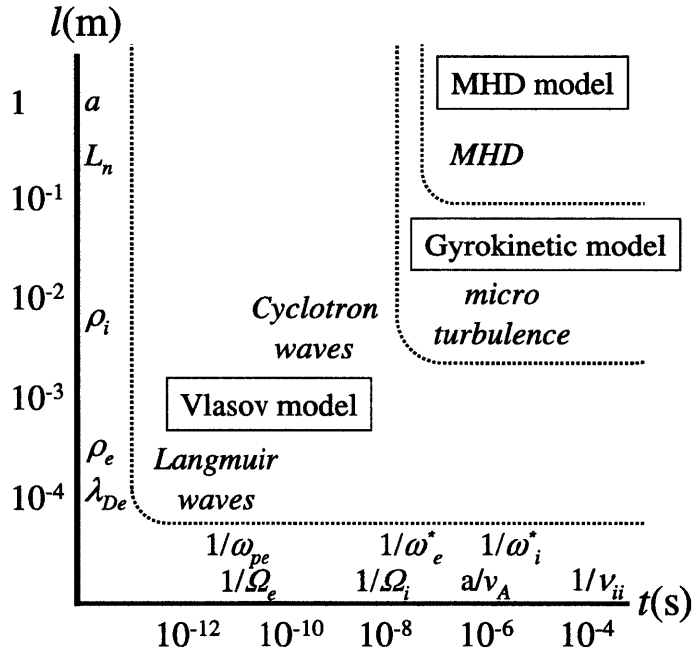

Figure 2-2: (The range of spatial and temporal scales which are described by the Vlasov equation and the gyrokinetic equation are shown. This figure is taken from [3].

In principle, a complete description of all plasma dynamics is contained in the Newton-Maxwell set of equations. However, the large number of particles contained in a Debye sphere and the long range nature of the interactions of these particles makes solving for individual particle motions unnecessary and utterly intractable. As a result, a statistical approach is taken where particles are characterized by a statistical distribution function. This slightly reduced set of equations is represented by the Maxwell-Boltzmann equation that is essentially an equation of motion for the distribution function in 6-D phase space.

The Boltzmann equation can be written as [3]:

$$\frac{\mathrm{D}f_s}{\mathrm{D}t} = \frac{\partial f_s}{\partial t} + \{f_s, H_s\} = C(f_{s'}, f_s) \tag{2.46}$$

where for arbitrary functions F and G

$$\{F, G\} = \frac{\partial F}{\partial q_i}\frac{\partial G}{\partial p_i} - \frac{\partial F}{\partial p_i}\frac{\partial G}{\partial q_i} \tag{2.47}$$

and

$$H_s(q,p) = \frac{1}{2m_s} \mid \vec{p} - \frac{e_s}{c}\vec{A} \mid^2 + e_s\phi \tag{2.48}$$

is the single particle motion Hamiltonian as a function of particle position (q) and momentum (p) and where ϕ and $\vec{A}$ are the electrostatic and vector potentials respectively. Here $C(f_{s'}, f_s)$ represents the collision operator for two particle interaction. In the limit of $C(f_{s'}, f_s) = 0$, equation 2.46 is reduced to the collisionless Vlasov equation.

Despite the simplification from the full Newton-Maxwell system of equations, this set of equations describes a huge range of spatio-temporal scales as demonstrated in Figure 2-2. To further reduce the spatial and temporal scales described and thus reduce the complexity required to solve the set of equations, the gyrokinetic model was developed. The gyrokinetic model effectively eliminates the fastest time scale phenomenon ($\omega > \Omega_s$) by transforming from particle position coordinates to gyro-center coordinates. This eliminates the fast gyro motion of the particles while preserving necessary kinetic effects associated with finite Larmor radius and reduces the problem from a 6D to a 5D one. This simplification makes the numerical solution of the nonlinear gyrokinetic equation possible. In depth derivations of the gyrokinetic equations can be found here [35, 36, 37, 3]. The gyrokinetic equation for the particle distribution function in gyro-center coordinates, $\bar{f}_s$, can be written in the following form:

$$\frac{\partial \bar{f}_s}{\partial t} + \frac{d\bar{\mathbf{R}}}{dt} \cdot \frac{\partial \bar{f}_s}{\partial \bar{\mathbf{R}}} + \frac{d\bar{u}}{dt}\frac{\partial \bar{f}_s}{\partial \bar{u}} = < C[\bar{f}_s] > \tag{2.49}$$

where $\bar{\mathbf{R}}$ is the gyrocenter position, $\bar{u}$ is the gyrocenter velocity, and $< C[\bar{f}_s] >$

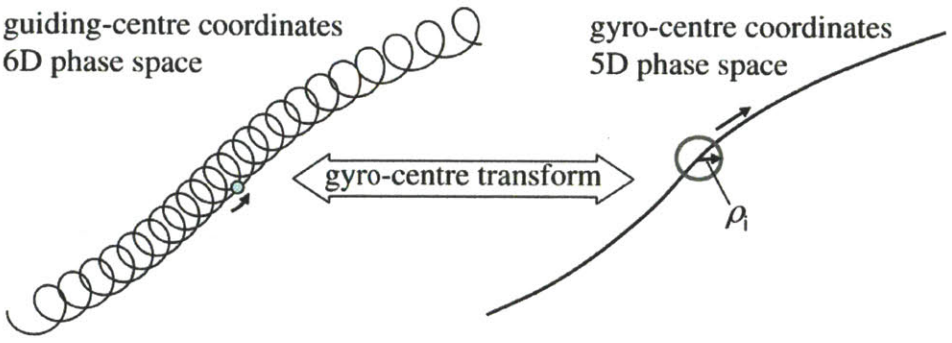

Figure 2-3: (A cartoon showing the conversion from guiding center to gyro-center coordinates is shown. This figure is taken from [3].

denotes the gyrophase averaged collision operator. This equation fully describes the evolution of the particle distribution function. The gyrokinetic equation is valid in the following ordering:

$$\frac{\omega}{\Omega_s} \sim \frac{k_\parallel}{k_\perp} \sim \frac{v_E}{v_{th,s}} \sim \frac{\delta n_s}{n_0} \sim \frac{B_1}{B_0} \sim \frac{\rho_s}{L_n} \sim \epsilon \tag{2.50}$$

Here ω is the characteristic frequency of the turbulence, $k_\parallel = \vec{k} \cdot \vec{b}$ is the parallel wavenumber, $k_\perp = \mid \vec{k} \times \vec{b} \mid$ is the perpendicular wavenumber, v_E is the perturbed $\vec{E} \times \vec{B}$ velocity, B_1 is the perturbed magnetic field, B_0 is the equilibrium field, ρ_s is the Larmor radius, $L_n = n_0 / \mid \nabla n_0 \mid$ is the characteristic density scale length, and ϵ is the gyrokinetic smallness parameter. Given the ordering of the gyrokinetic equation, it is believed that it offers a physical description of the low frequency (relative to the cyclotron frequency) plasma turbulence which is thought to dominate transport levels in the core of tokamak plasmas. The dominant nonlinearity arises from the $E \times B$ nonlinearity entering the gyrokinetic equation through the $\frac{d\bar{\mathbf{R}}}{dt}$ term. Nonlinear terms in the gyrokinetic equation lead to the coupling of unstable modes and the development of plasma turbulence. Additionally, the full nonlinear gyrokinetic equation includes the physics required to describe self-generated turbulence suppression mechanisms such as zonal flows. It is believed that the gyrokinetic model contains sufficient physics to describe the turbulent transport processes which are responsible for the observed transport levels. This includes the physics associated with ITG,

TEM, and ETG turbulence and their nonlinear interactions. Nevertheless, it is clear that even the complex gyrokinetic equations are an approximate model of the full complexity of turbulent transport in fusion plasmas.

2.4 Overview of Existing Impurity Transport Research

Investigations of impurity transport have been performed on fusion devices worldwide. Impurity confinement and transport has been studied in tokamaks, stellarators, reversed-field pinches, and other plasma confinement schemes worldwide. This section is intended to give an overview of existing experimental results from impurity transport studies in the core of tokamak plasmas.

2.4.1 The Evolution of Impurity Transport Studies

Early investigations of impurity transport can be traced back to the 1970s with measurement of emission from intrinsic impurities. Dedicated study of the impurity confinement times have been reported on Alcator A, Alcator C, JET, Tore Supra, and Alcator C-Mod. On Alcator A measured impurity confinement times of injected silicon and molybdenum were found to be much shorter than neoclassical predictions [38, 39], providing evidence of anomalous impurity transport. Large databases of impurity confinement times were collected in a variety of plasma conditions to create impurity confinement time scaling laws. The Alcator C scaling law indicated that measured impurity confinement times were dependent on q_{95}, Z_{eff}, a, R, and the charge and mass of the background gas, Z_{bg} and m_{bg} [40]. A joint study performed by Mattioli *et al.* on JET and Tore Supra measured impurity confinement times demonstrated dependencies on plasma current ($I_p^{0.31}$), the plasma volume ($V_p^{0.70}$), and the heating power per particle ($(P_{in}/n_e)^{-0.57}$) [41]. Even more recent investigations into the impurity confinement time scalings were performed on Alcator C-Mod by Graf *et*

al. which found dependencies on both I_p and P_{tot} [42].

The arrival of more numerous and novel spectroscopic measurements provided an opportunity to depart from the simple 0-D model of impurity transport provided by measurement of the impurity confinement time and allowed for the first 1-D measurements of radial particle transport. Such analysis has been carried out with varying levels of sophistication to determine impurity transport coefficients on most major tokamaks worldwide. Much of this work has been carried out on the major European tokamaks such as JET [43, 16, 44, 45], Tore Supra [41, 46, 47], ASDEX-Upgrade [48, 49, 50], and TCV [51, 52]. Common investigations including the Z dependence of impurity transport, changes with input power and heating method, and changes with the current profile will be discussed here.

2.4.2 RF Effects on Impurity Transport

The effect of applied RF power has also been investigated in a number of devices. The most recent of these studies was performed by Valisa *et al.* on JET [43]. This work focused on the effect of central ICRH in H-mode discharges which is of particular relevance to this thesis since C-Mod is primarily heated by ICRH. Trends in the individual transport coefficients, D and V, were difficult to distinguish. Despite these problems, they report a flattening of the impurity peaking with increased input power which is correlated with changes in the ion temperature gradient. Also on JET, Puiatti *et al.* looked at the effects of minority and mode conversion heating in JET H and L-mode plasmas [16]. They found significant inward impurity convection was present in situations of hydrogen minority heating which was in contrast to effectively zero convection in mode conversion heated plasmas. Dux *et al.* investigated the local dependence of impurity transport on ECH heating on the ASDEX-Upgrade tokamak [48]. It was observed that increased ECH heating could increase the diffusion coefficient inside of $r/a = .25$ to highly anomalous levels. More recently on ASDEX, Sertoli *et al.* used multiple experimental techniques to look at the local effects of ECH heating on impurity transport using Argon measurement [49]. They found significant

inward pinch in the middle of the stiff gradient region and results which were generally consistent with the previous work on ASDEX-Upgrade. It should be emphasized that it is unlikely that direct effects of RF heating should have any significant effect on core impurity transport. RF heating most likely affects impurity transport levels through modification of the plasma profiles which in turn enhance or suppress plasma turbulence and modify transport levels. In Chapter 7 of this thesis we will investigate the effects of RF heating on impurity transport in the context of turbulence driven transport.

2.4.3 q Profile Dependent Impurity Transport

Although much more limited, investigations into the current/q profile dependence of impurity transport have been performed. Early work was performed on JET using simple models for the transport coefficient profiles by Giannella *et al.* [44]. They observed strong anomalous transport levels and concluded that the q profile shape was a crucial parameter in determining the impurity transport coefficient profiles. Mattioli *et al.* looked at the transition region from low to high diffusion coefficient values and tried to relate it to the location of the $\hat{s} = r/qdq/dr = 0.5$ or the $q = 1$ surface [41] on Tore Supra. Their work suggested that this transition occurred at the $\hat{s} = 0.5$ location in the plasma. The most recent work on q profile dependent impurity transport (other than the work presented here) was performed on the TCV tokamak by Scavino *et al.* [52]. They report a transition from inward to outward values of impurity convection which occurs at $q_{95} \sim 4.5$. The relatively little work on this subject and the clear dependence of q profile effects on the impurity transport level (evidenced by impurity confinement time scalings) motivated much of the work presented here.

2.4.4 The Z Dependence of Impurity Transport

Investigations into the Z dependence of impurity transport have been performed on numerous machines with no real consensus. On the Tore Supra tokamak Guirlet *et al.* used multiple techniques of impurity introduction to explore differences in low and medium Z impurities. They found no clear Z dependence on the impurity transport coefficients in their work [47]. Additional investigations were performed later by Parisot *et al.* which looked at Al and Ge impurity transport. Although there was some evidence of a trend in the measured impurity confinement times, more in-depth analysis of the transport coefficient profiles resulted in a largely inconclusive result on the Z dependence of the impurity transport [46]. On the JET tokamak Giroud *et al.* used CXRS measurement of Ne and Ar to look at the peaking of low and medium Z impurities [45]. No peaking dependence with impurity Z was found. Dux *et al.* studied the Z dependence in ASDEX-Upgrade H-mode discharges and found that with rising Z the impurity transport became more dominated by inward impurity convection[50]. Despite fairly extensive research on this subject, no clear conclusion has yet been developed.

2.4.5 Miscellaneous Investigations

The scope of impurity transport work has by no means been limited to only the results described above. Additional investigations have been performed on many of the major tokamaks. Early investigations were performed by Rice *et al.* on the Alcator C-Mod tokamak to model L and H-mode discharges [53]. Aided by measurements of a heavy ion beam probe, Horton *et al.* performed experiments into the mechanisms of impurity transport on the TEXT tokamak [54]. Scavino *et al.* investigated the dependence of shaping effects on measured impurity confinement times and transport coefficient profiles in TCV [51]. Guirlet *et al.* looked at laser blow-off injected nickel transport in the core of Tore Supra discharges [55]. Most recently, Villegas *et al.* reported a measured dependence of the diffusion coefficient on the electron temperature

gradient in the core of Tore Supra [56].

2.4.6 Modeling of Impurity Transport

The last decade of impurity transport research has seen the development of numerous quasi-linear models to describe observed behavior. This is an active area of research which can be found in the literature in the following references [15, 57, 58, 59, 60, 61, 62, 63, 64]. Generally, these models consist of two mechanisms which are used to model the turbulent impurity pinch, namely the thermodiffusive pinch and the curvature pinch. Although, newer models include additional mechanisms and even electromagnetic effects. As these models have become more developed, experimental investigations have used them to interpret their experiments, often finding qualitative agreement. Work which provides comparison with quasilinear impurity transport models can be found in any of the following references [47, 46, 56, 16, 43, 49]. However, these models have generally been unable to quantitatively reproduce the measured impurity transport levels. Until this thesis work and the associated papers, no model had demonstrated both quantitative and qualitative agreement with experimental impurity transport levels and comparisons of experimental impurity transport experiment with nonlinear gyrokinetic simulations had never been performed.

Chapter 3

Diagnostic Tools on Alcator C-Mod

3.1 Studying Trace, Non-Intrinsic, Time-Evolving Impurities

As discussed in Chapter 1, the study of impurity transport is motivated by the need for clean fusion plasmas and good energy confinement. It is believed that in most situations, transport in the tokamak core is dominated by turbulence driven unstable by free energy in the background plasma profiles. Measured levels of cross field particle, energy, and momentum transport are the result of the formation of turbulent structures in the plasma core. Trace impurities are not expected to effect the character of the turbulence and should act effectively as a passive tracer, transported in and out of the plasma by the turbulent structures created by the background profiles and providing a useful tool for understanding the characteristic turbulence.

In most current tokamaks, passive and active spectroscopic measurements routinely monitor the intrinsic impurity concentrations. Measurement of intrinsic impurity density or emissivity profiles provides some information on the dynamics of the impurity transport. However, most of these impurities have poorly characterized sources and may exhibit significant recycling (i.e. a cycle of implementation and release from material surfaces). Non-intrinsic, non-recycling impurities, by definition, have no background level and their source can be well diagnosed. As a result, analysis

of their measurement is not complicated by unknown source profile and time histories or require background subtraction procedures.

Additionally, studying the time-evolving density response of a known impurity source can provide more information than observation of steady state profiles. The particle continuity equation describes the time evolution of the impurity density profile.

$$\frac{\partial n}{\partial t} = -\nabla \cdot \Gamma + S \tag{3.1}$$

Where Γ is the particle flux and S represents sources and sinks. As addressed in Chapter 2, it is well documented that the observed impurity flux is not well described by a purely diffusive process, namely:

$$\Gamma = -D\nabla n \tag{3.2}$$

Where the total particle flux is denoted by Γ and D represents the diffusion coefficient for the species, typically measured in m^2/s. A more appropriate description for both bulk particle and impurity flux has been found to be of the form [20]:

$$\Gamma = -D\nabla n + Vn \tag{3.3}$$

The transport coefficients, D and V, represent the diffusive and convective contributions respectively to the particle flux. In this model, the diffusion coefficient, D (m^2/s), is strictly a positive definite quantity while the convective velocity, V (m/s), is radially inward for negative values and outward for positive values. If we consider steady state, in the absence of sources, the total particle flux must be equal to 0 and it follows from Equation 3.3 that:

$$\frac{\nabla n}{n} = \frac{V}{D} \tag{3.4}$$

In this situation, measurement of the impurity density profile (i.e. ∇n and n) provides no information on the separate values of diffusion and convection, only on their ratio,

V/D. However, if we consider and measure time-evolving profiles, the impurity flux can be deduced from the continuity equation. This measurement therefore allows us to separate the out the diffusive and convective contributions. For this reason, observation of non-intrinsic, time-evolving, impurity density profiles is desirable and motivates the study of impurity transport using laser blow-off.

3.1.1 Impurity Introduction via Laser Blow-Off

The desire to study trace levels of non-intrinsic, time evolving impurities, led to application of the laser blow-off technique to fusion plasma research. The laser blow-off technique was first pioneered by Friichtenicht [65]. His work showed that a high-powered laser incident on a coated glass slide can result in efficient generation of a directed "beam" of low energy neutrals (< 10 eV). A qualitative description of the physical process of laser ablation of thin film materials is as follows. A thin film of a selected material, often a metal, is vapor deposited on the surface of a glass slide and arranged such that a high-powered (> 450 mJ/pulse) laser is incident first on the uncoated side of the slide. The laser propagates through the glass and is absorbed by the deposited material, partially ionizing the materials and creating a local plasma. The plasma "hot spot" expands and ingests additional material, cooling in the process, until it penetrates the surface of the thin film and expands into vacuum as a low energy, directed neutral beam in the direction of the laser beam. The laser pulse's photon energy is effectively transferred to the directed kinetic energy of the ablated atoms, making it an ideal source for a short timescale, controlled impurity source. The deposited material thickness, laser power density, and ablated spot size represent free parameters for tuning the desired magnitude of the neutral beam. The versatility of this neutral source and the development of commercially manufactured pulsed laser systems has made this technique a valuable tool for studying impurity transport in tokamaks. The laser blow-off technique was first applied in 1975 by Marmar [66]. Since that time, laser blow-off systems have been installed on tokamaks worldwide to aid in impurity and heat transport studies [46, 49, 67, 16, 68, 51, 69]. The ability to introduce trace amounts of non-recycling, non-intrinsic impurities at

what is effectively a delta function in time and space, motivated the design and construction of the Alcator C-Mod multi-pulse laser blow-off system.

3.2 The Alcator C-Mod Multi Pulse Laser Blow-off System

3.2.1 System Design Goals

The multi-pulse laser blow-off system was designed to meet four operational requirements. These were:

- Non-perturbative introduction of neutral impurities to the plasma edge.
- The ability to ablate a wide range of target Z.
- Multi-pulse injection capability with precise pulse timing on a 100 ms time scale.
- Remote operation of beam steering and ablated spot size.

The following sections describe the hardware aspects of the system which allow for achievement of these goals.

3.2.2 Hardware Setup

Design of the multi-pulse laser blow-off system hardware drew from aspects of the previous Alcator C-Mod laser blow-off system [67] and the system currently operational at the ASDEX-Upgrade tokamak [70]. Figure 3-1 shows a picture of the multi-pulse laser blow-off system mounted on Alcator C-Mod's B-port. This section briefly describes the main components of the laser blow-off system including the optical, vacuum, and electronics setup of the system. For additional detailed discussion of the hardware aspects, the reader is referred to Appendix A of this thesis.

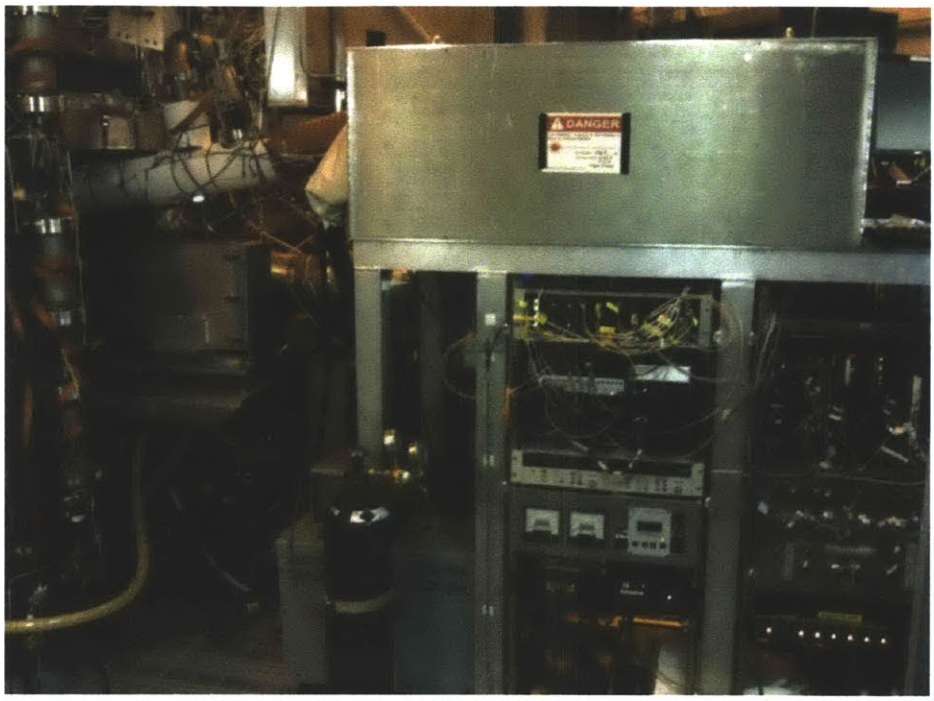

Figure 3-1: Pictured is the multi-pulse laser blow-off system mounted on the Alcator C-Mod tokamak.

Optical Systems

The Alcator C-Mod laser blow-off system was first installed during the 2009 campaign. Unlike its predecessor from the mid to late 90s, it employs a multi-pulse ND:YAG laser ($\lambda = 1064$ nm) built by Continuum lasers (Surelite II-10 model). This system operates at 10 Hz with a pulse energy of 0.68 J to perform thin film ablation. Selection of the laser pulse energy was based on previous laser ablation results utilizing YAG laser systems [70]. This laser blow-off system is versatile and has demonstrated the ability to ablate a wide range of target Z. For all studies described here, thin films consisting of 10 nm of chromium, to aid in laser absorption in the material, and 2 microns of CaF_2 were used. This choice was made based on typical densities and temperatures operated in Alcator C- Mod ($n_e > 1 \times 10^{20}$ m^{-3} and $T_e > 2$ keV). Since the ionization energies of lithium and helium-like calcium are $\sim$ 1.15 and 5.12 keV respectively, He-like calcium is the dominant core ($0.0 \leq r/a \leq 0.75$) charge state in a typical L-mode plasma and fluorine is typically full stripped by the middle of the

pedestal (outer 5% of the plasma), making CaF_2 visible in both core and edge views. Results from both lab tests and other Alcator experimental runs have shown that Al (Z=13), Fe (Z=26), Ni (Z=28), Nb (Z=41), Mo (Z=42), and W (Z=74) are also easily ablated by this system. These additional impurities may be utilized in future impurity transport studies on C-Mod.

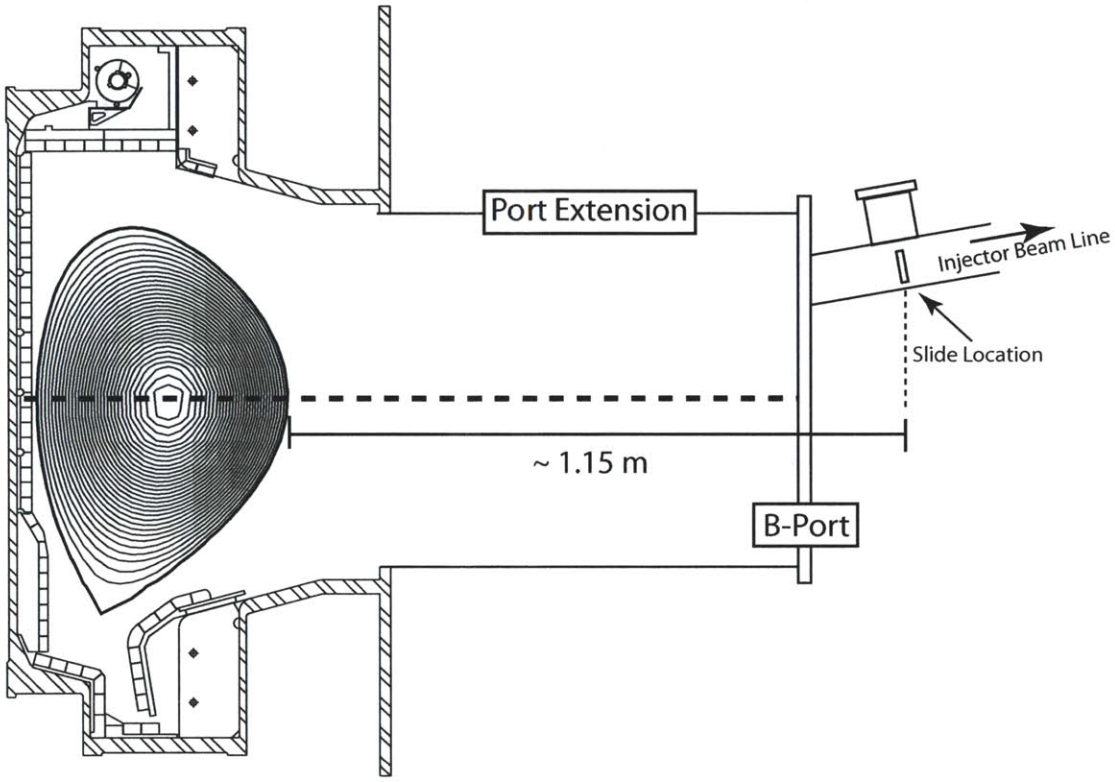

Figure 3-2: A cartoon of the impurity injector's location on B-port relative to the plasma is shown.

Each laser pulse is incident upon the optical train shown in Figure 3-3. Its purpose is to focus and steer the beam to the desired location on the slide. The laser is first defocused by an -500 mm focal length lens to avoid power densities exceeding the damage thresholds for the optical components. All optical components are made of BK7 or fused silica and coated to optimize transmission of the main laser wavelength. In practice the damage thresholds are not approached at any point in the optical train. A colinear 670 nm diode laser is used to indicate the location of the main (infrared) beam. As shown in Figure 3-3, this is achieved by ensuring the beams are aligned

through the first mirror (Reflectivity $\sim$ 99% @ 1064 nm and Transmission $\sim$ 80% @ 670nm). A wide range of power densities is obtained through manipulation of the mechanical iris and the optical train's focal length. A long focal length (1146 mm) converging lens is translated up to 200 mm along the optical axis via a remote controlled linear stage. Lens translation and iris manipulation alters the system's

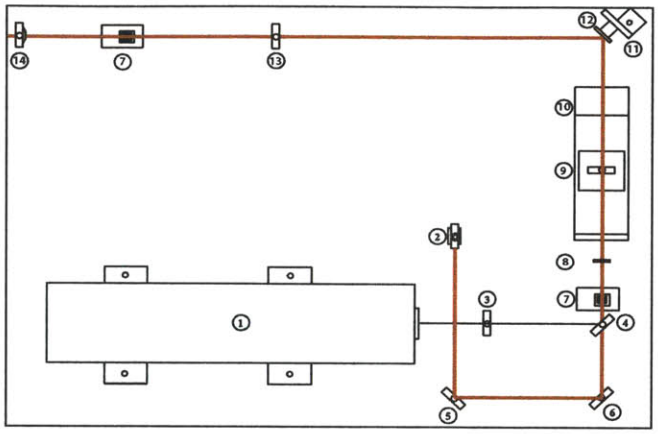

1. Nd:YAG laser (10 Hz rep rate, 1064nm, 680mJ/pulse)
2. Diode Alignement Laser (633 nm)
3. Plano-Concave Diverging Lense (f=-500 mm, BK7 Glass)
4. Mirror (BK7 Glass, R~99% @ 1064 nm, T~80% @ 670 nm)
5. Silvered Glass Mirror
6. Silvered Glass Mirror
7. Photodiode Housing/Photodiode
8. Mechanical Iris (1 inch max apeture)
9. Plano-Convex Converging Lense (f=1146 mm, Fused Silica)
10. Linear Translation Stage (200 mm travel)
11. Motorized Mirror Mount (+/- 97 mrad)
12. Piezo Electric Mirror Mount (Tip/Tilt 4 mrad)
13. Plano-Convex Converging Lense (f=1146 mm, Fused Silica)
14. Wedge Prism (10 degrees @ 1064 nm)

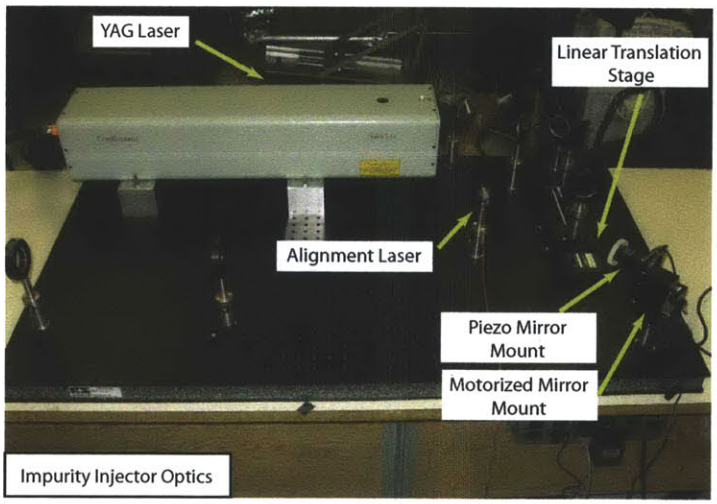

Figure 3-3: (Top) The layout of the final optical system is shown. (Bottom) An early arrangement of the impurities injector optics is shown in the setup lab. Most of the key optical components are shown.

focal length and power density, allowing for ablated spot sizes ranging from 0.5 to 7 mm in diameter. This corresponds to an almost 200x increase in the ablated area.

These aspects are essential to ensure both efficient ablation and control of the number of introduced impurities, making non-perturbative operation possible under different experimental conditions.

Unlike most previous laser blow-off systems, this system was designed such that multiple ablations can be achieved during single plasma shot with precise timing. Multi-pulse operation is achieved with a design unique to laser blow-off systems. Most existing systems use slide transition to achieve multi-pulse operation. Instead, the system developed for this thesis couples the 10 Hz repetition rate of the laser flashlamp with a fast piezo- electric mirror steering system. The piezo-electric mirror mount is manufactured by Piezosystems Jena and allows for up to 4 mrad of tip and tilt by the application of -10 to 150 V to each axis. This piezo system is mounted to an RS232 driven motorized mirror mount capable of +/- 97 mrad manufactured by Zaber. On fast time scales ($\cong$ 100 ms) the piezo-electric mount is used for beam steering while inter-shot movement is provided by the stepper motor system. This combination allows for up to 10 reproducible injections during the flat-top of a single plasma discharge (typically 1s) and up to 300 injections in a single day of tokamak operation for a single 50 $\times$ 50 mm slide.

Vacuum System

While the laser system operates in air, the target slide must be inside the tokamak vacuum system. The interface between the impurity injector's optical system and the C-Mod torus is a glass window at the end of the beam line. The beam line measures approximately 1 meter in length and is mounted at 10 degrees to the midplane on the B-port flange of Alcator C-Mod (see Figure 3-2). The basic setup of this system is demonstrated in Figure 3-4. Vacuum is achieved using both mechanical and turbo pumping systems manufactured by Pffefier vacuum. Vacuum pressure is measured using 3 separate convectron gauges down to 10^{-4} Torr, and an ionization gauge for pressures down to 10^{-10} Torr. With proper baking of the system, pressures of 1×10^{-7} Torr are routinely achieved, adequate for transient exposure to the C-Mod torus vacuum. The system is mechanically and electrically isolated from Alcator via a

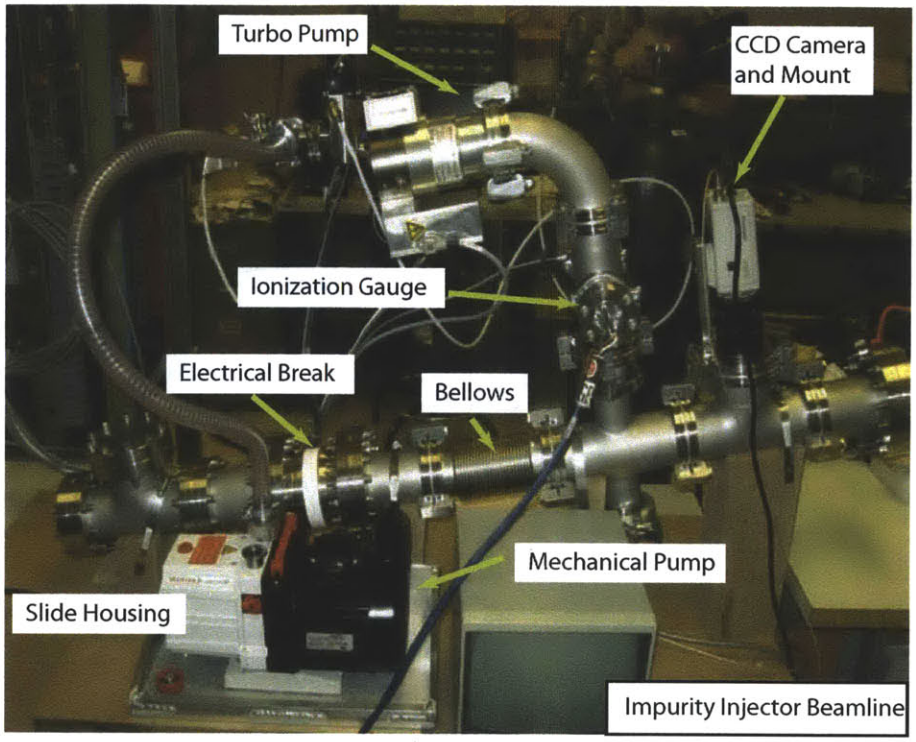

Figure 3-4: The impurity injector beamline is shown in the setup lab. This figure shows many of the key aspects of the system.

bellows and ceramic break respectively. To maximize the transmission of laser blow-off neutrals introduced into the plasma, the target slide is housed directly in front of the torus interface valve. A 3D model of the slide holder is shown in Figure 3-5. Using a simple model of the neutral transmission to the plasma edge indicates that, with the current beam line setup, 55 to 85% of laser blow-off neutrals are transmitted to the plasma edge following ablation. This model assumes a ± 13 degree spread of the neutrals upon ablation and that any neutral impacting a material surface is lost. Under these assumptions, the limiting aperture appears to be the port extension on b-port.

Electronic Systems

Limited access to the C-Mod cell during tokamak operation requires remote control capability of the laser blow-off system. Measurements of vacuum pressure, gauge

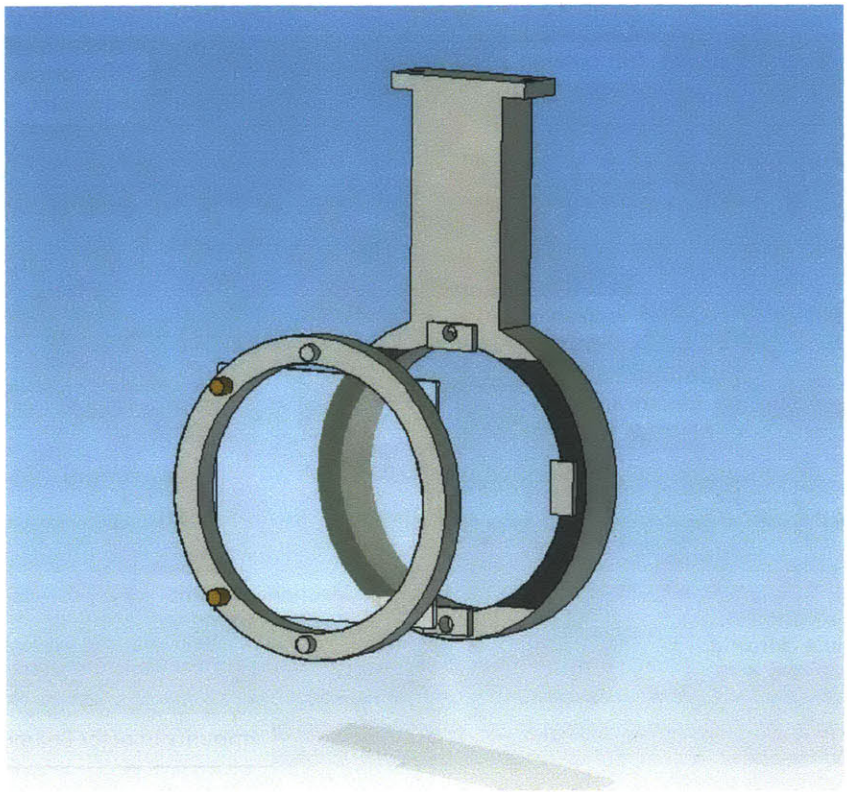

Figure 3-5: A solid edge model of the impurity injector's slide holder is shown. In this figure the face of the slide holder is expanded. When in use, a $50 \times 50 \times 1$ mm glass slide is sandwiched between the front plate and the body of the slide holder.

voltage, turbo pump rotation frequency, pump status, and temperature measurement of the beamline are reported through the systems Programmable Logic Controller (PLC). Interface with the PLC is provided by the RSVIEW program which allows for almost fully remote operation of the laser blow-off system. Visual confirmation of laser ablation and beam positioning is provided by a CCD video camera observable in the Alcator C-Mod control room. For diagnostic purposes, all signals used for laser triggering, energy measurement, and movement of the piezo-electric mirror mount, are split and digitized for shot by shot monitoring. Measurement of the main beam energy is provided at two separate locations along the optical train (see Figure 3-3). A standard glass slide is used to remove small (a few %) beam fractions and direct it to a photodiode housing. The photodiode signals are then amplified and monitored remotely. An analog output module is used for remote operation of the piezo-electric

laser beam steering system and external laser triggering. High voltage amplifiers convert 0 to 5 V output of the analog output module to 0 to 150 V needed to drive each piezo axis. TTL signals provided by the analog output module externally enable the laser flash lamps and trigger laser q-switching. Operation of the stepper motor mirror mount and linear translation stage is performed using RS232 commands. An in-cell computer allows for remote login access and between shot manipulation of course beam steering and focusing. Further details of the electronic systems can be found in Appendix A.

3.3 Laser Blow-off Injection Characterization

Much of previously published work on laser ablation has focused on characterization of the produced laser blow-off neutrals via lab bench testing [66, 65]. Here we focus on the basic characteristics of typical laser blow-off injection following its introduction into the plasma environment. This section discusses the characterization of the injected impurities from measured source time histories, changes in Z_{eff}, the impurity confinement time, the reproducibility of injections and their non-perturbative introduction into the plasma.

3.3.1 Measurement of the Laser Blow-off Source

For all experiments described here, fiber optics were installed to view the impact location of laser blow-off neutrals at the plasma edge and their ionization. A 420 ± 10 nm filter coupled to the fiber optics and a photomultiplier allowed for measurement of multiple Ca I lines and provided an accurate time history of the laser blow-off neutral source at the edge. Since the ionization mean free path of calcium neutrals at a typical C-Mod edge is of order a few mm, this measurement provides a good indication of the calcium influx localized at the plasma edge. The intensity of the emission makes it possible to obtain excellent signal to noise and provides evidence of small amounts of slowly moving clusters of blown-off material. All of the results presented here are consistent with the more detailed assessment of the laser blow-off neutral

sources performed by Marmar *et al.* [66]. If it is assumed that single CaF_2 molecules make up the initial spike in the signal, these particles would have a directed energy of slightly less than 1 eV. An unintentional byproduct of laser blow-off, secondary clusters of blown-off material arrives at the plasma approximately $10 - 15\times$ later than the initial signal of blown-off neutrals, indicating that they are approximately $100\times$ more massive than the initial blown-off neutrals. Figure 3-6 demonstrates a

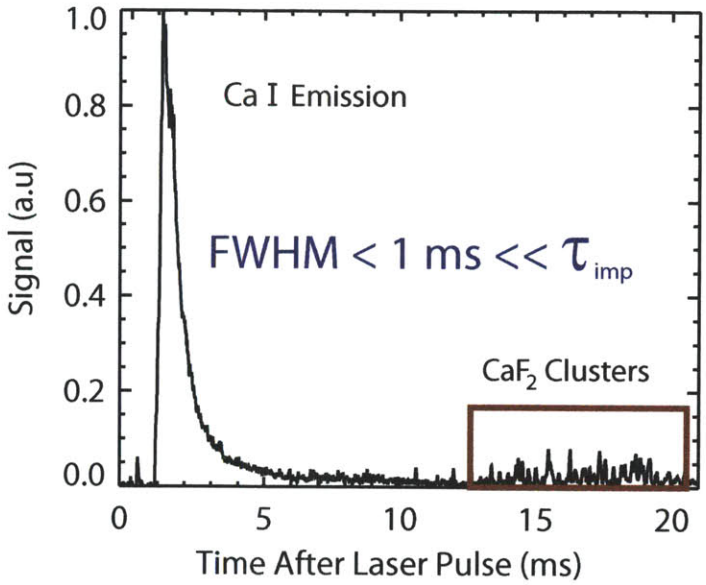

Figure 3-6: The time history of the measured laser blow-off (Ca I emission) source is shown. The initial pulse of free neutrals occurs shortly after the laser blow pulse. Approximately 15 ms after the laser pulse, clusters of blown off material arrive at the plasma edge.

typical injection measurement and the presence of clustered material which arrives at the plasma after the initial pulse of free neutrals. Although small, the contribution of these clusters can be observed spectroscopically, and must be considered when attempting to explain measured spectroscopic brightness time histories (See Figure 3-8). Nonetheless, the measurement of Ca I provided a direct measurement of the calcium ionization source in the boundary plasma which is required for transport analysis. It is important to note that the FWHM of the atomistic injected impurity source is < 1 ms $\ll \tau_{imp}$. This makes the laser blow-off neutral atom source effectively a delta function in time when compared to global transport time scales.

3.3.2 Estimating Impurity Density from ΔZ_{eff}

Although the exact amount of impurities introduced into the plasma via laser blow-off is not known. Impurity densities can be estimated through simple arguments based on changes in Z_{eff}. Typical ablated spot sizes range from .5 to 3.5 mm in most experiments and result in the introduction of a small number of impurity particles per injection. Changes in Z_{eff}, as obtained here through visible bremsstrahlung measure-

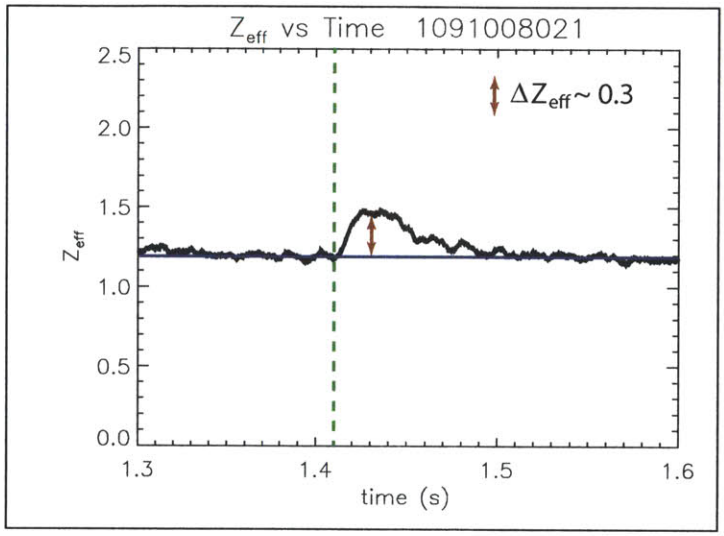

Figure 3-7: The change in Z_{eff} obtained through visual bremsstrahlung measurement is shown following a laser blow-off injection at 1.41 seconds.

ment, are indicative of the number of injected particles. From the definition of Z_{eff} the impurity density that results is:

$$n_z = \frac{\Delta Z_{eff} n_e}{(Z_{imp})(Z_{imp} - 1)} \tag{3.5}$$

The average ion charge state of calcium and fluorine in the plasma are $\sim$ 18 and 9 respectively, the average Z of the injected material (CaF_2) is 12 and therefore 36 total electrons are contributed to the plasma per CaF_2. For the injection scenario shown in Figure 3-7, Δ Z_{eff} $\sim$ 0.3. This indicates that of the order of 7.15×10^{16} ($\sim$ .00024 n_e) CaF_2 molecules have been introduced into the plasma. Given a typical operational spot size of $\sim$ 2.5 mm in diameter and a CaF_2 density of 3.18 g/cm^3 ,

this suggests that about 2.4×10^{17} CaF_2 are ablated off the slide. Therefore only a fraction ($\sim$ 29%) of the ablated particles actually make it into the plasma core during a typical L-mode injection. The remainder of the injection is either ionized by the laser and deflected by the magnetic field or is ionized and lost from the highly turbulent scrape-off layer before reaching the core plasma. Based on these numbers, a slightly less than a 1% change would be expected in the electron density following an injection.

3.3.3 The Impurity Confinement Time, τ_{imp}

CaF_2 injections were introduced into a wide range of C-Mod plasmas and a simple confinement time analysis was performed on the soft x-ray and High Resolution X-Ray Spectrometer (HiReX) brightness signals. A complete description of these diagnostics can be found in the following section. To characterize the global impurity confinement of L, I, and H-mode plasmas, spectroscopic signals were fit using a simple model for the decay of the signal. A single laser blow-off pulse creates a transient impurity influx into the plasma after which the impurity density radial profile shape reamins constant by the impurity density decreases exponentially. During this phase the impurity density decays away with the following form [51].

$$n_z(r,t) = \sum_k A_k n_k(r) e^{\frac{-t}{\tau_k}} \tag{3.6}$$

The fundamental eigenfunction is defined to be the impurity confinement time, τ_{imp}. Figure 3-8 demonstrates the temporal evolution of He-like Ca following a CaF_2 laser blow-off pulse. The exponential fit to the decay phase is performed well after the peak ($\sim$ 30 ms after the laser pulse) to ensure that all ionization events at the plasma edge have occurred and only the fundamental eigenfunction is reflected by the inferred τ_{imp}. The impurity confinement time is therefore determined by fitting an exponential function:

$$\propto e^{\frac{-t}{\tau_{imp}}} \tag{3.7}$$

to the measured brightness versus time signals.

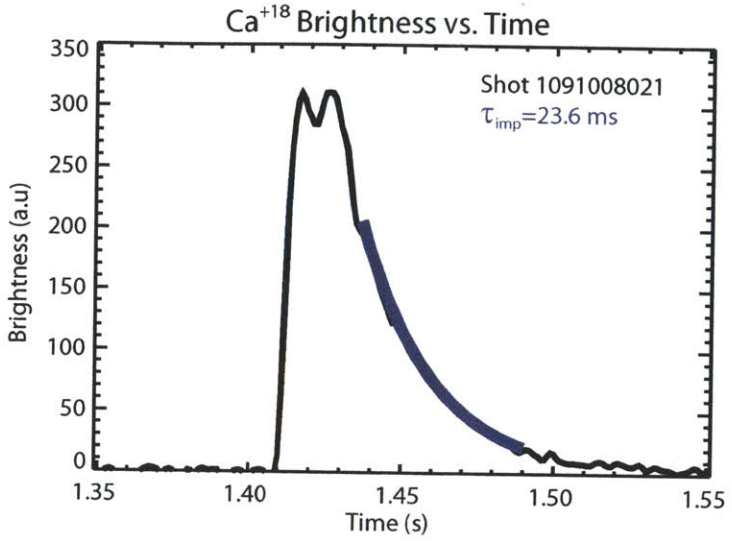

Figure 3-8: The exponential decay of calcium on the x-ray spectrometer signal and the fit to the exponential decay (blue line). The injection occurs at 1.41 seconds. The secondary peak (at $\sim$ 1.43 sec) in the brightness signal is the result of cluster formation during the injection

3.3.4 Reproducibility of Injections

The reliability of injections created by laser blow-off is demonstrated by their reproducibility in measured signals. Comparison of the source signals, as shown in Figure 3-9, demonstrates the similarity between the laser blow-off produced neutral source for multiple injections into a stationary plasma discharge. The reproducibility of these injections is of particular relevance to this work. As will be discussed in further detail in Chapter 4, brightness data from multiple, steady state, impurity injections are often combined into a single data set to improve the temporal resolution of the measurements. This technique implicitly assumes that each injection time history is repeatable. In practice, the source time histories of the source are found to be quite reproducible and the amplitude of steady-state injections are repeatable within approximately $+/-10\%$.

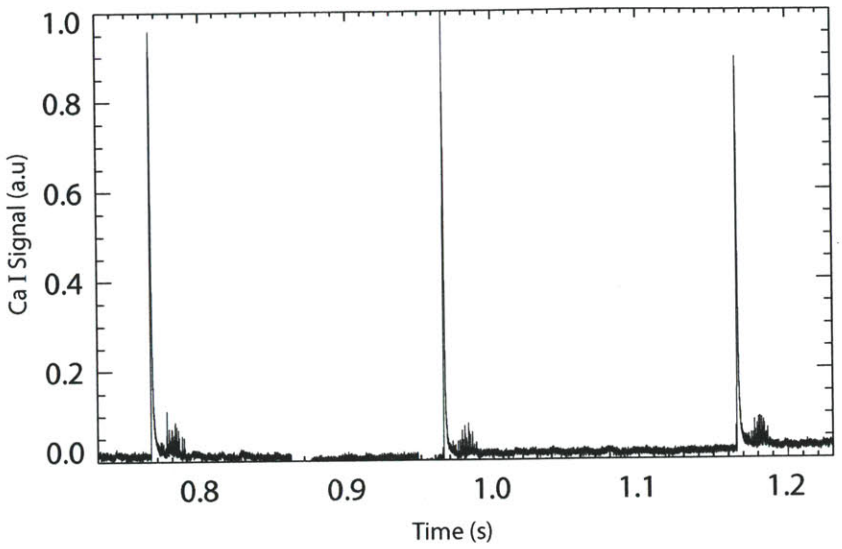

Figure 3-9: Three injections into a steady-state plasma discharge are indicated by edge plasma Ca I emission. Typical repeated injections indicate their source amplitude is reproducible to within approximately $+/-10\%$. The presence of clusters following the main injection can be noted after each injection.

3.3.5 Non-Perturbative Operation

As discussed previously, turbulent transport is driven by the free energy in the gradients of plasma profiles. Trace impurity injection via laser blow-off ensures that the transport properties measured are characteristic of the non-perturbed, pre-injection plasma profiles which dictate the turbulence properties. For the purposes of transport experiments "non-perturbative" is quantified as less than 10% change in the electron density and temperature with minimal effect on density fluctuations [61]. In practice the change in the core electron density and temperature is usually $\ll 10\%$. These injections may be characterized as a tracer for the bulk particle transport. Non-peturbative injections are obtained through manipulation of the system's focal length, laser power density, and ablated spot size. An example of an non-perturbative impurity injection into Alcator C-Mod is shown in Figure 3-10.

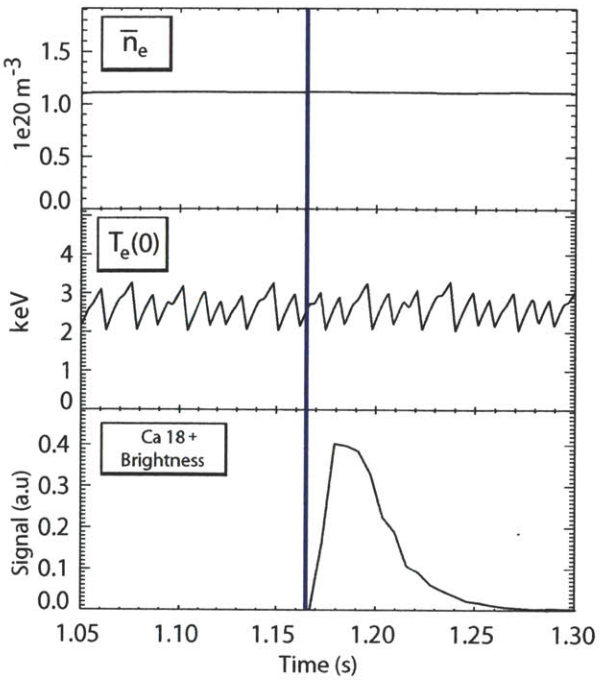

Figure 3-10: The effect of an injection on major plasma parameters (n_e, and T_e) is demonstrated. The injection occurs at 1.41 sec.

3.4 Determination of Background Plasma Profiles on Alcator C-Mod

As discussed in Chapter 2, the physical quantities which drive impurity transport in both collisional and turbulent transport theory are the background plasma profiles and their gradients. In this work, we wish to compare the predictions of neoclassical and turbulent transport models to experimental transport levels. In order to make accurate comparison between theory and experiment, the uncertainty in experimental profiles (n_e, T_e, T_i, and q) and their derivatives must be minimized. The extensive diagnostic suite present on the Alcator C-Mod tokamaks makes such measurement possible. Using some of the most advanced measurements techniques currently available, the error in turbulence drive and suppression terms is reduced to levels which allow for quantitative comparison of experiment with turbulence models. This section covers descriptions of the main diagnostic systems utilized in this thesis work and provides examples of the measurement quality.

3.4.1 Electron Density and Temperature Measurement Using Thomson Scattering

The Thomson scattering system operating on Alcator C-Mod is an essential diagnostic for transport studies. An in-depth description of this system can be found here [71, 6]. It features two distinct systems which provide both core and edge measurement of n_e and T_e. Two identical Q-switched Continuum brand Nd:YAG lasers are operated sequentially to provide 60 Hz operation of the Thomson system. Measurement of scattered light along the vertical Thomson chord is obtained using twenty-two, single-strand quartz fibers for the edge Thomson system and up to fourteen additional fibers which constitute the core Thomson scattering system. This system can ultimately provide measurement of both n_e and T_e at approximately 16 ms intervals with equivalent radial resolution of $\Delta R = 1$ cm (5% of a) in the core and $\Delta R = 1 - 2$ mm in the plasma edge. Profile measurements provide by the core

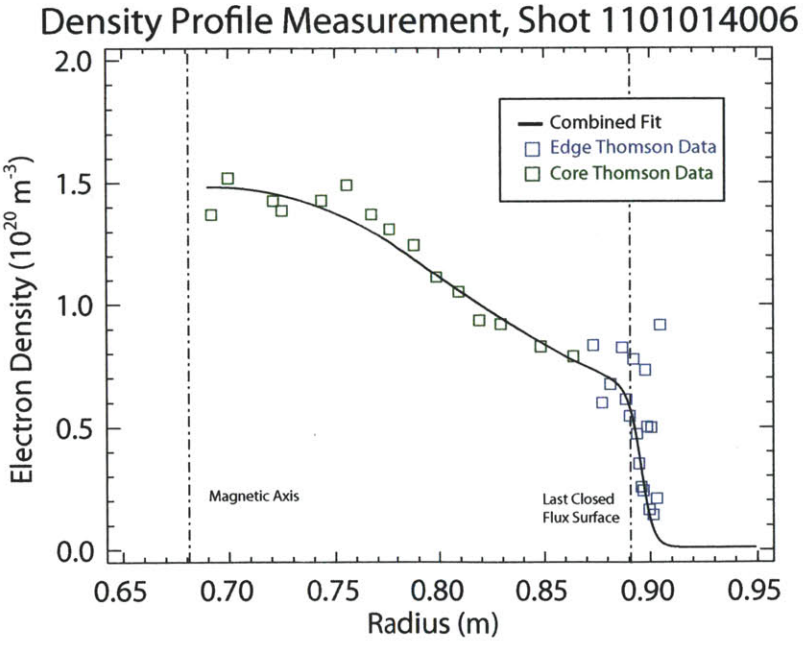

Figure 3-11: An example of Thomson scattering density profile measurement is shown for the core and edge systems. The solid line indicates the FiTS generated b-spline fit to the measured data.

and edge Thomson scattering systems are demonstrated in Figure 3-11 and Figure

3-12 for a typical Alcator C-Mod L-Mode discharge. Absolute density calibration of these measurements is made through comparison with Electron Cyclotron Emission (ECE) cut measurements in discharges with secular increases in core density. Unlike the temperature profile, which is also measured using ECE measurement, the density profile measurements provided by Thomson scattering are the only direct density profile measurement available. Thomson scattering data provided the basis for all profiles used in experimental and gyrokinetic analysis presented in this thesis.

3.4.2 Electron Cyclotron Emission Temperature Measurement

Additional measurement of the electron temperature is provided by three separate ECE systems on Alcator C-Mod [72, 73, 74]. These measurements feature superior temporal resolution to the Thomson scattering system and serve to complement the data obtained from Thomson measurement. An example of all temperature measurements can be found in Figure 3-12. All three systems present on C-Mod use second harmonic X-mode emission. For typical C-Mod operational densities and parameters, measurement of the electron temperature is provided from the plasma core to the edge and is localized by its dependence on the value of B_ϕ. Two of these high time resolutions measurements are provided by grating polychoromator systems. These two systems, GPC1 and GPC2 consist of 9 and 18 channels respectively. Additional ECE measurement is provided by the Fusion Research Center ECE (FRECE) system operated by the Texas collaboration on Alcator C-Mod. This system provides up to 32 additional channels with even higher temporal resolution. Estimated error bars for ECE measurements (10%) are often lower than those estimated for T_e measured from Thomson scattering in the core. As a result, the combination of these systems with the existing Thomson measurements plays a crucial role in constraining the normalized electron temperature gradient scale length, an important quantity which drives turbulence in the plasma core.

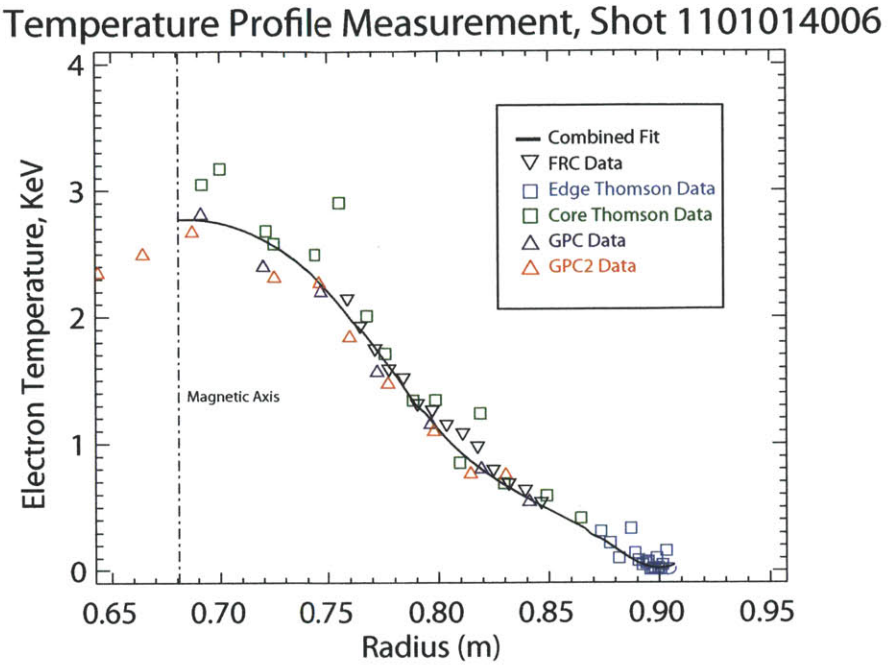

Figure 3-12: An example of Thomson scattering and ECE temperature profile measurements are shown for an L-mode discharge. The solid line indicates the FiTS generated b-spline fit to the measured data.

3.4.3 Profile Fitting of n_e and T_e

Smooth profile fits of the background electron density and temperature profile are obtained using the FiTS code developed by Darin Ernst and Kirill Zhurovich. FiTS offers a GUI for removing outlying temperature and density data and performing smoothing in both space and time. Separate functional fits are applied to the core and edge data. In the core, data are fit using a b-spline fitting routine which allows for user specification of the order and number of knots allowed in the fit. In practice, the order and number of knots used is kept relatively small to avoid introduction of false structure into the core profile shapes. The reduced χ^2 is reported to the user for each fit. For the fits used in this work, the reduced χ^2 was generally found to approximately equal to 1 for the temperature profile fits and often less than 1 for the density profile fits. Attempts to raise the density reduced χ^2 to a value of 1 were generally unsuccessful. Edge data are fit using a tanh function to model the pedestal region of the plasma. A user specified blending region is set in FiTS

which determines the radial locations over which the edge and core fits are combined in a smooth manner. The program is built around the Thomson time base and therefore allows for profile fitting at approximately 16 ms intervals during the plasma shot. In practice, only data obtained from the core and edge Thomson system is used for density profile fitting, while the temperature profile allows for the use of all temperature measurements for constraint of the temperature profile fits. An example of FiTS generated electron density and temperature profiles can be found in Figures 3-11 and 3-12.

3.4.4 Measurement of T_i and V_ϕ

Accurate measurement of the ion temperature and toroidal rotation profiles is essential for meaningful comparison of experiment with simulation. As the Ion Temperature Gradient mode is often the dominant plasma instability and drives the majority of energy and particle transport, measurement of (ITG) drive term, a/L_{T_i} is of great importance for turbulence studies. Furthermore, rotation effects, specifically the E $\times$ B shearing rate arising from radial gradients in the electric field, have been shown to suppress turbulent fluctuations and reduce transport levels, making measurement of the velocity profile essential for turbulence modeling [75].

Measurement of both the ion temperature profile and rotation velocity is provided by **Hi**gh **re**solution **X**-ray Spectrometer with **S**patial **R**esolution (HiReX Sr.). A description of this diagnostic can be found here [7]. HiReX Sr. is an imaging x-ray spectrometer used to measure spectra of the He-like and H-like charge states of argon in the spectral range of 3.94 Å $< \lambda <$ 4.00 Å and 3.72 Å $< \lambda <$ 3.80 Å respectively. This system employs 4 Pilatus 100 x-ray detectors for imaging of the spectra which can operate at photon counting rates up to 1 MHZ. In practice, data acquisition times are limited by a detector readout time of approximately 3 ms. Argon is introduced at trace levels at the beginning of the discharge via gas puffing for routine measurement of T_i and V_ϕ. These measurements are limited to the extent of the He and H-like argon charges state. For typical C-Mod densities and temperatures, this limits accurate profiles to approximately $0.0 \leq r/a \leq 0.8$. Spectral moments of the measured data

represent a set of integral equations which can be solved for the profiles of interest such as density, velocity, and temperature. Exact details of these equations can be found here [76, 77]. Tomographic inversion techniques are applied to extract the desired kinetic profiles, T_i and V_ϕ. It is assumed that good collisional coupling between argon and the main ions (< 10 ms) relative to the energy confinement time implies that $T_{argon} \simeq T_i$. Absolute measurement of V_ϕ is performed through locked-mode calibration on dedicated discharges during an operational day. It is assumed that locked mode shots exhibit no toroidal rotation and the measured velocity therefore indicates the velocity zero. Specific limitations of the T_i and V_ϕ data used in this thesis will be discussed in later chapters.

3.5 Impurity Radiation Diagnostics

The following section provides a brief introduction to the spectroscopic diagnostic suite utilized for impurity transport studies on Alcator C-Mod. Example measurements from each diagnostic and descriptions of their relevance to this thesis work are presented.

3.5.1 High Resolution X-ray Spectrometer with Spatial Resolution - HiReX (Sr.)

The HiReX Sr. spectrometer used for determination of T_i and V_ϕ profiles and described in the previous section, is the workhorse diagnostic for the impurity transport studies in thesis. The unique spatial and temporal resolution of this spectrometer makes time evolving profile measurement of core impurity charge states possible. The standard setup for this spectrometer views the He-like and H-like charge states of argon. However, for this work, the H-like argon crystal was replaced with a crystal capable of viewing the He-like charge state of calcium. This leaves only the He-like argon measurement to provide the experimental T_i profiles. For typical densities (1.0×10^{20} m^{-3}) and temperatures (3 keV), the He-like calcium charge state (Ca^{18+})

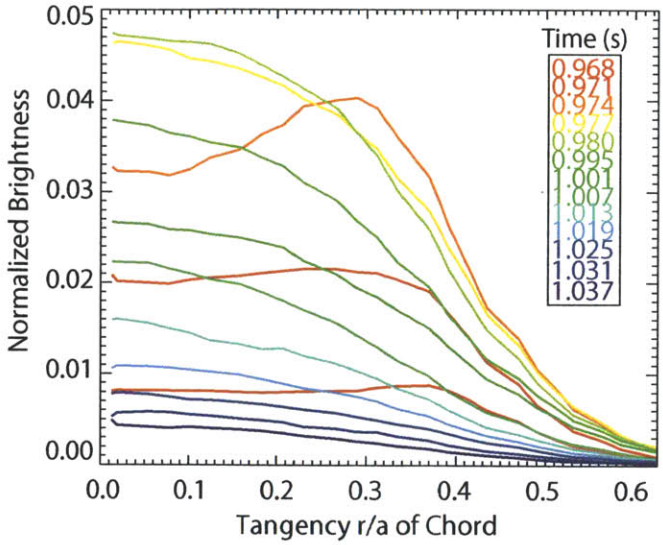

Figure 3-13: Measured He-like (Ca^{18+}) brightness profiles are shown. Selected time slices are shown to demonstrate the evolution of the profile after an impurity injection (.965 sec).

(ionization energy of $\sim$ 5.1 keV) has the highest fractional abundance and provides measurable profiles from approximately $0.0 \leq r/a \leq 0.6$ (see Figure 3-14). With the calcium-viewing crystal installed, the system views the spectral range from 3.16 to 3.23 Å. This includes the w, x, y, and z lines of He-like calcium. Emission from the w (resonance) line at 3.17 Å was used for all measurements presented here. Time resolution of these measurements can, in principle, be reduced to almost 3 ms. However, for typical L-mode plasma conditions, good signal to noise ratio requires operation with approximately 6 ms time resolution. To ensure pixel to pixel variation of the detector was not a problem, the system was exposed to an Iron-55 source (5.9 keV). It was concluded from this test that of only an $\sim$ 2% pixel to pixel variation would be present in the measurement of injected calcium brightness. Figure 3-13 illustrates line integrated brightness profiles of the He-like Ca charge state following a laser blow-off injection as measured by the HiReX Sr. diagnostic.

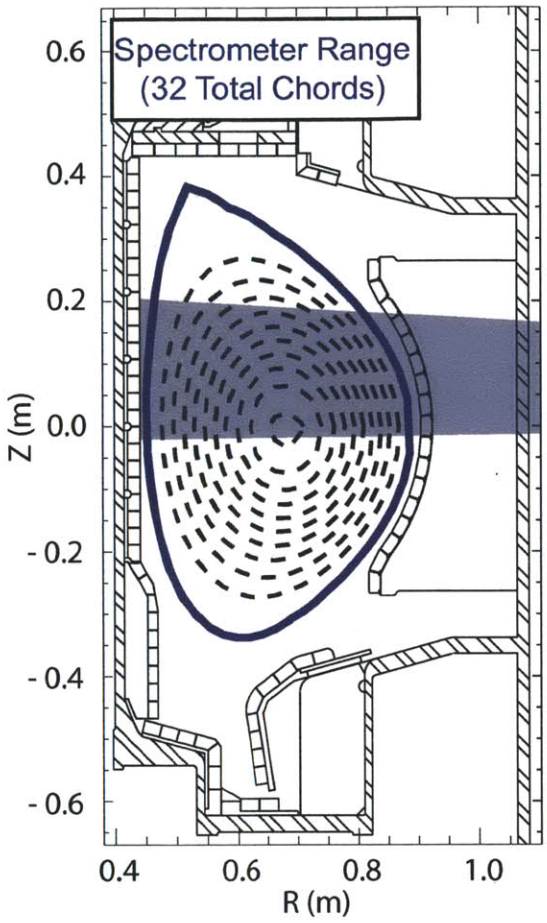

Figure 3-14: The approximate viewable range for the HiReX Sr. spectrometer is shown by the shaded region. This region is comprised of 32 total line integrated measurements.

3.5.2 The X-Ray and Extreme Ultraviolet Spectrometer (XEUS)

Additional measurement of calcium charge states is provided by the **X**-ray and **E**xtreme **U**ltraviolet **S**pectrometer, known as XEUS. XEUS is a single chord, flat field, grating spectrometer setup to provide an approximately core plasma view at an angle of 6.5 degrees relative to the midplane (see Figure 3-15). Spectral coverage includes x-ray and extreme ultraviolet portions of the spectrum from approximately 10 to 70 Å. Line emission from multiple charge states of calcium (Li, Be, B-like, etc.) is included within this portion of the spectrum. A typical spectrum following an calcium laser blow-off injection is shown in Figure 3-16. However, due to the

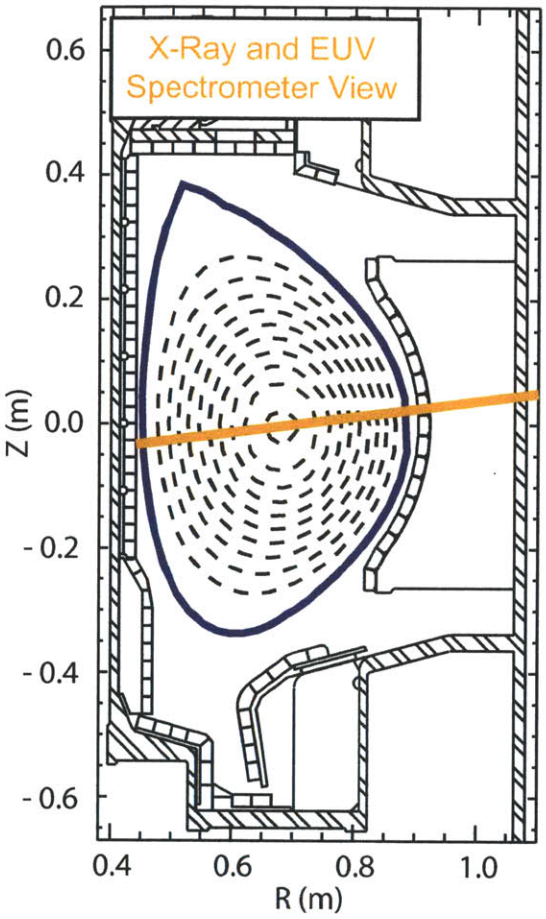

Figure 3-15: The single chord view provided by the XEUS spectrometer is shown.

reliability of the atomic physics data available, only Li-like Ca emission at 18.68 Å was utilized during these studies. This line is well separated from other background and calcium lines and provides good signal to noise for typical plasma conditions. Fast framing CCD capabilities of the system allow for routine operation with time resolution of 5 ms. However, resolution of down to 2.5 ms was utilized during this work to best resolve transient behavior following laser blow-off injection. Future work on this spectrometer will add spatially resolving components and allow for both core and edge spatial coverage.

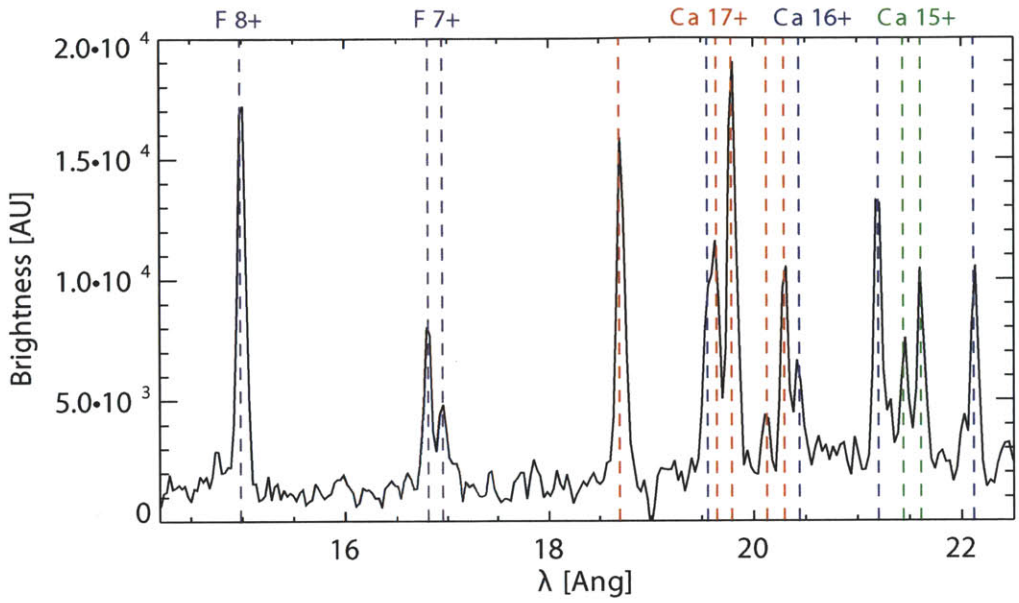

Figure 3-16: A typical spectrum measured by the XEUS spectrometer is shown following a CaF_2 injection. Line emission from the Li, Be, and B-like calcium charge states is visible. Image from Reference [4].

3.5.3 High Resolution X-ray Spectrometer - HiReX (Jr.)

The primary measurement used for global impurity confinement time analysis was provided by the HiReX spectrometer [78]. This spectrometer is the predecessor of the HiReX Sr. spectrometer described earlier in the section and known colloquially as the HiReX Jr. spectrometer. Originally installed as a one of five identical spectrometers for measurement of the ion temperature profile via puffed argon gas, only a single spectrometer remains mounted on the Alcator C-Mod K-port. HiReX is a von Hamos type spectrometer with sufficient spectral resolution to measure Doppler broadening and shifts. Spectral coverage of the spectrometer exist from 2.8 to 4.0 Å with a resolving power of $\lambda/\Delta\lambda = 4000$. Data acquisition rates for this spectrometer are operated at 1KHz, more than sufficient for resolving both the influx and decay phases following an impurity injection. The resonance line (3.17 Å) of the He-like calcium charge state (Ca^{18+}) charge state is routinely measured using this spectrometer setup and used for the determination of impurity confinement time. Using a view that is typically tangent $r/a = 0.3$, this spectrometer provides line integrated brightness

measurement of Ca^{18+}. The core view of this spectrometer, good signal to noise following a laser blow-off injection, and its excellent temporal resolution make it ideally suited for these studies. Observed calcium emission following a laser blow-off injection is shown in Figure 3-17. Note the clear resolution of both the influx and decays phases of the impurity injection.

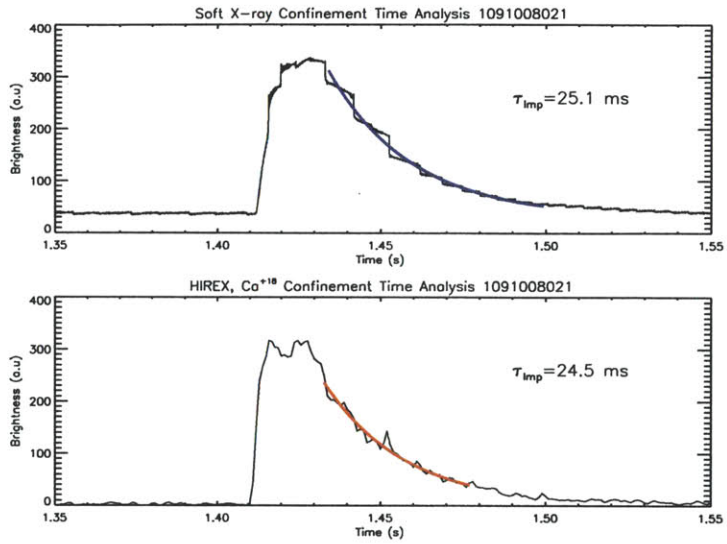

Figure 3-17: Plots of brightness versus time measurement following a laser blow-off injection are shown. Measurement was provide by soft x-ray imaging (a) and HiReX Jr. (b). Both diagnostics have sufficient time resolution to resolve the influx and decay phases and are shown to provide almost identical values for the impurity confinement time. The presence of sawteeth provide the step-like features in the soft x-rays.

3.5.4 Soft X-ray Imaging

Four soft x-ray imaging systems are operational on Alcator C-Mod. A complete description of these systems can be found in references [71, 79]. Each system contains a 38-element photodiode array with 3 μs response time and radial chord spacing of less than 2 cm. Beryllium foil filters eliminate collection of visible, UV, and ultrasoft x-rays from the system. The two core viewing arrays use $50-\mu$m foils optimized for viewing greater than 2 keV photons, while the two edge viewing arrays feature $10-\mu$m filters optimized for photons below 500 eV. The various poloidal views of the core arrays allow for tomographic reconstruction of the 2D x-ray emissivity. Soft x-

ray data were utilized in this work for the determination of the impurity confinement time. Emission from core calcium charge states (H, He, Li-like) is clearly observed following laser blow-off injection. An example of these measurements and their use in confinement time determination is shown in Figure 3-17a.

Chapter 4

Impurity Transport Analysis Tools on Alcator C-Mod

In Chapter 3, the set of diagnostic tools used during this thesis work was presented. Here we introduce the software tools used to analyze the data provided by laser blow-off injection and spectroscopic measurement. Brief descriptions of the iterative synthetic diagnostic procedure developed around the impurity transport code STRAHL, the power balance code, TRANSP, and the gyrokinetic code, GYRO, are provided. Specific emphasis is put on their application to the analysis of core impurity transport on Alcator C-Mod.

4.1 Determination of Experimental Impurity Transport

4.1.1 The Governing Equations of Impurity Transport

The equations governing impurity transport are a set of coupled partial differential equations representing continuity for each charge state of the impurity species namely:

$$\frac{\partial n_z}{\partial t} = -\nabla \cdot \vec{\Gamma}_z + Q_z \tag{4.1}$$

The impurity flux for a particular charge state is represented here as Γ_z and Q_z represents the sources and sinks for each charge state ; namely ionization, recombination, and charge exchange processes. The system of equations is coupled through the source/sink terms. Writing out the source and sink terms explicitly we can express Equation 4.1 as:

$$\frac{\partial n_z}{\partial t} = -\nabla\cdot\vec{\Gamma}_z - (n_e I_z + n_e R_z + n_H \alpha_z) n_z + n_e I_{z-1} n_{z-1} + (n_e R_{z+1} + n_H \alpha_{z+1}) n_{z+1}. \quad (4.2)$$

where I_z is the ionization rate coefficient for an impurity species with ionization stage Z, R_z is the recombination rate coefficient for radiative and di-electronic recombination from ionization stage Z, and α_z is the charge exchange coefficient. It is important to note that in tokamak geometry, all of these quantities will have a radial dependence.

Previous measurement of particle transport in non-inductive scenarios have demonstrated the need for a non-diffusive term in the particle flux [20]. Therefore, the flux is assumed to consist of a diffusive contribution, which is proportional to the density gradient for the species, and a convective contribution proportional to the density. This is written as:

$$\vec{\Gamma}_z = -D\nabla n_z + V n_z \quad (4.3)$$

Where D and V are the familiar flux-surface averaged diffusive and convective transport coefficients. The solution of Equation 4.2 provides a complete description of the time dependent impurity density profile in the plasma.

4.1.2 Evaluation of the Impurity Transport Equations Using STRAHL

Analytic solutions to the impurity transport equations (Equations 4.2 and 4.3) do not exist. As a result, the impurity transport code STRAHL [80] was used to solve the coupled system of equations. STRAHL employs an unconditionally stable Crank-Nicolson scheme to solve the set of coupled equations represented by equation 4.2 using radially dependent input values of D(r) and V(r). The details of STRAHL's

numerical scheme are outside the scope of this thesis but the reader is referred to reference [81] for additional information.

In order to simulate the transport equations, STRAHL must be provided with a set of input data. The following inputs are required for numerical solutions of the transport equations:

- The measured time history of the neutral impurity source.
- Atomic physics data. (ionization, recombination, and photon emission rates)
- The measured background plasma profiles for n_e and T_e.
- Plasma geometry information from an MHD equilibrium reconstruction (EFIT).
- Profiles for the diffusion and convection coefficients.

The laser blow-off source measurement described in Chapter 3 provides the time dependent source of neutral impurities which is used as the input to the STRAHL code. Source rates were provided for approximately 20 ms following laser blow-off injection to resolve the initial laser blow-off neutral source as well as the trailing clusters of material.

Atomic physics data used in this analysis was provided by the Atomic Database and Analysis Structure (ADAS) [82]. ADAS provides high quality atomic physics data for fusion applications. STRAHL is capable of reading standard ADAS file formats and was provided with ionization, recombination, and photon emissivity data obtained from the online database of atomic physics data, Open ADAS [82]. Use of a standardized format which is openly available is important to ensure the reproducibility of this work.

Raw Thomson and ECE profile data were b-spline fit using the FiTS code and the resulting profiles were provided to STRAHL. Plasma geometry information is provided to STRAHL with the assumption of a stationary plasma geometry throughout the STRAHL run time. To ensure the validity of this assumption, all analysis was constrained to stationary portions of the discharge. For consistency, standard analysis EFIT was used for both specification of the plasma geometry and the mapping of

the n_e and T_e profiles to the midplane.

Two options are available for the input of transport coefficient profiles into STRAHL. Profiles can be specified using simple parameterized models for both D and V profiles which allows for faster execution, but restricts the possible profile shapes. Alternatively, the user is able to specify radial knot locations on which to specify values for D and V. Values between the specified knots are obtained through straightforward linear interpolation. Although slightly less efficient in computational time, this approach allows for completely independent variation of the transport coefficient values at each radial knot location and was used throughout this work. STRAHL assumes that the transport coefficients, D and V, are flux-surfaced averaged, radially dependent, and time independent.

STRAHL can not be executed in a time-independent mode and requires finite simulation time. All discharges analyzed in this work exhibited L-mode particle confinement and required 100 ms of simulation time (the amount of time stepped forward in the solution of Equation 4.2). Given a typical L-mode impurity confinement time of 20 ms this interval properly resolves both the influx and decay phases following an impurity injection. With this setup, execution times were approximately 2-3 seconds.

Following the execution of a STRAHL run, the charge state density profiles are returned as a function of time. An example of STRAHL simulated impurity density profiles using realistic transport coefficient profiles is shown in Figure 4-1. Provided with the appropriate photon emission atomic physics data, STRAHL can calculate the emissivity profile of desired line emission. The local line emission is known to be a function of the electron density, impurity charge state density, and the local electron temperature. This relation can be written as:

$$\epsilon = n_e n_z f(T_e) \tag{4.4}$$

Generation of modeled emissivity profiles which correspond to measured impurity line emission provide the necessary information needed to infer the experimental transport coefficient profiles using an iterative synthetic diagnostic built around STRAHL's

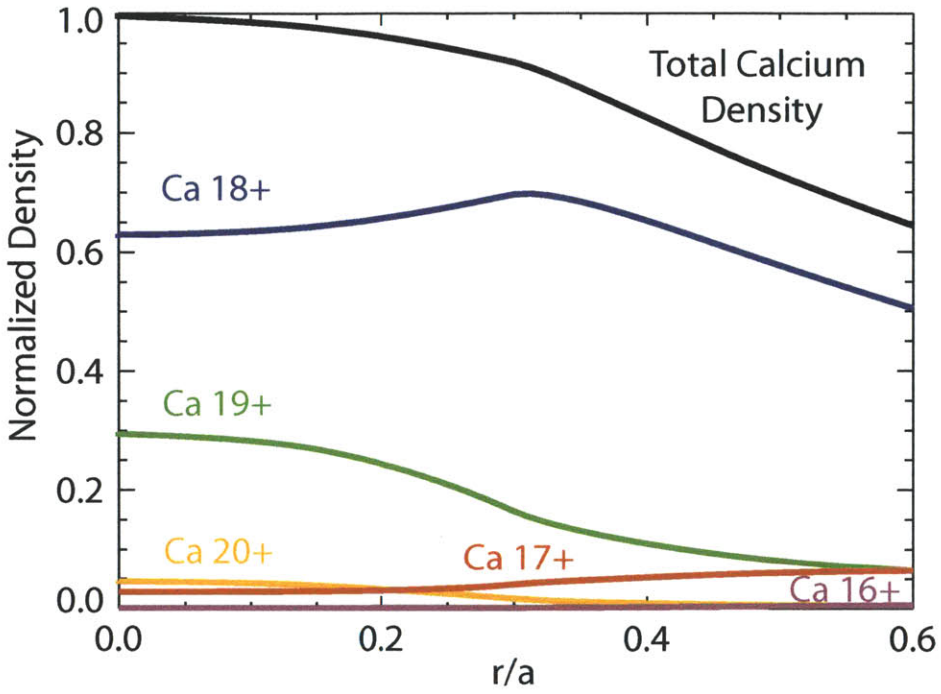

Figure 4-1: STRAHL generated impurity density profiles are shown in the experimentally relevant region ($0.0 \leq r/a \leq 0.6$) following a laser blow-off calcium injection.

output.

4.1.3 Determination of Experimental Transport Profiles Using an Iterative Synthetic Diagnostic

The experimental impurity transport coefficient profiles were determined by coupling STRAHL output with an iterative, χ^2 minimization method built around a synthetic diagnostic. The synthetic diagnostic and the complementary set of software tools for χ^2 minimization and iteration were developed specifically for this thesis work and allow not only for the determination of experimental impurity transport profiles but also the rigorous investigation of uncertainties in the derived transport. In all work presented here, two core spectroscopic measurements were used: Time evolving, radial profiles of Ca^{18+} (He-like Ca) provided by the HiReX Sr., soft x-ray spectrometer and the single chord Ca^{17+} (Li-like Ca) measurement provided by the XEUS soft x-ray/VUV spectrometer. An overview of the methodology implemented by the

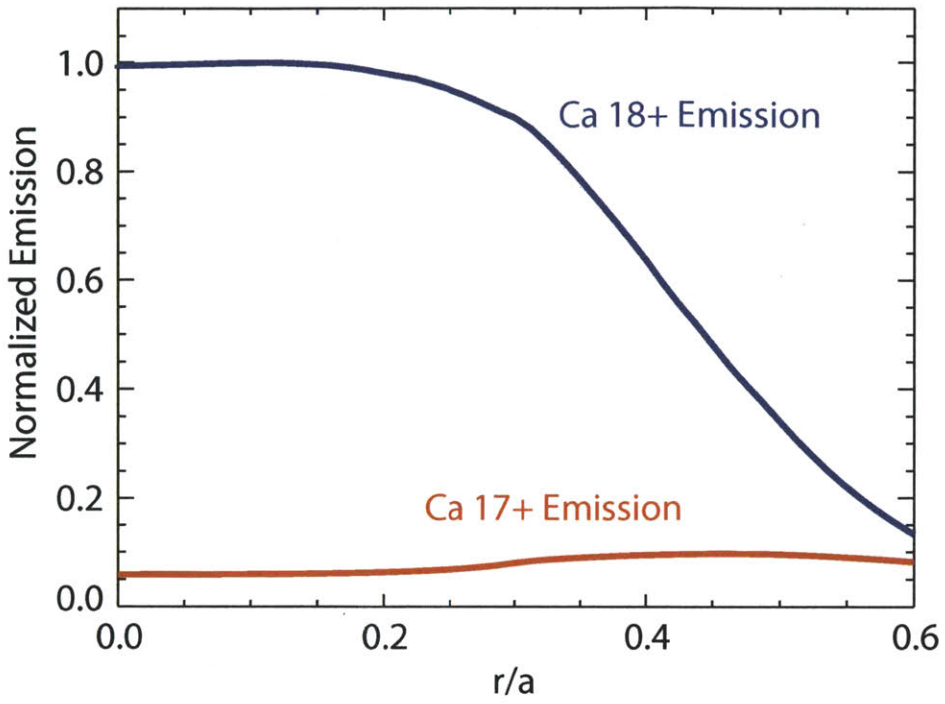

Figure 4-2: STRAHL generated emission profiles for the measured Ca^{18+} and Ca^{17+} lines are shown in the experimentally relevant region ($0.0 \leq r/a \leq 0.6$) $\sim$ 30 ms after a laser blow-off calcium injection.

iterative synthetic diagnostic is presented below but more detail can be found in Appendix C.

Execution of the iterative synthetic diagnostic requires an initial guess for the transport coefficient profiles and the additional STRAHL input data specified in the previous section. Data from the HiReX Sr. and XEUS diagnostics is loaded and processed such that background emission is subtracted and all signals are on identical time bases. To improve the temporal resolution of the primary He-like calcium measurement, data from 3 impurity injections into stationary plasma conditions is organized in time relative to the laser blow-off injection and combined into a single dataset. The possible error introduced using this procedure is discussed later in this chapter.

Execution of STRAHL generates emissivity profiles for the He-like calcium (Ca^{18+}) resonance line located at 3.17 Å and the Li-like calcium (Ca^{17+}) line located at 18.68Å. It is assumed throughout the analysis that the emissivity is constant on a flux surface.

While results on poloidal asymmetry of impurities were recently reported by Reinke et al. [83], the flux surface asymmetries for calcium appear to be quite small in the plasma core. Under this assumption, the STRAHL generated emissivity profiles are line integrated along the experimental lines of sight for both the HiReX Sr. and XEUS spectrometers. A total of 33 modeled and measured views of plasma emission are available for comparison. This consists of 32 line integrated views of Ca^{18+} with tangency radii extending out to $r/a \sim 0.6$ and a single line integrated view of Ca^{17+} emission which extends through the plasma core for typical plasma operation. The modeled/experimental views used in the analysis are demonstrated in Figure 4-3. In

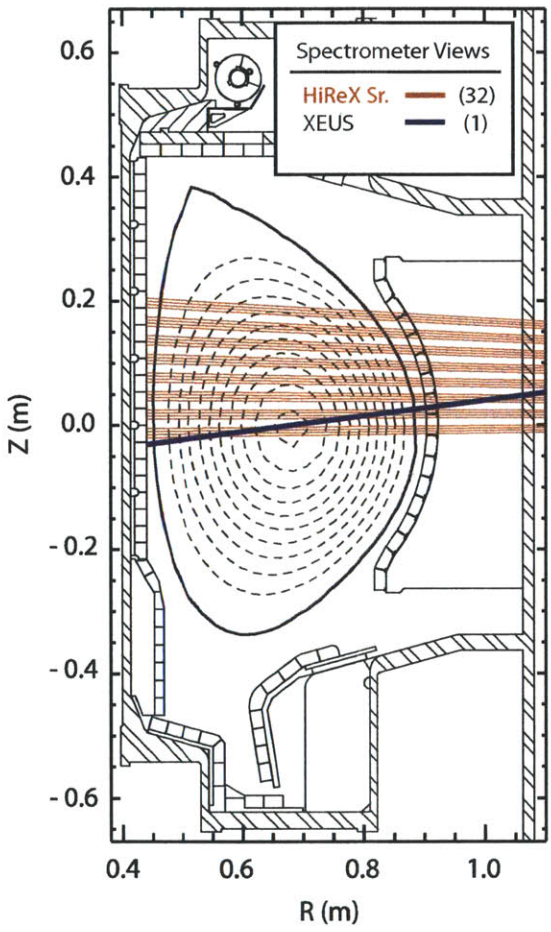

Figure 4-3: The 33 total views provided by the HiReX Sr. and XEUS spectrometers are shown. STRAHL generated emissivity profiles are line integrated along these views to compare with measured signals.

the absence of absolutely calibrated measurement, both modeled and measured signals are identically normalized while conserving the radial variation of the brightness profile. An unbiased measure of the agreement between the measured and STRAHL modeled spectroscopic signals is given by the following relation:

$$\chi^2 = \sum (\frac{S_{measured} - S_{STRAHL}}{\sigma})^2 \tag{4.5}$$

Where $S_{measured}$ and S_{STRAHL} are the measured and STRAHL simulated signal strength and σ is the estimated standard deviation of each data point.

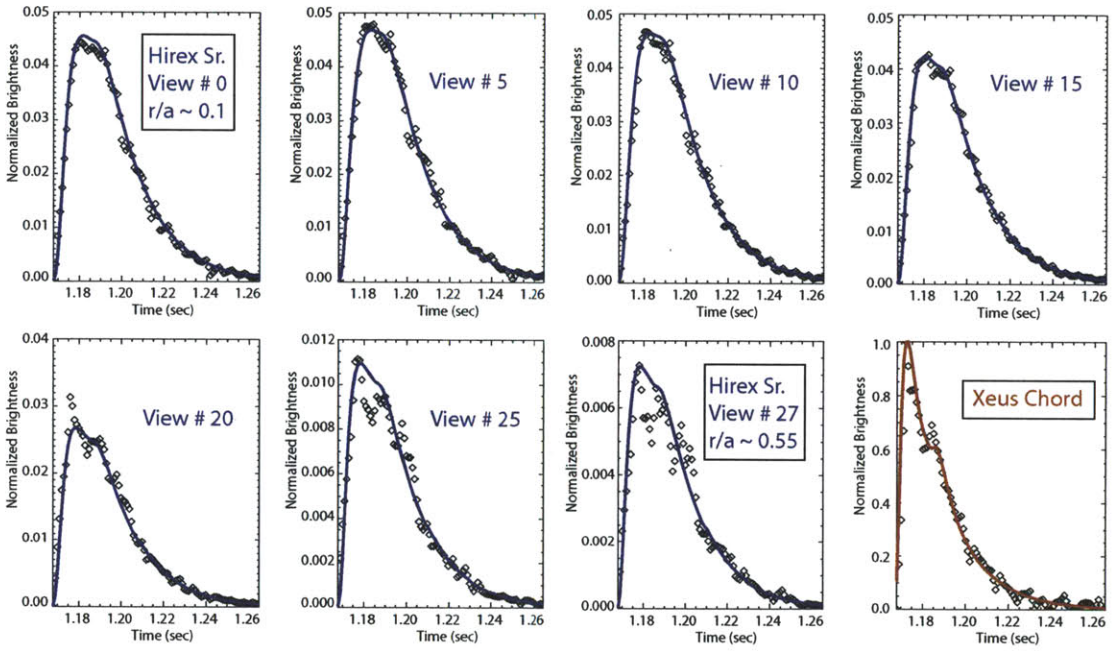

Figure 4-4: Seven HiReX Sr. line integrated brightness time histories and the XEUS brightness time history are compared with the synthetic emission generated by STRAHL. Measured data is represented by black diamonds and synthetic emission is shown by blue and red lines. The HiReX views are roughly equally spaced from the core to $r/a \sim 0.55$.

The process described above was coupled to the nonlinear least squares fitting routine MPFIT [84] to determine the experimental values of the impurity transport coefficients through iteration. The algorithm minimizes χ^2 through modification of the D and V profiles initially specified by the user. In typical operation of the code,

each transport coefficient profile consist of 6 radial knots which are allowed to independently vary in magnitude with each iteration of MPFIT. This is done in a manner that will minimize the difference in the modeled STRAHL emission and the measured emission of the He-like and Li-like Ca charge states. To reduce the sensitivity to the second derivative at the plasma core and eliminate instability within the code, the innermost two radial knots are forced have identical values. This enforces the boundary condition $dn_z/dr = 0$. Second derivative sensitivity has been demonstrated previously by Dux et al. [48]. Although the measured Ca^{18+} (He-like Ca) signals are limited to roughly the region $0.0 \leq r/a \leq 0.6$ (for typical L-mode conditions), the measured emission of the Li-like charge state is highest where the emission of the He-like charge state is low. It therefore offers important information for constraining transport in regions of weak He-like signal. Two radial knots are positioned outside the measurement region ($r/a \geq 0.6$) and allowed to freely vary. These external

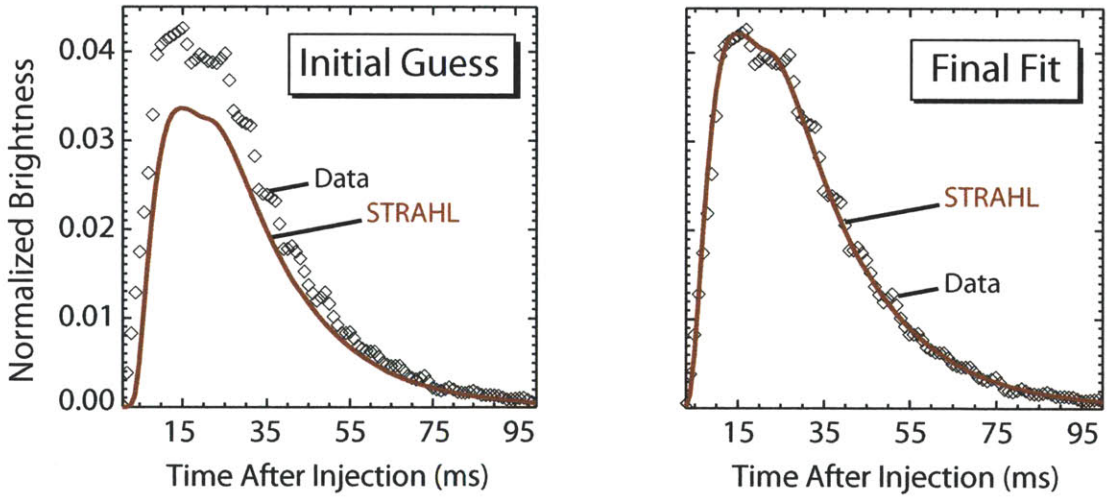

Figure 4-5: The measured (black points) and STRAHL modeled (red) brightness time history for a core HiReX Sr. view is shown. The comparison using the initial guess for the D and V profiles (left) and the final, χ^2 minimized profiles (right) is shown.

knots are less constrained by measurement (only the Ca^{17+} and source measurements are present in this region) but adjust such that the outermost measured signal is appropriately reproduced. Similar χ^2 minimization techniques have been applied in previous impurity transport studies [16, 46, 49]. The values of D and V are modified

by MPFIT coupled with the synthetic diagnostic until χ^2 is reduced to a minimum. An example of the synthetic HiReX Sr. and XEUS data compared with the measured signals is demonstrated in Figure 4-4 for various views. The values of D and V which best reproduce the measured signals are then quoted as the experimental impurity transport coefficient profiles.

To gauge the optimum number of fitting parameters (knots) used in the minimization process, the number of knots was initially kept to a minimum (3 in each D and V profile) and increased until the inclusion of additional knots no longer resulted in significant change in the returned χ^2 value. It was observed that increasing the number of knots much above 6 resulted in large variation of the knot values with very little change in the χ^2. For large, multi-parameter fits, the use of χ^2 minimization requires some care in the selection of initial transport profiles [85]. The complexity of the parameter space and the intrinsic noise in the data leads to the presence of numerous local minima. For this reason an exhaustive examination of the local and global minima present in the χ^2 space was performed using a Monte Carlo approach for selection of the initial guess. Given user-defined upper and lower limits for the values of D and V, random, uniformly generated values for the transport coefficients at each knot are used as the initial profiles for a STRAHL run. These upper and lower bounds are left intentionally quite large (D = [0 , 15] m^2/s, V = [-50 , 20] m/s). These intervals can be justified through very simple estimates. If we consider a global impurity confinement time of 20 ms and a minor radius of 0.21 m, the diffusion coefficient can be estimated by: $D = 0.21^2/.02 \sim 2.2$ m^2/s. A rough estimate of the convective velocity can also be obtained from the time required for core x-ray signals to peak following a laser blow-off injection. This time is approximately 12 ms. Therefore its estimated convective velocity moving from the edge to the core is: $V = 0.21/.012 = -17.5$ m/s. STRAHL is executed with the randomly generated starting values and allowed to undergo χ^2 minimization. This process is repeated approximately 300 times to determine what is believed to be the global minimum of the parameter space. After the approximate location of the global minimum of the space was identified, the start value used for all subsequent STRAHL runs was chosen

such that it lies in the vicinity of the the apparent global minimum.

4.1.4 Error Sources in Transport Coefficient Determination

Uncertainties in the experimental data propagate through the impurity transport code to the determined transport coefficients. Three sources of error were identified as: 1) photon statistics and background, 2) normalization and combination of multiple injections, and 3) uncertainty in the background plasma density and temperature profiles.

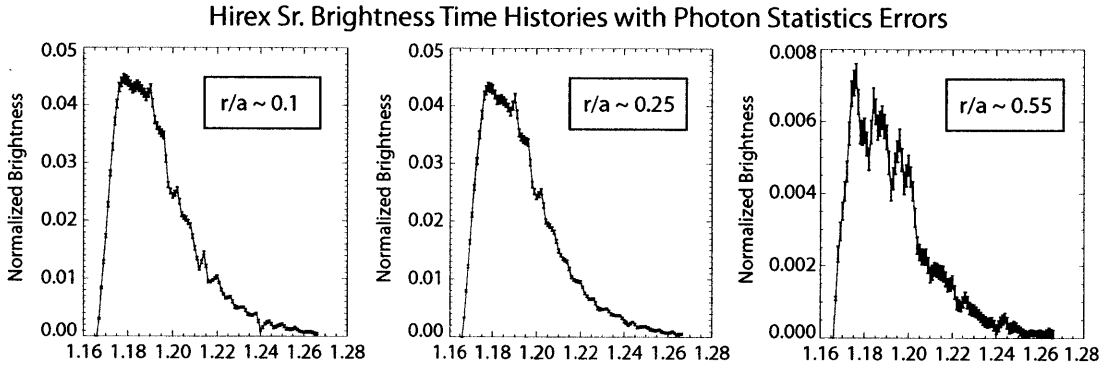

Figure 4-6: The error bars due to photon statistics for 3 HiReX Sr. views are shown.

Uncertainity introduced by photon statistics and small variations in background emission were calculated and included in the experimental error bars used in the χ^2 minimization. The lack of any calcium intrinsic to the plasma, selection of a stationary analysis period, and measurement of a specific transition resulted in good signal to noise and small error introduction purely from photon statistics and background subtraction.

As mentioned in the previous section, emission from multiple impurity injections was combined during the steady state portion of the discharge to improve the effective temporal resolution of the primary measurement. After background subtraction, each injection was normalized to the maximum measured brightness value for that injection. The maximum brightness was determined through a polynomial fit of the peak in the measured brightness time history for the particular line of sight. Error in

the peak value due to fitting has been estimated to be of order 1.5% through Monte Carlo fitting of down sampled simulated data sets and was included in the experimental error bars used in the χ^2 minimization.

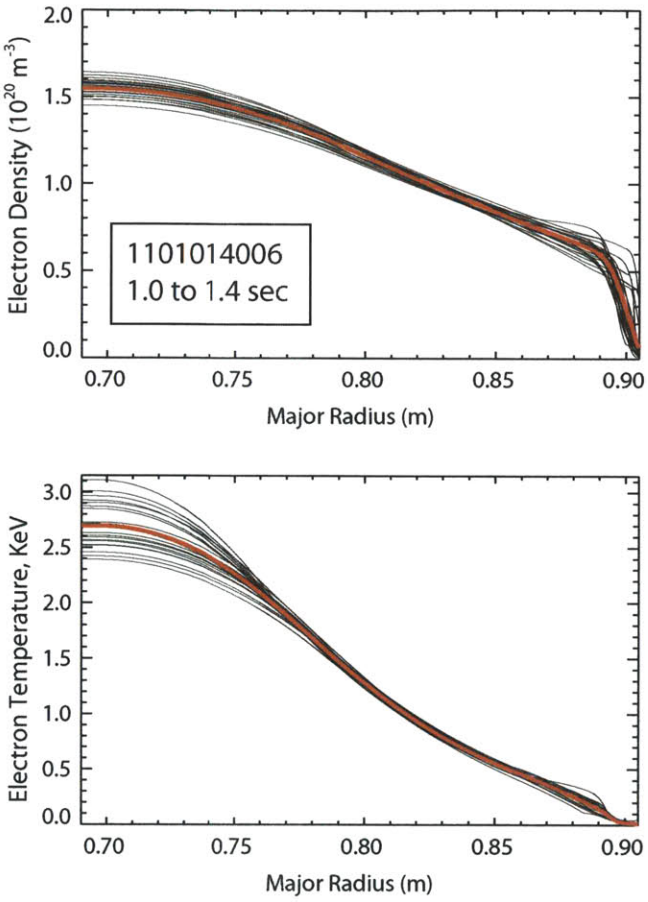

Figure 4-7: The electron density and temperature profiles for a stationary portion of a discharge are shown. Approximately 25 time slices, obtained from individual Thomson scattering times, are over plotted with the red curve indicating the mean profiles.

In these studies, uncertainty in the background plasma profiles were the dominant source of error in the determined impurity transport coefficients. Time averaged profiles of n_e and T_e were determined over the stationary portion of the discharge and used as the input profiles for STRAHL. During stationary periods the statistical variation from this mean profile is assumed to approximate error bars on the density and temperature profiles. The profile variation during a stationary portion of a discharge

is shown in Figure 4-7. To account for this variation, and to determine its propagation to the transport coefficients, approximately 40 STRAHL runs were performed where the density and temperature profiles were varied within the experimental error bars and the transport was rederived through the iterative procedure described above. The strong dependence of the local emission on electron temperature, especially in the region of low Ca^{18+} density, can result in significant error and must be considered when analyzing the uncertainty in the derived transport coefficients.

The profiles quoted as the experimental transport profiles represent the χ^2 weighted mean from 40 STRAHL runs. Each STRAHL run consisted of variations of the background density and temperature profiles as well as small variations in the radial location of the knots. The derived error bars represent the χ^2 weighted standard deviation from the mean and are typically found to increase with radius as result of decreasing signal at the edge.

4.2 Power Balance Calculation Using TRANSP

In order to understand transport processes, we must first understand the transfer of energy and particles in an out of the plasma. Determining these flows requires knowledge of the sources, sinks, and background profiles of a wide range of quantities.

Despite our best efforts to create ever more innovative and robust methods of plasma confinement, plasmas consistently demonstrate a tendency to reduce density and temperature gradients through transport of heat and particles. It is desirable to both measure the transport level and to understand the physical processes responsible for the transport of heat and particles. This motivates much of tokamak research and ultimately motivates the work presented here. To this point in the thesis, we have discussed the governing equations for particle and impurity transport in detail. However, an understanding of energy and momentum transport is also needed to describe the full temporal and spatial evolution of a plasma discharge. In this section we discuss the use of numerical power balance codes to solve the couple transport equations for particles, energy, and momentum which allow for calculation of experimental

transport levels.

4.2.1 Numerical Transport Codes and Power Balance

A good general overview of the structure and implementation of numerical transport codes such as TRANSP can be found in references [86, 87]. The basics of numerical transport codes can be boiled down to solving the set of conservation equations governing particle and energy balance of ions and electrons. This is achieved using a series of input quantities which are provided by experimental measurement and numerical models to determine unknown quantities. To reduce the complexity of the problem, numerical transport codes take advantage of fast transport time scales along the magnetic field and the use of flux coordinates to reduce the governing equations to a set of "1 1/2-D" equations which represent a 1-D transport model which use a 2-D plasma equilibrium [86]. The following overview of these equations is based on their implementation into the power balance code, TRANSP and will for simplicity assume circular flux surfaces so that the radial coordinate, r, is used. In reality, the code accounts for the non-circular plasma geometry found in Alcator C-Mod.

The governing equations for heat transport are the electron and ion energy conservation equations:

$$\frac{3}{2}\frac{\partial}{\partial t}(n_e T_e) + \nabla \cdot \vec{q_e} + \nabla \cdot (\frac{5}{2} n_e T_e \vec{v_e}) - \vec{v_e} \cdot \nabla(n_e T_e) = S_e \tag{4.6}$$

and

$$\frac{3}{2}\frac{\partial}{\partial t}(n_i T_i) + \nabla \cdot \vec{q_i} + \nabla \cdot (\frac{5}{2} n_i T_i \vec{v_i}) - \vec{v_i} \cdot \nabla(n_i T_i) = S_i \tag{4.7}$$

with

$$S_e = \frac{j^2(r)}{\sigma(r)} + P_{e,heating} - P_{ionization} - P_{rad} - \frac{3m_e}{m_i}\frac{n_e}{\tau_e}[Z](T_e - T_i) \tag{4.8}$$

$$S_i = P_{i,heating} + P_{neut} + \frac{3m_e}{m_i}\frac{n_e}{\tau_e}[Z](T_e - T_i) + n_i n_0 < \sigma v >_{cx} (T_i - T_0) \tag{4.9}$$

$$\vec{q_e} = n_e \chi_e \nabla T_e \tag{4.10}$$

$$\vec{q_i} = n_i \chi_i \nabla T_i \tag{4.11}$$

$$[Z] = \frac{1}{n_e} \sum_j \frac{n_j Z_j^2}{A_j} \tag{4.12}$$

The left hand sides of each equation (4.6 and 4.7) are identical with only the species indices changed. The first term represents the rate of change of energy for each species, the second term represents heat flux losses, the third term indicates convective losses, and the fourth term is the work of particles against the pressure gradient. The right hand side of each equation represents heat sources and sinks for each species. For the electrons, these consist of ohmic heating, direct auxiliary heating to the electrons, the power lost through ionization processes, losses due to radiation processes, and ion-electron equilibration. For the ions, the sources and sinks are: direct auxiliary heating to the ions, the energy gained through neutral ionization, ion-electron equilibration, and power loss due to charge exchange. The governing equations for particle transport are the electron and ion continuity equations. They have the familiar form:

$$\frac{\partial}{\partial t}(n_e) = -\nabla \cdot \Gamma_e(r,t) + S_{vol}(r,t) + S_{wall}(r,t) \tag{4.13}$$

and

$$\frac{\partial}{\partial t}(n_i) = -\nabla \cdot \Gamma_i(r,t) + S_{vol}(r,t) + S_{wall}(r,t) \tag{4.14}$$

Where S_{vol} denotes volume particle sources (such as neutral beams and pellet injection) and S_{wall} represents the sources and sinks of particles originating at the wall. These equations (4.6 - 4.14), coupled with the energy conservation equations represent the basis of all power and particle balance codes. Evaluation of this set of equations requires a number of known and unknown quantities. A majority of the needed quantities are obtained via routine measurement in most tokamaks (n_e, T_e, T_i, P_{rad}, j). The missing quantities are obtained via calculation or modeling, often using externally developed codes which are integrated into the numerical transport code as separate modules. These quantities include σ, v_e, v_i, n_0, $P_{heating}$, S_{wall}, and S_{vol}. An overview of the methods used for the calculation of these quantities is well outside the scope of this work but the reader is referred to [86, 87, 88] for a more

in-depth overview of the equations and models described in this section.

4.2.2 The Role of TRANSP in this Work

The use of TRANSP in this work served two main purposes: Determination of the experimental values of the electron and ion heat fluxes, Q_e and Q_i and remapping of experimental data, taken in 3D space, onto a consistent 1D radial grid for input into turbulent transport codes.

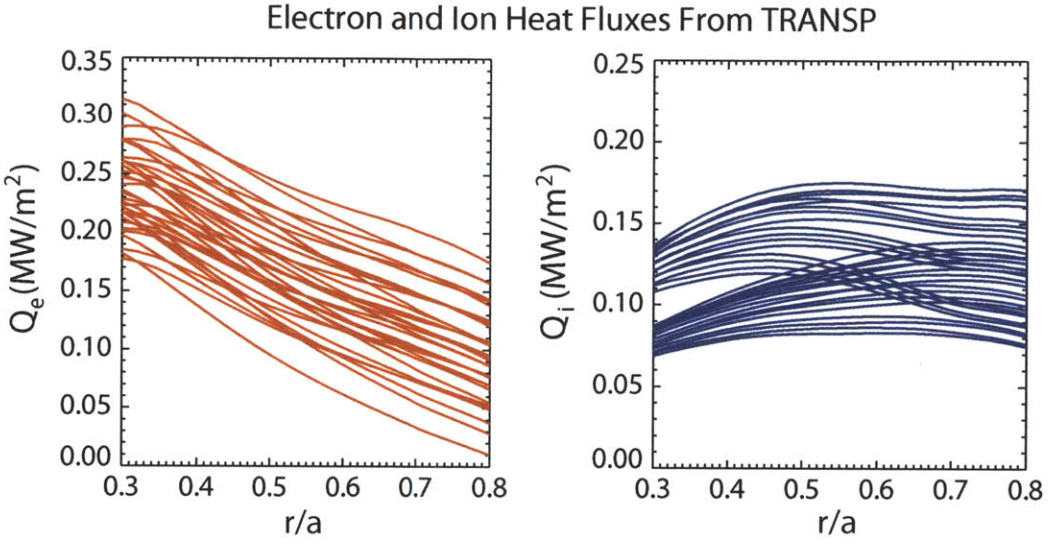

Figure 4-8: An example of the TRANSP calculated electron and ion heat fluxes is shown for 32 different runs where the values of n_e, $P_{absorbed}$, T_e, T_i, and Z_{eff} were varied within estimated uncertainties. Theses runs provide an estimate of the plausible uncertainty ranges of heat flux found in the experiment.

Determination of the experimental electron and ion heat fluxes is essential for comparison with turbulence codes. Since turbulent transport is thought to dominate observed transport levels and neoclassical contributions are often small or negligible in the plasma confinement zone, predictions of turbulent heat fluxes obtained through turbulence simulation should approximately match the heat flux observed experimentally. Therefore, obtaining not only calculated values for the experimental heat fluxes but also an estimate of the uncertainties in these values is of great importance when attempting quantitative comparison of turbulence simulation with experiment. Many

of the quantities relevant for the calculation of the electron and ion heat fluxes are measured experimentally and their measurement uncertainties have been studied by their respective diagnosticians. These are: n_e, T_e, T_i, and Z_{eff}. However, the absorption efficiency of the Ion Cyclotron Resonance Heating (ICRH) is typically not a measured quantity. TRANSP is coupled with the TORIC code [89, 90] to solve the wave equation and calculate wave propagation and absorption in the plasma. This model for the ICRH absorption is required to obtain the experimental profiles of the electron and ion heat fluxes and motivates the use of TRANSP in this work. Varying the the experimental inputs within their estimated uncertainty and performing ensembles of TRANSP runs can determine the propagation of uncertainty to the experimental heat flux values which are compared with output of turbulence codes. An example of this analysis is demonstrated in Figure 4-8. More detail on the TRANSP analysis performed and the importance of determining the uncertainty in the experimental heat flux will be presented in the following chapter.

The TRANSP code also functions as an intermediary between experimental data and the input files needed for gyrokinetic simulation of plasma turbulence. Using the IDL interface, PreTRANSP, input data from numerous diagnostics is provided to TRANSP. Although input data may be provided on any number of different radial grids ($r/a, \psi, R_{major}$), TRANSP maps all quantities to a single coordinate system, the square root of the normalized toroidal flux, ρ. With all experimental values on the same grid, output values are extracted to create input files for gyrokinetic codes. Translation of TRANSP output to the gyrokinetic input files needed for the code, GYRO was performed using the TRGK code developed at Princeton Plasma Physics Lab. A chart outlining the workflow required for gyrokinetic input file generation is shown in Figure 4-9.

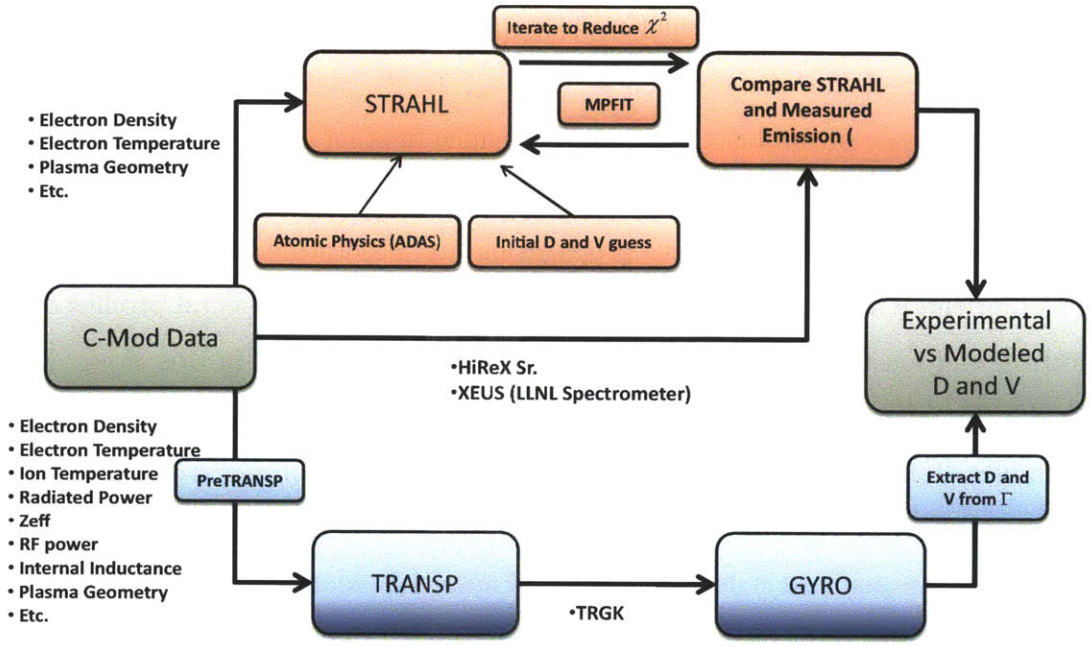

Figure 4-9: A chart outlining the workflow used to extract impurity transport coefficients using STRAHL, performing TRANSP calculations, and steps used in GYRO simulation.

4.3 Gyrokinetic Simulation Using GYRO

4.3.1 GYRO Overview

All simulation of plasma microturbulence performed during this thesis work used the GYRO code developed by Candy and Waltz [91, 92] at General Atomics. An important part of this work is to assess the degree to which the gyrokinetic model, and more specifically, the implementation of this model in the GYRO code, contains sufficient physics for the quantitatively accurate simulation of tokamak discharges in the plasma confinement zone. GYRO is an Eulerian, δf code that is, it solves the gyrokinetic equation for the perturbed part of the distribution function, δf, under the assumption of background Maxwellian electrons and ions [93]. For a detailed de-

scription of the numerical schemes employed by modern gyrokinetic codes the reader is referred to [3]. Simulations can be performed with realistic plasma equilibrium [94], electromagnetic effects (finite β), up to 5 total ion species, collisions, and adiabatic, drift-kinetic, or gyrokinetic descriptions of each species. GYRO simulations may also include rotation effects and $E \times B$ shearing rates which are calculated self consistently from the experimental rotation profiles.

Both local (flux-tube) and global simulations are possible using GYRO. Local simulation corresponds to the $\rho_* = \rho_s/a \rightarrow 0$ (with $\rho_s = c_s/\Omega_{ci}$, $\Omega_{ci} = eB/m_i c$, and $c_s = \sqrt{T_e/m_i}$) limit of the gyrokinetic-Maxwell equations. This type of simulation ignores profile variation, such that fixed values of profiles and the relevant gradient scale lengths are fixed across the simulation domain. In contrast, global simulation incorporates the real variation of the plasma profiles across the simulation domain. However, due to the non-periodic boundary conditions, these global simulations require the existence of boundary or buffer regions at the edge of the simulation domain [95]. These buffer regions are imposed numerically in a manner which does not affect the simulation results in the interior of the simulation domain. An example of global, nonlinear GYRO simulation and the buffer regions is shown in Figure 4-10. Candy *et al.* demonstrated the agreement of the local and global approaches at values of approximately $1/\rho_* > 300$ [96]. All nonlinear gyrokinetic work performed for this thesis relied on global simulation. Use of global simulation allowed for straightforward comparison of experimental impurity transport coefficient profiles with the gyrokinetic predictions and eliminated the need for 4 or 5 local simulations to obtain the information from a single global simulation.

4.3.2 Linear Gyrokinetic Simulation

Although nonlinear gyrokinetic simulation represents the most comprehensive simulation of plasma microturbulence, the substantial time and computing requirements demanded by these simulations often makes them impractical for routine or exploratory calculations. Linear gyrokinetic simulation can provide insight into character of the plasma turbulence present in experimental discharges with quick turn-around (exe-

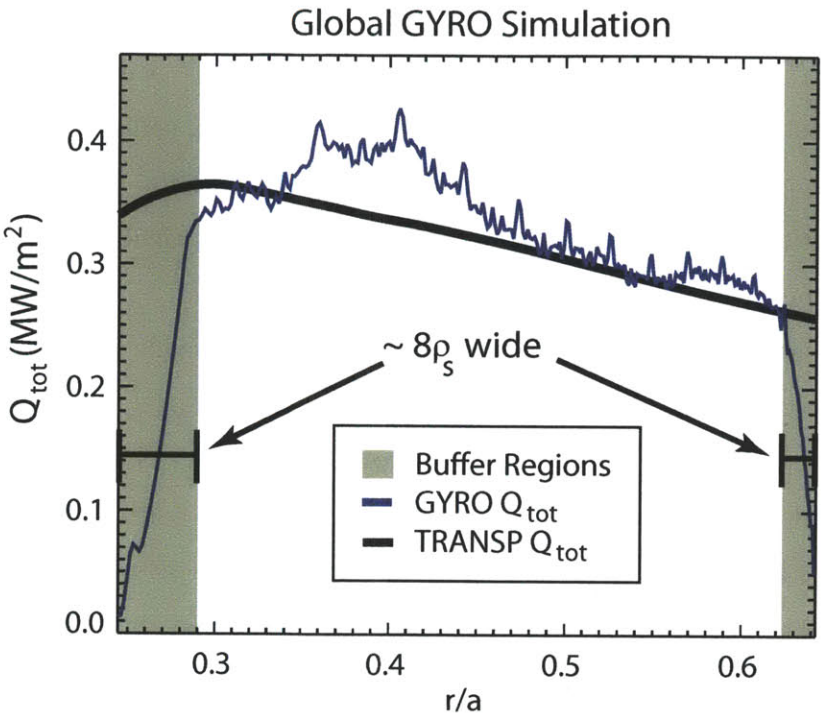

Figure 4-10: An example of global, GYRO simulated total heat flux is compared with the TRANSP values of Q_{tot}. The shaded regions represent the buffer zones of the global simulation.

cution time $\sim$ 60 sec on 16 processors) with only the use of local computing facilities such as the LOKI cluster [97] at MIT. GYRO includes the ability for either eigenvalue and initial value solution to the linear gyrokinetic equation. All linear stability analysis presented here was performed using initial value simulation. This type of simulation is limited to resolving the real frequency and growth rate of only the most unstable linear mode at a particular value of $k_\theta \rho_s$. All perturbed quantities (electrostatic potential is shown) are assumed to be of the form:

$$\delta\phi_n(r,\theta,t) = \phi_n(r,\theta)e^{-i\omega t+\gamma t} \tag{4.15}$$

Where n is the toroidal mode number, ω is the real frequency and γ is the linear growth rate. We can relate the toroidal mode number to the poloidal wavenumber,

k_θ through the following relation:

$$k_\theta = \frac{nq}{r} \tag{4.16}$$

An example of the real frequency and growth rate spectrum up to $k_\theta \rho_s \cong 1.0$ obtained from linear, local, initial value GYRO value simulation is shown in Figure 4-11. From

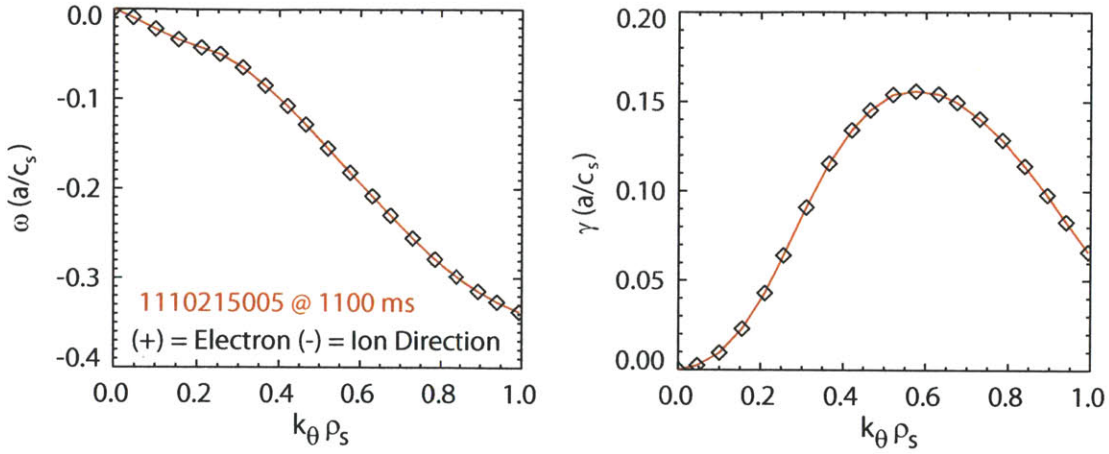

Figure 4-11: An example of linear GYRO simulation results is shown. Twenty separate linear simulations were used to determine the real frequency and growth rate spectrum up to $k_\theta \rho_s \cong 1.0$. Positive/negatives values of the real frequency indicate modes rotating in the electron/ion diamagnetic drift directions.

these simple linear simulations we can have an idea of types of instabilities present in the plasma. The sign of the real frequency is indicative of the propagation direction of the unstable mode in the plasma frame. By looking at the $k_\theta \rho_s$ spectrum of the linear growth rate, we can assess the scale of the turbulence which is most unstable in the plasma. In the example shown in Figure 4-11 the peak of the growth rate spectrum occurs at approximately $k_\theta \rho_s = 0.5$ which indicates the wavelength of the most unstable (low-k) modes are approximately 4π times as large as the local value of ρ_s and they rotate in the ion diamagnetic drift direction. These characteristics are suggestive of ion temperature gradient (ITG) type turbulence. However, this picture is overly simplified since it neglects the nonlinear interactions between different modes and the nonlinear saturation of the resulting turbulence. For this reason, nonlinear simulation is performed.

4.3.3 Nonlinear Gyrokinetic Simulation

Nonlinear gyrokinetic simulation currently represents the most comprehensive model of microturbulence which is numerically tractable. These simulations solve for the perturbed distribution function and its nonlinear saturation. From the perturbed distribution, the perturbations to the electromagnetic fields can be obtained. In general, these simulations are still quite demanding and require access to massively parallel computing facilities. All nonlinear simulations discussed in this work were performed on the National Energy Research Supercomputing Center (NERSC) using between 512 and 1024 processors and 10,000 to 40,000 CPU hours per case. Inclusion of additional impurity species, increasing the number of toroidal modes (increased simulation box size), and running simulations up to higher-k values can result in simulation times which are prohibitively long. As a result, simulations are often performed with the minimum required fidelity to resolve the physics of interest and convergence studies are performed to ensure that additional resolution does not alter the results.

The detailed implementation of the GYRO is out of the scope of this thesis. However, the reader is referred to the GYRO technical guide for a complete description of the code [95]. Here we describe the basics of nonlinear GYRO simulation. Simulation of the tokamak is performed using N toroidal modes with a spacing, Δn. Spacing of the toroidal modes corresponds to simulation of a toroidal wedge with a width of $2\pi/\Delta n$. The number of toroidal modes and their spacing is chosen such that they span the desired range of $k_\theta \rho_s$. However, in the case of global simulation, the quantity q/r varies across the simulation domain and therefore the maximum simulated $k_\theta \rho_s$ value at the inner bound of the simulation domain tends to exceed the value at the outer bound. Quoted values of $k_\theta \rho_s$ for nonlinear simulations correspond to the average value across the simulation domain. To ensure accurate simulation of the plasma turbulence, simulation box sizes must be sufficiently large as to encompass many turbulent eddy widths. For this work, this corresponded to box sizes of $L_x \sim 100\rho_s$ and $L_y > 40\rho_s$. As will be discussed in later chapters, spot checks were performed during nonlinear GYRO simulation work to ensure that box size increases did not alter the

results.

The goal of the nonlinear gyrokinetic simulation performed for this thesis was to investigate the dynamics of impurity transport. For GYRO "production" runs, simulations were performed with drift-kinetic electrons, gyrokinetic ions, and 3 gyrokinetic impurity species specified with normalized gradient scale lengths at values of 0.5, 1.0, and 1.5 $\times$ a/L_{n_e}. Nonlinear GYRO simulation outputs the flux-surfaced averaged impurity flux for each species as a function of radius and time. The impurity transport coefficients, D and V, were determined from the three output values of the impurity flux. The output impurity flux for each species was cast into the following form:

$$\frac{\Gamma_z}{n_z} = -D\frac{\nabla n_z}{n_z} + V \tag{4.17}$$

Where Γ_z is the output particle flux from GYRO for each impurity species, n_z is the impurity density, and D and V are the flux surface averaged diffusive and convective impurity transport coefficients. Plotting Γ_z/n_z vs $-\nabla n_z/n_z$ and performing a linear fit to the data allows one to obtain the impurity diffusion coefficient from the slope and the convective velocity from the y-intercept. The accuracy of this assumed form for the impurity flux will be discussed in more detail in Chapter 5. Post processing routines were developed as part of this work to modify GYRO inputs, analyze the code outputs, and ultimately extract the flux-surfaced averaged impurity transport coefficients for comparison with experimental results obtained via laser blow-off and the iterative synthetic diagnostic.

Chapter 5

Quantitative Comparison of Experiment with Nonlinear Gyrokinetic Simulation of Impurity Transport

Previous impurity transport work has aimed predominantly at analyzing experimentally observed transport coefficients qualitatively using quasilinear gyrokinetic models [15, 16]. This chapter describes the first comparison of nonlinear gyrokinetic simulation with experimental impurity transport in the core of an Alcator C-Mod plasma discharge. This comparison is accompanied by an in depth investigation of error and sensitivity in the experiment and simulation, respectively, and serves as the starting point for impurity transport model validation. The remainder of this chapter is organized as follows: Section I briefly overviews the experimental discharge and the diagnostic setup employed to determine the plasma profiles. Section II discusses the gyrokinetic simulation setup, the initial methodology used to determine the predicted impurity transport, and linear analysis of discharge. Section III presents the direct comparison of the experimental results with gyrokinetic simulation and and sensitivity analysis of the predicted transport profiles to a range of turbulence-relevant param-

eters. Section IV details a new approach used to perform gyrokinetic simulation for comparison with experimental impurity transport.

5.1 Description of the Experiment

The work presented in this chapter focuses on the analysis of a single Alcator C-Mod [98] L-mode discharge. The discharge studied was run with a toroidal field of 5.3 T and a plasma current of 0.8 MA. During the 1.0 sec current flattop, a total of 1.0 MW of ICRH heating power was introduced by two separate antenna operating at 78 and 80 MHZ (on axis, hydrogen minority heating) which resulted in a core electron temperature of $\sim$ 2.7 keV and a core density of $\sim$ 1.5e20 m^{-3}. Although not ideal for turbulent transport studies, sawtooth instability is generally unavoidable in C-Mod and is present for the entire discharge length. Due to the presence of sawtooth oscillations, most of the gyrokinetic work was restricted to outside of the sawtooth inversion radius to reduce or eliminate the influence of MHD driven transport phenomenon which are not included in the gyrokinetic model. In order to avoid H-mode, yet maintain the capability to vary the heating power substantially, the L-H power threshold was raised by operating in Upper Single Null (USN) configuration with the ion ∇B drift away from the active x-point. Figures 5-1 and 5-2 show the time traces for key discharge parameters and the input plasma profiles used for the GYRO simulations respectively. Experimental analysis of this discharge focuses on the stationary portion from approximately 1.0 to 1.4 seconds while the plasma profiles used for gyrokinetic simulation are nominally based on profiles at $t = 1.1$ seconds. Ion temperature and toriodal velocity simulation profiles were time averaged over the stationary portion of the discharge to reduce uncertainty.

Measurements of the plasma profiles were provided by the extensive diagnostic suite [71] described in Chapter 3 of this thesis. For completeness, a brief overview is provided here. A 33 channel Thomson scattering system [6] was used to provide both edge and core electron density and temperature measurements with 16 ms time resolution. Additional electron temperature measurement was provided by 3 sepa-

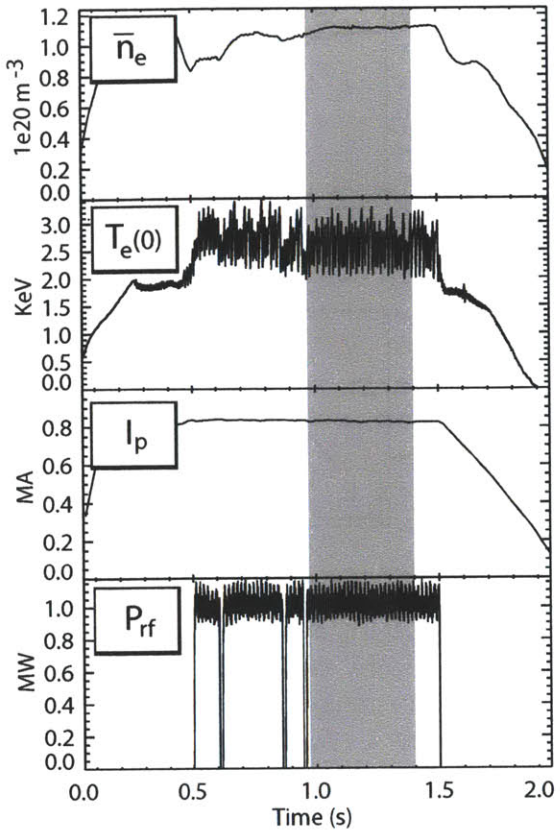

Figure 5-1: Time traces of basic plasma parameters for the analyzed discharge are shown. The oscillations in the central T_e are due to sawteeth. The shaded region indicates the time interval used for experimental analysis, 0.965 to 1.40 seconds, with laser blow-off injections occuring at 0.965,1.165, and 1.365 seconds.

rate electron cyclotron emission (ECE) systems which serve to significantly reduce error in the measured electron temperature profiles [72, 73, 74]. Ion temperature and toroidal rotation profiles were determined using the spherically bent x-ray crystal spectrometer, HiReX Sr., which is capable of providing spatially resolved spectra of Ar^{+16} line emission [7]. Tomographic inversion techniques were applied to measured spectra to determine profiles of ion temperature and toroidal velocity. This measurement requires argon gas puffing into the plasma and is limited by the presence of the Ar^{+16} charge state. For the discharge of interest, the abundance of this charge state is diminished near the plasma edge and limits the accurate determination of these profiles to inside of r/a = 0.75. The Z_{eff} values used in this paper are assumed to

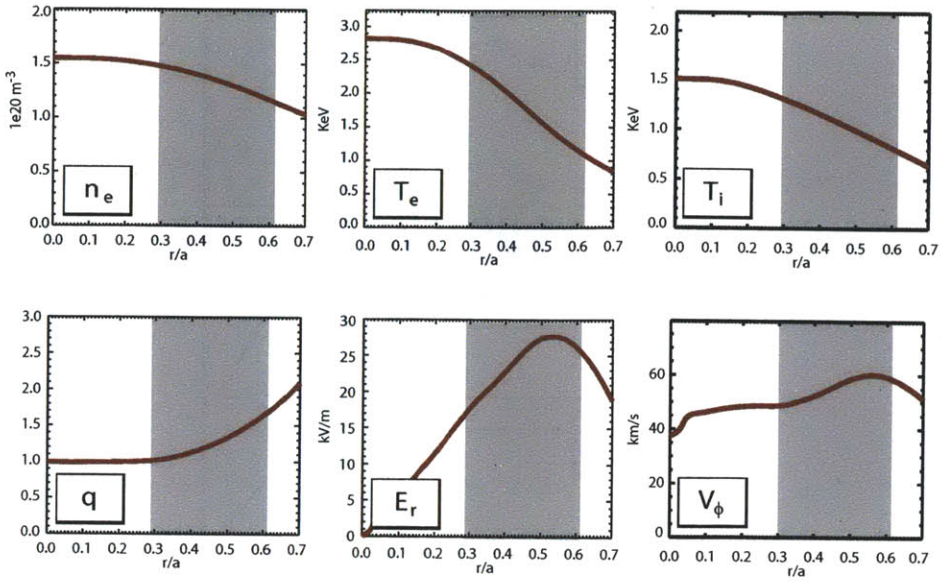

Figure 5-2: The plasma density, temperature, and toroidal rotation profiles used as inputs to the GYRO simulation are shown.The shaded region is the approximate extent of the global, gyrokinetic simulation domain. Ion temperature and toroidal velocity profiles are limited to $0.0 \leq r/a \leq 0.7$ due to larger uncertainty in the edge measurement.

be constant across the simulation domain and were calculated through a neoclassical calculation which can be found here [99]. These calculated Z_{eff} values, together with estimates of plasma impurity content, were shown to be consistent with the measured neutron rate and ion temperature profiles within experimental uncertainty.

The full array of spectroscopic diagnostics described in Chapter 3 was available for this analysis. Measured profiles of the He-like (Ca^{18+}) charge state of calcium were provided by the HiReX Sr. spectrometer and a single chord measurement of the Li-like (Ca^{17+}) was provided by the XEUS VUV spectrometer. Additionally, determination of the laser blow-off source time history was provided by measurement of Ca I emission. The density and temperatures obtained in this discharge, combined measurements of the impurity source, full time evolving profiles of the He-like calcium charge state, and an effective boundary condition provided by measurement of Li-like calcium allowed for unique determination of impurity transport inside of $r/a = 0.6$.

5.1.1 Experimental and Neoclassical Transport Profiles

The methodology described in Chapter 4 was applied to the discharge of interest to determine the experimental transport coefficient profiles. The results of this analysis are presented in Figure 5-3. From left to right the experimental values of the diffusion

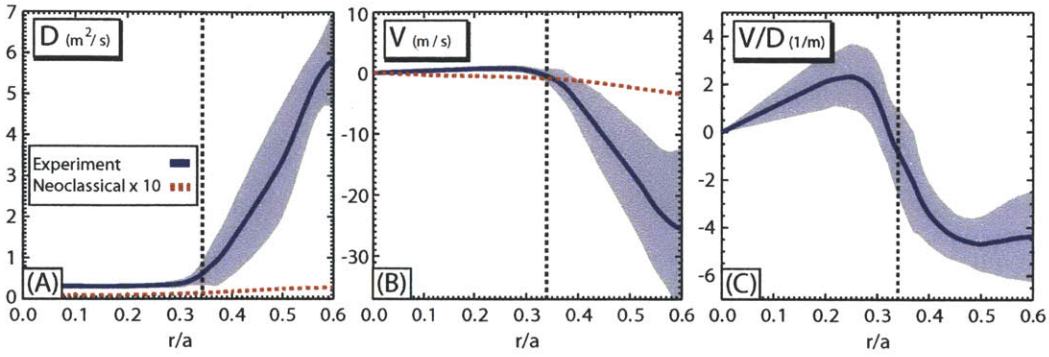

Figure 5-3: The experimentally derived and neoclassical impurity transport coefficients are shown: (a) Diffusion coefficient, (b) Convective Velocity, and (c) Peaking Factor. The mean values of experimental coefficient profiles are shown by a solid blue line. The shaded regions surrounding the mean profile (blue) indicate the estimated errors on the transport coefficient profiles. The neoclassical impurity transport coefficients (dashed red) are multiplied by a factor of 10 for comparison. The estimated radial location of the sawtooth inversion radius is indicated by the dotted black line.

coefficient, convective velocity, and peaking factor (the ratio $\frac{V}{D}$) are plotted over the radial region $0.0 \leq r/a \leq 0.6$. Due to the reduced Ca^{18+} brightness profile towards the outside of the measurement region as well as the strong dependence of the local emission on electron temperature and its uncertainty, the error bars on the measurement are significant and increase towards the edge of the measurement region. The results of this analysis are found to be qualitatively consistent with previous impurity transport measurements from JET, Tore Supra, and ASDEX-Upgrade [16, 46, 49]. The neoclassical values of the diffusion coefficient and convective velocity calculated using the NEO code [100] are also shown in Figure 5-3. Experimental values of the transport coefficients are shown to greatly exceed the neoclassical predictions across the profile which suggests that neoclassical transport, which is the irreducible amount of collision-dependent transport in a tokamak, is playing a negligible role in the impurity transport. This supports the idea that another mechanism is dominating

the transport, i.e. drift wave turbulence. Inside of the sawtooth inversion radius, the values of core diffusion and convection are found to be quite small. MHD activity dominates the transport in this region and frequent sawtooth crashes (sawtooth period $\sim$ 8 ms) tend to maintain a relatively flat impurity density profile. Outside of the inversion radius, in the so called plasma confinement zone, both impurity diffusion as well as inward impurity convection are found to increase significantly with peak values of the diffusion coefficient ($\sim$ 5.8 m^2/s) occurring around $r/a = 0.6$ with a corresponding minimum in the convective velocity ($\sim$ -25 m/s), where negative velocity indicates an inward "pinch". It is speculated that transport in this region is driven by plasma turbulence which can be simulated using nonlinear gyrokinetic codes. In steady state, in the absence of core sources, $\Gamma_z = 0$. It follows that:

$$\frac{V}{D} = \frac{\nabla n}{n} \tag{5.1}$$

Therefore, the experimental peaking factor profile suggest significant peaking of the steady state impurity density in the confinement zone with a flatter, even slightly hollow, profile inside of the inversion radius.

5.2 Gyrokinetic Simulation Setup

5.2.1 Linear Stability Properties of the Discharge

The GYRO code [92] was used to perform both linear and nonlinear gyrokinetic simulation of the experimental discharge. The linear stability properties of the discharge are summarized in Figure 5-4. Contours of the linear growth rate, γ normalized to c_s/a, for the most unstable mode in the range of $k_\theta \rho_s \cong$ [0.25 , 0.75] are shown for a scan of the turbulence drive terms, a/L_{T_i} and a/L_n (Figure 6a-c) and a/L_{T_i} and a/L_{T_e} (Figure 6d-f) on the x and y axes respectively. Here, a is the plasma minor radius, $\rho_s = c_s/\Omega_{ci}$ is the sound speed gyroradius, $\Omega_{ci} = eB/m_i c$ is the ion gyrofrequency, and $c_s = \sqrt{T_e/m_i}$ is the sound speed. The normalized gradient scale length, a/L_x, for a given quantity x is defined as $-a\nabla x/x$. The range of $k_\theta \rho_s$ was chosen to best display

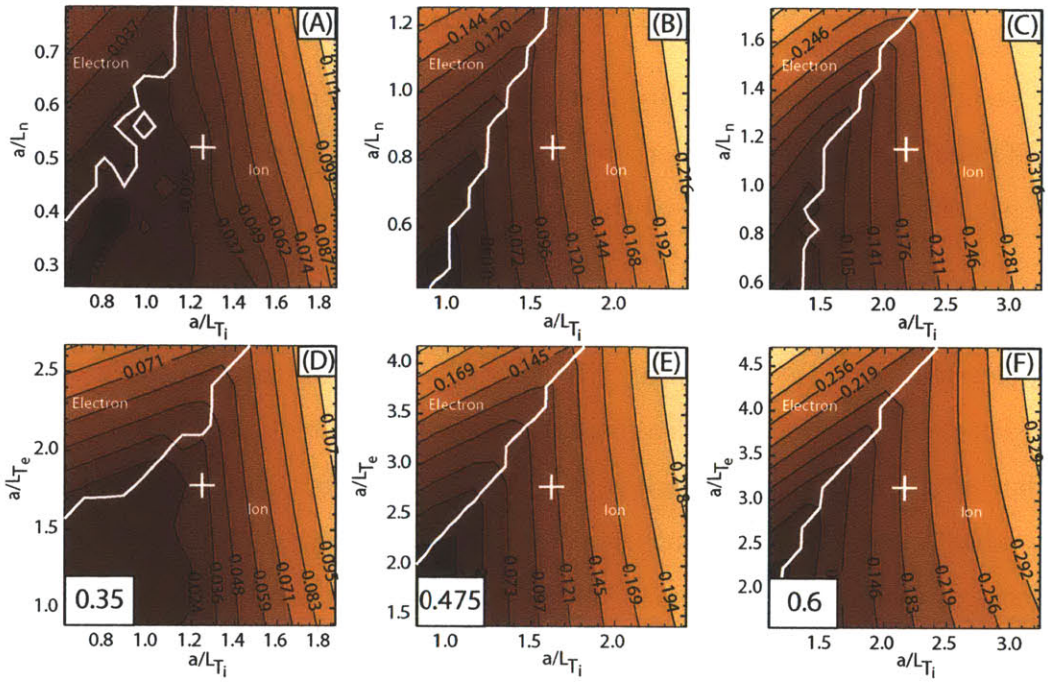

Figure 5-4: Contours of the growth rate, γ (a/c_s), of the most unstable mode in the range $k_\theta \rho_s$ = [0.25 , 0.75] are shown for scans of a/L_{T_i} vs. a/L_n (Figures 6a-c) and a/L_{T_i} vs. a/L_{T_e} (Figures 6d-f) at 3 radial locations ($r/a = 0.35, 0.475, 0.6$). The experimental values are indicated by the + sign and the solid white line separates modes with negative and positive real frequencies, which rotate in the ion and electron diamagnetic drift directions respectively. The lack of sensitivity to changes a/L_{T_e} and a/L_n is clearly demonstrated. The discharge is found to be ITG unstable at all radial locations.

a shift from ion to electron direction in the low-k linear growth rate spectrum which indicates a shift in the dominant instability from Ion Temperature Gradient driven (ITG) to Trapped Electron Mode (TEM). The solid white line indicates the boundary between modes rotating in the ion and electron diamagnetic drift directions and the + sign indicates the location of the experimental values of a/L_{T_i} and $a/L_{T_e}(a/L_n)$. The dominant mode in the experimental case at all radial locations rotates in the ion diamagnetic drift direction. For a fixed value of $a/L_{T_e}(a/L_n)$, the linear growth rate clearly increases/decreases with the corresponding increase/decrease in a/L_{T_i}. Additionally, shifts of a/L_{T_e} and a/L_n around the experimental points lead to minimal changes in the linear growth rate. Since the growth rate is clearly linked to the ion temperature gradient, these plasmas are classified as ITG dominated.

5.2.2 Global, Nonlinear GYRO Simulation Setup

The results of the linear stability analysis were used to motivate global, nonlinear GYRO simulations. Ion temperature gradient-type turbulence has been shown to have significant contributions to the turbulent heat flux below for $k_\theta \rho_s < 1.0$ [3]. Therefore, the nonlinear simulations performed here considered only contributions from turbulence in the low frequency range, $0.0 \leq k_\theta \rho_s \leq 1.15$. These values of $k_\theta \rho_s$ clearly include the low-k peak in the turbulent heat flux which occurs at $k_\theta \rho_s \approx 0.4$. The turbulent heat flux driven at the highest simulated value of $k_\theta \rho_s$ is $< 10\%$ of that driven by the low-k peak in both the electron and ion channels. This suggests that higher-k contributions can be neglected. Electrostatic simulations were performed including $E \times B$ shear, parallel velocity effects, and drift kinetic electrons with realistic mass ($\sqrt{m_D/m_e} = 60.6$). The physical simulation domain covered a region from $r/a = 0.29 - 0.62$ which was simulated with 8 toroidal modes ($\Delta n = 15$) spanning $n = [0 - 105]$. The corresponding simulation box size was $\sim 100\rho_s(L_x)$ by $40\rho_s(L_y)$. Additional simulations were performed with 16 toroidal modes to ensure adequate resolution and accurate determination of both particle and heat transport. Only modest differences are present between the two simulations and are summarized in Figure 5-5. Although finite, these differences will be shown to be small compared

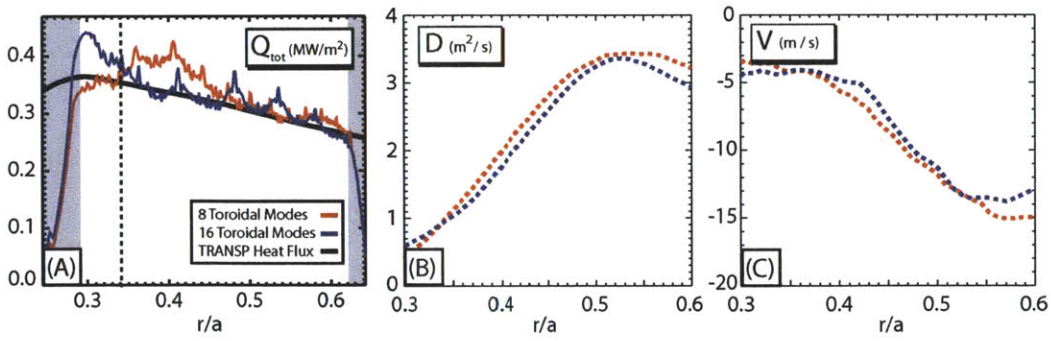

Figure 5-5: (a) Comparison of the GYRO predicted heat flux between simulations using 8 (red) and 16 (blue) toroidal modes is shown. Simulation buffer regions are represented by shaded regions. Small differences are seen in the predicted diffusion (b) and convective velocity (c) profiles for simulation with 8 and 16 toroidal modes. These differences were found to be small compared with the simulation sensitivity to plasma parameters

with the sensitivity to plasma parameters. It was therefore concluded that the use of 8 toroidal modes demonstrated sufficient ability to resolve impurity transport results. Additional spot checks were performed with 16 toroidal modes throughout the sensitivity analysis to once again validate the choice of 8 toroidal modes. Three trace ($\sim .001 n_e$) impurity species were included to provide the predicted impurity transport profiles, without affecting the underlying turbulent dynamics. In order to compare with the measured impurity transport, each species was given identical charge and mass characteristics to that of He-like calcium ($Z = 18, A = 40$) but different values of impurity density gradient scale length namely, 0.5, 1.0, 1.5 $\times$ $\nabla \mathrm{n}_e$. The output impurity flux for each species was cast into the following form:

$$\frac{\Gamma_z}{n_z} = -D\frac{\nabla n_z}{n_z} + V \tag{5.2}$$

Where Γ_z is the output particle flux from GYRO for each impurity species, n_z is the impurity density, and D and V are the flux surface averaged diffusive and convective impurity transport coefficients. Plotting Γ_z/n_z vs $\nabla n_z/n_z$ and performing a linear fit to the data allows one to obtain the impurity diffusion coefficient from the slope and the convective velocity from the y-intercept. This linear fit is shown in Figure 5-6 for the discharge of interest. It is found that the linear fit is an very accurate model for the GYRO output trace impurity fluxes, with one-sigma errors on the linear fitting coefficients of order 1×10^{-5}.

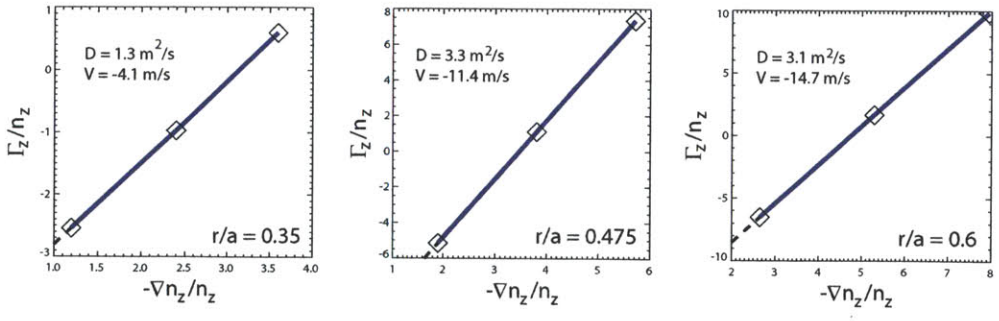

Figure 5-6: The linear fit of the GYRO predicted values of Γ_z/n_z vs $-\nabla n_z/n_z$ is shown at 3 radial locations, $r/a = 0.35$, 0.475, and 0.6.

5.3.2 Sensitivity of Gyrokinetic Impurity Transport Using Q_{tot} Matched Simulation

To provide a rigorous quantitative comparison of the GYRO simulated impurity transport with the experimental transport results, the sensitivity of the GYRO simulated transport to a wide range of turbulence relevant parameters was investigated. This analysis was performed using the Q_{tot}-matched GYRO simulation case as a reference. Within estimated uncertainties in the experimental values, the simulated impurity transport coefficients were found to be most sensitive to changes in a/L_{T_i}, q, and n_i/n_e. However the sensitivity to a/L_{T_e}, a/L_n, T_e/T_i, and $\gamma_{E\times B}$ was also studied.

The sensitivity of heat and particle transport to TEM drive terms (a/L_{T_e} and a/L_n) was found to be relatively small within ± 10 and $\pm$ 20% changes of the experimental profiles (see Figure 5-10. This result is consistent with the ITG nature of the discharge and the lack of sensitivity of the most unstable linear mode to changes in both a/L_n and a/L_{T_e} which was demonstrated in Figure 5-4. The ion temperature profile was scaled to modify the electron to ion temperature ratio, T_e/T_i, within estimated errors of $\pm 23\%$. These modifications also showed little effect on the determined impurity transport coefficients. This is a somewhat surprising result given the sensitivity of ITG turbulence on the this ratio and will be the subject of further investigation. Due to the absence of external momentum sources on C-Mod, levels of core rotation and $E \times B$ shearing rates are observed to be relatively small in L-mode. Here we define the $E \times B$ shearing rate using the GYRO definition [102]:

$$\gamma_{E\times B} = \frac{r}{q}\frac{\partial \omega_0}{\partial r} \tag{5.6}$$

with

$$\omega_0 = -c\frac{\partial \phi}{\partial \psi} \tag{5.7}$$

Where ψ is the poloidal flux divided by 2π and ϕ is the electrostatic potential. The experimental shearing rate at $r/a = 0.475$ is approximately 25% of the linear growth rate and was expected to have little effect on the simulated transport. A $\pm 50\%$

the TRANSP calculated electron and ion heat fluxes individually was investigated. GYRO predicted electron heat flux was found to be systematically low (between $\sim$ 10 and 60%) compared with power balance calculation as demonstrated in Figure 5-7. Attempts to increase the predicted electron heat flux were unsuccessful over a large

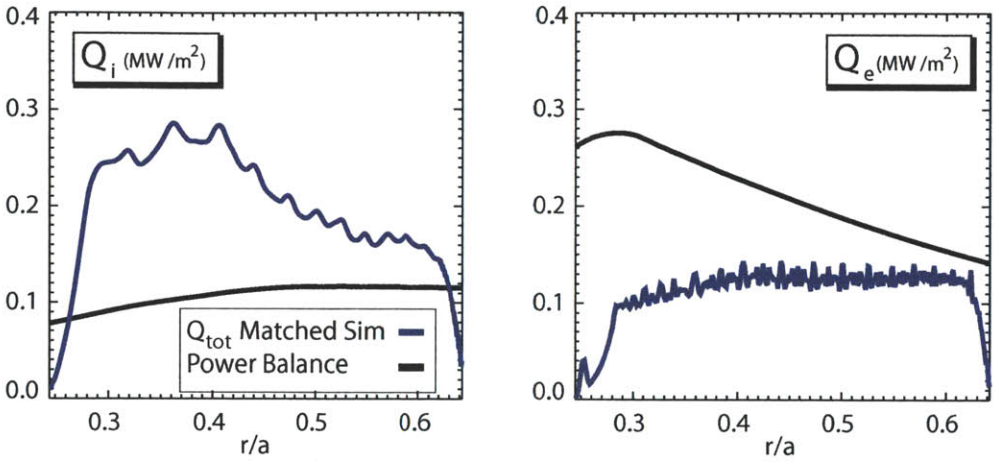

Figure 5-7: The individual electron and ion heat fluxes for the Q_{tot}-matched GYRO base case are shown. Notice the overestimate of the ion heat flux relative to the experimental value to compensate for an underestimated electron heat flux.

portion of the simulation domain. It was found that modification of the TEM drive terms a/L_{T_e} and a/L_{n_e} well outside of error bars ($\sim$ 50%) was required to matched Q_e and Q_i separately. Based on this analysis, flux matching to the total power balance heat flux, Q_{tot}, was performed through small modification of the ITG drive term to obtain a realistic turbulence level.

To determine the approximate level of agreement that should be sought between the TRANSP calculated and GYRO predicted heat fluxes, a series of TRANSP runs were performed. Realistic levels of error were assumed in the values of n_e (10%), T_e (10%), T_i (15%), Z_{eff} (20%), and $P_{absorbed}$ (10%) and 32 permutations of these assumed errors were performed. The resulting ranges in the mean Q_e, Q_i, and Q_{tot} values are shown in Figure 5-8a over the GYRO simulation domain. The approximate range of the mean power balance total heat flux is $\pm$25%. It should be emphasized that the values obtained through this method represent experimental ranges and not error bars. They can be viewed more appropriately as upper and lower limits of the

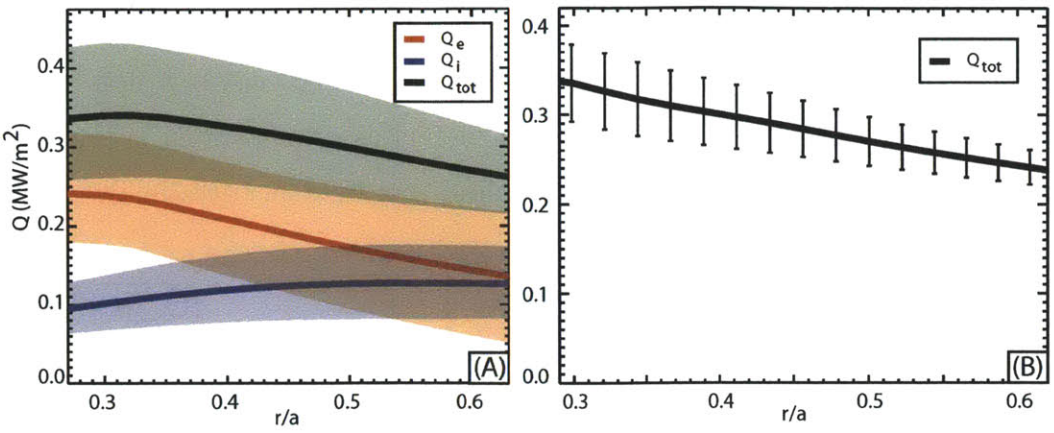

Figure 5-8: (a) Ranges of the mean TRANSP calculated heat fluxes, Q_{tot} (Black), Q_e (Red), and Q_i (Blue), found by 32 TRANSP runs with variations of experimental inputs. (b) Using the experimental inputs of all quantities, the average total heat flux calculated by TRANSP is shown with one sigma error bars obtained from time averaging from 0.965 to 1.40 seconds.

possible heat flux values. Statistical variation of the power balance calculated heat fluxes was obtained through time averaging from 0.965 - 1.40 seconds of the plasma discharge. The statistical error in the total power balance heat flux is shown in Figure 5-8b and represents a lower bound on the total heat flux error bar. These errors are found to be of order 10%. Q_{tot}-matched GYRO simulations were performed such that the GYRO prediction agrees with the TRANSP calculated heat flux within $\sim$ 15% to ensure agreement well within the calculated range of Q_{tot}.

5.3 Quantitative Comparison of Measured and Simulated Impurity Transport

5.3.1 Comparison of Experiment with a Q_{tot}-Matched GYRO "Base Case"

The experimentally derived impurity transport is compared with the flux-matched GYRO "base case" simulation in Figure 5-9. Plotted left to right are comparisons of the experimental and simulated diffusion coefficient, convective velocity, and

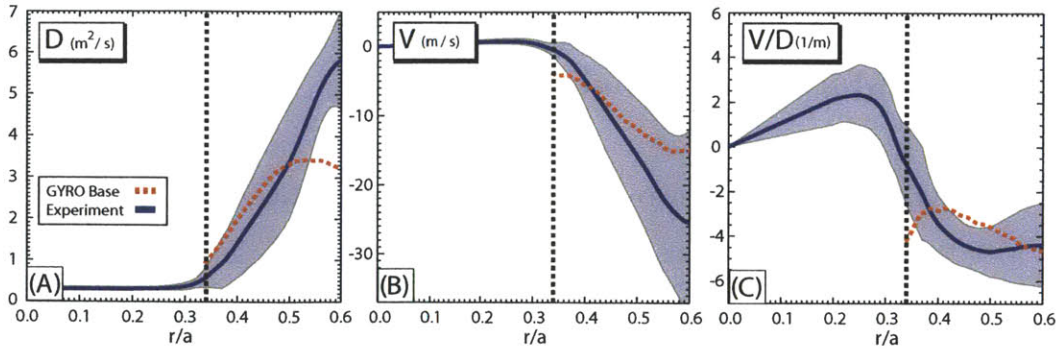

Figure 5-9: Measured and GYRO predicted impurity transport are shown for the diffusion coefficient (a), the convective velocity (b), and the peaking factor (c). The dotted line represents the location of the sawtooth inversion radius.

peaking factor. The comparison extends over the entirety of the physical GYRO simulation domain located outside of the sawtooth inversion radius, approximately $0.34 \leq r/a \leq 0.6$. In this region, where transport is thought to be dominated by turbulence, simulated transport profiles are found to be in general agreement with the experimental values within the calculated uncertainties. Simulated diffusion demonstrates agreement with experiment inside of $r/a = 0.55$ while underestimating the diffusion by $\sim$ 1.5x outside of this region. Inward convection is found in both simulation and experiment and agreement within calculated experimental uncertainty is found across the GYRO simulation domain. The steady state radial profile shapes are also consistent between simulation and experiment. This is demonstrated through comparison of the simulated and experimental peaking factors, $\frac{V}{D}$, (Figure 5-9c). The results of the sensitivity analysis presented later in this section indicate that the ratio $\frac{V}{D}$ exhibits a reduced sensitivity to uncertainty in turbulence-relevant parameters relative to the values of D and V separately. This indicates that the GYRO predicted $\frac{V}{D}$ is a robust result. Agreement of the simulated and experimental peaking factors implies agreement in the steady state impurity density profiles.

5.2.3 Obtaining Flux Matched Simulations

Outside of the sawtooth inversion radius, it is assumed that MHD activity is negligible and the heat flux calculated by power balance is the sum of the neoclassical and turbulent contributions. Power balance calculated neoclassical thermal diffusivities are found to be small compared to the calculated effective thermal diffusivity ($\chi_{e,neo} \ll \chi_{i,neo} \ll \chi_{eff}$). Therefore neoclassical contributions were neglected and it was assumed that the power balance total heat flux was the direct result of turbulence. Here the GYRO calculated heat flux (in MW/m^2) is given by [101]:

$$Q = \langle \int d^3v (mv^2/2) \delta f \delta v_x |\nabla r| \rangle \tag{5.3}$$

with

$$\delta v_x = \frac{1}{B}[\hat{b} \times \vec{\nabla}(\delta\phi - \frac{v_\parallel}{c}\delta A_\parallel)] \cdot \hat{r} \tag{5.4}$$

and

$$Q_{tot} = Q_e + Q_i \tag{5.5}$$

Where $\langle\rangle$ indicates a flux surface average, r is the midplane minor radius, δf is the perturbed distribution function for each species, and $\delta\phi$ and $\delta A_\parallel$ are the fluctuating electrostatic and vector potential respectively. Under the assumption of turbulent heat flux, and in light of the ITG dominated nature of this plasma, small modifications were made to the ion temperature gradient scale length, a/L$_{T_i}$, such that the GYRO simulated total heat flux matches that calculated by the power balance code TRANSP [88]. In all regions of the simulation domain that are clearly outside of the sawtooth inversion radius (as calculated from ECE measurement), necessary modifications were within the estimated a/L$_{T_i}$ error bars ($\sim$ 20%). However, inside of this region, modification of the measured ion temperature gradient scale length outside of error bars was required to match the TRANSP calculated heat flux. This is unsurprising since the gyrokinetic model does not include MHD phenomenon and therefore is not useful inside of this region. The existence of additional solutions (combinations of the turbulence drive terms a/L_{T_i}, a/L_{T_e}, and a/L_{n_e}) which can match

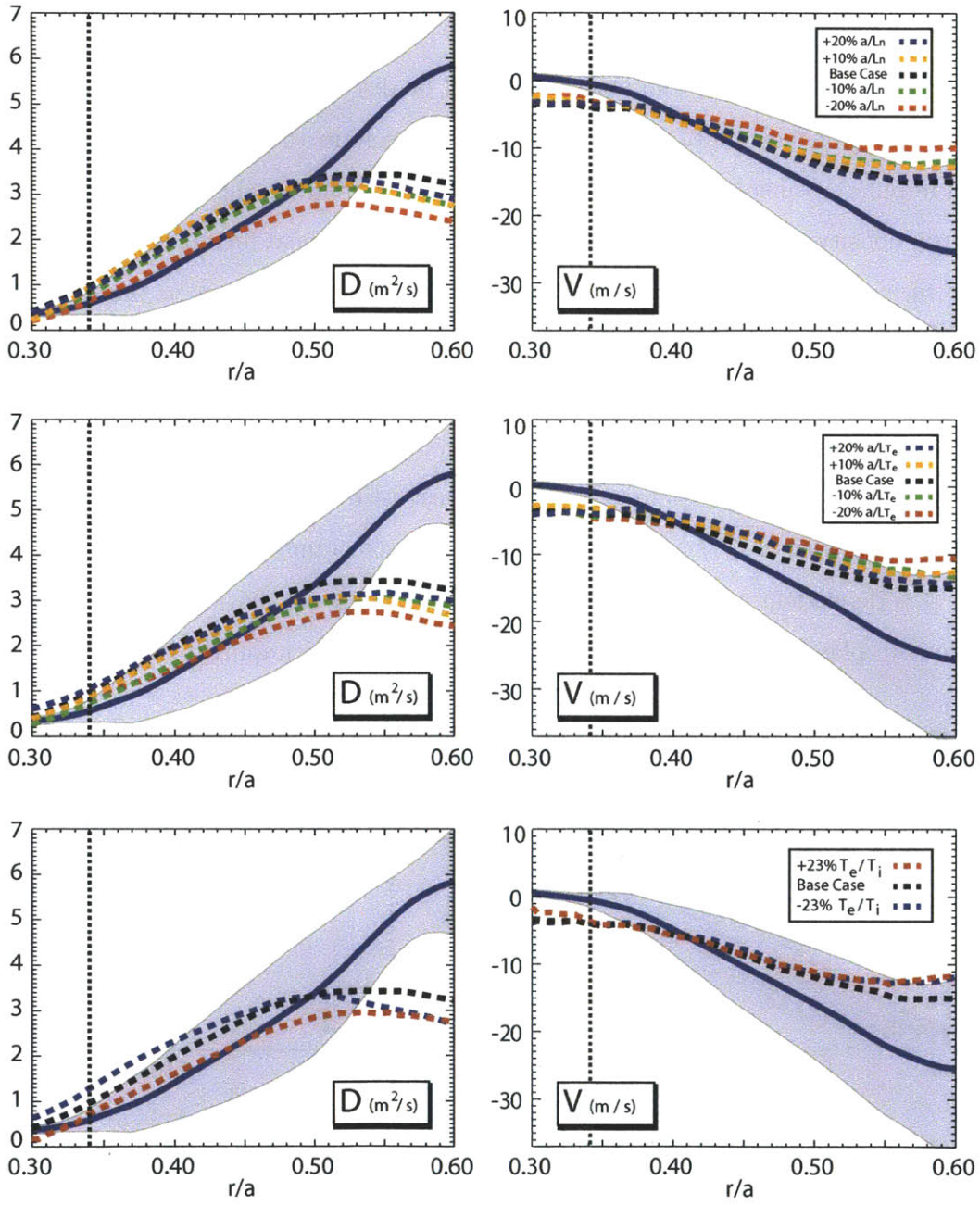

Figure 5-10: The sensitivity analysis to the parameters a/L_n, a/L_{T_e}, T_e/T_i around the GYRO base case simulation is shown. Although finite, these sensitivities are small compared to uncertainties in other turbulence relevant parameters. The solid line indicates the experimental values of the transport coefficients.

scan of the E×B shearing rate was performed which confirmed the linear picture and showed little effect of shearing rate on the heat and impurity fluxes. Therefore these terms will be ignored as significant sources of uncertainty in the simulated impurity transport and the three dominant sources will be discussed.

The level of fuel dilution plays an important role in the determination of simulated impurity transport. Increased impurity content reduces the ratio of bulk ion to electron density, n_i/n_e, and reduces the driven turbulent heat flux at fixed turbulence drive terms. For the simulated discharge the largest contribution to the calculated Z_{eff} comes from the medium and high Z impurities, argon and molybdenum. Estimates of the fractional impurity content of low (Z=5), medium (Z=18), and high (Z=42) Z intrinsic impurities were made based on spectroscopic measurement of core emission and the observed neutron rate. The best estimate for this discharge indicates $n_i/n_e = 0.95$ with a $Z_{eff} = 1.7$. Uncertainty in this estimate is difficult to quantify since it is dependent on accuracy of the neoclassical Z_{eff} calculation and assumptions of the core plasma emission. The sensitivity of simulated impurity transport to dif-

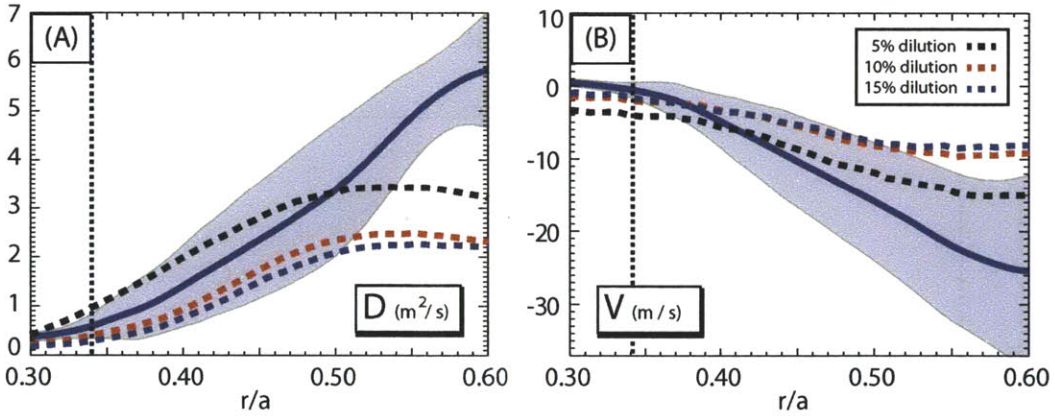

Figure 5-11: The sensitivity of the GYRO predicted diffusion (a) and convection (b) to different levels of dilution is shown. The flux matched base case has an estimated 5% dilution ($n_i/n_e = .95$). The measured transport coefficients are shown with error bars for comparison (solid blue line with shaded region). The dotted line indicates the location of the sawtooth inversion radius.

ferent levels of fuel dilution is shown in Figure 5-11 where the Q_{tot}-matched base case is represented by the 5% dilution simulation. Results from the 10% dilution should

be viewed as a bounding value for the experimental dilution level since the predicted total heat flux approximately matches the minimum of the power balance total heat flux range (Figure 5-8a). Additionally, levels of dilution exceeding 10% are in clear disagreement with measured neutron rates and the calculated Z_{eff}. Increasing dilution to the 10% level yields an approximately 40% reduction in the simulated diffusion and inward convection.

The ITG nature of the low-k turbulence suggests that modification of the ion temperature profile would result in a significant modification of the driven heat and particle flux. The behavior of the linear stability was confirmed by nonlinear simulations. Figure 5-12 demonstrates the sensitivity of the impurity transport coefficients

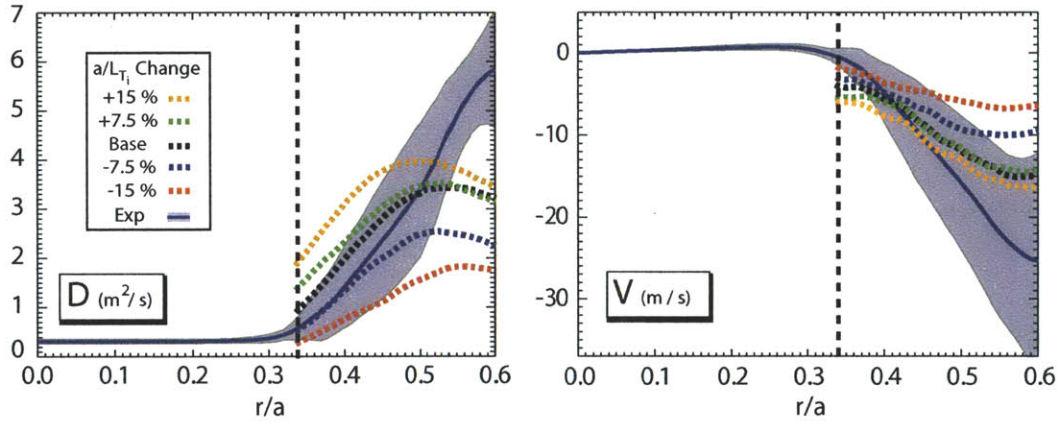

Figure 5-12: The simulated impurity transport resulting from ±7.5% and ±15% scans of a/L_{T_i} around the GYRO base case are shown.

to changes of ±7.5% and ±15% in a/L_{T_i}. Modification of a/L_{T_i} by ±7.5% corresponds roughly to simulated heat fluxes that match the maximum and minimum of the TRANSP calculated heat flux ranges (Figure 5-13). Therefore the predicted transport for these cases represents bounding values of derived impurity transport if simultaneous matching of the total heat flux is required. Interestingly, the simulated transport coefficients are found to be more sensitive to reductions in the drive term than to increases in the drive term. Decreased ITG drive results in large decreases in diffusion and inward convection while increased drive has a more complicated effect. For cases with increased ITG drive, simulations using only 8 toroidal modes were

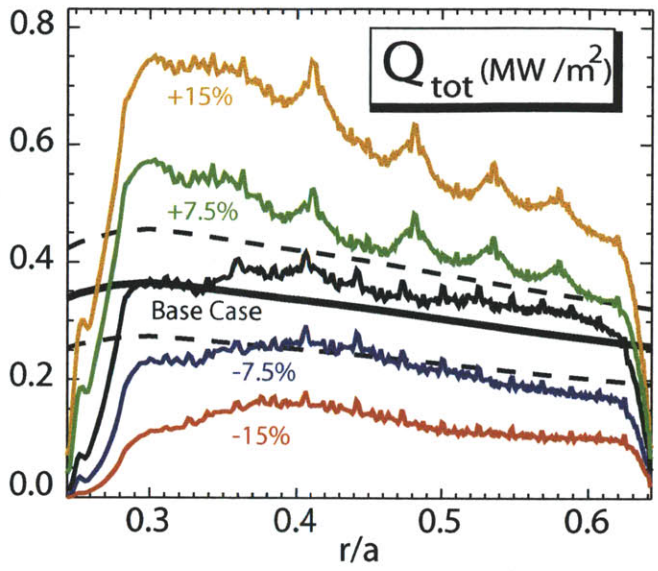

Figure 5-13: The values of Q_{tot} for all of the simulations in the a/L_{T_i} scan are shown. The solid black line indicates the TRANSP calculated value and the dotted black lines indicate the ±25% error ranges on this quantity. The GYRO base case with a ±7.5% change in a/L_{T_i} approximately matches the lower/upper bounds of the power balance Q_{tot} range.

found to be insufficient and 16 modes were required. Without this increase in box size (L_y), an apparent saturation is present in the impurity transport at increased values of a/L_{T_i}. When the box size is increased, the saturation no longer exists but a nonlinear response of the transport coefficients to a/L_{T_i} remains. This behavior is generally absent in the GYRO simulated heat flux implying a nonlinear response of impurity transport and a linear response of the heat flux to a/L_{T_i}. A more in-depth investigation into this phenomenon is presented at the end of this section.

The dependence of particle and impurity transport on safety factor and magnetic shear profile has been the subject of much investigation [62, 61]. The presence of a magnetic shear dependent curvature pinch is predicted to drive a strong inward pinch for monotonically increasing q profiles. Nonlinear gyrokinetic impurity transport sensitivity results demonstrate a dependence on modification of the q profile. Figure 5-14 shows the response of the simulated transport coefficients on ± 5% and ±10% scaling of the q profile. During this scan, the toroidal mode separation, Δn,

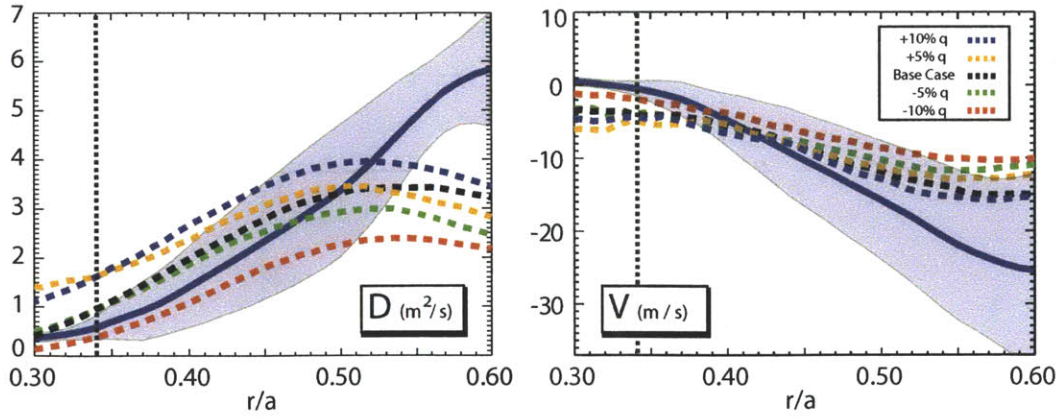

Figure 5-14: The sensitivity of the predicted impurity transport coefficients to changes of $\pm$ 5% and $\pm$ 10% changes of the q profile is shown. In these scans, the magnitude of q was varied without altering the magnetic shear profile. The measured transport coefficients are shown with error bars for comparison (solid blue line with shaded region). The dotted line indicates the location of the sawtooth inversion radius

was modified such that the maximum simulated value of $k_\theta \rho_s = 1.15$ was approximately maintained. It should be noted that this scaling of the q profile does not change the magnetic shear profile, $r/qdq/dr$. Unlike flux tube simulations, global gyrokinetic simulations do not allow for independent variation of q and magnetic shear. Therefore the effect of magnetic shear has not been tested here. From this analysis, the sensitivity to the q profile is shown to be less pronounced than the sensitivity to a/L_{T_i} and n_i/n_e but will still play an important role in any quantitative comparison with experiment. To verify results of the q profile sensitivity, additional simulations using larger box sizes (16 toroidal modes) were performed with largely unchanged conclusions.

The behavior of the main ion and electron particle fluxes were also briefly investigated during the sensitivity scans to see if the null-flux condition was satisfied. Investigation of the electron particle flux at mid-radius during a density ramp indicates that of order $1 \times 10^{19}\ m^{-2}s^{-1}$is the typical flux of particles at mid radius. Using this as our reference value, and defining a value of $1 \times 10^{18}\ m^{-2}s^{-1}$ as a satisfactory null flux condition, we can now examine the flux in the GYRO base case simulation. Shown in Figure 5-15 is the sensitivity of the electron particle flux to a/L_n and a/L_{T_i}.

Where the gyro-Bohm flux normalization is $6.22 \times 10^{20}\ m^{-2}s^{-1}$. Therefore, with our

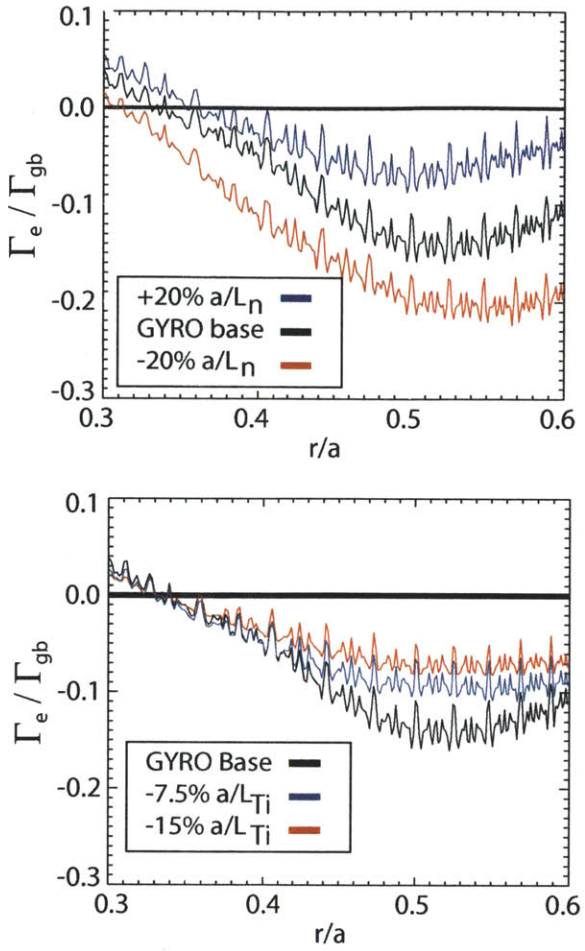

Figure 5-15: Changes in the gyro-Bohm normalized electron particle flux with changes in the value of a/L_n and a/L_{T_i} are shown.

previously stated condition, we would need a value of $\Gamma/\Gamma_{gb} \sim .002$ to satisfy the null flux condition. It is clearly seen that the GYRO base case simulation does not satisfy this criterion over a majority of the simulation domain. However, changes to the value of a/L_n and a/L_{T_i} are also found to have significant effects on the local value of the particle flux and it is possible that changes to turbulence-relevant parameters, even within experimental uncertainty, could lead to an effective null flux condition. Further investigation into this transport channel is left as the subject of future gyrokinetic model validation work.

In light of the sensitivity analysis presented in this section, it is clear that the

uncertainty in the turbulence relevant parameters, n_i/n_e, a/L_{T_i} and q factors into determining agreement or disagreement with measured impurity transport coefficient profiles. Although the GYRO base case simulation demonstrates general agreement with both the diffusive and inward convection observed experimentally, it is still possible to modify sensitive simulation parameters, while still maintaining agreement with the total heat flux within the calculated power balance ranges (cases of $\pm 7.5\%$ in a/L_{T_i}, 10% dilution, $\pm 10\%$ in q), to improve the agreement between simulation and experiment.

5.3.3 The Separation of Heat and Particle Transport

The possible separation of heat and impurity particle transport observed during the a/L_{T_i} sensitivity study presented in the previous section was the subject of further investigation. Additional nonlinear gyrokinetic simulations were performed to better understand the observed effects. These simulations were based on the Q_{tot} matched base case simulation and represent a scan of the a/L_{T_i} profile with $\pm 7.5, 15$, and 30% from the GYRO base case simulation. It should be noted that a value of a/L_{T_i} either 30% higher or lower than the experimental value is outside of the estimated error bars for this quantity. However, to investigate a possible nonlinear relationship of particle flux compared to heat transport, these simulations were performed. A normalized value of both the heat and impurity flux was evaluated from each simulation. Evaluation of the impurity flux was performed here with a value of $\nabla n_z/n_z = 1.0$. The results of this analysis are shown in Figure 5-17 at a radial location of $r/a = 0.6$. This plot illustrates a number of interesting aspects of turbulence driven particle and heat transport.

Experiment and simulation have demonstrated the existence of a ITG critical gradient in tokamak plasmas. Below a critical value of a/L_{T_i} there is insufficient drive for turbulent heat transport driven by ITG turbulence. The value of a/L_{T_i} where the ITG turbulence "turns on" is known at the critical gradient. Dimits showed that the critical gradient found through linear gyrokinetic simulation differs from the nonlinear calculated value [103]. This results from the interaction of the self generated

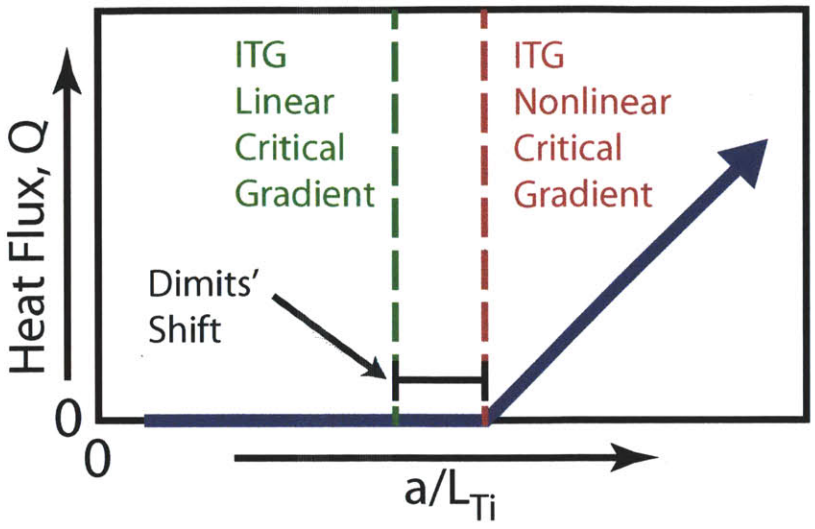

Figure 5-16: A cartoon summarizing the aspects of the ITG critical gradient is shown. The nonlinear critical gradient is observed as a result of the a/L_{T_i} sensitivity analysis performed around GYRO base case.

zonal flows which tend to suppress the ITG turbulence, resulting in an upshift in the calculated value of the critical gradient. As a result, the difference between these two critical gradient values is known as the Dimits' shift. Figure 5-16 summaries the key features of the ITG critical gradient.

In the simulations performed, a clear linear relationship of the simulated heat flux exists above a critical value of a/L_{T_i}, namely the nonlinear critical gradient for ITG turbulence. Interpolation of the linear behavior to its x-intercept value suggests the critical gradient occurs about 25% below the GYRO base case a/L_{T_i} profile. A more complicated behavior is observed in the impurity flux. Above the critical ITG gradient, the particle flux initially exhibits an approximately linear increase with increased values of a/L_{T_i}. However, it is clear that for values of a/L_{T_i} above the GYRO base case values a saturation of the impurity flux begins to occur. These results indicate different responses to increased turbulence drive for particle and heat transport. However, the approximately identical x-intercept of both the impurity and heat flux values suggests they have a common drive namely, ITG turbulence. At this time, the reason for this saturation is not understood. The first step should be to inves-

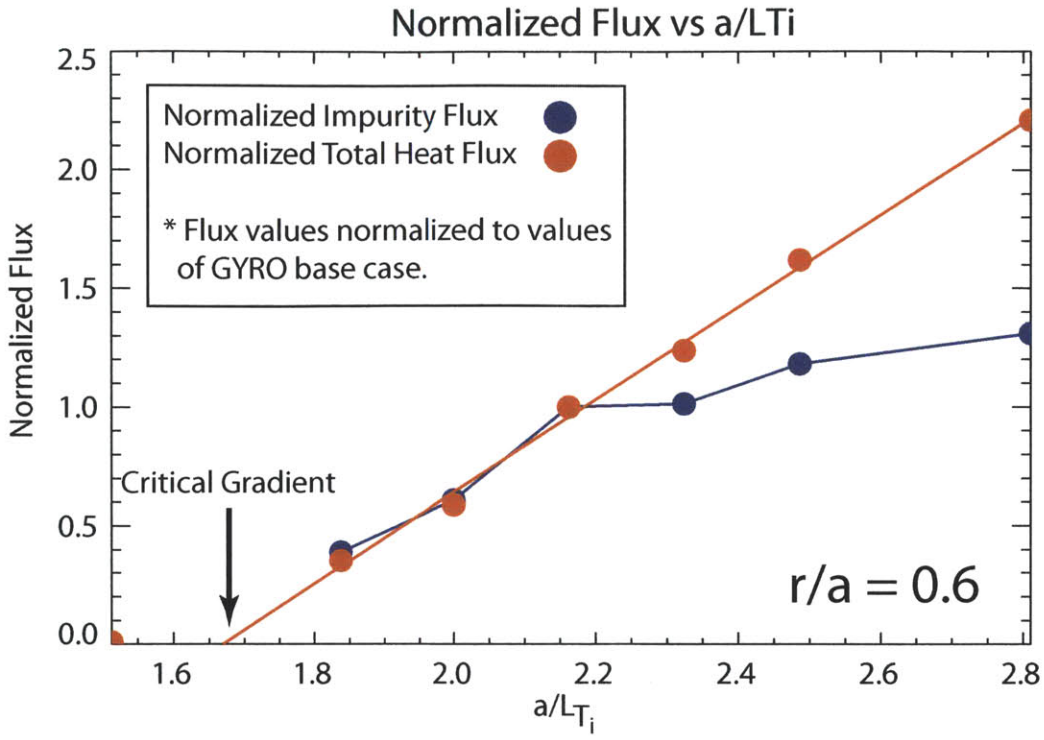

Figure 5-17: Normalized values of the impurity flux (blue) and total heat flux (red) are shown for a scan of the ITG drive term, a/L_{T_i}, around the Q_tot-matched base case simulation at $r/a = 0.6$. The expected linear relationship between the total heat flux is recovered quiet well and the value of the ITG critical gradient is well demonstrated. Above the base case values, a saturation occurs in the particle flux which indicates a separation between the particle and heat transport dynamics.

tigate whether additional resolution needs to be added to the simulations with high turbulence drive (i.e high values of a/L_{T_i}). Since all experimental comparison in this work exists at values of a/L_{T_i} equal to or below that of the GYRO base case, these investigations will be left as the subject of future work.

5.4 Comparison with Q_i Matched Gyrokinetic Simulation

All gyrokinetic simulations presented to this point were Q_{tot}-matched or represented scans around the Q_{tot}-matched base case simulation. In this section we present a new approach where the GYRO simulated ion heat flux was matched to the power balance

value while allowing Q_{tot} to drop below experimental levels. Initial simulation using the experimental profile of a/L_{T_i} tended to slightly overestimate the ion heat flux across the simulation domain. On average an $\sim$ 14% reduction of the experimental a/L_{T_i} profile was required to obtain a Q_i-matched simulation, where the value of Q_e in this simulation was ignored. The results of this new simulation are summarized in Figure 5-18. As demonstrated in 5-18a and b, inside of $r/a = 0.52$ we find agree-

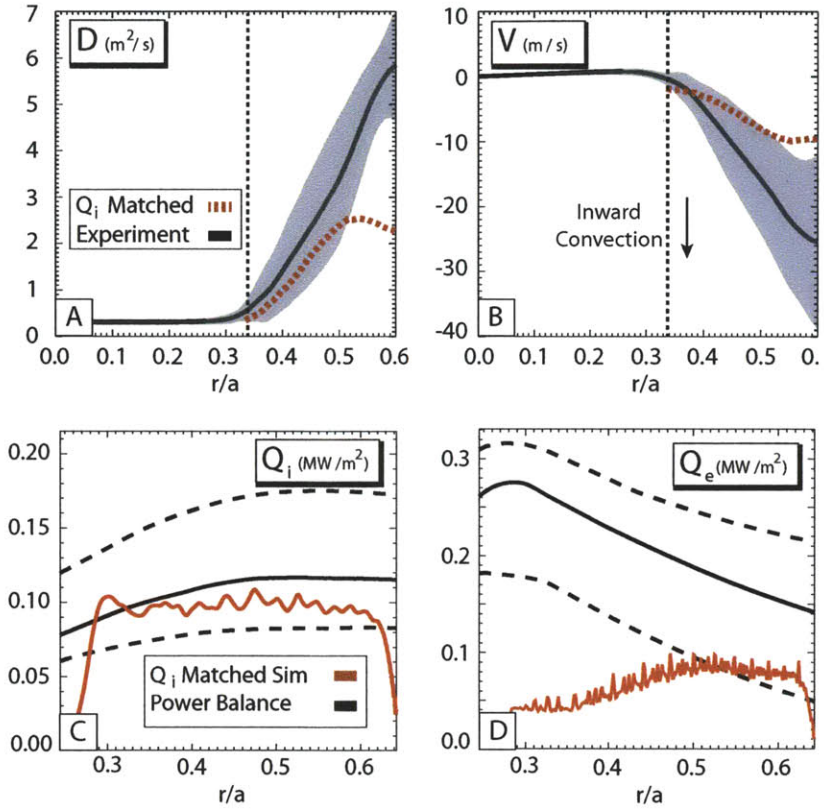

Figure 5-18: (Results from Q_i matched GYRO simulation are plotted. Both impurity transport results (a and b) and simulated heat fluxes (c and d) are shown. The dotted black line indicates power balance calculated ranges for Q_e and Q_i. Good agreement is demonstrated for power balance and GYRO simulated ion heat flux, whereas electron heat flux is systematically underestimated. Q_i matched simulation is shown to result in decent or slightly underestimated simulated impurity transport relative to experiment.

ment within experimental uncertainty between simulation and experiment in both the diffusion coefficient and the convective velocity. Outside of this region, simulation is found to lie outside of the experimental uncertainties and to underestimate

both quantities by $\sim$ 2x relative to the mean experimental values. It is interesting to note that both quantities in this simulation lie on the low side of the experimental error bars (are below the mean value of the experimental diffusion and inward convection). Figure 5-18 demonstrates clear agreement between the power balance and gyrokinetic simulated ion heat flux across the simulation domain for this Q_i-matched simulation.

In terms of impurity transport, similar levels of agreement between the experiment and simulation exist for both the Q_{tot} and Q_i-matched simulations. However, there is a fundamental difference between these simulations that motivates the remainder of this thesis work to use Q_i-matched simulation. As can readily be seen in Figures 5-19c and d, the Q_{tot}-matched GYRO base case simulation obtains its match of the total heat flux by increasing the ion heat flux above the TRANSP calculated uncertainty ranges (Figure 5-8) to effectively compensate for an underestimated electron heat flux. This results in a simulation which is not believed to be consistent with the experimental observations. In contrast, the Q_i-matched simulation presented in Figure 5-18 displays good agreement within the uncertainty ranges in the ion heat flux, clearly underestimates the electron heat flux, and displays agreement with experimental impurity transport inside of $r/a = 0.52$. Therefore, simultaneous agreement of two transport channels (ion heat and impurity particle channels) is found in this Q_i-matched simulation. Furthermore, there are at least two arguments as to why the electron heat flux is systematically underestimated by these simulations. The GYRO simulations considered here were optimized for studying impurity transport and only included contributions from long wavelength ITG/TEM type turbulence ($k_\theta \rho_s \leq 1.15$). High-k TEM and Electron Temperature Gradient (ETG) type plasma turbulence was therefore omitted from these simulations but could play an important role in meaningful simulation of the electron heat flux. However, the inclusion of these high-k modes is not expected to significantly modify the particle transport or ion heat flux since the wavelength of these modes is small compared with the impurity and ion Larmor radii. This expectation has been confirmed by high-k GYRO simulation (which included $k_\theta \rho_s$ contributions up to $\sim$ 2.5) of a similar C-Mod discharge. High-k

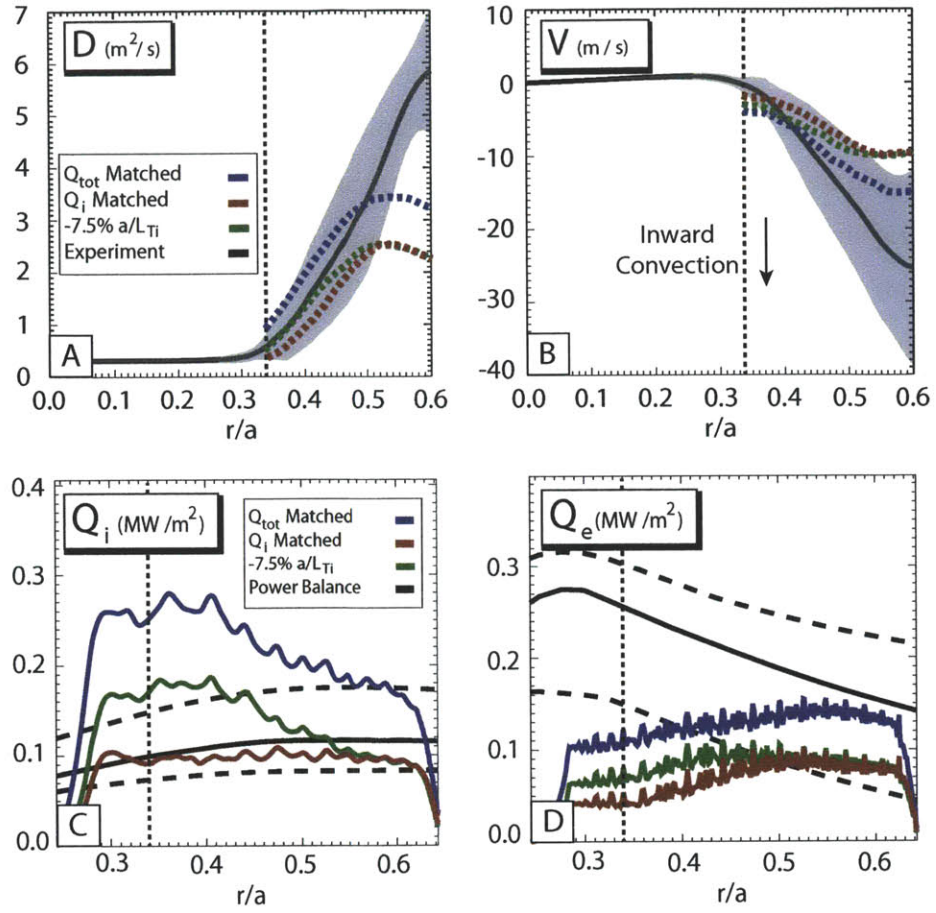

Figure 5-19: (The experimental impurity transport (a nd b), ion (c), and electron (d) heat fluxes are compared with 3 GYRO simulations: the GYRO base case, the Q_i-matched simulation, and a 7.5% reduction in a/L_{T_i} from the GYRO base case. These simulations clearly display the differences in the Q_i and Q_{tot}-matched approaches.

modes ($k_\theta \rho_s > 1$) were shown to drive non-negligible levels of electron heat flux while not significantly altering the simulated impurity transport. Therefore, the impurity transport results found from the Q_i-matched simulation would not be expected to vary significantly with the addition of high-k contributions. Alternatively, the model used may lack the necessary description of electron dynamics which is needed to simulate all of the experimental electron heat flux (i.e. gyrokinetic vs. drift kinetic electrons). Investigation of these possibilities is computationally quite intensive and is out of the scope of this thesis. We note that investigation of electron heat transport in fusion plasmas is an active and challenging area of research.

Therefore, we conclude that given the parameters of the simulations presented here, the use of Q_i-matched GYRO simulation is most consistent with experimental observations. Furthermore, agreement between simulated and experimental impurity transport and electron heat flux can simultaneously be improved through small modification of turbulence-relevant parameters while maintaining a match to the experimental ion heat flux within estimated uncertainties. In light of these observations and the sensitivity analysis presented earlier in this chapter, the remainder of the gyrokinetic simulations presented in this thesis focus on Q_i-matched simulation with the knowledge that modest quantitative disagreements can probably be resolved with small modifications to turbulence-relevant parameters in these simulations.

Chapter 6

Experimental and Gyrokinetic Analysis of I_p Dependent Impurity Transport

As discussed in Chapter 2 of this thesis, impurity transport has been the subject of extensive investigation on fusion devices worldwide [45, 16, 46, 48, 68]. Despite this work, clear dependencies of impurity transport coefficients, D and V, with engineering parameters are less common and often contradictory. A physical understanding of the mechanisms controlled by engineering parameters and their effects on the driven impurity transport remains incomplete. The neoclassical model of impurity transport has been shown, in most cases, to be insufficient to describe measured transport levels [16, 46]. It is generally accepted that the observed "anomalous" transport in the core is the result of drift wave-type plasma turbulence [12]. Interpretation of experimental impurity transport observations has, to this point, been predominantly limited to the application of quasilinear models coupled with linear gyrokinetic simulation [15, 61, 46, 16, 57]. Since it generally believed that turbulence dominates the transport found in the plasma core, the most logical experiments would be designed to test the effect of singular turbulence-relevant parameter changes on the measured impurity transport. However, in practice these experiments are often prohibitively difficult and we are limited to the set of engineering tools available on any one device

at any one point in time. For this reason, changes in engineering parameters are normally used to study impurity transport dependencies. This work attempts to identify clear trends of impurity transport coefficients with changes in an easily accessible engineering parameter, namely the plasma current, I_p. It is likely that gross changes of engineering parameters will result in modification of multiple turbulence-relevant parameters. However, gyrokinetic simulation provides an important tool for sorting out the dominant changes which occur with these gross changes in engineering parameters. The work presented in this chapter summarizes an experimental I_p scan. This scan was analyzed using gyrokinetic simulation to interpret the experimental measurements in terms of changes in background plasma turbulence and to validate the impurity transport predicted by the gyrokinetic model.

6.1 Motivation for Engineering Parameter Scans

During the 2009 and 2010 run campaigns on Alcator C-Mod, over 300 laser blow-off injections of trace CaF_2 were introduced into L-mode plasma discharges operated with a wide range of plasma parameters. A database of impurity confinement times was created from the injection data and a new Alcator C-Mod impurity confinement scaling law was produced. Power law fits of the collected injection data were attempted based on both physics and engineering parameters. Here we define "physics" parameters as quantities which have been identified through theory and experiment as influencing plasma turbulence. However, accurate estimates of these parameters, particularly those requiring profile gradients were not consistently available and motivated the use of engineering quantities at the fitting parameters for this work. All injections included in this database were collected using CaF_2 laser blow-off injection at trace levels. The HiReX Jr. spectrometer was employed to measure the He-like calcium charge state with sufficient temporal resolution for accurate impurity confinement time determination. The engineering parameters considered in this study were typical of those used for global energy confinement: I_p, κ, δ, n_e, B_T, P_{tot}, l_i, q_{95}, and Z_{eff}. The regression analysis was performed such that an initial variable for fit-

ting was user specified and the subsequent fitting variables were chosen according to their relative reduction in the χ^2. At each variable selection step, correlation between variables was checked to ensure the independence of selected fitting parameters. Additional parameters were added to the regression only if a significant reduction in χ^2 was achieved with the new parameter included. Parameters which did not result in a significant reduction of the χ^2 were omitted. A description of this linear regression methodology can be found here [104]. Through this method, the following power law scaling for the impurity confinement time (given here by τ_s) was derived for the impurity injection database.

$$\tau_s = 17.28 I_p^{.68} P_{tot}^{-.15} B_T^{.19} \tag{6.1}$$

Where I_p is in MA, P_{tot} is in MW, and B_T is in Tesla and τ_s is in ms. A plot of the injection database (includes measured impurity confinement times, i.e. the e-folding time after laser blow-off) compared to the impurity confinement scaling is shown in Figure 6-1. Significant scatter is present in the database but it should be noted that estimated error bars for each inferred impurity confinement time are typically found to be of the order 2 ms. It is interesting to compare the derived parameter scalings with the commonly referenced L-mode energy confinement scaling, $\tau_{ITER-89}$ [105]. The expression for L-mode energy confinement can be written as:

$$\tau_{ITER-89} = .048 I_p^{.85} R^{1.2} a^{.3} \kappa^{.5} n_e^{.1} B_t^{.2} m_{bg}^{.5} P_{tot}^{-.5} \tag{6.2}$$

Where m_{bg} is the mass of the background gas. Since all injections included in the impurity injection database were introduced into D_2 plasmas operated with no significant variation in the plasma major or minor radius, geometric variables and the mass of the background gas were no included in the impurity scaling law. However, similarities between the impurity confinement scaling and the energy confinement scaling are obvious. Similar scalings with plasma current and toroidal magnetic field are found and a reduction of confinement with increase input power is also present.

The strong dependence of impurity confinement on plasma current ($\tau_{imp} \propto I_p^{.68}$)

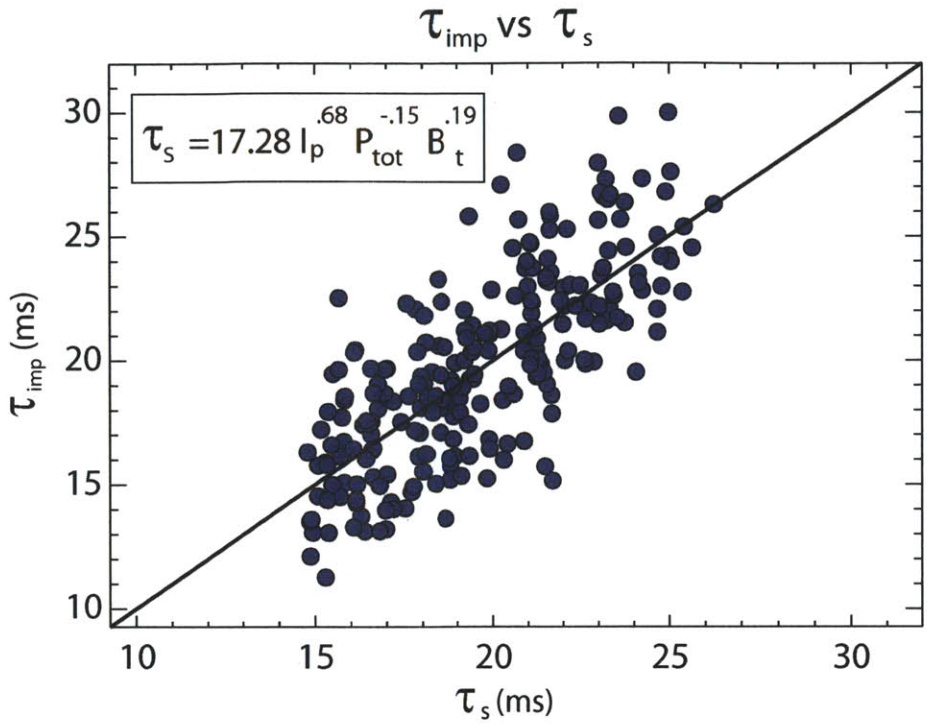

Figure 6-1: Measured impurity confinement times are plotted compared to the prediction of the impurity confinement time scaling law for all injections in the injection database. Only L-mode impurity confinement times are included here.

is best demonstrated in Figure 6-2 where average impurity confinement times (up to 4 injections) are plotted as a function of plasma current. This scan was performed at fixed values of P_{ICRH}, $n_e(0)$, and B_t. The results of this work are consistent with similar analysis on other tokamaks. On Alcator C impurity confinement was found [40] to scale as $1/q$ or $\propto I_p$ and a joint analysis of JET and Tore Supra data found a $I_p^{.31}$ dependence of impurity confinement [41]. The scalings with I_p and P_{tot} are also consistent with the previous impurity confinement scaling on Alcator C-Mod [42] based on a smaller impurity confinement data set. It is clear that the diagnosed I_p dependence varies in its strength from one study to another. Differences could be the result of databases which include subtle transition between confinement regimes such as the linear ohmic confinement regime (LOC,saturated ohmic confinement regime (SOC), L to I-mode transitions, and even operation with the ∇B drift operated towards or away the active x-point. However, the consistent observation of

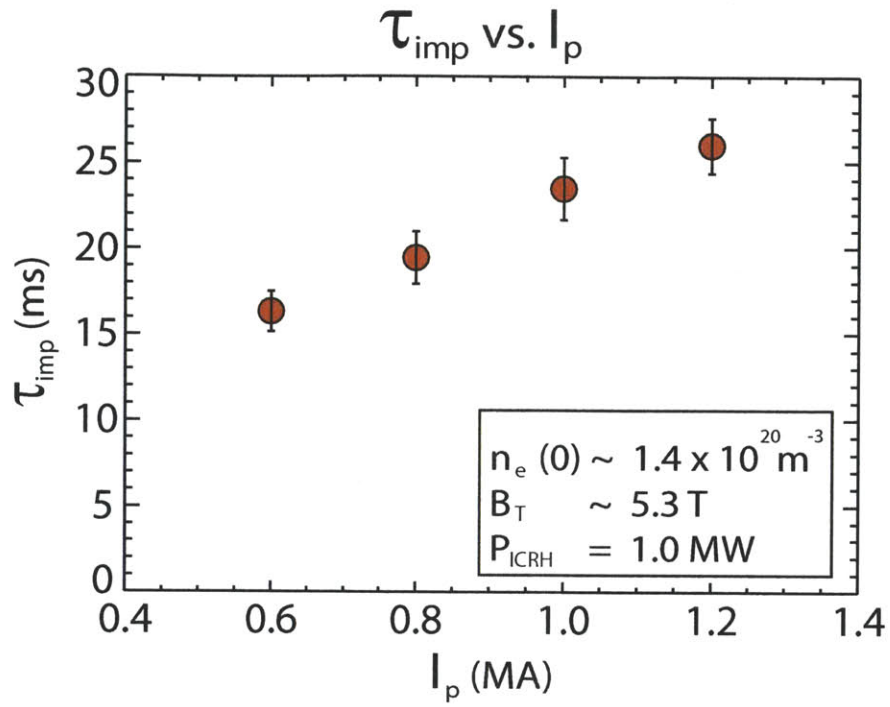

Figure 6-2: At fixed P_{ICRH}, $n_e(0)$, and B_t, impurity confinement times with estimated error bars are plotted as a function of I_p.

I_p dependent impurity transport and the results of the new Alcator C-Mod impurity confinement scaling provided motivation for a more detailed analysis of changes in impurity transport observed with plasma current.

6.2 Description of the Experiments

6.2.1 Setup of the Experimental I_p scan

The plasmas studied in this chapter constitute a scan of plasma current performed on the Alcator C-Mod tokamak. In an attempt to isolate the effects of plasma current on the derived impurity transport, the current scan was performed at fixed toroidal field (5.3 T), plasma shape, ICRH input power ($P_{ICRH} = 1.0$ MW), and central density of 1.5e20 m^{-3}. Four separate discharges were performed with plasma currents of 0.6, 0.8, 1.0 and 1.2 MA. Time traces of key plasma parameters are plotted in Figure

6-3. To raise the power threshold and avoid transition to H-mode, all discharges were

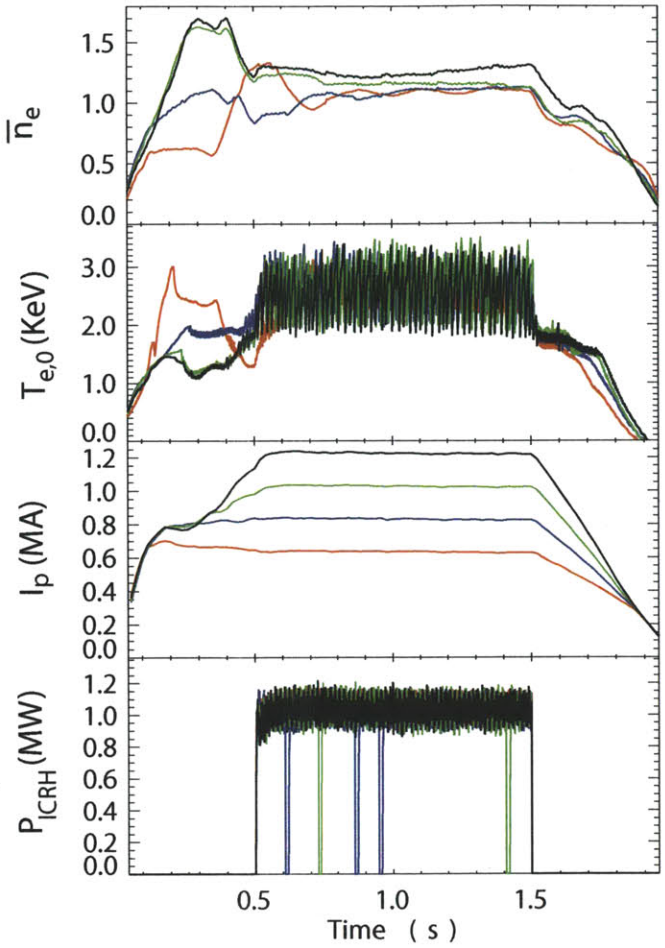

Figure 6-3: Time traces for key parameters are plotted for each discharge in the I_p scan.

operated in upper single null (USN) configuration with the ion ∇B drift away from the active x-point. None of the studied discharges show any indication of transition to high confinement regimes and are characterized as standard USN L-mode plasma discharges. Sawteeth were present in all plasmas and the radial extent of the inversion radius was determined through electron cyclotron emission (ECE) and soft-xray measurement. As a result, gyrokinetic analysis of these discharges is only reported outside of the sawtooth inversion radius at each current, where the effects of MHD driven transport are assumed to be minimal.

6.2.2 Description of Diagnostic Setup and Measurements

An in depth description of the diagnostic suite used in this work was presented in Chapter 3 of this thesis. However, a brief description of exact measurements utilized is presented here for completeness. Measurement of the plasma profiles needed for experimental and gyrokinetic transport analysis was provided by Alcator's diagnostic suite [71]. Electron density and temperature profile measurement was performed using a combination of a 33 channel Thomson scattering system [6] and 3 separate ECE systems [72, 73, 74]. Data from these measurements was used to obtain the smooth, b-spline fitted plasma profiles used for the experimental and gyrokinetic analysis. Ion temperature and toroidal velocity profiles were obtained using He-like argon (Ar^{16+}) spectra measured by a spherically bent x-ray crystal spectrometer [7]. Edge gas puffing was employed to introduce non-intrinsic argon into the plasma at levels which provide good signal to noise but do not significantly alter the background plasma. Ion temperature and toroidal velocity profiles were obtained from the measured argon spectra using tomographic inversion techniques. These profiles are limited to regions where He-like argon emission is sufficiently high. As a result, the exact radial extent of the diagnosed T_i and V_ϕ profiles varies with changes in plasma parameters. Good quality profile data were obtained inside of $r/a = 0.75$ for all discharges of interest. The values of Z_{eff} used in the gyrokinetic analysis were obtained from a model for neoclassical resistivity using the expressions found in reference [99] and are assumed to be radially constant over the simulation domain. These values of Z_{eff} are consistent with spectroscopically constrained estimations of impurity concentration (n_i/n_e) and the measured neutron rate within estimated experimental uncertainties.

6.2.3 Description of the Experimental Analysis Methodology

Impurity transport coefficient profiles were determined for all discharges in the I_p scan. The methodology employed to determine the experimental profiles is briefly outlined here but a detailed description can be found in Chapter 4 of this thesis. The combination of a multi-pulse laser blow-off system [106] and the available spec-

troscopic measurements on Alcator C-Mod allows for the accurate determination of impurity transport coefficient profiles from $0.0 \leq r/a \leq 0.6$. All experiments presented here featured trace injection of non-intrinsic, non-recycling calcium impurities introduced via the laser blow-off technique. Light from neutral calcium introduced at the plasma edge is measured spectroscopically to resolve the time history of the laser blow-off generated source. The full, time evolving brightness profile of the He-like (Ca^{18+}) charge state is measured using the x-ray crystal spectrometer described earlier in this section, HiReX Sr. An additional single chord measurement of the Li-like (Ca^{17+}) charge state is provided by an x-ray and extreme ultraviolet (EUV) spectrometer, XEUS. The core view of this spectrometer measures the time history of Ca^{17+} emission and provides an effective boundary condition for the measured profiles of Ca^{18+}. A synthetic diagnostic built around the impurity transport code STRAHL [80] is used to simulate emission from each diagnostic view. STRAHL assumes that the impurity flux can be written as the sum of diffusive and convective contributions, namely:

$$\Gamma_z = -D\nabla n_z + V n_z \tag{6.3}$$

Where both D and V, the flux surface averaged diffusive and convective transport coefficients, are assumed to be time-independent with only radial dependence. The D and V profiles which are found to best reproduce measured brightness data via the synthetic diagnostic are quoted as the experimental impurity transport coefficient profiles. Similar χ^2 minimization approaches have been employed on ASDEX-Upgrade [48], JET [16], and Tore Supra [46]. A Monte Carlo analysis technique is used to assess experimental error in the derived impurity transport coefficient profiles due to error in the background electron density and temperature profiles. Once again, the reader is referred to reference [68] or Chapter 4 for the experimental analysis methodology and determination of uncertainties.

6.3 I_p Dependent Impurity Transport in the Alcator C-Mod Core

6.3.1 Experimental Observations of Core Impurity Transport with I_p

The methodology described above was used to determine impurity transport coefficients profiles for all four plasma discharges in the I_p scan. The resulting transport coefficients are shown in Figure 6-4. The solid lines indicate the mean derived transport coefficients for each of value of I_p. These curves demonstrate a clear trend in the measured impurity transport with increasing values of plasma current. Error bars were determined using a Monte Carlo approach for each discharge in the current scan, but for clarity of presentation they are only displayed on the 1.0 MA discharge. These

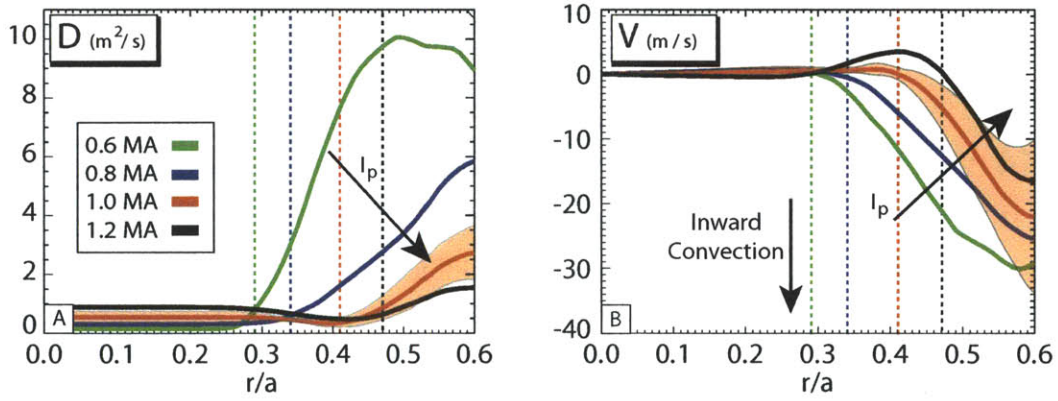

Figure 6-4: The experimentally derived impurity transport coefficients are plotted for all discharges in the I_p scan. The measured impurity diffusion coefficient (a) is found to decrease significantly with increased plasma current while a much more modest decrease in the mean inward convection (b) is observed. Representative errors bars are shown on the 1.0 MA discharge and the dotted lines represent the approximate location of the sawtooth inversion radius at each current.

error bars are representative of the relative uncertainty present in the results at all values of plasma current. Large uncertainty in the measured convective velocity, despite the clear organization of the mean impurity transport coefficients with plasma current, may reflect systematic errors in the measured electron density and temperature

profiles (e.g the Thomson scattering calibrations). However, since these discharges were performed almost sequentially, any systematic errors are likely to be correlated shot to shot. In the outer half of the measurement region, a doubling of I_p from 0.6 to 1.2 MA is found to result in an $\sim$ 7x reduction in the mean impurity diffusion while only reducing the mean inward convection by $\sim$ 3x. These changes would suggest an increase in the impurity peaking factor, V/D, with increased plasma current. Unfortunately, the large errors associated with the convective velocity obscure trends near the edge of the measurement region. The transition from core (MHD dominated) to confinement zone (turbulence dominated) impurity transport is clearly observed in the measured diffusion coefficients. The I_p scan was performed at a fixed toroidal field of $B_t = 5.3$ T with approximately fixed plasma shape. Therefore, the location of the sawtooth inversion radius shifts radially outward with increasing plasma current as expected. The location of the inversion radius is particularly relevant for determining the radial region where meaningful comparison with gyrokinetic simulation is possible. The sawtooth inversion radii, as determined from ECE and soft x-ray measurement, occur at $r/a = 0.29, 0.34, 0.41, 0.47$ for plasma currents of 0.6, 0.8, 1.0, and 1.2 MA respectively. At these approximate radial locations, a transition from low levels of core diffusion to monotonically increasing values of diffusion is observed. Similar transition between core and confinement zone diffusion has been observed previously [68, 16, 46]. This behavior will be shown below to be the result of small normalized gradient scale length (low turbulence drive) inside of the sawtooth inversion radius.

6.3.2 Changes in Turbulence-Relevant Parameters with Plasma Current

Modification of the plasma current affects the plasma profiles which play key roles in the drive and suppression of the turbulent modes generally believed to be responsible for the observed levels of impurity transport. Examination of the plasma profile changes from the I_p scan provides insight into changes in turbulence. The left column of Figure 6-5 (a-d) shows $\sim$ 400 ms time-averaged profiles of electron density, electron

temperature, ion temperature, and q for the I_p scan. The right column (Figure 6-5e-h) shows the corresponding turbulence drive/supression terms namely, a/L_{n_e}, a/L_{T_e}, a/L_{T_i}, and $\hat{s}$ (magnetic shear) over the radial range $0.25 \leq r/a \leq 0.75$. This range was chosen to best demonstrate changes in turbulence-relevant parameters in the plasma confinement zone, where gyrokinetic simulation is most applicable. With I_p modifi-

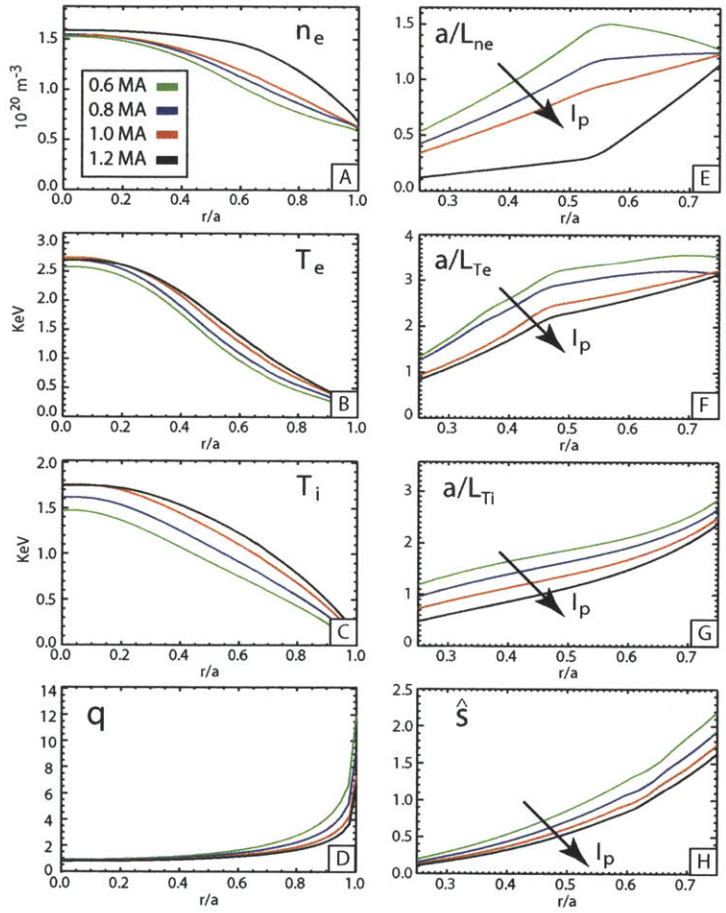

Figure 6-5: Plasma profiles (a-d) and their corresponding turbulence drive/suppresion terms are shown (e-h) for all discharges in the I_p scan. The black arrow indicates the direction of increasing I_p. All drive/suppresion terms are observed to decrease with increasing plasma current in the confinement zone.

cation changes are observed in all of the turbulence-relevant parameters. However, the most significant effects occur in a/L_{n_e}, q, and $\hat{s}$. Increased plasma current leads to a broadening of both the electron and ion temperature profiles which in turn leads to a reduction in the gradient scale length in the confinement zone. A similar effect is

observed in the electron density. It is interesting to note the significant density profile change in the 1.2 MA discharge. Despite the similarity of this discharge to the 1.0 MA case, a 2x reduction in the measured value of a/L_{n_e} is found as a result of a much broader density profile. This is in strong contrast to the smaller changes observed in other turbulence-relevant terms. However, the central density, $n_{e,0}$, remains relatively unchanged when compared to all other discharges in the current scan. It is generally found that a/L_n, a/L_{T_e}, a/L_{T_i}, q and $\hat{s}$ all decrease with increasing plasma current. A decrease in both the Trapped Electron Mode (TEM) (a/L_n and a/L_{T_e}) and Ion Temperature Gradient (ITG) (a/L_{T_i}) turbulence drive terms would suggest a reduction in the overall turbulence level at high current but reduction of the turbulence suppression term, $\hat{s}$, would lead to an increase in the overall turbulence level. The overall effect of these profile changes on the characteristic plasma turbulence, if any, is unclear. Therefore, linear stability analysis was performed to look for qualitative changes in the turbulence character (i.e. from ITG-dominated to TEM-dominated) during the I_p scan.

6.3.3 Linear Gyrokinetic Analysis of the I_p Scan

The GYRO code [92] was used to study changes in the linear stability properties of discharges in the I_p scan. The stability properties of both the 0.6 (Figure 6-6a-c and 6-7) and 1.2 MA (Figure 6-6d-f and 6-7) discharges are presented. It should be noted that a full linear analysis of all discharges in theses studies was performed. The qualitative behavior of the 0.8 and 1.0 MA discharges can be determined by straightforward interpolation between results from the 0.6 and 1.2 MA cases. Contours of the growth rate of the most unstable linear mode in the range $k_\theta \rho_s \sim [0.25 - 0.75]$ are plotted at 3 radial locations, $r/a = 0.35$, 0.475, and 0.6, for scans of a/L_{T_i} and $a/L_{T_e}/a/L_n$ on the x and y axes respectively . Here we define $\rho_s = c_s/\Omega_{ci}$ as the sound speed gyroradius, $\Omega_{ci} = eB/m_i c$ as the ion gyrofrequency, and $c_s = \sqrt{T_e/m_i}$ as the sound speed. The color scheme employed indicates low linear growth rates with darker colors and large linear growth rates with lighter colors. The selected $k_\theta \rho_s$ range was chosen to best display a shift from ITG to TEM dominated turbulence in the low-k spectrum since

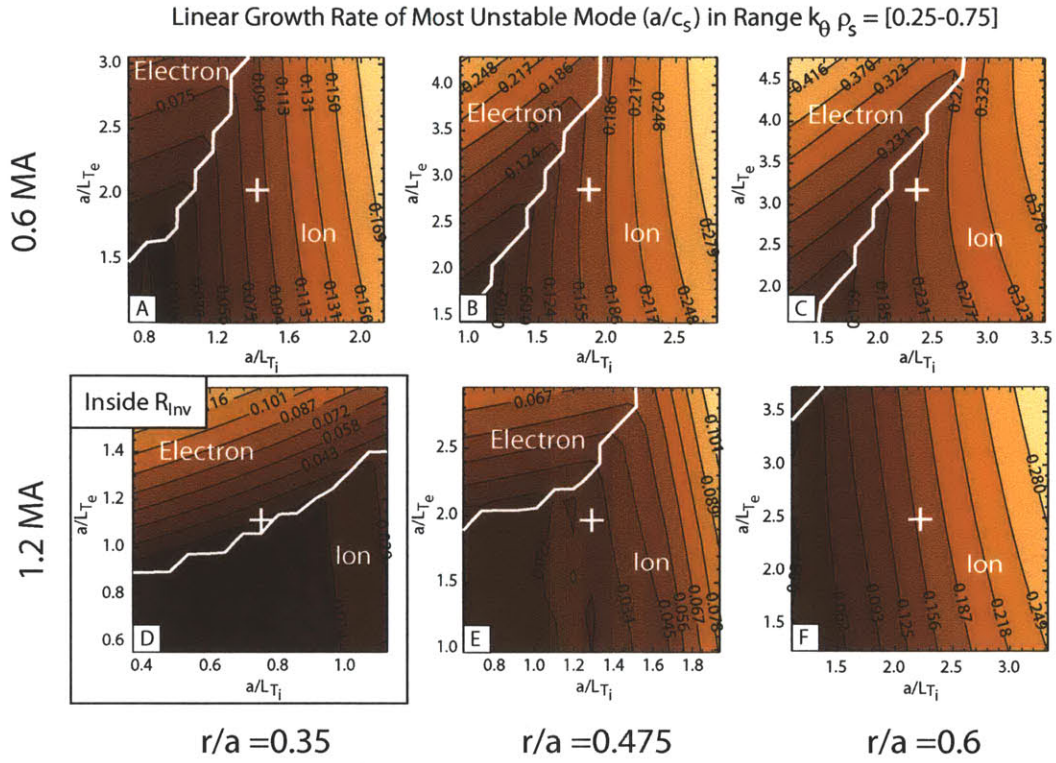

Figure 6-6: Contours of the growth rate of the most unstable linear mode are plotted for the lowest (0.6 MA, Figure 5a-c) and the highest (1.2 MA Figure 5e-f) currents in the I_p scan. 3 radial locations, $r/a = 0.35$, 0.475, and 0.6 are shown. The x-axis plots values of a/L_{T_i} and the y-axis plots values of a/L_{T_e}. The white line indicates the boundary between modes rotating in the ion and electron diamagnetic drift direction and the "+" sign indicates the experimental location. It is found that both plasmas are ITG dominated but are stable inside of the sawtooth inversion radius.

these modes are often responsible for the dominant contributions to heat and particle transport. The solid white line indicates the boundary between modes rotating in the ion and electron diamagnetic drift direction and the + sign indicates the location of the experimental values of the gradient scale lengths at each radial location. Note the change of scale in each plot. At $r/a = 0.6$ the most unstable linear mode in both the 0.6 and 1.2 MA discharges is rotating in the ion diamagnetic drift direction and is sensitive to changes in a/L_{T_i}. Therefore we characterize both plasmas (at $r/a = 0.6$) as being dominated by ITG-type turbulence. Farther into the plasma, at $r/a = 0.475$ both discharges are still ITG unstable. However the sawtooth inversion radius for the 1.2 MA discharge lies just inside this location and as a result the linear

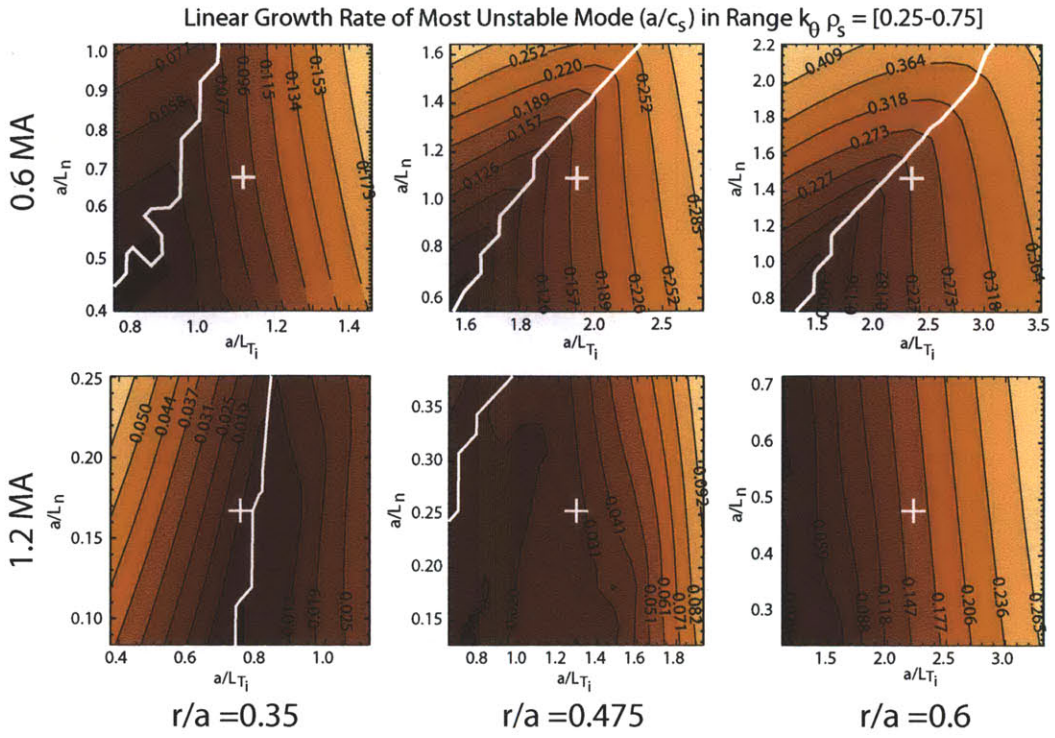

Figure 6-7: Contours of the growth rate of the most unstable linear mode are plotted for the lowest (0.6 MA, Top) and the highest (1.2 MA Bottom) currents in the I_p scan. 3 radial locations, $r/a = 0.35$, 0.475, and 0.6 are shown. The x-axis plots values of a/L_{T_i} and the y-axis plots values of a/L_n. The white line indicates the boundary between modes rotating in the ion and electron diamagnetic drift direction and the "+" sign indicates the experimental location.

growth rate has been greatly reduced. At $r/a = 0.35$ the 0.6 MA discharge remains ITG unstable. In contrast, $r/a = 0.35$ lies inside of the sawtooth inversion radius for the 1.2 MA discharge. Small values of a/L_{T_i} are present inside of the inversion radius, resulting in stabilization of low-k ITG and TEM-type turbulence. This is a robust result, observed in the linear stability analysis at all values of plasma current. This result explains the observation of reduced diffusion and convection inside of the sawtooth inversion radius in the experimental impurity transport coefficient profiles.

6.4 Quantitative Comparison of Simulated and Measured Impurity Transport

6.4.1 Setup of the Nonlinear GYRO Simulations

The GYRO code was used to perform all gyrokinetic simulations presented in this paper. GYRO is an Eulerian, δf, initial value code which is capable of both local and global simulation. All simulations presented here were global with an approximate physical simulation domain of $0.29 \leq r/a \leq 0.62$ and contributions of $k_\theta \rho_s$ up to ~ 1.15 included. This range of $k_\theta \rho_s$ was chosen to capture the dynamics of the long wavelength Ion Temperature Gradient (ITG) and Trapped Electron Mode (TEM) turbulence which is thought to dominate turbulent ion transport. Simulation of this $k_\theta \rho_s$ range was performed using 8 toroidal modes in most simulations reported. This resulted in approximate box sizes of $100\rho_s(L_x)$ by $40\rho_s(L_y)$. However, numerous spot checks were performed throughout the analysis to ensure that larger box sizes did not significantly effect the simulated impurity transport results. All simulations were electrostatic, included drift kinetic electrons with a realistic mass ratio ($\sqrt{m_D/m_e} = 60.6$), rotation, and $E \times B$ shear effects. Simulated values of the impurity transport coefficients were inferred from GYRO's output impurity flux. Each simulation included three He-like calcium trace impurity species, at $\sim .001 n_e$. Each impurity was specified with a different value of the impurity density gradient scale length, $-a\nabla n_z/n_z$ where n_z is the impurity density and a is the plasma minor radius. The simulated diffusive and convective contributions to the impurity flux are derived from the following equations:

$$\frac{\Gamma_z}{n_z} = -D\frac{\nabla n_z}{n_z} + V \tag{6.4}$$

where for an arbitrary species, the particle flux from GYRO is defined as [101]:

$$\Gamma = \langle \int d^3v \delta f \delta v_x |\nabla r| \rangle V'(r) \tag{6.5}$$

with

$$\delta v_x = \frac{1}{B}[\hat{b} \times \vec{\nabla}(\delta\phi - \frac{v_\parallel}{c}\delta A_\parallel)] \cdot \hat{r} \tag{6.6}$$

Here $V(r)$ is the volume enclosed by the flux surface, $V'(r) = dV(r)/dr$, δf is the perturbed distribution function for a given species, $\delta\phi$ is the fluctuating electrostatic potential, and $\delta A_\parallel$ is the parallel fluctuating vector potential. A linear fit of Γ_z/n_z versus the quantity $-\nabla n_z/n_z$ yields the diffusion coefficient and convective velocity from the slope and y-intercept respectively. The simulated quantities $(D, V, Q_i, Q_e, Q_{tot})$ quoted in this paper are average values obtained from time averaging over long simulation time periods, typically of order $\sim 450(a/c_s)$.

6.4.2 Reproduction of the I_p Scan Using Nonlinear GYRO Simulation

Global, nonlinear GYRO simulation of all discharges in the I_p scan was used to assess the gyrokinetic model's ability to reproduce the observed trend of impurity transport coefficients with I_p and to provide a quantitative comparison of simulated and measured impurity transport. Figure 6-8 demonstrates the comparison between measured and simulated diffusion and convection for all discharges in the I_p scan. Gyrokinetic turbulent transport is not dominant inside of the sawtooth inversion radius, therefore simulated transport coefficient profiles were truncated to show only results outside of the sawtooth inversion radius for each respective discharge. The upper radial bound of the comparison is set by the maximum radius for accurate measurement of impurity transport. The arrow in Figure 6-8 indicates the direction of increasing plasma current. In light of the discussion earlier in this section, all simulations presented here included modification of the experimental a/L_{T_i} profiles to match the GYRO simulated ion heat flux, Q_i, to the experimental power balance ion heat flux. Although there was variation in the amount of modification needed across the profile, the average percent change in a/L_{T_i} (from the experimental value) for each discharge was: -10% for the 0.6 MA discharge, -14% for the 0.8 MA discharge, $+2\%$ for the 1.0 MA discharge, and a -1% change for the 1.2 MA discharge. Before discussing

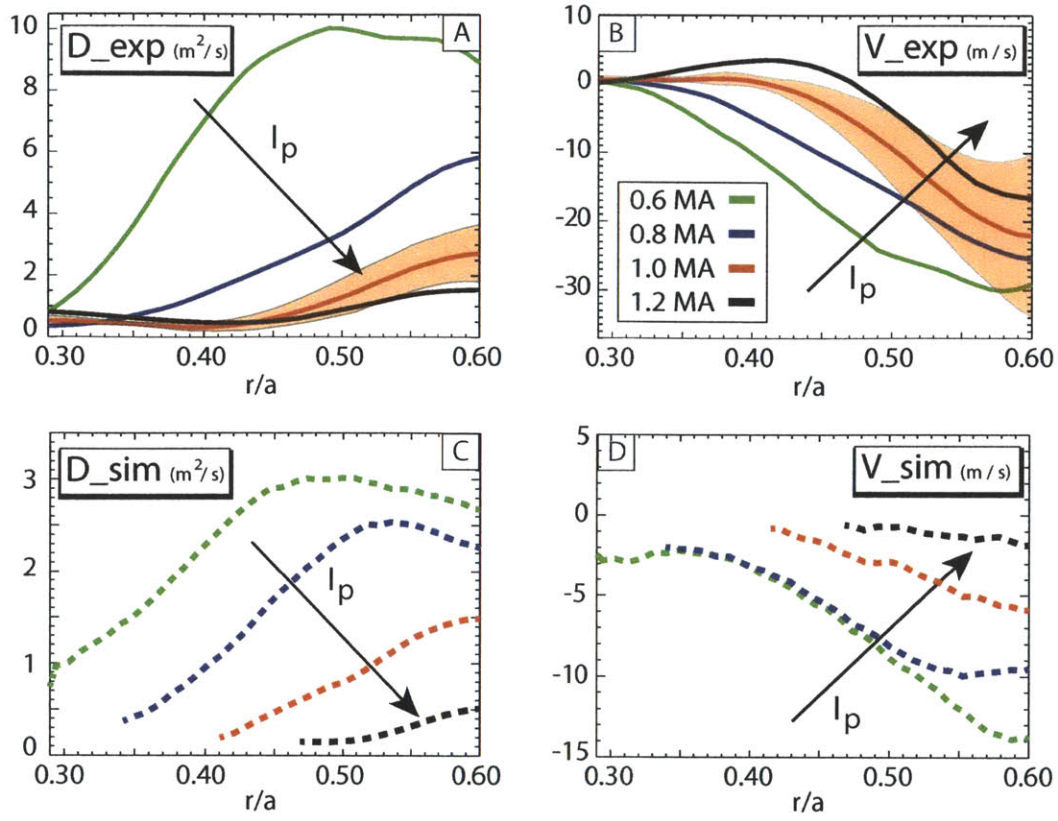

Figure 6-8: Measured impurity transport (a-b) is compared with global, nonlinear gyrokinetic simulation (c-d) for discharges in the I_p scan. The arrow indicates the direction of increasing I_p. Relatively consistent radial profile shapes are reproduced by simulation. Additionally, both trends of decreased diffusion and convection are recovered by the simulated I_p scan.

quantitative agreement or disagreement, not two key features demonstrated in Figure 6-8. First, the shape of the simulated profiles for both D and V are found to be consistent with the experimentally determined transport coefficient profile shapes. Second, ion heat flux matched simulations display the ability to accurately reproduce the experimental I_p trends. The trends of decreased impurity diffusion and inward convection with increased plasma current are found to be well reproduced by nonlinear simulation. However, as demonstrated in Figure 5-18, ion heat flux matched simulations tend to systematically underestimate the power balance calculated electron heat flux across the simulation domain. This underestimate tends to be larger at high values of plasma current. In fact, the 0.6 MA discharge shows agreement

within experimental uncertainty between simulated and experimental values of Q_i and Q_e outside of $r/a = 0.4$ as demonstrated in Figure 6-9 well outside the sawtooth inversion radius.

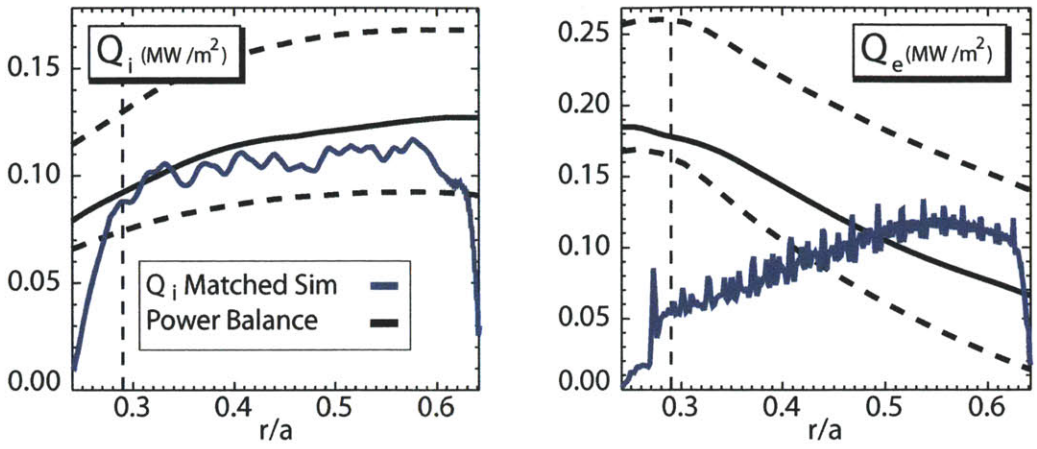

Figure 6-9: The power balance calculated Q_i and Q_e is compared with the Q_i-matched simulation values for the 0.6 MA discharge. The solid black line indicates the experimental heat fluxes and the dotted black lines indicate crude estimates of the uncertainty ranges. The vertical dashed line gives the approximate location of the sawtooth inversion radius.

It is interesting to note the differences in the low-k real frequency, ω, and linear growth rate, γ, spectrum from the 0.6 and 1.2 MA discharges shown in Figures 6-10 and 6-11 at $r/a = 0.6$. As reported in the previous section it was found that the mode with the largest linear growth rate in $k_\theta \rho_s \cong [0.25 - 0.75]$ is in the ion direction (-) in both discharges. However, unlike the 1.2 MA case which has only modes rotating in the ion direction, the 0.6 MA discharge has most unstable linear modes which rotate in the electron direction (+) for values of $k_\theta \rho_s < 0.5$. It is an open question as to whether this difference in linear stability is related to the better observed agreement in the 0.6 MA nonlinear simulation.

As discussed above, multiple changes in turbulence drive and suppression terms are observed in the I_p scan. It was demonstrated that linear stability analysis does not predict a change in the character of the most unstable low-k turbulence with a factor of two increase in the plasma current (0.6 to 1.2 MA). Despite this observa-

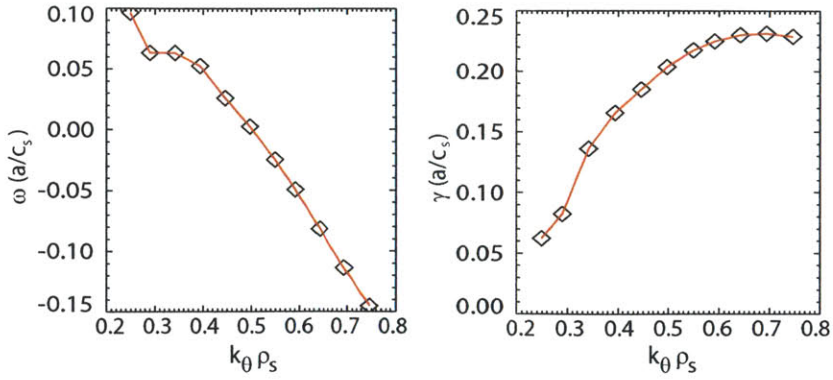

Figure 6-10: The real frequency, ω, and growth rate, γ, obtained from linear GYRO analysis for the 0.6 MA discharge is shown as a function of $k_\theta \rho_s$ at $r/a = 0.6$. Frequencies in the electron/ion diamagnetic drift direction are denoted by positive/negative values respectively.

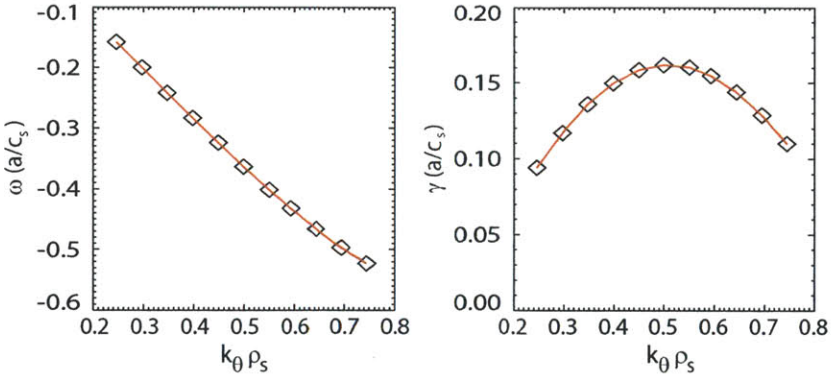

Figure 6-11: The real frequency, ω, and growth rate, γ, obtained from linear GYRO analysis for the 1.2 MA discharge is shown as a function of $k_\theta \rho_s$ at $r/a = 0.6$

tion, clear trends were found in both impurity diffusion and convection with increased plasma current. Furthermore, these trends are well reproduced by Q_i-matched global, nonlinear gyrokinetic simulation. In an attempt to identify the physical change (in turbulence drive or suppression terms) most responsible for the observed changes in impurity transport, a series of nonlinear simulations were performed around the GYRO base case, a Q_{tot}-matched global, nonlinear simulation performed on the 0.8 MA discharge of the current scan. To best determine the effects of single turbulent drive/suppression term changes on simulated impurity transport, profiles of n_e and q from the 0.6, 1.0, and 1.2 MA discharges were inserted one at a time into the GYRO base case simulation (the 0.8 MA discharge). These profiles were chosen due to the

large observed changes in both a/L_{n_e}, q, and $\hat{s}$ during the I_p scan. This resulted in 6 additional simulations which were identical to the GYRO base case simulation, with the exception of a modified q or n_e profile. The bulk ion and impurity density profiles were appropriately adjusted to maintain quasineutrality. Since GYRO consistently demonstrated the ability to reproduce observed radial profile shapes, the results of this series of simulations compared with experiment is presented in Figure 6-12 at $r/a = 0.5$. The radial location chosen can be varied without significantly altering the

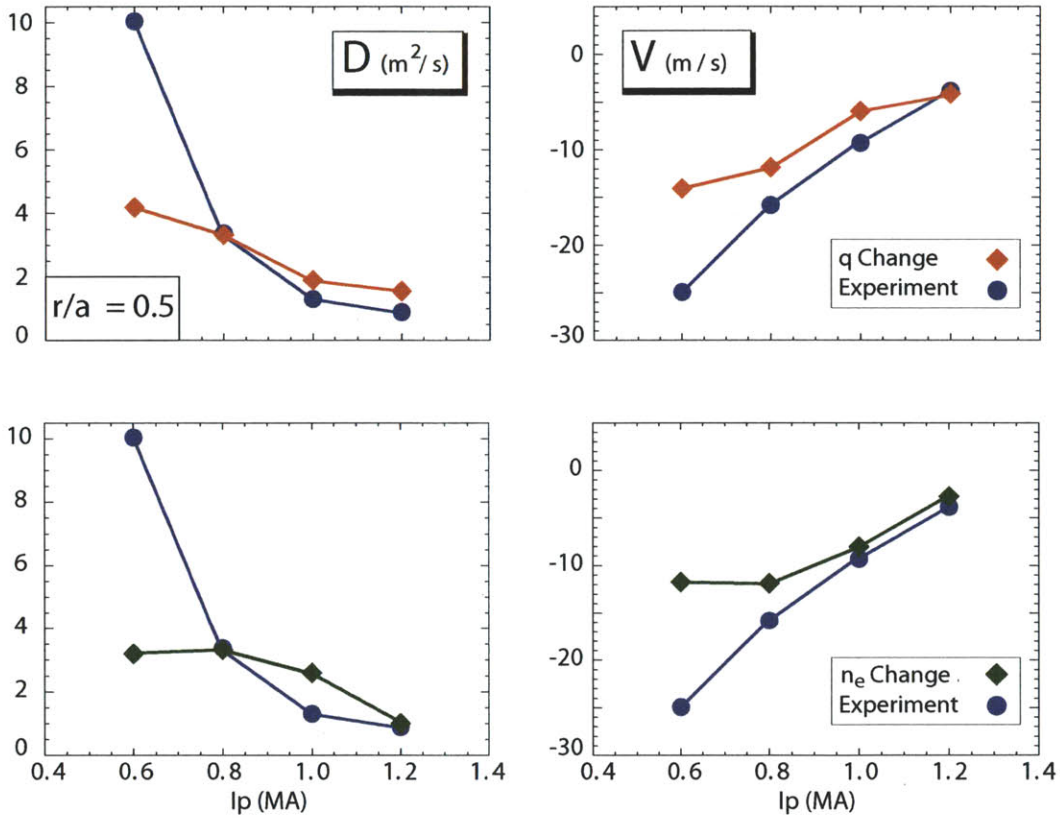

Figure 6-12: Attempts to reproduce the observed I_p trend through changes in single turbulence drive term changes are shown at $r/a = 0.5$. Electron density (and a/L_{n_e}) changes (c and d) result in a concave down trend of diffusion and a concave up trend of inward convection which does not agree with experiment. Safety profile changes better reproduce the trends in D and V, suggesting an important role of q in the observed I_p trend.

conclusions. Substitution of both the q and n_e profiles modifies the simulated impurity diffusion and convection and both modifications generally exhibit a decrease in

diffusion and inward convection with increased plasma current. However, n_e modification results in a concave down/up trend in decreased diffusion/inward convection which is opposite the experimental trend in diffusion and inconsistent with the approximately linear trend of the measured inward convection. In contrast, q profile changes produce a slightly concave up trend with plasma current and demonstrates an approximately linear trend in the simulated inward convection. This attempt to sort out the effect of individual profile changes on the observed I_p trend, does not provide a clear indication of the dominant physical change but suggests that q profile effects play an important role. However, it is most likely that the self consistent modification of the all plasma profiles is needed to best match the experimentally observed trend with I_p.

The ability of nonlinear gyrokinetic simulation to reproduce experimental profile shapes, as demonstrated in Figure 6-8, allows for a simplified quantitative comparison between experiment and the Q_i-matched GYRO simulations presented earlier in this section. Examining a single radial location of $r/a = 0.5$ allows for easier assessment of quantitative agreement or disagreement of all discharges simultaneously. Quantitative comparison of the measured and gyrokinetic simulated impurity transport coefficients is shown in Figure 6-13 as a function of I_p. Once again, it is observed that the exper-

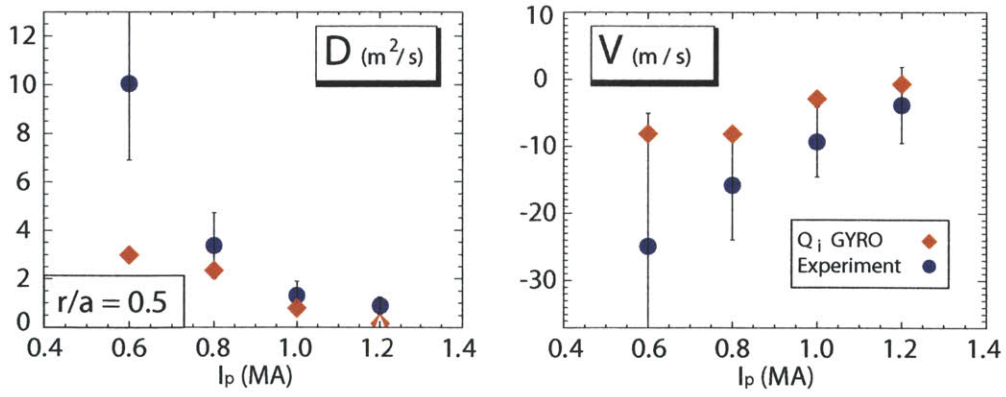

Figure 6-13: Nonlinear GYRO simulation (red) is compared directly with measured impurity transport coefficients (blue) at the radial location, $r/a = 0.5$ for all currents. Reasonable quantitative agreement is found between simulation and experiment for the 0.8, 1.0, and 1.2 MA discharges and the transport coefficient trends with I_p are well reproduced.

imental trends of decreased diffusion and inward convection with increased plasma current are well recovered by nonlinear gyrokinetic simulation. Furthermore, when experimental uncertainty in the measured transport is considered, general agreement is found in both D and V for the 0.8, 1.0, and 1.2 MA discharges. In all of these cases the values of diffusion and inward convection tend to be approximately 2x lower than the mean experimental values yet lie within experimental uncertainties. It should be emphasized here that the sensitivity analysis described earlier in this section was performed on the 0.8 MA discharge of the current scan and significant sensitivities to n_i/n_e, q and a/L_{T_i} were identified. Given a similar nature of the turbulence character for all discharges considered here, it is reasonable to expect similar sensitivities exist at all values of I_p. Therefore, quantitative agreement at each plasma current can most be improved within the experimental uncertainty in Q_i and other turbulence-relevant parameters. The 0.6 MA discharge is a unique case. The simulated value of impurity diffusion clearly disagrees with the experimental value and its uncertainty estimate in this discharge. The exact source of this discrepancy is unclear. However, we note the large uncertainties in the experimental impurity transport for this discharge which are the result of a slightly lower overall electron temperature profile, uncertainty in the T_e measurement, and the strong dependence of He-like calcium emission on T_e in this temperature range. Overall, it is observed that Q_i-matched nonlinear, gyrokinetic simulation is capable of reproducing the trend of decreased diffusion and inward convection with increased plasma current while demonstrating quantitative agreement with experiment in the 0.8, 1.0, and 1.2 MA discharges.

Chapter 7

Initial Results on the Input Power Dependence of Impurity Transport

In Chapter 6, experimental and gyrokinetic analysis of a dedicated I_p scan was presented. Motivation for dedicated experiments was provided by the new Alcator C-Mod impurity confinement time scaling (Equation 6-1) which indicates that the measured impurity confinement times are a function of both I_p and the total input power P_{tot}. This chapter describes the initial results from a dedicated experimental scan of P_{tot}. Experimental and gyrokinetic analysis attempts to shed light on the physics behind the observed P_{tot} dependence of impurity transport and serves to complement the existing results of the I_p scan.

7.1 Description of the Experiments

7.1.1 Experimental Setup of the P_{tot} scan

This section describes the experimental setup utilized during the P_{tot} scan and the summarizes the available diagnostic tools. As demonstrated by Equation 6-1, the dependence the impurity confinement time on the total power is a relatively weak, namely $P_{tot}^{-.15}$. Therefore, it is expected that significant modification of the total

input power would be required to generate a noticeable change in the inferred impurity transport coefficients. To achieve such a change, various levels of Ion Cyclotron Resonance Heating (ICRH) (hydrogen minority) were introduced into three separate plasma discharges. An approximately 3 fold increase in the total input power (P_{ICRH} = 1.0 , 2.5 , 3.3 MW) was obtained. The total input power, P_{tot} is equal to the sum of ohmic and auxiliary heating power, $P_{OH} + P_{ICRH}$. Time traces of some basic plasma parameters are shown in Figure 7-1. In an attempt to isolate the

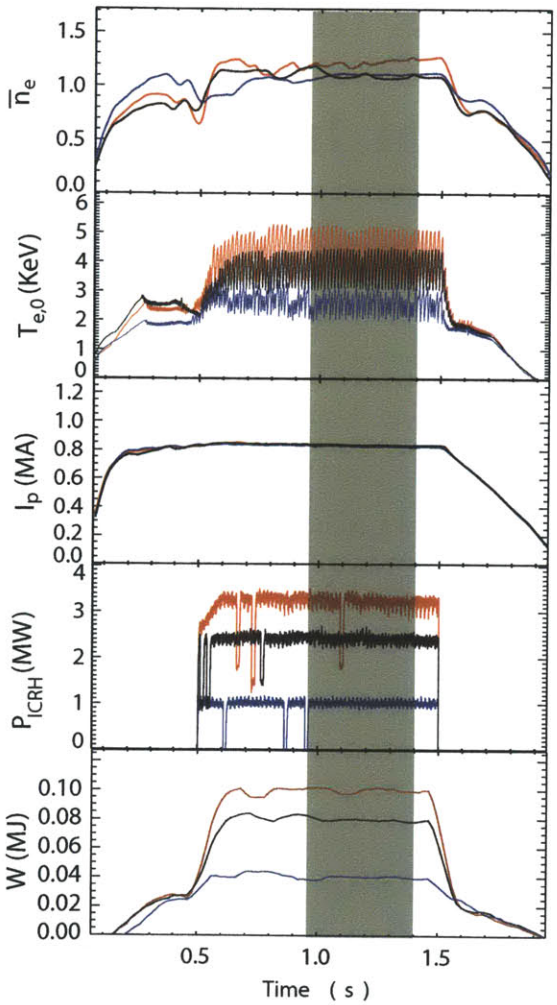

Figure 7-1: Time traces for line averaged density, core electron temperature, plasma current, and ICRH input power are shown for discharges in the P_{tot} scan. The shaded region indicates the approximate time region used for analysis.

effects of input power, these discharges were operated at approximately fixed central

density (1.5×10^{20} m^{-3}), plasma current (0.8 MA), toroidal magnetic field of (5.3 T), and plasma shape. Sawtooth activity is present throughout the discharges but the location of the inversion radius remains approximately fixed throughout the scan. To avoid transition to H-mode and maintain low particle confinement conditions, the discharges were operated in the upper single null (USN) configuration, with the ion ∇B drift away from the active x-point which tends to significantly raise the H-mode power threshold and therefore avoids the L to H transition at high input power levels. However, operation in these conditions can result in L to I-mode transition. Although no trace of the weakly coherent mode (WCM) is observed on the available fluctuation diagnostics (magnetics, PCI and reflectometer measurement), the highest input power discharge (3.3 MW) does show an edge electron temperature pedestal and values of H98 which reach or exceed a value of 1. These are two of the key characteristics for I-mode discharges [107]. It is clear that no transition to H-mode confinement (which is known to drastically affect particle and energy confinement) occurs but there are indications that the 3.3 MW plasma has transitioned into I-mode. The implications of the possible confinement regime transition from L to I-mode in these discharges will be discussed later in this chapter.

7.1.2 Description of Diagnostic Setup and Measurements

The diagnostic setup used during this scan was identical to that of the I_p scan described in the previous chapter. All discharges were optimized for the measurement of time-evolving He-like calcium profiles using the HiReX Sr. diagnostic and the single chord, Li-like calcium charge state measurement provided by the XEUS x-ray and EUV spectrometer. Four identical impurity injections of CaF_2 were introduced into each discharge at $0.765, 0.965, 1.165$, and 1.365 seconds. However, since stationary plasma conditions are needed for the experimental impurity transport analysis, only data from the last 3 injections were utilized. To allow for gyrokinetic analysis, all background density and temperature profile measurements were enabled (Thomson and all ECE systems). Argon puffing was performed during each discharge to resolve the ion temperature and toroidal rotation profiles. However, due to the high

electron temperatures reached, significant burnout of the He-like argon charge state (hollowing of the brightness profile) was observed for these discharges. This resulted in unreliable measurement of ion temperature and toroidal rotation near the plasma core ($r/a \leq 0.4$). Due to the relatively low operational density, the accuracy of the Bremsstrahlung based Z_{eff} measurement is uncertain. Therefore, all Z_{eff} values used during analysis were provided by the neoclassical calculation [99] with bootstrap current corrections.

7.2 Changes in Turbulence-Relevant Parameters with P_{tot}

In this section we look at changes in the drive and suppression terms for the turbulent modes thought to dominate impurity transport in the tokamak core (Ion Temperature Gradient Driven modes (ITG) and Trapped Electron modes (TEM)) which occur during the input power scan. Observation of these parameter changes provides insight into the possible changes in turbulence character which occur with increased P_{tot}. In the left hand column of Figure 7-2 (a-d) the measured profiles n_e, T_e, T_i and q during the input power scan are shown. The right hand column, Figure 7-2 (e-h), shows the corresponding turbulence drive terms over $0.4 \leq r/a \leq 0.75$. This region was chosen to best demonstrate the changes in the tokamak confinement zone, where reliable data is available and turbulence is thought to dominate. It is important to note again that accurate determination of the ion temperature profile in the plasma core was not possible for the highest input power discharges due to burnout of the measured argon charge state. Therefore, the plotted profiles are limited to regions where the data is believed to be reliable. Further discussion of the criteria used to defined the regions of profile inaccuracy and other data limitations can found at the end of this chapter. A modest change in the electron density gradient scale length, a/L_{n_e}, is observed from 1.0 to 2.5 MW but no change appears to occur between the 2.5 and 3.3 MW discharges. It should be noted that edge Thomson density and temperature

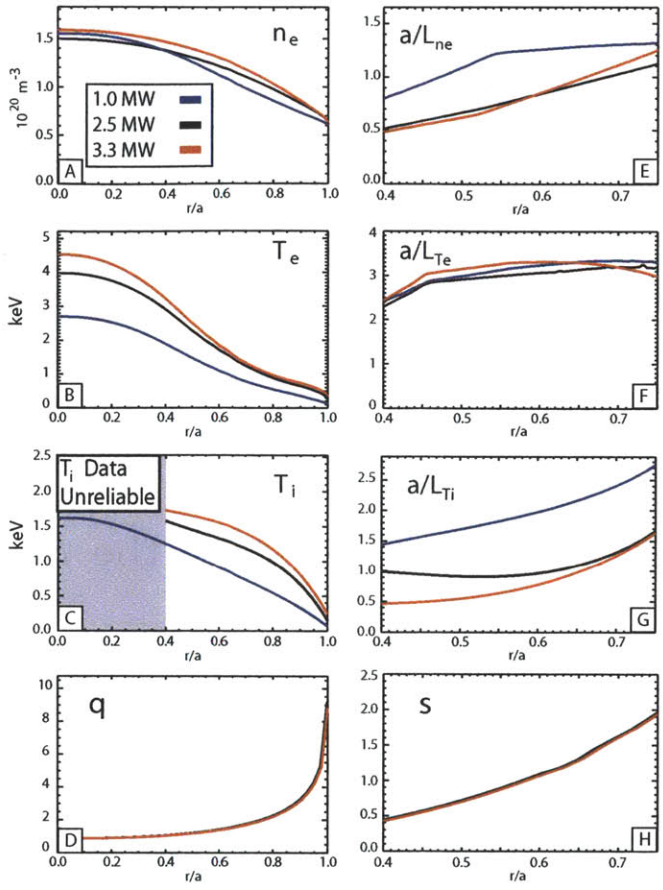

Figure 7-2: Plasma profiles (a-d) and their corresponding turbulence drive/suppresion terms are shown (e-h) for all discharges in the P_{tot} scan. Due to the burnout of the T_i measurement, data from the 2.5 and 3.3 MW discharges is unreliable inside of $r/a = 0.4$. The ITG drive term, a/L_{T_i} is found to decrease significantly with increased P_{tot}. Note the change of x-axis scale for plots e-h.

data were not available for the 2.5 MW discharge. Data from a similar discharge were inserted to allow for profile fitting of the electron density and temperature. These profiles should not be used outside of r/a=0.8. Despite an $\sim$ 2x increase in the central electron temperature which occurs due to increased total power, there is no significant modification of the electron temperature gradient scale length, a/L_{T_e}, or the magnetic shear profile, $\hat{s}$. This is in contrast to the changes observed in the measured ion temperature gradient scale length, a/L_{T_i}, which is found to significantly reduce with increasing input power as a result to both an increased magnitude of the ion temperature and a flattening of the temperature gradient in the confinement zone.

Reduction of the ITG drive term with increased power may lead to stabilization of the ITG-type turbulence and would be expected to result in significantly decreased turbulent particle transport. However, mostly unchanged TEM drive terms would suggest any significant TEM contributions would remain present or even be enhanced due to decreasing collisionality at high input power. A complete linear stability analysis of all three discharges was performed to best interpret the changes in the turbulence drive terms and investigate any possible changes in the character of the plasma turbulence which might occur.

7.3 Linear Stability Analysis of the P_{tot} Scan

To best understand if changes in the turbulence character occur due to the observed changes in turbulence-revelent parameters during the P_{tot} scan, the gyrokinetic code GYRO [92] was used. The analysis performed on these discharges was very similar to to that performed on the I_p scan. Figure 7-3 demonstrates the results of a full linear stability analysis performed on the three discharges in the total power scan. Two radial locations are shown in each figure, $r/a = 0.475$ and 0.6. Locations farther into the plasma core were omitted due to large uncertainty in the ion temperature profile measurement approaching the center of the plasma. Contours of the growth rate of the most unstable linear mode in the range $k_\theta \rho_s \sim [0.25 - 0.75]$ are plotted at the 2 radial locations for scans of a/L_{T_i} and a/L_{T_e} on the x and y axes respectively. Here we define $\rho_s = c_s/\Omega_{ci}$ as the sound speed gyroradius, $\Omega_{ci} = eB/m_i c$ as the ion gyro frequency, and $c_s = \sqrt{T_e/m_i}$ as the sound speed. As with the I_p scan stability presented in the previous chapter, the color scheme employed indicates low linear growth rates with darker colors and large linear growth rates with lighter colors. The selected $k_\theta \rho_s$ range was chosen to best display a shift from ITG to TEM-type turbulence in the low-k spectrum since these modes are often responsible for the dominant contributions to heat and particle transport. The solid white line indicates the boundary between modes rotating in the ion and electron diamagnetic drift direction and the + sign indicates the location of the experimental values of a/L_{T_e} and a/L_{T_i}

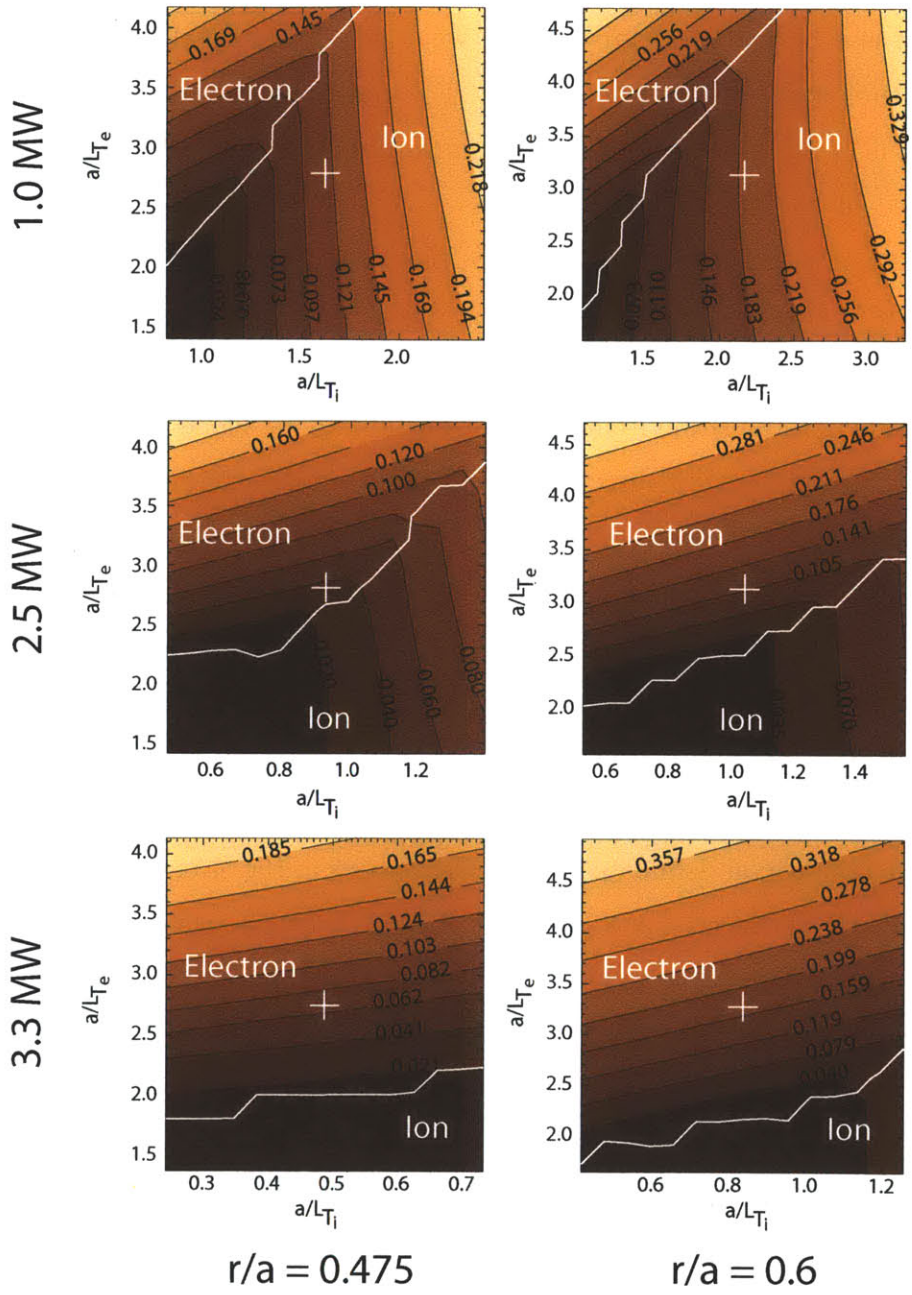

Figure 7-3: Contours of the growth rate of the most unstable linear mode are plotted for all 3 discharges in the P_{tot} scan. 2 radial locations, $r/a = 0.475$, and 0.6 are shown. The x-axis plots values of a/L_{T_i} and the y-axis plots values of a/L_{T_e}. The white line indicates the boundary between modes rotating in the ion and electron diamagnetic drift direction and the "+" sign indicates the experimental location.

at each radial location. It is found that both radial locations of the 1.0 MW heated discharge have the most unstable linear mode rotating in the ion diamagnetic drift direction and have a linear growth rate which is sensitive to the changes in the ion temperature gradient scale length, a/L_{T_i}. For this reason, we characterize the plasma as being ITG unstable at both locations investigated at 1.0 MW. This conclusion is supported by the negative real frequency, ω (+ for electron, - for ion diamagnetic drift direction), and linear growth rate, γ, plotted in Figure 7-4a for this discharge at $r/a = 0.475$. However, as the ICRH input power is increased to 2.5 and then to 3.3 MW, the reduction in a/L_{T_i} reduces the growth rate for the dominant ITG modes. This results in a transition from the most unstable linear mode rotating in ion to the electron diamagnetic drift direction. The location of the experimental point relative to the ion/electron drift direction boundary would suggest that the 2.5 MW case still has significant subdominant contributions provided by ITG turbulence. This is supported by the real frequency and growth rate spectrum shown in Figure 7-4b. This discharge classified as being in a mixed mode regime, where a combination of both ITG and TEM type turbulence contributes significantly to the overall transport level. Further increase in heating power to 3.3 MW pushes the experimental profiles firmly into the region dominated by modes rotating in the electron diamagnetic drift direction as demonstrated in Figure 7-4c. In this discharge, the most unstable linear mode at both $r/a = 0.475$ and 0.6 rotates in the electron diamagnetic drift direction and is unaffected by changes in the ITG driven term a/L_{T_i}. Instead they are sensitive to changes in the TEM drive term, a/L_{T_e}. The value of η_e for this discharge is $\eta_e \geq 4$ at both locations which using the definition stated by Ernst [108] implies the plasma is electron temperature gradient TEM dominated.

The change in the turbulence character from and ITG dominated plasma at low input power values (1.0 MW) to high input power (3.3 MW) is best demonstrated in Figure 7-5. Since it was demonstrated in Figure 7-2 that is was predominately the ITG drive term, a/L_{T_i} affected during the P_{tot} scan, the map of a/L_{T_e} and a/L_{T_i} stability space is approximately identical for all discharges within the scan. Therefore, the linear stability results obtained from the 1.0 MW discharge are, to good approx-

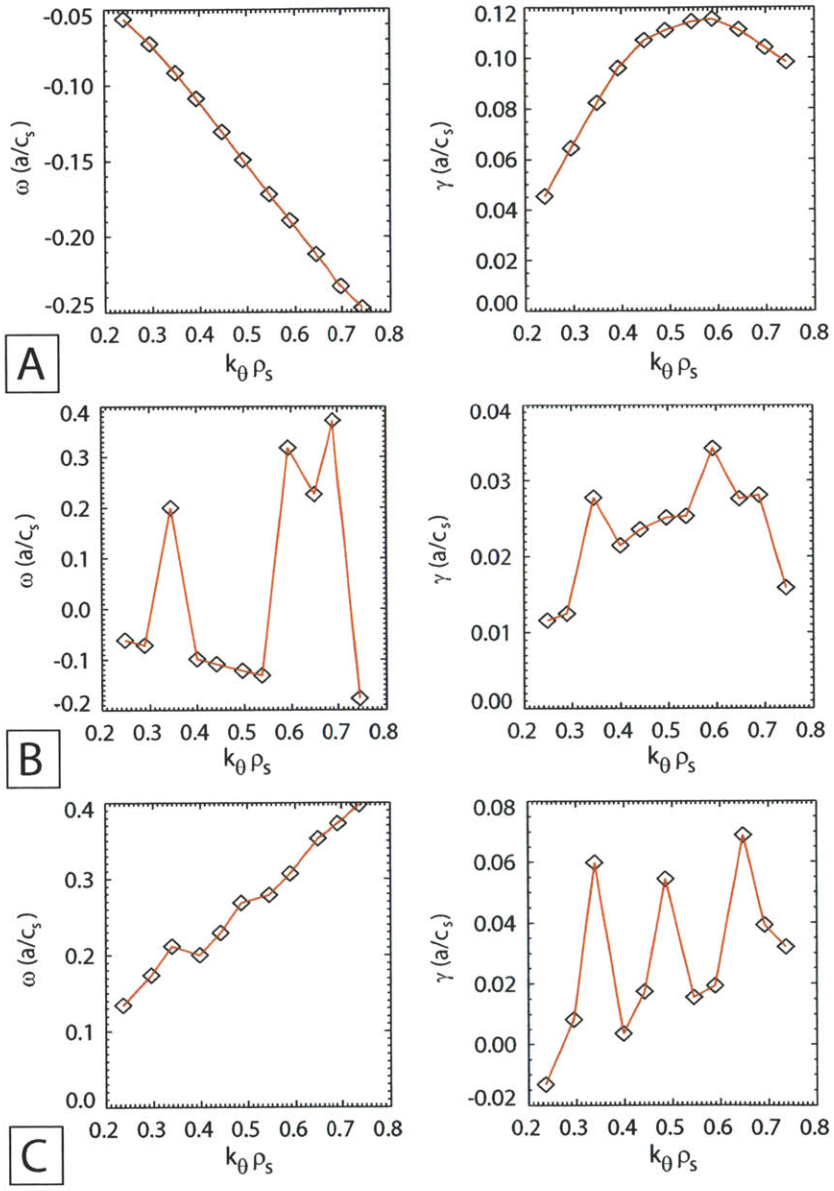

Figure 7-4: The real frequency, ω,(+/− = electron/ion direction) and growth rate, γ, obtained from linear GYRO analysis for the 1.0 (a), 2.5 (b), and 3.3 (c) MW discharge is shown as a function of $k_\theta \rho_s$ at $r/a = 0.475$

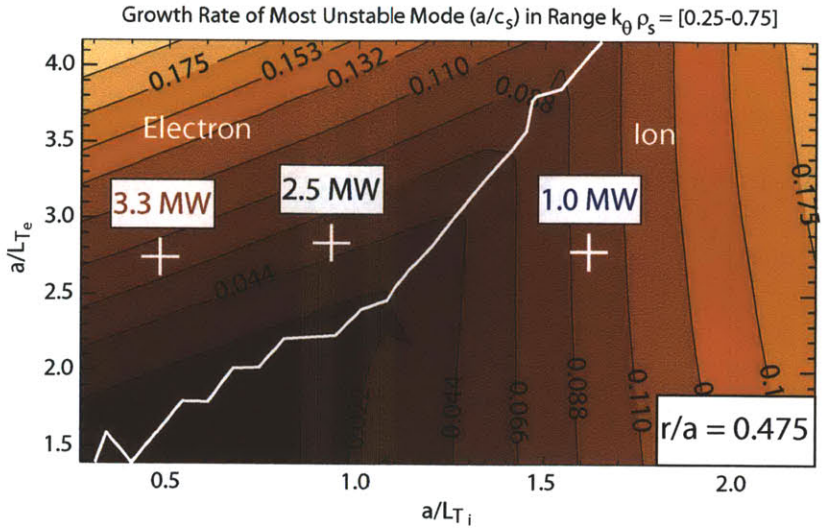

Figure 7-5: Contours of the growth rate of the most unstable linear mode are plotted which are approximately correct for all 3 discharges in the P_{tot} scan at a radial location of $r/a = 0.475$. The x-axis plots values of a/L_{T_i} and the y-axis plots values of a/L_{T_e}. The white line indicates the boundary between modes rotating in the ion and electron diamagnetic drift direction and the "+" sign indicates the experimental location. The transition from ITG to TEM-type turbulence which occurs during the P_{tot} scan is clearly visible.

imation, representative of the stability results for the 2.5 and 3.3 MW discharges. Figure 7-5 demonstrates an expanded version of the stability plots shown in Figure 7-3 which includes a wide range of a/L_{T_i} values at a radial location of $r/a = 0.475$. The experimental values of the 1.0, 2.5, and 3.3 MW cases are over plotted on this stability map to best demonstrate the transition from ITG to TEM type turbulence which occurs with increased input power.

7.4 Experimental Observations of P_{tot} Dependent Core Impurity Transport

Using the synthetic diagnostic and iteration techniques developed around the impurity transport code STRAHL, the methodology described in Chapter 4 was used to extract impurity transport coefficient profiles for all discharges in this scan. Impurity transport coefficient profiles in the radial region $0.0 \leq r/a \leq 0.6$ are shown in Fig-

ure 7-6. The error bars were derived through the Monte Carlo approach described

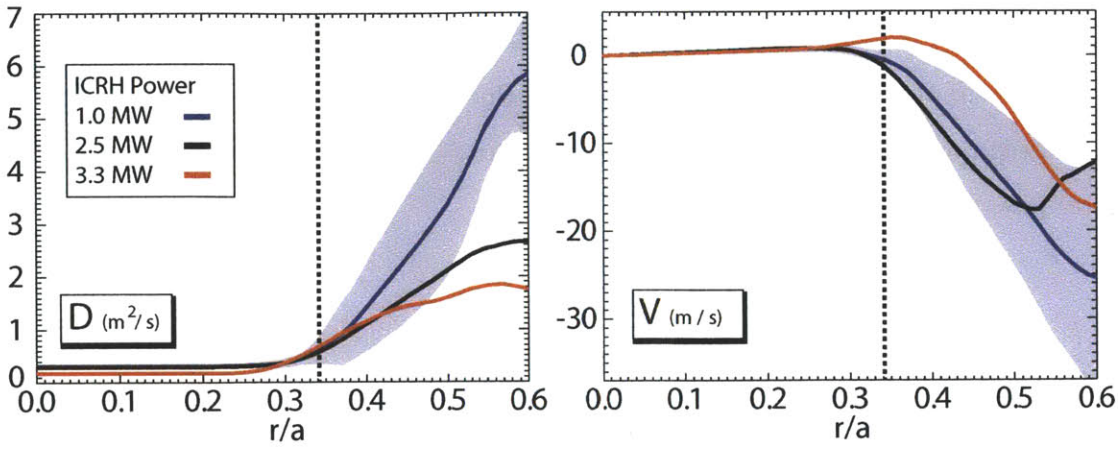

Figure 7-6: The experimentally derived impurity transport coefficients are plotted for all discharges in the P_{tot} scan. The measured impurity diffusion coefficient (a) is found to decrease significantly with increased total power while no significant trend is observed in the convective velocity (b). Representative errors bars are shown on the 1.0 MW discharge. The vertical dashed line indicates the approximate location of the sawtooth inversion radius.

in Chapter 4 and are plotted on the inferred transport coefficients for only the 1.0 MW discharge. These errors are representative of the relative uncertainty in all discharges presented here. The dotted line plotted indicates the approximate location of the sawtooth inversion radius for these discharges. The existence of two distinct regions of impurity transport is once again demonstrated in these results. Inside of the inversion radius, we find low levels of diffusion and convection. As discussed in Chapter 6, transport in this region is dominated by sawtooth activity and exhibits turbulence drive terms which are insufficient for exciting most turbulent modes and for driving significant particle transport. Outside of this region, the magnitude of both the inferred diffusion and convective velocity increase significantly. Large values of the diffusion and convection are observed, peaking at approximately 5.8 m^2/s for the diffusion coefficient and around 25 m/s for the convective velocity. Both of these values are found in the 1.0 MW discharge. Increasing the total power to 2.5 and 3.3 MW results in approximately 2x and 3x reductions in the measured diffusion coefficient are observed in the outer regions of the measurement ($r/a \geq 0.5$). However, this

is not accompanied by a corresponding reduction in the measured convective velocity. Outside of experimental uncertainty, the inferred convective velocity demonstrates no clear trend with increased total power. The measured reduction in the diffusion coefficient implies an increase in the mean value of the peaking factor occurs with increasing power and steeper steady state impurity density profiles at higher levels of total power.

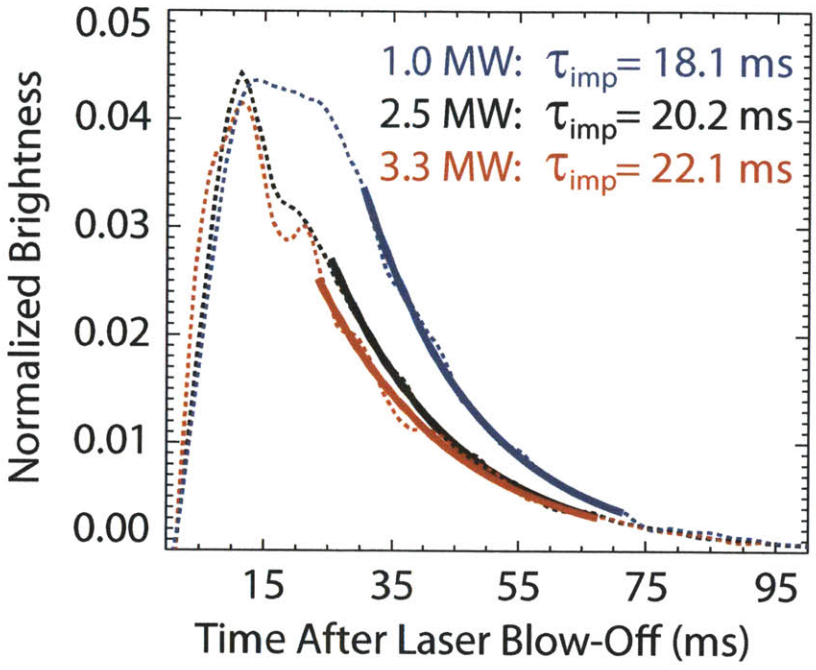

Figure 7-7: The brightness time histories of impurity injections (Ca^{18+} emission) into the 1.0, 2.5, and 3.3 MW discharges are shown by dashed lines. The measured confinement times, with the exponential fits shown as solid lines, are found to slightly increase with increased input power.

As demonstrated in Figure 7-7, there is a slight increase in the measured impurity confinement time (as determined by Ca^{18+} emission) which occurs with increased input power. An increase in the measured impurity confinement time is expected from a reduction in impurity diffusion at approximately fixed inward convection. Since there is a factor of 3 decrease in the experimental diffusion coefficient (from

r/a=0.5 to 0.6), one might expect a significant increase in the overall confinement time with input power. However, the impurity confinement time is a global quantity and only partial profiles of the impurity transport coefficients ($0.0 \leq r/a \leq 0.6$) are determined here. Given the observed changes in the edge (the development of a temperature pedestal at high input power), which imply changes in the turbulence, it is reasonable to believe that there are changes in the impurity transport which occur outside $r/a = 0.6$ and affect the impurity confinement time. As demonstrated by Figure 7-8, determination of the impurity confinement time from the Ca^{17+} (Li-like) emission actually supports this idea. Emission from the Li-like charge state comes

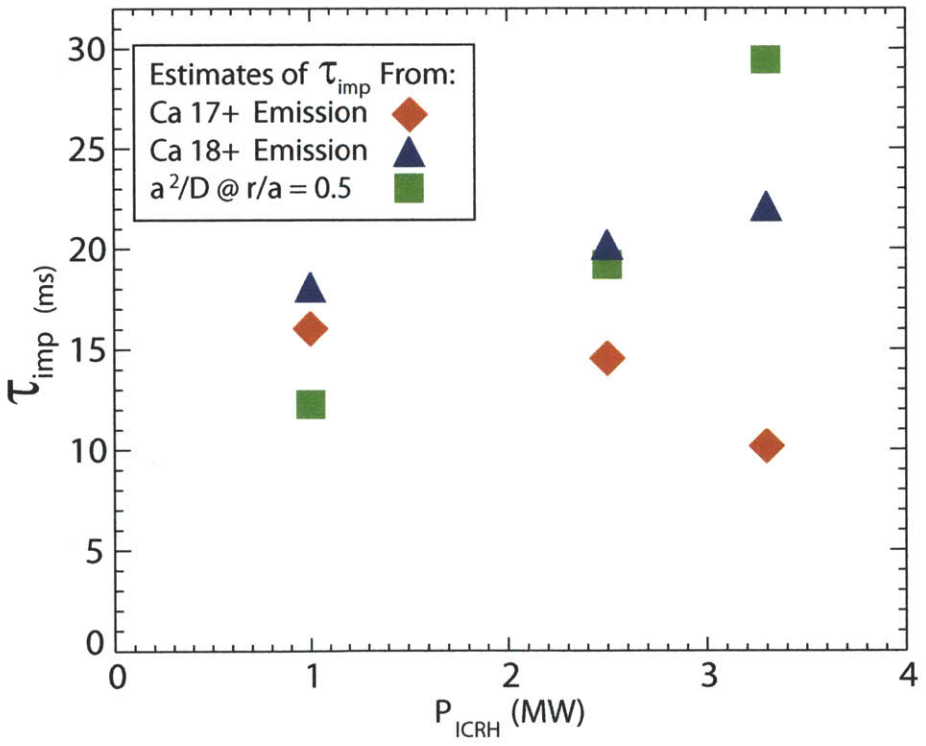

Figure 7-8: The measured confinement times derived from measurement of Ca^{18+} and Ca^{17+} emission compared to a simplistic estimate of the confinement time based on the experimental diffusion coefficient at r/a=0.5.

primarily from outside the region of Ca^{18+} emission and is therefore more sensitive to changes in edge transport. In contrast to the slight trend of increased impurity confinement observed from He-like calcium emission, a decrease in the Li-like calcium impurity confinement time with increasing input power is found. This is suggestive

of enhanced edge particle transport in the high (2.5 and 3.3 MW) input power discharges relative to the low (1.0 MW) input power discharge and could explain why the changes in the derived confinement times from He-like emission are much less dramatic than what would be expected by a factor of 3 decrease in the measured diffusion (as seen from r/a= 0.5-0.6).

It should also be noted that the slight increase in the measured impurity confinement times for theses discharges is inconsistent with the weak $P_{tot}^{-.15}$ dependence discussed earlier in this chapter. However, it is unclear whether or not direct comparison of these discharges is entirely justified as a measure of P_{tot} dependent changes in standard L-mode impurity transport. As discussed earlier in this chapter, there are some indications that the high input power discharges may transition to the enhanced confinement I-mode regime. The low particle confinement characteristics of this regime make it difficult to distinguish from standard L-mode discharges. Furthermore, the behavior of discharges operated in the unfavorable ∇B drift direction appears to exhibit some fundamental differences from standard discharges operated in the favorable ∇B drift direction, namely a lack/reduction of power degradation of the energy confinement when operating in unfavorable ∇B drift direction. The differences between these two categories of discharges are under investigation in the context of ongoing I-mode research efforts on Alcator C-Mod.

7.5 Discussion of Data Quality and Preliminary Nonlinear Simulation

Due to the lack of reliable T_i and V_ϕ data available for the high powered discharges, extension of this analysis from simple linear gyrokinetic to the full nonlinear gyrokinetic simulation was not thoroughly pursued. As was discussed in Chapter 3, both ion temperature and toroidal rotation profiles are obtained from inversion of HiReX Sr. line integrated H-like and He-like argon brightness measurements. However, to obtain the necessary impurity transport data the H-like argon crystal was removed and only

the He-like argon data was available for these experiments. The high electron temperatures obtained during this scan resulted in "burnout" of the He-like argon charge state. This refers to the hollowing of the brightness profile at the plasma core which negatively effects the inversion routines used to generate ion temperature and toroidal rotation profiles. An example of this charge state burnout is shown in Figure 7-9. Here, the measured HiReX Sr. He-like argon brightness profiles from the 1.0, 2.5, and

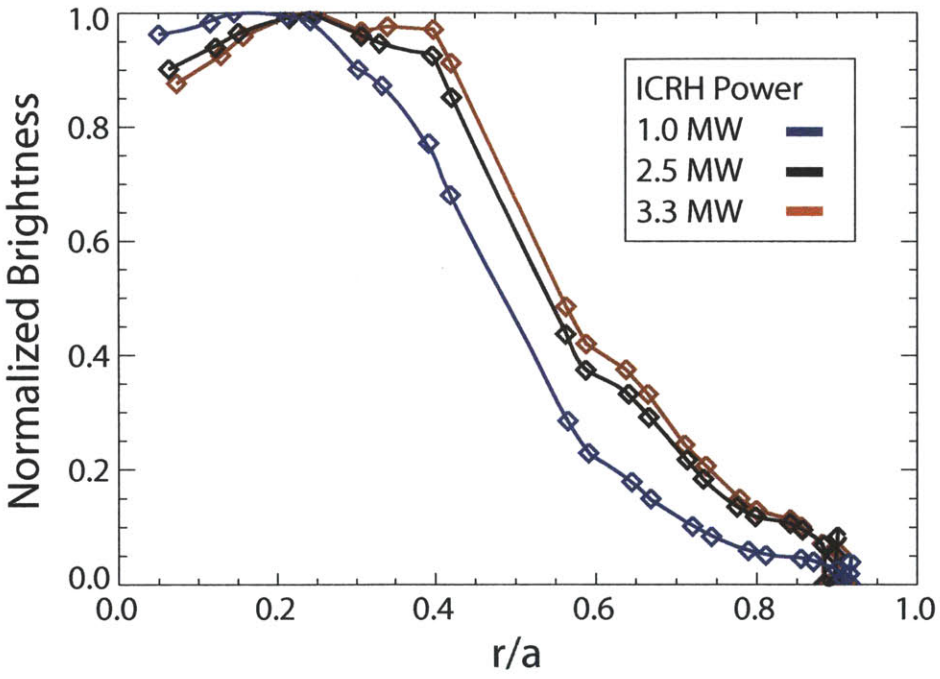

Figure 7-9: The measured HiReX Sr. argon brightness profiles for the 1.0, 2.5 and 3.3 MW ICRH discharges are shown. Notice the off axis peaking of the brightness profiles and the hollowing of the profile inside of the peak for the high input power cases.

3.3 MW discharges are plotted as a function of radius. Data from these runs is only assumed to be reliable outside of peak in the measured argon brightness. However, at this point it is still unclear if effects of the burnout propagate to radii outside of this location. In the 1.0 MW discharge the peak of the bright profile occurs near the plasma center but shifts outwards with increasing electron temperature to $r/a \sim 0.25$ at 2.5 MW and $r/a \sim 0.3 - 0.4$ at 3.3 MW. In light of the sensitivity analysis of gyrokinetic calculation presented in Chapter 5, it is clear that large uncertainty in

the ion temperature and its gradient scale length can easily lead to uncertainty in nonlinear simulation results exceeding 100%, making such simulations uninformative. As a result, only preliminary investigation of the high input power shot (3.3 MW) was performed with nonlinear simulation and linear simulation was limited to outside of the peak in the measured argon brightness profile.

Preliminary nonlinear simulation results of the 3.3 MW discharge provide some useful insights for future work. Using only the experimental profiles, low-k (up to $k_\theta \rho_s \simeq 1.0$), nonlinear gyrokinetic simulation was performed. This simulation resulted in extremely low levels of both ion and electron heat flux relative to the experimental values ($\sim 1/10^{\text{th}}$). It was found that large (up to $\sim 75\%$) increases above the experimental values of a/L_{T_i} were required to obtain simulations with heat flux approaching the experimental values. In light of the results presented in Chapter 5 and earlier in this chapter, this result is unsurprising. The linear stability analysis indicates that the 3.3 MW discharge is dominated by TEM turbulence. Therefore, simulation of low-k, ion-scale turbulence is not be expected to accurately predict the experimental heat fluxes. Additional simulations were performed which included contributions from $k_\theta \rho_s$ up to ~ 2.5 and 16 toroidal modes. Combined with modest increases ($\sim 20\%$) in a/L_{T_e} and a/L_n, these simulations began to approach experimental levels of electron heat flux and very low levels of impurity transport ($D < 0.4$ m^2/s and $V < 1$ m/s) were predicted. No additional simulations of this discharge were performed since validation quality results could not be achieved due to the experimental uncertainty in the ion temperature profile. However, these preliminary results indicate that multi-scale (low and high-k) simulations are most likely required for accurate simulation of this discharge. These simulations are computational extremely demanding and are out of the scope of this thesis work.

Chapter 8

Summary, Conclusions, and Future Work

8.1 Summary of this Thesis

The preceding chapters presented the development of new diagnostic tools, the experimental determination of impurity transport with realistic uncertainty estimates, and the first quantitative comparison of experimental impurity transport with nonlinear gyrokinetic simulation. This chapter provides a brief summary of the last 7 chapters and a discussion of possible future work in impurity transport and model validation.

The growing need for the study and understanding of impurity transport was described in detail in Chapter 1. Motivation for impurity transport investigation is provided by the need for dense, clean, fusion plasmas which exhibit long energy confinement times. An understanding of both the engineering dependencies of impurity transport as well as the physical mechanisms which dictate the measured transport levels is required for effective impurity control and, more broadly, for achieving the ultimate goal of a first principles predictive transport model.

Theoretical and experimental investigation of impurity and particle transport has existed since the first studies of magnetically confined fusion plasmas. As described in Chapter 2, classical collisional transport is modified by the toroidal geometry of tokamaks leading to the neoclassical transport model. However, even neoclassical

transport levels are much to small to explain impurity transport observed under most experimental conditions. It is believed that the "anamalous" transport levels found in almost all experiments are the result of drift wave type turbulence such as the candidate modes described in Chapter 2 (ITG, TEM, and ETG). Reduction of the Maxwell-Boltzmann equations to a 5-D set of equations known as the gyrokinetic-Maxwell equations is believed to capture the physics of the relevant spatial and temporal scales needed to describe drift wave turbulence and can be solved numerically with present day supercomputing facilities.

A wide variety of diagnostic tools are available for the study of impurity transport on Alcator C-Mod. As part of this thesis work, a novel, multi-pulse laser blow-off system was designed and constructed to allow for multiple impurity injections of trace, non-recycling, non-intrinsic impurities into the plasma. This system achieved all of its design goals and provided ideal measurement conditions for the study of impurity transport in the plasma core. A novel x-ray crystal spectrometer measurement provided time evolving, profile measurement of a single impurity charge state. These tools, coupled with accurate measurement of background plasma profiles, provided a unique environment which allowed for one of a kind experimental and gyrokinetic simulation comparisons.

A new approach to the determination of experimental impurity transport coefficient profiles ($0.0 \leq r/a \leq 0.6$) with realistic uncertainty estimates was developed for this work. A novel synthetic diagnostic was developed around the impurity transport code STRAHL to minimize differences between measured and synthetically modelled signals and to evaluate the propagation of uncertainty from the experimental profile and spectroscopic measurements to the inferred impurity transport. Realistic estimates of experimental uncertainty paved the way for detailed quantitative comparison with gyrokinetic simulation of turbulent impurity transport. Along the same lines, the propagation of uncertainty from profile measurements and RF absorption models to estimated uncertainty ranges of the power balance values of the ion and electron heat fluxes was also evaluated. These values were held up for comparison against output fluxes from the gyrokinetic code GYRO, making an assessment of their un-

certainty critical.

Using the unique tools developed as part of this work and the existing capabilities of C-Mod, the first quantitative comparison of experimental impurity transport with nonlinear gyrokinetic simulation was completed. An exhaustive analysis was performed on a standard, Alcator C-Mod, L-mode discharge. The neoclassical transport code, NEO, was used to definitively show that neoclassical transport levels are insufficient for explaining the experimental impurity transport levels in the core of Alcator C-Mod. The experimental results demonstrate the existence of two distinct regions, inside and outside of the sawtooth inversion radius. These regions of MHD and turbulence driven transport, exhibit low and high levels of diffusion respectively. Linear GYRO simulation of this discharge indicates the presence of ITG-type, low-k turbulence across the region of interest for gyrokinetic investigation, $0.3 \leq r/a \leq 0.6$. Initial nonlinear simulations were performed up to $k_\theta \rho_s \simeq 1.15$ and included small modification to the experimental ion temperature profiles such that the GYRO simulated total heat flux ($Q_e + Q_i$) matched the power balance value. It was found that the experimental diffusion, inward convection, and the peaking factor V/D were generally well reproduced by gyrokinetic simulation within the calculated experimental uncertainty.

The sensitivity of the gyrokinetic simulated impurity transport coefficients to uncertainties in a wide range of turbulence-relevant parameters was also investigated. These parameters included: a/L_{T_i}, q, n_i/n_e, a/L_{T_e}, a/L_n, T_e/T_i, and $\gamma_{E\times B}$. The dominant sensitivities were found to the quantities, a/L_{T_i}, q, and n_i/n_e as expected from theory. It was demonstrated that modifications to each of these terms can result in significant modification of the simulated impurity transport coefficient profiles. Within the uncertainty in the experimental values of the total heat flux, these drive terms can be modified (within error bars) to improve agreement between simulation and experiment. However, in each Q_{tot}-matched simulation it was observed that the GYRO simulated ion heat flux exceeded its experimental value to compensate for a systematically underestimated electron heat flux. This observation motivated simulations where the experimental values of a/L_{T_i} were modified within error bars to

match the GYRO simulated ion heat flux to the experimental value, ignoring the electron heat flux. These Q_i-matched simulations were found to exhibit agreement within error bars with the experimental values of ion heat flux and both impurity transport coefficients over a majority of the simulation domain. The systematically low electron heat flux could be attributed to the lack of simulated high-k turbulence or could indicate missing electron dynamics. The simultaneous matching of the ion heat and impurity particle transport channels in Q_i-matched simulation motivated their use in this work.

During the 2009 and 2010 run campaigns, over 300 impurity injections were introduced into a variety of Alcator C-Mod L-mode plasmas. The measured impurity confinement times were fit to a power law scaling which indicated a dependence of impurity confinement on P_{tot}, B_T, and I_p. The strong dependence of this scaling law on plasma current ($\tau_{imp} \propto I_p^{.68}$) motivated a dedicated scan of L-mode plasma discharges which used the newly developed techniques to extract impurity transport coefficient profiles. During a scan of plasma current from 0.6 to 1.2 MA at fixed density, field, and input power, decreasing values of both experimental diffusion and inward convection were found. In the confinement zone, a doubling of plasma current resulted in a factor of ~ 7 decrease in the experimental diffusion coefficient with a factor of ~ 3 reduction in the experimental inward convection. Linear GYRO simulation of these discharges suggested no significant change occurred in the character of the low-k turbulence during the scan and that all plasmas could be classified as ITG dominated. Nonlinear, Q_i-matched GYRO simulation was performed for the discharges in the plasma current scan. It was found that nonlinear simulation was able to both qualitatively and quantitatively reproduce the experimental trends and values of the impurity transport coefficient profiles, within experimental uncertainties, for the 0.8, 1.0, and 1.2 MA discharges. This work represents the first simultaneous agreement of gyrokinetic simulated impurity particle and ion heat transport with experiment.

Additional investigation into the physics dictating the dependence of measured impurity confinement on input power was also performed. A dedicated scan of input power was performed at fixed density, toroidal field, and plasma current to attempt

to sort out the physics of this dependence. Three discharges were performed with different levels of ICRH input power (1.0, 2.5, 3.3 MW). The determined impurity transport coefficient profiles demonstrated a significant reduction the experimental value of the diffusion coefficient outside of $r/a \sim 0.5$. In this region, an $\sim$ 3x reduction was found between the low (1.0 MW) and high (3.3 MW) input power discharges. In contrast, outside of experimental uncertainty, there was no measured reduction in inward convection occurred during this scan. A linear stability analysis was performed on the discharges in the input power scan. The low input power discharge was found to be ITG dominated, but as the total input power increased, the plasma demonstrated a transition from ITG to TEM dominated. This fundamental change in the character of the plasma turbulence presents a unique opportunity for testing turbulence models. However, due to poor data quality obtained inside of $r/a = 0.4$ for the high input power discharges, only preliminary nonlinear simulation of the high input power discharges was attempted. These simulations suggest that high-k, electron scale turbulence simulations are needed to match the experimental values of heat flux in high input power discharges.

8.2 Future Work

The work presented in this thesis represents another step in understanding the changes in turbulence which affect measured impurity transport levels and a first step in the validation of the gyrokinetic model of impurity transport. The results of this work should motivate additional investigation into impurity transport experiment and simulation on Alcator C-Mod and around the world. Here we briefly discuss future work in the fields of impurity transport and transport model validation on Alcator C-Mod.

The design and construction of the multi-pulse, laser blow-off system complemented an existing set of tools used to study of impurity transport on Alcator C-Mod. The current suite of spectroscopic diagnostics is arguably one of Alcator's strengths. The unique x-ray crystal spectrometer used in this work allowed for unique measurements of a single charge state of calcium with good spatial and temporal resolution.

However, the measurements of this spectrometer were limited such that accurate impurity transport measurements could only be obtained inside of $r/a \simeq 0.6$. It was found as part of this work that gyrokinetic simulation generally reproduces experimental impurity transport levels between $\sim 0.3 \leq r/a \leq 0.6$. However, previous application of the gyrokinetic model outside of $r/a \leq 0.6$, in the so called plasma transition zone ($0.6 \leq r/a \leq 0.85$), indicates that the model fails to accurately predict heat transport levels. To date, no comparisons of impurity transport experiment with simulation have been performed in this region. Proposed modifications to the XEUS x-ray spectrometer seek to expand its capabilities and allow for radial profile coverage of plasma emission in this region. Combined with the measurements of the x-ray crystal spectrometer and the appropriate line emission data, this should allow for the measurement of multiple charge states of injected calcium and provide effective coverage of the plasma throughout the transition zone. These combined measurements would serve to greatly constrain the experimentally derived impurity transport coefficient profiles and allow for a more comprehensive comparison of experimental impurity transport with gyrokinetic simulation to be performed.

The discussion of Q_{tot} and Q_i-matched gyrokinetic simulation presented in Chapter 5 of this thesis motivates additional simulation work. It was demonstrated that when Q_i-matched GYRO simulation was performed, agreement between experimental and simulated values of impurity transport and ion heat flux can be obtained within experimental uncertainty. However, an unexplained discrepancy in the electron heat flux persisted in both Q_{tot} and Q_i-matched simulation. The natural extension of this work is to attempt to understand and resolve this discrepancy. It is possible that the presence of high-k TEM and ETG type turbulence could represent the missing contributions to the electron heat flux. Due to the predominately low-k nature of the presented simulations, the dynamics of this type of transport is not fully resolved and could play a significant role in quantitative agreement of electron heat flux while leaving the ion-scale dynamics basically unchanged. In order to address this issue, the GYRO Q_i-matched simulation presented in Chapter 5 will be the subject of further investigation using high fidelity, multi-scale GYRO simulations.

It is often both desirable and difficult in tokamak experiments to change the character of the plasma turbulence. However, in light of the preliminary analysis presented in Chapter 7, The simple method of increasing input power in moderate density discharges appears to provide such an opportunity. These discharges allow for rigorous testing of cutting edge transport models, such as the gyrokinetic model, in conditions dominated by fundamentally different types of turbulence. More specifically, these conditions can provide testable predictions for the leading theoretical models which predict different particle and heat transport in response to different types of dominant turbulence. However, as discussed in Chapter 7, the data available from the input power scan was not of high enough quality to motivate significant nonlinear gyrokinetic work. At this time, experiments have been proposed on Alcator C-Mod which were motivated by the RF dependent impurity transport results and seek to both repeat and fill in the gaps present in this initial dataset with the highest quality impurity transport, ion temperature, and rotation data possible. This dataset would allow for the direct comparison of impurity transport in ion and electron dominated regimes and allow for the ability of nonlinear gyrokinetic simulation to accurately predict heat and particle transport levels in both of these turbulent regimes to be tested.

Appendix A

Laser Blow-Off Hardware and Control Systems

Chapter 3 of this thesis presented the basic layout of the multi-pulse laser blow-off system's optical, vacuum, and electronics systems. The focus of this appendix is to provide reference detail of the laser blow-off system, particularly in aspects pertaining to the control systems, electronics for laser timing, beam steering, and data acquisition.

A.1 Electronics Setup of the Laser Blow-off System

The laser blow-off system is controlled by two main electronic systems. These systems are a rack mounted PLC controller and a CPCI crate. This section will overview these systems and their function in the laser blow-off system operation.

The PLC is located in the impurity injector rack in the Alcator C-Mod cell (shown in Figure A-1). This controller runs a simple ladder logic program which is charged with monitoring the impurity injector systems. All vacuum controller components (convectron gauges, ionization gauge, turbo pumps) are controlled through the PLC's DC and AC output modules and are monitored using the analog input module. Out-

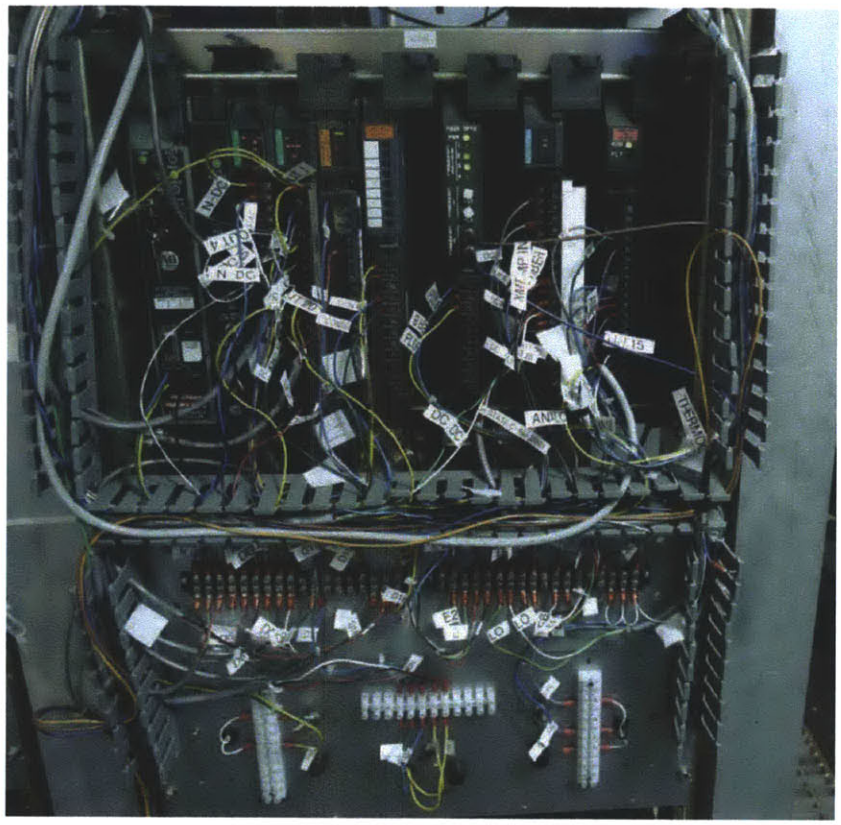

Figure A-1: A picture of the PLC electronics setup is shown.

put from the PLC is used to control the in-line valve (separating the main beamline from the foreline) as well as the mechanical and turbo pumps. Built into the PLC programming are a series of safety features which check the vacuum pressures and turbo pump operation to avoid damage to the system. If activated, these systems close the in-line valve and begin a controlled shutdown of the pumps. On a day to day basis, very little direct interaction is involved with the PLC electronics setup. All of the PLC systems are controlled via the RSVIEW GUI which will be described in the following section.

Laser triggering, piezo-electric mirror mount movement, and data acquisition is achieved using the CPCI crate and associated backplane electronics. A picture of these systems mounted in the electronics rack is shown in Figure A-2 The CPCI crate consists of three main components: A 32 channel digitizer, a timing module, and an analog output module. The timing module provides the necessary clock and trigger

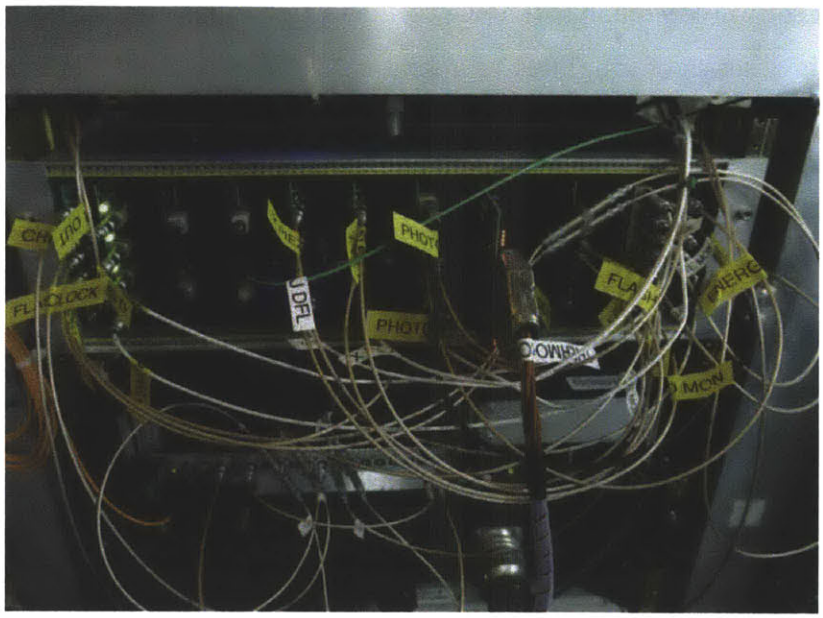

Figure A-2: A picture of the CPCI electronics and backplane is shown.

for the digitizer as well as a series of clocks used for laser timing. The 32 channels of the digitizer are connected to an electronics backplane which provides double pin LEMO connections for each channel. All signals are passed to these connections to collect all the necessary information for diagnosing the system's performance. Signals used to control the timing, laser triggering, and beam positioning are teed off and input into the electronics backplane for input into the digitizer. Additionally, a 16 channel analog output module is connected directly to the electronics backplane and allows for 0-10 V signal generation. These outputs are used to both drive the piezo-electric mount and to provide the necessary gated signals for laser triggering. The details of the piezo-electric system and the laser triggering will be explained in more detail later in this appendix.

A.1.1 The Remote Interfaces for the Electronic Systems

Two separate interfaces were developed for the remote operation of the impurity injector electronics. The PLC controller housed in the Alcator C-Mod cell is controlled via the RSVIEW software installed the laser blow-off computer located in the control

room. This software, similar to Labview, allows the user to interact with the PLC controller via a series of graphical representations. A picture of the RSVIEW GUI designed to control the impurity injector is shown in Figure A-3. Most of the features of this interface are self explanatory. From this screen, the operator can control all of the impurity injector vacuum systems, monitor the vacuum pressure via ionization and convectron gauges, and monitor the turbo pump operation. A built in heating tape system, for vacuum baking, is also controllable from this interface. This system

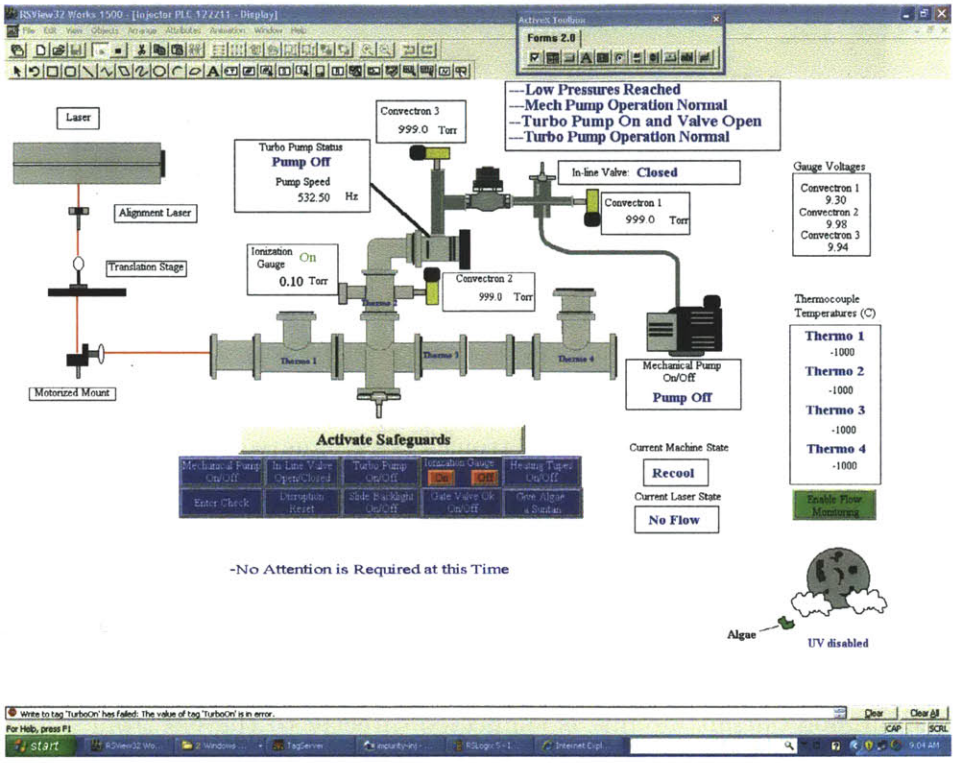

Figure A-3: A picture of the PLC GUI is shown. It should be noted that the system is disconnected in this picture so the measurements are meaningless.

consists of four thermocouple gauges and four heating tapes which are fed into a feedback system. Each thermocouple monitors the local temperature and increases the current in the corresponding heating tape until a temperature of approximately 90 degrees Celsius is reached. To avoid unsafe conditions, the tapes are shut off if any temperature exceeds 100 degrees Celsius. There are several additional safety systems which can be monitored through this interface as well. If the pressure measured by the convectron gauges rises to approximately 100 mTorr, the inline valve will close,

and the pumps will turn off. To warn of possible pump malfunction, indicator messages will appear if the rotation frequency of the turbo pump decreases to below 1400 Hz as well. The last feature added to this system involves control of UV lamp which was installed in the impurity injector's coolant loop. This lamp is operated during periods of machine down time to ensure that the laser's coolant loop remains free of algae and other microorganisms.

Setup of the laser timing and piezo-electric beam steering is controlled via an IDL interface. The control widget for these systems can be found in:

/user/local/cmod/codes/transport/run_imp_inj.pro

Screenshots of the different pages of this widget are shown in Figures A-4 and A-5. The first page of this interface allows the user to control advanced options of the laser's timing such as the q-switch delay and the digitization rate of the laser blow-off system's digitizer. Page 2 of the widget, the "Injection Setup" tab, allows the user to specify the timing of the laser blow-off injections. The first of these injections may be specified at an arbitrary time but all subsequent injections are forced to occur at 100 ms intervals following the first injection time. Control of the peizo-electric beam steering is found here. The user specifies the number of mm that they desire the beam to be steered in the positive x and negative y directions. An x and y position must be specified for each laser blow-off injection. If the user does not specify the injection positions, it will default to 0.0,0.0 for all injections. The "Run Test Shot" tab allows the user to toggle the impurity injector's timing system to sync with the C-Mod shot cycle or run independently. If running independently of the shot cycle, the user may perform test shots of the system to test alignment or laser positioning. The "Test Card" tab of the widget allows the user to ping both the DTAQ board and the server pcdaqeng1 to ensure the system is functioning properly.

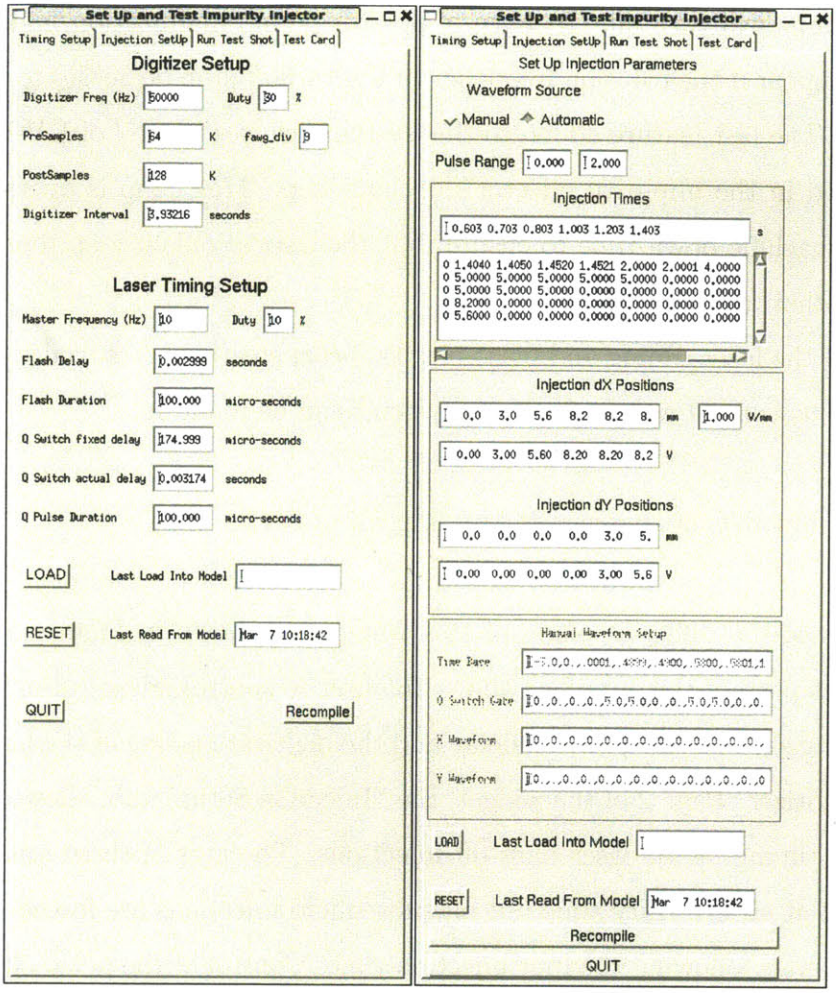

Figure A-4: Pages 1 and 2 of the impurity injector's control widget are shown. These pages allow for laser timing control and the control of piezo beam steering

A.1.2 Remote Laser Triggering

The ability to remotely trigger the impurity injector's laser system with precise timing is important for reliable operation of the system. This was achieved using a custom made laser timing card and the timing module in the impurity injector's CPCI crate. The basic operation is as follows:

Mounted in the system's electronics backplane is a digital fiber link (DFL) card which interprets the current machine state. The system is set up such that upon entering check state($\sim$ 30 seconds before the plasma shot) a signal is sent to the laser timing card. This signal triggers an internal 10 Hz clock which sends a negative going

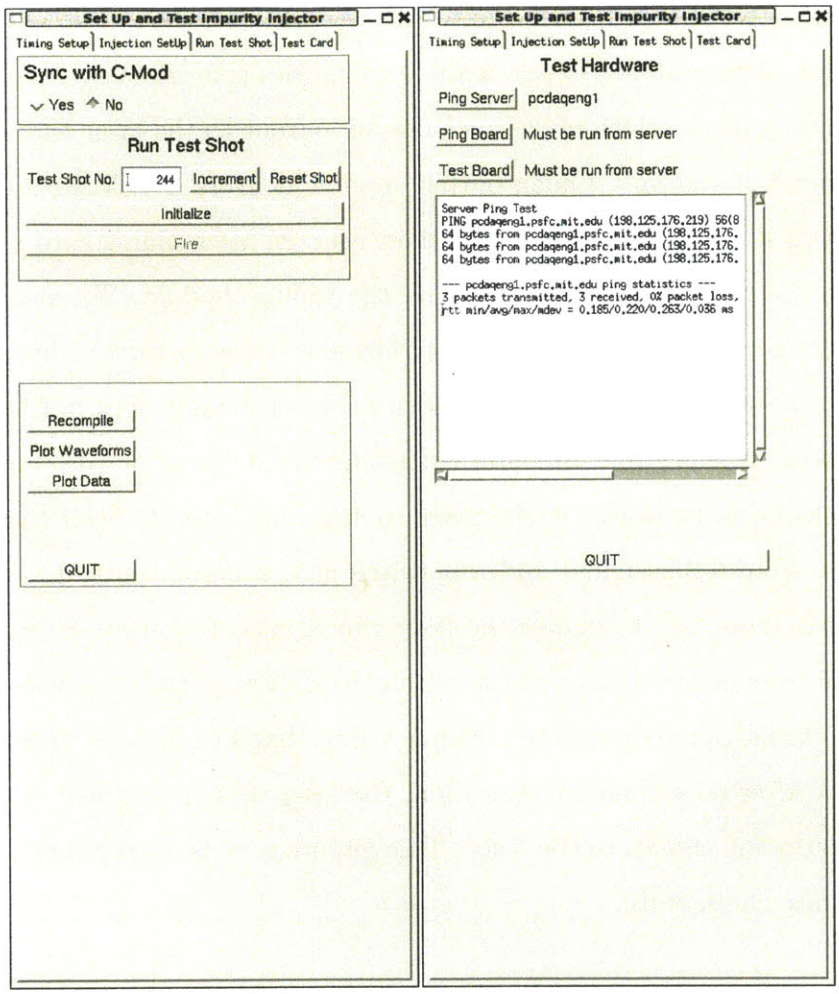

Figure A-5: Pages 3 and 4 of the impurity injector's control widget are shown. These pages allow the user to perform test shots and test communication with the CPCI crate.

TTL pulse (normal is high +5V state) to the laser power supply and causes the laser lamps to being to flash. This provides the required warm-up before generation of laser pulses. On receiving the event "POST_START", (-3.99 seconds) from the engineering encoder, the digitizer is triggered and a 10 Hz "master" clock is output by the timing module. This clock is fed into two other timing module channels to generate two delayed clocks (relative to the master clock) which correspond to the flashlamp clock and the q-switch clock. The flashlamp clock is delayed relative to the master clock such that a pulse will occur at precisely the user specified time of the first laser blow-off injection. The exact delay of the flashlamp clock is determined by the laser

blow-off control widget and written into the tree for each shot. The q-switch clock is delayed an additional $\sim$ 175 μs (a value found to optimize laser energy) relative to the flashlamp clock. Both of these clocks are output to the laser timing card. At $t = 0$ seconds the system's analog output module delivers a +5V gate to the laser timing card (2 second width) which switches from the laser timing card's internal 10 Hz clock to the flashlamp clock output by the timing module. To ensure that the laser does not receive a more than 1 pulse during a 100 ms interval, the laser timing card delays the switch from its internal clock to the flashlamp clock until at least 100 ms has passed. At this point, the laser is flashing based purely on the timing module generated clocks and pulses. If the laser timing card receives both the flash gate (which is on from 0-2 seconds) and a q-switch gate simultaneously (+5V from the analog output module), it triggers the laser timing card to output a negative going pulse at the next occurrence of the q-switch clock. This enables q-switching of the laser. The clocks/signals generated during a laser trigger are best demonstrated in Figure A-6. After 60 seconds of operation, the laser timing card will automatically disable all outgoing signals to the laser. This feature acts as a safeguard in the event of an indefinite check state.

Timing Module Inputs/Outputs

Channel 1-out - Digitizer Clock (50 kHz)

Channel 2-out - Trigger for Digitizer

Channel 3-out - Master clock (10 Hz) - To timing module channels 8 and 10

Channel 4-out - Delayed flash clock (10 Hz), - To laser timing card input 3

Channel 4-in - Master clock - From timing module channel 5

Channel 5-out - Delayed Q-switch clock (10 Hz) - To laser timing card input 5

Channel 5-in - Master clock - From timing module channel 5

Laser Timing Card Inputs

Input 1 - Check pulse from PLC

Input 2 - Recool pulse from PLC

Input 3 - Delayed flash clock - From timing module channel 7

Input 4 - Flash gate from analog output module

Input 5 - Delayed q-switch clock - From timing module 9

Input 6 - Q-switch gate from analog output module

Laser Timing Card Outputs

Output 1 - Flash pulse out to laser

Output 2 - Flash pulse monitor to digitizer

Output 3 - Q-switch pulse out to laser

Output 4 - Q-switch pulse monitor to digitizer

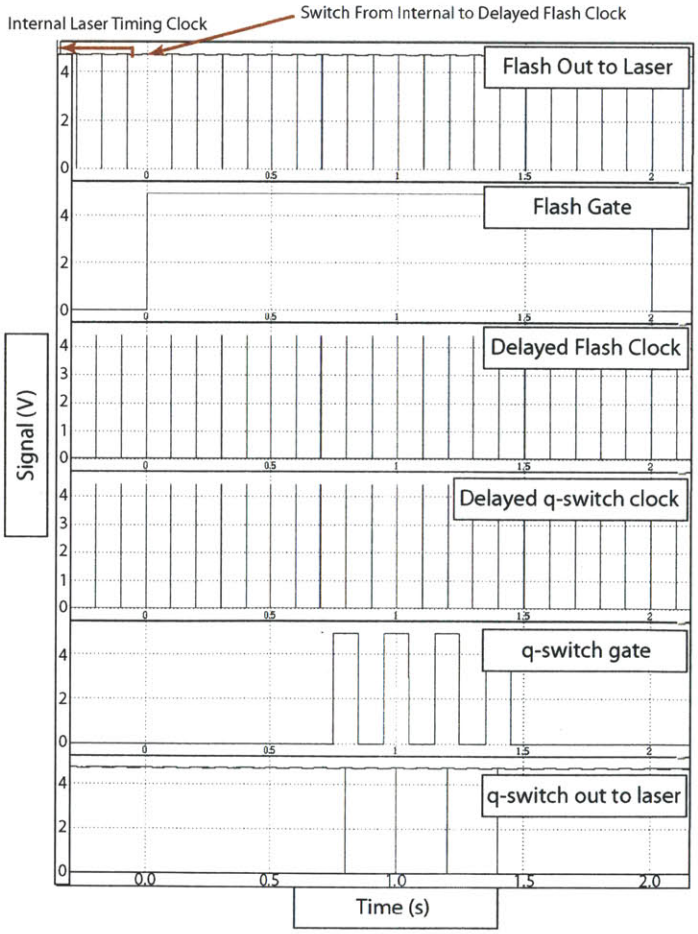

Figure A-6: The timing signals for laser triggering are shown.

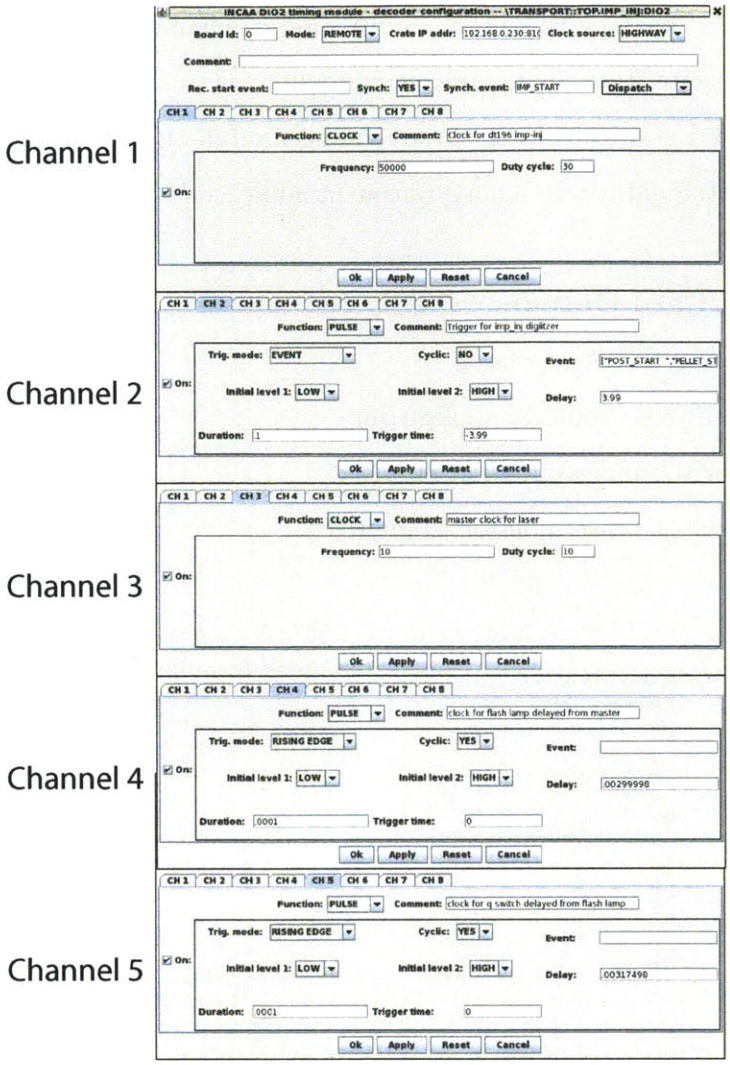

Figure A-7: Setup of all channels of the timing module are shown.

A.1.3 Remote Positioning Systems

Positioning of the primary (YAG) laser on the target is performed using two separate systems described in the main body of this thesis. Course movement of the beam on between shot time scales, is performed via the motorized mirror mount, while during shot beam movement is provided by the piezo-electric mirror mount. Figure A-8 demonstrates these two components. Control of the motorized mirror mount system (+/- 97 mrad of tip/tilt) is provided via RS232 commands which are passed to the

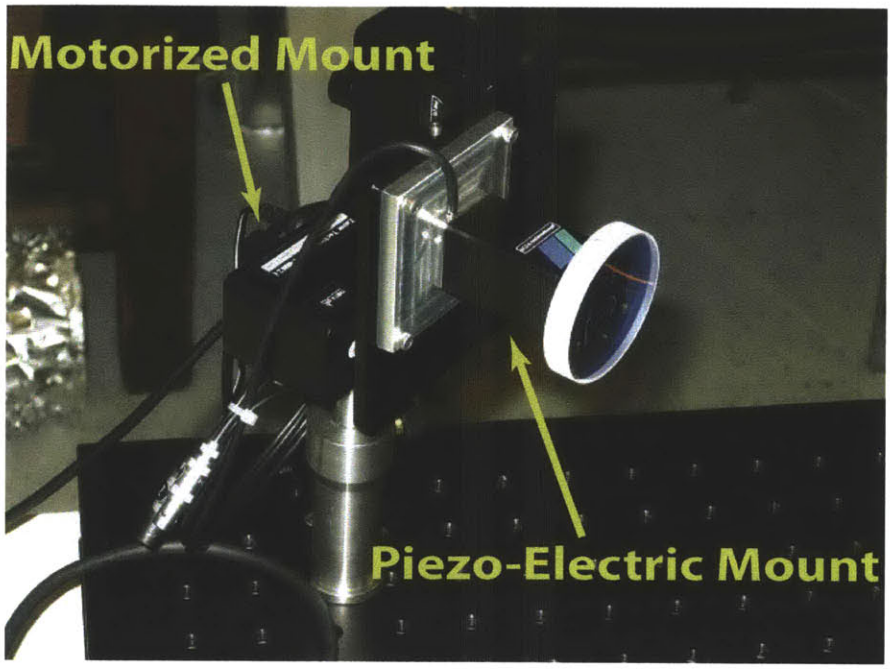

Figure A-8: Both the motorized and piezo-electric mirror mounts are shown. These allow for inner and intra shot movement of the laser position.

mount by a visual basic GUI interface. The control computer located on the impurity injector stand is linked via serial cable to this unit. During C-Mod operation, when access to the cell is limited, remote manipulation of the mirror mount performed by remote desktop connection to the (in cell) control computer. However, intrashot redirection of the beam is required for multi-pulse operation. Custom high voltage amplifiers located in the impurity injector electronics backplane take 0 to 10 V signals from the analog output module and convert them to 0 to 150 V. These signals are fed into each axis of the piezo-electric mirror mount, allowing for +/- 4 mrad of tip and tilt on time scales of less than 100 ms. Stepped waveforms are generated via the analog output module which allow for movement across the target slide during the shot and provides multi-pulse operational ability. An example of the input voltage to the high voltage amplifier is shown in Figure A-9.

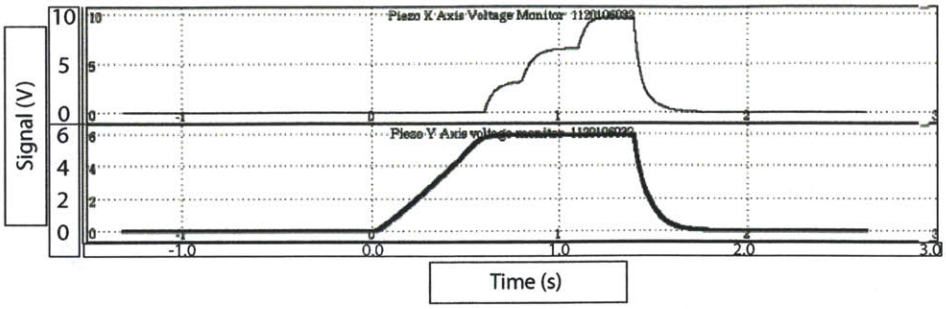

Figure A-9: The voltages output to each axis of the piezo are shown.

A.1.4 Verification of Position and Ablation

Visual confirmation of both the beam positioning and target ablation is of great importance to the operation of the laser blow-off system. This is achieved using a standard black and white CCD security camera (BNC out) which is linked via fiber optics to the closed circuit TV system in operation on Alcator C-Mod. The camera's view of the target slide cannot be direct due to geometric constraints and the requirement of a totally enclosed beam line. As a result, the camera is mounted approximately 90 degrees relative to the beam line. This is best demonstrated in figure A-10. The camera views down through a NW80 glass vacuum window where it

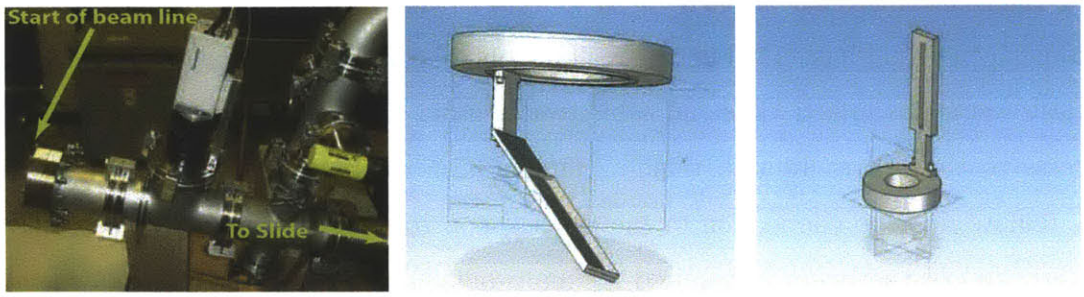

Figure A-10: (Left) The location and position of the camera is shown on the impurity injector beam line (Middle) A solid edge model of the silver mirror mount is shown attached to a mock up of the vacuum window. (Right) The camera mounting post attached to the vacuum window is shown.

views a reflection of the slide from a silvered glass mirror. This mirror is mounted at slightly greater than 45 degrees relative to the face of the vacuum window flange as to provide a view of the entire slide. However, to ensure that the mirror mount does

not block the laser transmission down the beam line, it only protrudes ~ 0.5 inches into the main beam line. The mirror and camera mounts are shown in Figure A-10.

Appendix B

STRAHL Synthetic Diagnostic and Iteration Tools

A series of codes were developed as part of this thesis to analyze experimental measurement of spectroscopic data and to extract impurity transport coefficient profiles. The general purpose of these routines is to process experimental data, process STRAHL output impurity emission, and to iterate the STRAHL code to infer the experimental impurity transport. This section will describe the main routines and functions used to perform this analysis. Because a complete description of STRAHL is out of the scope of this work, it is assumed in this description that the reader has some prior knowledge of the standard inputs needed for a STRAHL run. For more detail, the reader is referred to the STRAHL reference manual.

B.1 Introduction to the tools

The set of tools developed to implement a synthetic diagnostic and an iterative method of determining the impurity transport coefficient profiles is described here. These tools are contained in 6 primary files which are located in /home/nthoward/strahl/strahl/:

- **strahl.in**
- **run_strahl.pro**

- **load_strahl_data.pro**
- **write_strahl_files.pro**
- **compare_strahl_output.pro**
- **strahl_run_tools.pro**

A flow chart which briefly outlines the execution of a STRAHL run using these tools is shown in Figure B-1. More detail on the individual procedures can be found below.

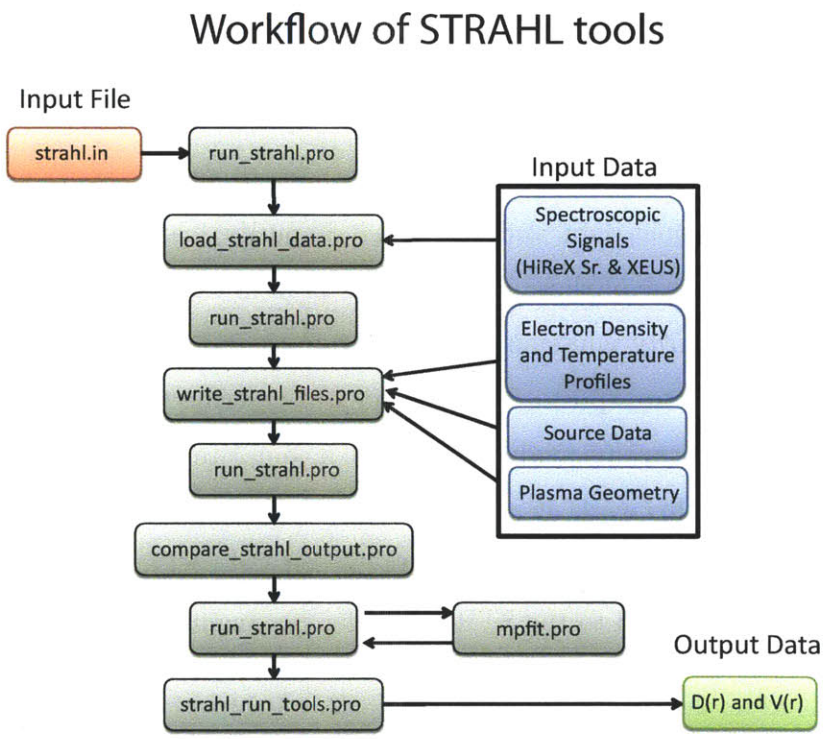

Figure B-1: A flow chart of the STRAHL workflow used in this work is shown.

B.1.1 Execution of the Codes

The initial execution of the codes listed above is best achieved using the **execute_strahl.pro** routine. From the complied STRAHL diectory, the command :

idl execute_strahl.pro

will compile all of the functions contained in the files listed above in the correct order and will call the **run_strahl.pro** routine to begin execution of the package of codes developed around STRAHL. The following sections will introduce the reader to the logical progression of the program and give brief descriptions of some of the key procedures and functions which are used.

B.1.2 run_strahl.pro

This procedure is the backbone of the tools built around STRAHL. Much of the logic of the code is contained in this code. Based on the user preferences which are read from the **strahl.in** file, the appropriate functions are called. All of the functions called by this procedure are contained in one of the five files listed below. Comments are present throughout this code which allow for a new user to follow the logical progression of the functions called in this procedure.

B.1.3 strahl.in

This file is the input file which drives all of the tools written around STRAHL. The flags and values set in this file are read by the function **strahl_read_in** and stored in a structure. The structure is passed to the individual functions and the input values and flags are used to control the course of the program. There are approximately 90 different flags or values which can be set in this file. This file is sufficiently commented to allow the new user to understand the flags and usage. For this reason, a much more complete description is omitted here.

B.1.4 load_strahl_data.pro

The main purpose of this procedure is to extract the raw spectroscopic data from the tree and process it appropriately for comparison with the STRAHL output. This

single procedure contains a large number of functions which are called to perform the data processing. Some of the main functions called will be described here. These are:

strahl_read_in - This function reads the file named strahl.in which includes all of the user specified flags and values for the iterative STRAHL run. It returns a structure named input which includes all the of data read from **strahl.in**

strahl_read_exp - This is the main routine for loading experimental data to be used in STRAHL. Currently this function is set up to take the input structure and return a structure of formatted experimental signals (Hirex Sr. and XEUS data) on a consistent timebase. This routine is written such that additional signals can be easily incorporated by straightforward extension.

format_sr_signal - This procedure is used to combine raw HiReX Sr. data from multiple injections into a single set of data. Individual injections are normalized and combined into a single data set. After combination, the signals and their photon statistic errors are put onto a 1 ms time base which is used throughout the package of codes written around STRAHL. A structure is returned containing the combined raw signal, the statistical error, and the appropriate timebase.

format_signal - This routine is a generalized formatting routine for any single chord measurement. In this work it was applied to the XEUS signal. It allows for an arbitrary, user specified, time resolution, a necessary feature since there is no well defined timebase for the XEUS data in the tree. Instead, the start of the signal rise is lined up with a user specified time from in the **strahl.in** file. This procedure returns a normalized (to its max value) signal, on a 1 ms timebase which begins at the start of the user specified rise time.

strahl_teeth - If the user specifies to include STRAHL's sawtooth model, this routine is called via a flag in the **strahl.in** file. This plots measured ECE or soft x-ray

signals in the user specified simulation interval and allows the user to click on the sawtooth crash times. This times are returned and will be written later for use in the STRAHL run.

strahl_inv - If the user specifies the use of STRAHL's sawtooth model, this routine allows the user to determine the approximate location of the sawtooth inversion radius. This is done by plotting core soft x-ray views and their corresponding tangency radii.

find_source - This routine reads the raw source time history measurement, allows the user to subtract the background, and formats the data in a manner such that the appropriate STRAHL source file can be written. Alternatively, if an existing source file is specified to be loaded, this routine ensures the timing is modified to be consistent with the start STRAHL run time.

B.1.5 write_strahl_files.pro

The main purpose of this procedure is collect data from the tree and output of the **load_strahl_data.pro** to write the files required for execution of STRAHL. Some of the main functions called will be described here. These are:

strahl_write_param - This routine is used to write both the source and the STRAHL parameters (main input) file used for STRAHL execution. To write this file it must be supplied with the input structure, information on where to obtain the source data (tree or existing source), sawtooth information, D and V profiles, and the radial grid for these profiles. If it is the first execution of this function, it will write a strahl.control file which tells STRAHL the correct files to read for execute. The output of this routine is a STRAHL source file and a STRAHL parameter input file.

strahl_write_files - This routine is used to write the input files which specify geometry and profile information to STRAHL. Under normal operation, this file reads

data from the analysis tree, constructs the STRAHL grids, normalized poloidal flux, and normalized rho_volume and maps n_e and T_e profiles read from FiTS save files to these grids. It then evaluates all the other needed geometric quantities from the EFIT and averages them over the STRAHL run time. Although time evolving background profiles may be specified, for this work only the average values where used. This data is then written to the appropriate STRAHL input files.

B.1.6 compare_strahl_output.pro

The main purpose of this procedure is to format data output from STRAHL and compare it with measured data. After the comparison is made, a chi-squared value of the comparison is returned. This procedure represents the synthetic diagnostic part of this work. Some of the main functions called will be described here. These are:

format_strahl_emiss - This routine takes the normalized square root of poloidal flux grid used by STRAHL and converts it to a dense grid of major radius values using analysis tree EFIT values for the specified STRAHL run time period. It also interpolates the STRAHL output emissivity onto the same dense radial grid. The output is a structure with the new radial grid, STRAHL emissivity, and simulation time included.

find_view_data - Whenever the STRAHL iteration routines are executed for the first time, this routine is called to store the geometry data calculated by the line integration routine. The line integration usually calculates this view information at each execution. Since this information is identical for each iteration, this data is stored and used at each additional execute for faster execution. This routine calls the line integration routine for the first time and stores the needed data in an output structure.

compare_strahl_data - This is the main routine for making a comparison of the STRAHL computed line integrated brightness with the measurement values. It uses the geometry information from the **find_view_data** routine to quickly evaluate the

line integrated brightness given an input emissivity profile. This routine checks for errors in the data and removes these points if present. If specified by the user, it will plot the measured and computed values of the brightness for a variety of HiReX Sr chords and the XEUS chord. Ultimately, this routine returns a number which is the χ^2 value for the iteration. Here the χ^2 is defined as:

$$\chi^2 = \sum (\frac{S_{measured} - S_{STRAHL}}{\sigma})^2 \tag{B.1}$$

Where $S_{measured}$ and S_{STRAHL} are the measured and STRAHL simulated data and σ is the estimated standard deviation of each data point.

strahl_mpfit - This is the function called by MPFIT to perform the nonlinear least-squares minimization. It takes the intial guesses for D and V, executes STRAHL and directs all output to strahl.txt. Then it calculates (through a call of the **compare_strahl_data** function) and prints χ^2 along with the values of D and V and the returns the value of χ^2 to MPFIT so that it can iterate.

B.1.7 strahl_run_tools.pro

This procedure includes a number of different routines which are used for determining the experimental values of the transport coefficients and plotting the results. The main functions included in this procedure are:

strahl_loop - This function is used to evaluate the transport coefficient profiles which result from a variation of the n_e and T_e profiles within their calculated errors. It takes the input structure generated from the **strahl.in** file as an input. Effectively, this function reads profiles for n_e and T_e from a FiTS save file, calls the appropriate functions to write the STRAHL input files, and executes MPFIT. Once MPFIT converges, it stores the radial grid used, the returned χ^2 value, and the values of the D and V. It repeats this process for a user specified number of n_e and T_e profiles. Additional flags can be set so that the radial grid varies slightly with each iteration. This function

then calls the function **form_profiles** for interpolation of the D and V profiles onto a 101 point r/a grid. A structure with the input structure, all of the trial χ^2 values, D and V values, and the final formed profiles is returned.

make_sim - This function is used to make a simulated data set for testing purposes. If the correct flags are set in **strahl.in**, this function is called after STRAHL runs once with a user specified set of D and V values. It then saves the STRAHL output as the experimental data and writes an IDL save file which can be loaded at a later time.

add_error - This function is used to add error to a simulated dataset. This feature allows for evaluation of error levels and their effect on the determination of the impurity transport coefficients. It is able to add periodic and statistical types of error at this time.

form_profiles - This function is called from **strahl_loop** and is used to interpolate from the STRAHL square root of normalized poloidal flux to a 101 point r/a grid. It then uses the χ^2 values returned from each iteration in strahl_loop to perform a weighted average and weighted standard deviation at each radial profile point. It returns the final D and V profiles, their standard deviations, and the new radial grid.

plot_strahl_results - This routine is used to plot the results from a series of STRAHL runs such as those output from **strahl_loop**. The profiles can be plotted with a large number of keywords which will not be covered here. This procedure is also set up to read GYRO output data, convert it to the STRAHL coordinates, and overplot the data. It allows for .eps output.

Appendix C

Shot List and Analysis Times

Shots Analyzed Using STRAHL, TRANSP, or GYRO Analysis				
Shot Number	STRAHL times	TRANSP Run ID	Linear GYRO time	Nonlinear GYRO time
GYRO "Base Case" Simulation – Chapter 5				
1101014006	0.965 – 1.4 sec	86735	1.1 sec	1.1 sec
Analysis of the I_p Scan – Chapter 6				
1101014005	0.965 – 1.4 sec	86734	1.0 sec	1.0 sec
1101014006	0.965 – 1.4 sec	86735	1.1 sec	1.1 sec
1101014007	0.965 – 1.4 sec	86736	1.09 sec	1.09 sec
1101014009	0.965 – 1.4 sec	86737	1.1 sec	1.1 sec
Analysis of the P_{Tot} Scan – Chapter 7				
1101014006	0.965 – 1.4 sec	86735	1.1 sec	1.1 sec
1101014011	0.965 – 1.4 sec	87041	1.1 sec	N/A
1101014012	0.965 – 1.4 sec	86774	1.1 sec	N/A
FiTS save files of n_e and T_e profiles are contained in /home/nthoward/profiles/original_fit/				

Appendix D

GYRO Software Tools

This appendix attempts to describe the software tools which were used to analyze the output of GYRO and modify GYRO runs in this thesis work. A brief description of these codes will be provided in this section.

D.1 GYRO Input File Generation and Modification Tools

A series of tools was developed for this work which allows for the generation of GYRO input files (input.profiles or INPUT_profiles) from the output of a TRANSP run as well as the modification of existing input.profiles files. These tools can all be found in the procedure **gyro_input_tools.pro**. It should be noted that the input file generation provided by the tools in **gyro_input_tools** was not used for this work since these files are currently insufficient for nonlinear GYRO simulation due to missing rotation data. Instead, only generation of input files from the PPPL tool, TRGK was used for the work presented in this thesis. However, modification of TRGK generated input files was performed using these tools. They can be found in /home/nthoward/gyro_input/ on the C-Mod cluster.

make_input_profiles - This is the procedure used to create an input.profiles file

from an existing TRANSP run. It calls the other functions described in this section and writes a file named input.profiles.(TRANSP run ID). Inputs are the TRANSP run ID, time, and the time averaging window.

read_input_profiles - This routine does a formatted read through an existing input.profiles file and returns a structure containing the arrays which were read from the input.profiles file.

read_transp_data - This routine reads through the TRANSP tree and extracts data from an existing TRANSP run. This data is time averaged using native TRANSP time averaging functions. All outputs are converted into the appropriate units which are needed for generation of a GYRO input file. The output of this procedure is a structure with all the data needed to generate a GYRO input file.

write_input_profiles - This function takes a structure of the required GYRO data (typically generated by read_transp_data or read_input_profiles) and does a formatted write of the data to a local file which is named input.profiles.(TRANSP run ID).

change_inputs - This function is a generalized version of David Mikkelsen's read_IN_prof_spl_Ti.pro routine. It allows the user to specify an existing input.profiles file, a grid of r/a points, and an array of values corresponding to the normalized gradient scale length at each radial location. This routine is generalized for any background profile that is user specified. The routine modifies the local gradients and reintegrates the gradient profile to obtain the new profile of the quantity.

D.2 Linear Stability Tools

A large number of linear GYRO simulations were performed as part of this work. This section describes the tools which were used to perform the linear simulations and generate the linear stability maps which were commonly shown in this work. All

of the routines used for linear stability evaluation are contained in the file named **make_stability.pro** on the LOKI cluster (/home/nthoward/gacode/gyro/sim/). A description of the main functions included in this procedure is found below:

make_stability - This is the main procedure used to create a set of linear GYRO simulations for the purpose of making a stability map. This routine allows the user to specify the two scanned variables (a/L_{T_i}, a/L_{T_e}, or a/L_n) and their values. Additionally it takes an array of $k_\theta \rho_s$ values, a radius to perform the analysis (in r/a), and a starting directory (as a string). If the "auto" keyword is specified, as it was throughout this work, the code defaults to a $k_\theta \rho_s$ range of [0.25, 0.75] (11 total values) and includes $\pm 50\%$ scans of the scanned variables using 15 different points to span this range. Execution of this code calls functions which read data in the out.gyro.run file from the starting directory to determine the experimental values of the scanning variables. The keyword "nosubmit" is used to create and write the appropriate input files in the GYRO directories without submitting them to the LOKI queue. The submission of these directories was managed using the **submit_all.sh** file which is described below.

write_lin_input - This function is used to write the input.gyro files needed for a linear stability run. Based on the user's selection of scanned variables set in **make_stability** the files are modified so that the appropriate scaling factor is applied to the normalized gradient scale lengths in each run.

read_lin_runs - Upon execution of make_stability an output file is generated. This file contains the input data which was used to execute make_stability. If these directories have been executed by GYRO, read_lin_runs first reads the information file to determine the number of directories which were made and extracts the real frequency, growth rate, the $k_\theta \rho_s$ value from each directory. This data is then output in a structure which can be read and replotted later as a linear stability map.

scan_ky - This is a simple function to do a quick scan of $k_\theta \rho_s$. Given a starting directory, r/a value, the range of $k_\theta \rho_s$, and the number of total runs, it creates and executes a series of linear GYRO simulations.

read_ky_scan - Given the starting directory and the number of points used in a simple ky scan, this function reads the real frequency, growth rate, and $k_\theta \rho_s$ values from the linear scan performed. It outputs a structure with all of this information.

submit_all.sh - This shell script does a controlled submission of linear GYRO runs to the LOKI queue. It should be used with a series of directories created by the make_stability function. It is designed to loop through the different directories which correspond to different values of scanned variables specified in make_stability. This script checks the number of currently submitted linear runs every 15 seconds. If the number of runs drops below 12 then it submits until this number is reached.

D.3 Nonlinear GYRO Tools

This section summarizes some of the numerical tools which were used to evaluate the nonlinear GYRO simulations described in this work. Over the course of this work a number of tools were developed, many of which became obsolete. This section will only focus on the tools which were explicitly used. It should be noted that the native GYRO tool, VUGYRO, was used for routine evaluation of nonlinear GYRO runs. However the routines here were used to extract the transport coefficients and make quick comparison of the experimental heat fluxes with the simulated values. These tools are located in ~/nthoward/GYRO/gyro/sim/Postgyro/ at NERSC.

gyro_calcs.pro - All of the evaluation of the nonlinear GYRO simulation was performed using this procedure. The various keywords allow the user to select the particular function of interest. This code has several required inputs. Since it was originally written to compare the fluxes from two separate nonlinear runs and make a guess for

the required gradient modification to obtain the experimental values, it still requires two completed GYRO directories as inputs. However, for the purposes of this work, the second directory is effectively ignored. The user must also specify a grid of values which span the GYRO simulation domain. Once again, this is for historical purposes and is mostly irrelevant for the results presented in this thesis. If the keyword "plot" is specified, the first directory is read and the experimental electron and ion heat fluxes are plotted and compared with the corresponding simulation heat fluxes in units of MW/m^2. If the keyword "compare" is set, only the total heat fluxes are compared and plotted. Finally, if the keyword "pflux" is set, the impurity particle fluxes are read from the output data and then impurity transport coefficients are extracted. When the "save" keyword is set an output structure is built by the code including the impurity transport coefficients and the ion and electron heat fluxes. This structure is typically exported to local machines for additional analysis.

Bibliography

[1] http://www.ipp.mpg.de/ippcms/eng/pr/fusion21/magnet/index.html.

[2] J. Wesson. *Tokamaks.* International Series of Monographs on Physics. Oxford University Press, 2004.

[3] X. Garbet, Y. Idomura, L. Villard, and T.H. Watanabe. Gyrokinetic simulations of turbulent transport. *Nuclear Fusion*, **50**(4):043002, 2010.

[4] M. L. Reinke, P. Beiersdorfer, N. T. Howard, E. W. Magee, Y. Podpaly, J. E. Rice, and J. L. Terry. Vacuum ultraviolet impurity spectroscopy on the Alcator C-Mod tokamak. *Review of Scientific Instruments.*, 81(10):10D736, 2010.

[5] J D Lawson. Some criteria for a power producing thermonuclear reactor. *Proceedings of the Physical Society. Section B*, 70(1):6, 1957.

[6] J. W. Hughes, D. Mossessian, K. Zhurovich, M. DeMaria, K. Jensen, and A. Hubbard. Thomson scattering upgrades on Alcator C-Mod. *Review of Scientific Instruments*, 74(3):1667–1670, 2003.

[7] A. Ince-Cushman, J. E. Rice, M. Bitter, M. L. Reinke, K. W. Hill, M. F. Gu, E. Eikenberry, Ch. Broennimann, S. Scott, Y. Podpaly, S. G. Lee, and E. S. Marmar. Spatially resolved high resolution x-ray spectroscopy for magnetically confined fusion plasmas (invited). *Review of Scientific Instruments.*, 79(10):10E302, 2008.

[8] J.P. Friedberg. *Plasma Physics and Fusion Energy.* Cambridge University Press, 2008.

[9] R.J. Goldston and P.H. Rutherford. *Introduction to Plasma Physics.* Taylor and Francis, 1995.

[10] A. Loarte, B. Lipschultz, A.S. Kukushkin, G.F. Matthews, P.C. Stangeby, N. Asakura, G.F. Counsell, G. Federici, A. Kallenbach, K. Krieger, A. Mahdavi, V. Philipps, D. Reiter, J. Roth, J. Strachan, D. Whyte, R. Doerner, T. Eich, W. Fundamenski, A. Herrmann, M. Fenstermacher, P. Ghendrih, M. Groth, A. Kirschner, S. Konoshima, B. LaBombard, P. Lang, A.W. Leonard, P. Monier-Garbet, R. Neu, H. Pacher, B. Pegourie, R.A. Pitts, S. Takamura, J. Terry, E. Tsitrone, the ITPA Scrape-off Layer, and Divertor Physics Topical Group. Chapter 4: Power and particle control. *Nuclear Fusion*, 47(6):S203, 2007.

[11] ITER Physics Expert Group on Confinement, Transport, ITER Physics Expert Group on Confinement Modelling, Database, and ITER Physics Basis Editors. Chapter 2: Plasma confinement and transport. *Nuclear Fusion*, **39**(12):2175, 1999.

[12] W. Horton. Drift waves and transport. *Review of Modern Physics*, **71**(3), (1999).

[13] Martin Greenwald. Verification and validation for magnetic fusion. *Physics of Plasmas*, 17(5):058101, 2010.

[14] P. W. Terry, M. Greenwald, J.-N. Leboeuf, G. R. McKee, D. R. Mikkelsen, W. M. Nevins, D. E. Newman, D. P. Stotler, , and and. Validation in fusion research: Towards guidelines and best practices. *Physics of Plasmas*, 15(6):062503, 2008.

[15] C. Angioni and A. G. Peeters. Direction of impurity pinch and auxiliary heating in tokamak plasmas. *Phys. Rev. Lett.*, 96:095003, Mar 2006.

[16] M. E. Puiatti, M. Valisa, C. Angioni, L. Garzotti, P. Mantica, M. Mattioli, L. Carraro, I. Coffey, C. Sozzi, and JET-EFDA contributors. Analysis of metal-

lic impurity density profiles in low collisionality Joint European Torus H-mode and L-mode plasmas. *Physics of Plasmas*, 13(4):042501, 2006.

[17] P. Helander and D. Sigmar. *Collisional Transport in Magnetized Plasmas.* Cambridge Monographs on Plasma Physics. Cambridge University Press, 2002.

[18] F. Chen. *Introduction to Plasma Physics and Controlled Fusion.* Springer, 1984.

[19] S.I. Braginskii. volume 1 of *Reviews of Modern Physics.* Consultants Bureau, 1965.

[20] C Bourdelle. Turbulent particle transport in magnetized fusion plasma. *Plasma Physics and Controlled Fusion*, 47(5A):A317, 2005.

[21] F. L. Hinton and R. D. Hazeltine. Theory of plasma transport in toroidal confinement systems. *Rev. Mod. Phys.*, 48:239–308, Apr 1976.

[22] S.P. Hirshman and D.J. Sigmar. Neoclassical transport of impurities in tokamak plasmas. *Nuclear Fusion*, 21(9):1079, 1981.

[23] G Fussmann, A R Field, A Kallenbach, K Krieger, K H Steuer, and The ASDEX Team. Impurity transport and neoclassical predictions. *Plasma Physics and Controlled Fusion*, 33(13):1677, 1991.

[24] Jan Weiland. *Collective Modes in Inhomogeneous Plasmas: Kinetic and Advanced Fluid Theory.* Series in Plasma Physics. Taylor and Francis, 2000.

[25] B. Coppi, M. N. Rosenbluth, and R. Z. Sagdeev. Instabilities due to temperature gradients in complex magnetic field configurations. *Physics of Fluids*, 10(3):582–587, 1967.

[26] M. Porkolab and G. S. Kino. Observation of a new type of instability in a thermal plasma. *Phys. Rev. Lett.*, 15:752–755, Nov 1965.

[27] M. Porkolab. Plasma instabilities due to ion temperature gradients. *Nuclear Fusion*, 8(1):29, 1968.

[28] J W Connor and H R Wilson. Survey of theories of anomalous transport. *Plasma Physics and Controlled Fusion*, 36(5):719, 1994.

[29] Jr. C. W. Horton and R. K. Varma. Electrostatic stability theory of tokamaks from two-component fluid equations. *Physics of Fluids*, 15(4):620–631, 1972.

[30] Jr. Wendell Horton, Duk-In Choi, and W. M. Tang. Toroidal drift modes driven by ion pressure gradients. *Physics of Fluids*, 24(6):1077–1085, 1981.

[31] B.B. Kadomtsev and O.P. Pogutse. Trapped particles in toroidal magnetic systems. *Nuclear Fusion*, 11(1):67, 1971.

[32] J. C. Adam, W. M. Tang, and P. H. Rutherford. Destabilization of the trapped-electron mode by magnetic curvature drift resonances. *Physics of Fluids*, 19(4):561–566, 1976.

[33] W. Horton, B. G. Hong, and W. M. Tang. Toroidal electron temperature gradient driven drift modes. *Physics of Fluids*, 31(10):2971–2983, 1988.

[34] F. Jenko and W. Dorland. Prediction of significant tokamak turbulence at electron gyroradius scales. *Phys. Rev. Lett.*, 89:225001, Nov 2002.

[35] P J Catto, W M Tang, and D E Baldwin. Generalized gyrokinetics. *Plasma Physics*, 23(7):639, 1981.

[36] E. A. Frieman and Liu Chen. Nonlinear gyrokinetic equations for low-frequency electromagnetic waves in general plasma equilibria. *Physics of Fluids*, 25(3):502–508, 1982.

[37] T. S. Hahm. Nonlinear gyrokinetic equations for tokamak microturbulence. *Physics of Fluids*, 31(9):2670–2673, 1988.

[38] E. S. Marmar, J. E. Rice, and S. L. Allen. Confinement of injected silicon in the Alcator-A tokamak. *Phys. Rev. Lett.*, 45:2025–2028, Dec 1980.

[39] W.L. Hodge, J. Castracane, H.W. Moos, and E.S. Marmar. A study of molybdenum radiation from Alcator A. *Journal of Quantitative Spectroscopy and Radiative Transfer*, 27(5):493 – 498, 1982.

[40] E.S. Marmar, J.E. Rice, J.L. Terry, and F.H. Seguin. Impurity injection experiments on the Alcator C tokamak. *Nuclear Fusion*, 22(12):1567, 1982.

[41] M. Mattioli et al. Laser blow-off injected impurity transport in L-mode Tore Supra plasmas. *Nuclear Fusion*, **38**(11), (1998).

[42] M. A. Graf. *Impurity Injection Experiments on the* Alcator C-Mod *Tokamak.* PhD thesis, Nuclear Engineering Dept., Mass. Inst. of Technology, 1995.

[43] M. Valisa, L. Carraro, I. Predebon, M.E. Puiatti, C. Angioni, I. Coffey, C. Giroud, L. Lauro Taroni, B. Alper, M. Baruzzo, P. Belo daSilva, P. Buratti, L. Garzotti, D. Van Eester, E. Lerche, P. Mantica, V. Naulin, T. Tala, M. Tsalas, and JET-EFDA contributors. Metal impurity transport control in JET H-mode plasmas with central ion cyclotron radiofrequency power injection. *Nuclear Fusion*, 51(3):033002, 2011.

[44] R. Giannella, L. Lauro-Taroni, M. Mattioli, B. Alper, B. Denne-Hinnov, G. Magyar, J. O'Rourke, and D. Pasini. Role of current profile in impurity transport in JET L mode discharges. *Nuclear Fusion*, 34(9):1185, 1994.

[45] C. Giroud, R. Barnsley, P. Buratti, I.H. Coffey, M. von Hellermann, C. Jupn, K.D. Lawson, A. Meigs, M. O'Mullane, A.D. Whiteford, K.-D. Zastrow, and the JET EFDA contributors. Method for experimental determination of Z dependence of impurity transport on JET. *Nuclear Fusion*, 47(4):313, 2007.

[46] T Parisot, R Guirlet, C Bourdelle, X Garbet, N Dubuit, F Imbeaux, and P R Thomas. Experimental impurity transport and theoretical interpretation in a Tore Supra lower-hybrid heated plasma. *Plasma Physics and Controlled Fusion*, 50(5):055010, 2008.

[47] R. Guirlet, D. Villegas, T. Parisot, C. Bourdelle, X. Garbet, F. Imbeaux, D. Mazon, and D. Pacella. Anomalous transport of light and heavy impurities in Tore Supra ohmic, weakly sawtoothing plasmas. *Nuclear Fusion*, 49(5):055007, 2009.

[48] R Dux, R Neu, A G Peeters, G Pereverzev, A Mck, F Ryter, J Stober, and ASDEX Upgrade Team. Influence of the heating profile on impurity transport in ASDEX Upgrade. *Plasma Physics and Controlled Fusion*, 45(9):1815, 2003.

[49] M Sertoli, C Angioni, R Dux, R Neu, T Putterich, V Igochine, and the ASDEX Upgrade Team. Local effects of ECRH on argon transport in L-mode discharges at ASDEX upgrade. *Plasma Physics and Controlled Fusion*, 53(3):035024, 2011.

[50] R. Dux et al. Z dependence of core impurity transport in ASDEX upgrade H-mode discharges. *Nuclear Fusion*, **39**(11), (1999).

[51] E Scavino, J S Bakos, R Dux, H Weisen, and TCV Team. Effects of plasma shape on laser blow-off injected impurity transport in TCV. *Plasma Physics and Controlled Fusion*, 45(11):1961, 2003.

[52] E Scavino, J Bakos, H Weisen, and TCV Team. Effects of ECRH power and safety factor on laser blow-off injected impurity confinement in TCV. *Plasma Physics and Controlled Fusion*, 46(5):857, 2004.

[53] J.E. Rice, J.L. Terry, J.A. Goetz, Y. Wang, E.S. Marmar, M. Greenwald, I.Hutchinson, Y. Takase, S. Wolfe, H. Ohkawa, and A. Hubbard. Impurity transport in Alcator C-Mod plasmas. *Physics of Plasmas*, **4**(5), (1997).

[54] W. Horton and W. Rowan. Impurity transport studies in the Texas Experimental Tokamak (TEXT). *Physics of Plasmas*, **1**(4), (1994).

[55] R. Guirlet, A. Sirinelli, T. Parisot, R. Sabot, J.F. Artaud, C. Bourdelle, X. Garbet, P. Hennequin, G.T. Hoang, F. Imbeaux, J.L. Sgui, D. Mazon, and D. Villegas. Particle transport in low core turbulence Tore-Supra plasmas. *Nuclear Fusion*, 50(9):095009, 2010.

[56] D. Villegas, R. Guirlet, C. Bourdelle, G. T. Hoang, X. Garbet, and R. Sabot. Experimental electron temperature gradient dependence of heavy impurity transport in fusion devices. *Phys. Rev. Lett.*, 105:035002, Jul 2010.

[57] C. Angioni, R.M. McDermott, E. Fable, R. Fischer, T. Putterich, F. Ryter, G. Tardini, and the ASDEX Upgrade Team. Gyrokinetic modelling of electron and boron density profiles of h-mode plasmas in ASDEX Upgrade. *Nuclear Fusion*, 51(2):023006, 2011.

[58] C Angioni, R Dux, E Fable, A G Peeters, and the ASDEX Upgrade Team. Non-adiabatic passing electron response and outward impurity convection in gyrokinetic calculations of impurity transport in ASDEX Upgrade plasmas. *Plasma Physics and Controlled Fusion*, 49(12):2027, 2007.

[59] C. Angioni, L. Carraro, T. Dannert, N. Dubuit, R. Dux, C. Fuchs, X. Garbet, L. Garzotti, C. Giroud, R. Guirlet, F. Jenko, O. J. W. F. Kardaun, L. Lauro-Taroni, P. Mantica, M. Maslov, V. Naulin, R. Neu, A. G. Peeters, G. Pereverzev, M. E. Puiatti, T. Putterich, J. Stober, M. ValoviC, M. Valisa, H. Weisen, and A. Zabolotsky ASDEX Upgrade Team JET EFDA Contributors. Particle and impurity transport in the Axial Symmetric Divertor Experiment Upgrade and the Joint European Torus, experimental observations and theoretical understanding. *Physics of Plasmas*, 14(5):055905, 2007.

[60] C Angioni, E Fable, M Greenwald, M Maslov, A G Peeters, H Takenaga, and H Weisen. Particle transport in tokamak plasmas, theory and experiment. *Plasma Physics and Controlled Fusion*, 51(12):124017, 2009.

[61] N. Dubuit, X. Garbet, T. Parisot, R. Guirlet, and C. Bourdelle. Fluid simulations of turbulent impurity transport. *Physics of Plasmas*, 14(4):042301, 2007.

[62] S. Futatani, X. Garbet, S. Benkadda, and N. Dubuit. Reversal of impurity pinch velocity in tokamaks plasma with a reversed magnetic shear configuration. *Phys. Rev. Lett.*, 104:015003, Jan 2010.

[63] T. Hein and C. Angioni. Electromagnetic effects on trace impurity transport in tokamak plasmas. *Physics of Plasmas*, 17(1):012307, 2010.

[64] H. Nordman, T. Fulop, J. Candy, P. Strand, and J. Weiland. Influence of magnetic shear on impurity transport. *Physics of Plasmas*, 14(5):052303, 2007.

[65] J.F. Friichtenicht. Laser-generated pulsed atomic beams. *Review of Scientific Instruments*, **45**(1), (1974).

[66] E.S. Marmar et al. System for rapid injection of metal atoms into plasmas. *Review of Scientific Instruments*, **46**(9), (1975).

[67] M.A. Graf et al. Spectroscopic measurement of impurity transport coefficients and penetration efficiencies in Alcator C-Mod plasmas. *Review of Scientific Instruments*, **66**, 1994.

[68] N.T. Howard, M. Greenwald, D.R. Mikkelsen, M.L. Reinke, A.E. White, D. Ernst, Y. Podpaly, and J. Candy. Submitted to Nuclear Fusion.

[69] D.G. Whyte, E. Haddad, B.C. Gregory, and G. Able. Characterization of a laser ablation impurity injector for the tokmamak de varennes. *Fusion Science and Technology*, 20:399, 1991.

[70] R. Neu. Behavior of laser ablated impurities in ASDEX-Upgrade discharges. *European Physics Society*, (1995).

[71] N.P. Basse et al. Diagnostic systems on Alcator C-Mod. *Fusion Science and Technology*, **51**, (2007).

[72] S. K. Guharay, D. A. Boyd, R. F. Ellis, F. J. Stauffer, and C. J. Lasnier. A 19 channel fast grating polychromator for ECE measurements in the MTX tokamak. *Review of Scientific Instruments*, 61(11):3520–3523, 1990.

[73] G. Taylor, C.K. Phillips, G. Schilling, J.R. Wilson, A. Hubbard, S.J. Wukitch, and E. Nelson-Mebly. *Bulletin of the American Physical Society*, 43:1821, 1998.

[74] J. W. Heard, C. Watts, R. F. Gandy, P. E. Phillips, G. Cima, R. Chatterjee, A. Blair, A. Hubbard, C. W. Domier, and N. C. Luhmann. High resolution electron cyclotron emission temperature profile and fluctuation diagnostic for Alcator C-Mod. *Review of Scientific Instruments*, 70(1):1011–1013, 1999.

[75] D. R. Ernst. *Momentum Transport, Radial Electric Field, and Ion Thermal Energy Confinement in Very High Temperature Plasmas.* PhD thesis, Physics Dept., Mass. Inst. of Technology, 1997.

[76] Ronald E. Bell. An inversion technique to obtain full poloidal velocity profiles in a tokamak plasma. *Review of Scientific Instruments*, 68(2):1273–1280, 1997.

[77] I. Condrea, E. Haddad, B. C. Gregory, and G. Abel. Local poloidal and toroidal plasma rotation velocities and ion temperature in a tokamak plasma obtained with a matrix inversion method considering asymmetries. *Physics of Plasmas*, 7(9):3641–3653, 2000.

[78] J. E. Rice and E. S. Marmar. Five-chord high-resolution x-ray spectrometer for Alcator C-Mod. *Review of Scientific Instruments*, 61(10):2753–2755, 1990.

[79] T. Sunn Pedersen and R. S. Granetz. Edge x-ray imaging measurements of plasma edge in Alcator C-Mod. *Review of Scientific Instruments*, 70(1):586–590, 1999.

[80] R. Dux. Report ipp 9/82. *MPI fur Plasmaphysik, Garching*, (2006).

[81] R. Dux. *STRAHL User Manual.* Max-Plank-Institut fur Plasmaphysik, ipp/30 edition, 2006.

[82] http://www.adas.ac.uk/.

[83] M L Reinke, I H Hutchinson, J E Rice, N T Howard, A Bader, S Wukitch, Y Lin, D C Pace, A Hubbard, J W Hughes, and Y Podpaly. Poloidal variation of high-Z impurity density due to hydrogen minority ion cyclotron resonance heating on Alcator C-Mod. *Plasma Physics and Controlled Fusion*, 54(4):045004, 2012.

[84] C. B. Markwardt. Non-linear Least-squares Fitting in IDL with MPFIT. In D. A. Bohlender, D. Durand, & P. Dowler, editor, *Astronomical Data Analysis Software and Systems XVIII*, volume 411 of *Astronomical Society of the Pacific Conference Series*, page 251, September 2009.

[85] P. Bevington and K. Robinson. *Data Reduction and Error Analysis for the Physical Sciences*. McGraw-Hill, 2002.

[86] J. Ongena, M. Evrard, and D. McCune. Numerical transport codes. *Transactions of Fusion Technology*, 33(2T):181–191, 1998.

[87] R.J. Hawryluk. An empirical approach to tokamak transport. *Physics of Plasmas Close to Thermonuclear Conditions*, 1:19–46, 1980.

[88] http://w3.pppl.gov/transp/.

[89] M Brambilla. Numerical simulation of ion cyclotron waves in tokamak plasmas. *Plasma Physics and Controlled Fusion*, 41(1):1, 1999.

[90] J. C. Wright, P. T. Bonoli, M. Brambilla, F. Meo, E. D'Azevedo, D. B. Batchelor, E. F. Jaeger, L. A. Berry, C. K. Phillips, and A. Pletzer. Full wave simulations of fast wave mode conversion and lower hybrid wave propagation in tokamaks. *Physics of Plasmas*, 11(5):2473–2479, 2004.

[91] J. Candy and R.E. Waltz. An eulerian gyrokinetic-maxwell solver. *Journal of Computational Physics*, 186(2):545 – 581, 2003.

[92] J. Candy and R. E. Waltz. Anomalous transport scaling in the DIII-D tokamak matched by supercomputer simulation. *Phys. Rev. Lett.*, 91:045001, Jul 2003.

[93] C. Holland, L. Schmitz, T. L. Rhodes, W. A. Peebles, J. C. Hillesheim, G. Wang, L. Zeng, E. J. Doyle, S. P. Smith, R. Prater, K. H. Burrell, J. Candy, R. E. Waltz, J. E. Kinsey, G. M. Staebler, J. C. DeBoo, C. C. Petty, G. R. McKee, Z. Yan, and A. E. White. Advances in validating gyrokinetic turbulence models against L- and H-mode plasmas. *Physics of Plasmas*, **18**(5):056113, 2011.

[94] R. L. Miller, M. S. Chu, J. M. Greene, Y. R. Lin-Liu, and R. E. Waltz. Noncircular, finite aspect ratio, local equilibrium model. *Physics of Plasmas*, 5(4):973–978, 1998.

[95] J. Candy and E. Belli. *GYRO Reference Guide.* General Atomics, 2011.

[96] J. Candy, R. E. Waltz, and W. Dorland. The local limit of global gyrokinetic simulations. *Physics of Plasmas*, 11(5):L25–L28, 2004.

[97] http://loki.psfc.mit.edu.

[98] E.S. Marmar and Alcator C-Mod Group. The Alcator C-Mod program. *Fusion Science and Technology*, **51**, (2007).

[99] O. Sauter, C. Angioni, and Y. R. Lin-Liu. Neoclassical conductivity and bootstrap current formulas for general axisymmetric equilibria and arbitrary collisionality regime. *Physics of Plasmas*, **6**(7):2834–2839, 1999.

[100] E A Belli and J Candy. Kinetic calculation of neoclassical transport including self-consistent electron and impurity dynamics. *Plasma Physics and Controlled Fusion*, 50(9):095010, 2008.

[101] C. Holland, A. E. White, G. R. McKee, M. W. Shafer, J. Candy, R. E. Waltz, L. Schmitz, and G. R. Tynan. Implementation and application of two synthetic diagnostics for validating simulations of core tokamak turbulence. *Physics of Plasmas*, 16(5):052301, 2009.

[102] R. E. Waltz and R. L. Miller. Ion temperature gradient turbulence simulations and plasma flux surface shape. *Physics of Plasmas*, 6(11):4265–4271, 1999.

[103] A. M. Dimits, G. Bateman, M. A. Beer, B. I. Cohen, W. Dorland, G. W. Hammett, C. Kim, J. E. Kinsey, M. Kotschenreuther, A. H. Kritz, L. L. Lao, J. Mandrekas, W. M. Nevins, S. E. Parker, A. J. Redd, D. E. Shumaker, R. Sydora, and J. Weiland. Comparisons and physics basis of tokamak transport models and turbulence simulations. *Physics of Plasmas*, 7(3):969–983, 2000.

[104] O. Kardaun. *Classical Methods of Statistics*. Springer, 1st edition, 2005.

[105] P.N. Yushmanov, T. Takizuka, K.S. Riedel, O.J.W.F. Kardaun, J.G. Cordey, S.M. Kaye, and D.E. Post. Scalings for tokamak energy confinement. *Nuclear Fusion*, 30(10):1999, 1990.

[106] N.T. Howard, M. Greenwald, and J.E. Rice. Characterization of impurity confinement on Alcator C-Mod using a multi-pulse laser blow-off system. *Review of Scientific Instruments*, **82**, 2011.

[107] D.G. Whyte, A.E. Hubbard, J.W. Hughes, B. Lipschultz, J.E. Rice, E.S. Marmar, M. Greenwald, I. Cziegler, A. Dominguez, T. Golfinopoulos, N. Howard, L. Lin, R.M. McDermott, M. Porkolab, M.L. Reinke, J. Terry, N. Tsujii, S. Wolfe, S. Wukitch, Y. Lin, and the Alcator C-Mod Team. I-mode: an H-mode energy confinement regime with l-mode particle transport in Alcator C-Mod. *Nuclear Fusion*, 50(10):105005, 2010.

[108] D. R. Ernst, J. Lang, W. M. Nevins, M. Hoffman, Y. Chen, W. Dorland, and S. Parker. Role of zonal flows in trapped electron mode turbulence through nonlinear gyrokinetic particle and continuum simulation. *Physics of Plasmas*, 16(5):055906, 2009.